UNIVERSITÀ DI PARMA

UNIVERSITÀ DEGLI STUDI DI PARMA

DOTTORATO DI RICERCA IN
INGEGNERIA INDUSTRIALE

CICLO XXXVIII

MODELLAZIONE MULTISCALA, INDAGINE SPERIMENTALE E APPLICAZIONI STRUTTURALI DI FIBRE DI NANOTUBI DI CARBONIO

Coordinatore:
Chiar.mo Prof. Alessandro Tasora

Tutore:
Chiar.mo Prof. Gianni Royer-Carfagni

Co-Tutore:
Chiar.mo Asst. Prof. Claudio Boni

Dottorando: Vincenzo A. Muratore

Anni Accademici 2022/2023 - 2024/2025

UNIVERSITÀ DI PARMA

UNIVERSITÀ DEGLI STUDI DI PARMA

PHD PROGRAM IN
INDUSTRIAL ENGINEERING

XXXVIII CYCLE

MULTISCALE MODELING, EXPERIMENTAL INVESTIGATION AND STRUCTURAL APPLICATIONS OF CARBON NANOTUBE FIBERS

Ph.D. Course Coordinator:
Prof. Alessandro Tasora

Thesis Advisor:
Prof. Gianni Royer-Carfagni

Thesis Co-Advisor:
Asst. Prof. Claudio Boni

Candidate: Vincenzo A. Muratore

Academic Years 2022/2023 - 2024/2025

A coloro che, in timido silenzio, ascoltano il mondo intorno,
possano trovare il coraggio di far sentire la propria voce,
perché in loro spesso risiedono idee di alto valore.

To those who, in timid silence, listen to the world around them,
may they find the courage to let their voice be heard,
for within them often lie ideas of great value.

Preface

The doctoral program has been for me much more than an academic journey: it was a unique opportunity for personal and professional growth, allowing me to explore new areas of knowledge and to face complex challenges, developing autonomy, curiosity, and determination. This experience has taught me to observe carefully, to reflect deeply, and to cultivate the patience necessary to turn ideas into tangible results, understanding the value of scientific rigor combined with creativity.

Those that help reduce our impact on the environment are meaningful innovations. Carbon NanoTube Fibers (CNTFs) represent a promising alternative to traditional materials such as steel, enabling high performance with minimal environmental impact. The possibility of developing lightweight, strong, potentially zero-emission, and recyclable materials motivated me to pursue this topic, combining scientific curiosity with a sense of responsibility toward the planet.

Looking beyond the scientific results, I believe that every research endeavor should represent a small contribution toward a more conscious future, hopefully founded on knowledge, respect, and kindness, in which humans rediscover the true meaning of life in family and nature communion. A tomorrow free from selfishness, yet oriented toward mutual commitment and the common good; where science and technology are not tools of domination, but bridges of harmony between humanity and the world around it. A world in which abundance does not equate to waste, but to care: in reusing what is old, repairing what is broken, and recognizing value even in the simplest forms of existence.

Abstract

This doctoral dissertation investigates the multiscale mechanical behavior of Carbon NanoTube Fibers (CNTFs), adopting a bottom-up, micro-to-macro approach that integrates theoretical modeling, experimental validation, and manufacturing innovation. The research develops a coherent framework spanning from the fundamental properties of individual Carbon NanoTubes (CNTs) to their aggregation as fibers to form structural elements such as yarns and ropes and their integration into advanced hybrid composite laminates.

This work begins with an overview of the history, properties and applications of CNTs, highlighting the challenges of translating their extraordinary nanoscale performance into macroscopic assemblies. A micromechanical model is then introduced to evaluate the effective tensile stiffness of CNTFs, accounting for CNTs modulus, misalignment, van der Waals interactions, and cross-linking effects. Building upon this foundation, the dissertation advances into the geometry and mechanics of twisted yarns, where analytical formulations based on differential geometry are validated through experiments on twisted rubber filaments, used as a macroscopic analogue for CNT-based structures.

The subsequent work focuses on the modeling and manufacturing of CNTF yarns, where analytical predictions and experimental campaigns are combined to optimize yarn geometry and performance. A dedicated yarn-making mechanism was designed, enabling the production of CNTF yarns with tailored properties. The effect of torsional loading on both single CNTFs and multi-fiber yarns is further examined, providing new insights into the role of twist in modulating stiffness, failure strain, and overall structural behavior.

Finally, the study addresses the integration of CNTFs into carbon fiber composite laminates, targeting improved damage tolerance and energy absorption in intrusion scenarios. Hybrid laminates with CNTF interlayers were experimentally tested, and a data-driven approach was employed to obtain the optimal configuration for the specimen as a function of geometry and material parameters.

Overall, this research establishes a systematic understanding of CNTFs and twisted yarn-like structures across scales, from the mechanics of single assemblies to their application in structural composites. By bridging modeling, experimental investigation, and composite design, the dissertation contributes both fundamental insights and practical strategies for exploiting CNTFs in next-generation lightweight, high-performance materials for aerospace, automotive, and defense applications.

Contents

Chapter 1

Introduction

1.1 Background

Since their discovery in the early 1990s, Carbon NanoTubes (CNTs) have drawn considerable attention due to their unique combination of properties, including outstanding mechanical strength, high electrical and thermal conductivities, and low density [1, 2]. These cylindrical nanostructures, composed of rolled-up sheets of graphene, represent one of the most promising building blocks in the field of nanotechnology and advanced materials science and have inspired significant scientific activity worldwide, crossing several disciplines [3].

However, translating the remarkable properties of individual nanotubes to the macroscale has been a persistent challenge. A major breakthrough in this pursuit is the development of Carbon NanoTube Fibers (CNTFs), macroscopic fibers composed of aligned CNTs. This innovation has opened new possibilities for the development of next-generation materials [4, 5]. By assembling CNTs into continuous threads, researchers have created lightweight, strong, conductive, and potentially sustainable fibers that can be integrated into structural and functional systems across sectors such as aerospace, electronics, textiles, and energy.

Beyond their exceptional intrinsic properties, CNTFs are also being explored within the context of sustainable material production. For instance, methane pyrolysis methods can generate CNTs alongside hydrogen, offering a pathway to low-emission or zero-carbon footprint manufacturing. Initiatives like the *Carbon Hub* [6] are actively promoting such technologies, aiming to transform natural gas into value-added carbon materials and clean energy without CO_2 emissions.

Despite significant progress, the full potential of CNTFs is still limited by a number of scientific and engineering challenges. These include scaling properties from the nanoscale to the macroscale, improving mechanical efficiency, and integrating fibers into complex material architectures. The hierarchical nature of CNTF assemblies, spanning from individual nanotubes to twisted yarns as shown in Figure 1.1, necessitates a comprehensive, multiscale approach that combines modeling, experimentation, and manufacturing optimization [7, 8].

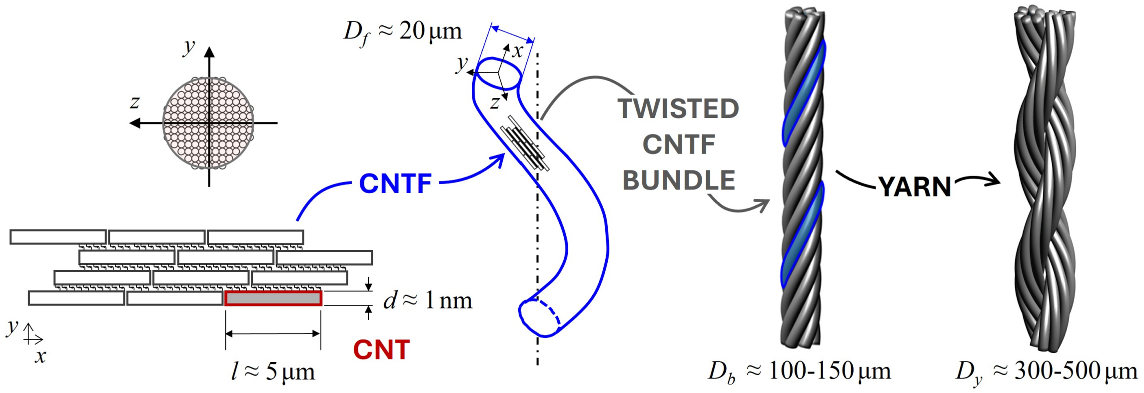

Figure 1.1. Schematic overview of the multiscale investigation approach, from nanotubes to yarns.

This doctoral research fits within this broader effort, aiming to advance the understanding and application of CNTF-based materials, presenting a systematic *micro-to-macro* investigation of CNTF materials. It integrates numerical modeling, experimental mechanics, and composite design, with the ultimate goal of developing reliable predictive tools and design strategies for high-performance CNTF-based components.

Co-funded by the Italian National Recovery and Resilience Plan (PNRR), and carried out in collaboration with both academic and industrial partners, the work involved a cross-disciplinary effort that included experimental testing, process development, and modeling across multiple scales.

In particular, the collaboration with *DexMat*[1], Inc., a U.S.-based company specializing in CNTF production, enabled experimental campaigns on CNTF yarns and provided valuable insights into fiber manufacturing processes. Moreover, a technology transfer collaboration with *Dallara*[2] SpA facilitated the exploration of CNTF integration into advanced composite structures, with particular emphasis on enhancing crash resistance and anti-intrusion performance for motorsport applications.

1.2 Objectives

This doctoral dissertation investigates the multiscale mechanical behavior of CNTFs, adopting a bottom-up, micro-to-macro approach. Building on a multiscale and multidisciplinary framework, the research seeks to bridge the gap between the nanoscale properties of individual CNTs and the macroscale performance of CNT-based yarns and composite structures. The ultimate goal of this work is to provide a scalable and

---

[1] DexMat, Inc. — Leading producer of conductive CNTFs, Houston, TX. https://dexmat.com/

[2] Dallara SpA — an Italian company specializing in the design and manufacturing of high-performance racing vehicles, Varano de' Melegari (PR). https://www.dallara.it/

experimentally validated methodology for the design and mechanical modeling of hierarchical CNT-based fibrous systems, establishing both fundamental understanding and practical guidelines for their structural integration. The main objectives of this thesis are outlined below.

- To develop an analytical model for the prediction of the effective tensile stiffness of CNTFs, accounting for nanoscale interactions and arrangement of CNTs.
- To explore and formalize the mechanics of twisted rod systems, establishing a theoretical model for the analysis of multi-ply yarns made of CNTFs.
- To experimentally validate the proposed analytical and numerical models through a surrogate system of twisted rubber yarns, enabling a controlled study of the role of prestress and twisting.
- To investigate the torsional dependence upon the mechanical properties of CNTFs and multi-fiber bundles, both experimentally and theoretically.
- To design and manufacture CNT-based yarns by bundling and twisting CNTFs, and to control their mechanical properties (e.g., tensile strength, toughness, creep resistance) based on the twist angle, number of plies, and geometrical parameters.
- To automatize the yarn-making process by using desired yarn parameters (e.g., bundle and yarn diameter, number of bundles and filaments, twist rate) as input, and providing the optimal machine speed parameters as output, thereby consistently producing yarns with peak mechanical properties.
- To implement CNTFs in hybrid composite laminates, evaluating their performance as interleaving layers in carbon fiber reinforced structures, particularly in anti-intrusion applications.

1.3 Outline

The work is organized in seven main chapters, in addition to this introduction. The chapters unfold from the fundamentals of CNTs to the study of individual CNT-based assemblies and gradually proceeds toward the design and optimization of complex twisted yarns and their integration in advanced high-performance composite laminates, combining theoretical modeling, experimental validation, and manufacturing innovation. The contents are structured as follows:

Chapter 2 – From Carbon NanoTubes to CNT-based materials

This chapter provides a comprehensive overview of CNTs, tracing their historical development and highlighting the key factors underlying their central role in modern materials science. Since their formal identification by Iijima in 1991, CNTs have attracted extensive research interest owing to their exceptional mechanical strength, high aspect ratio, electrical conductivity, and thermal performance. The chapter reviews their classification, synthesis methods, and typical structural defects, and presents an overview of the various macroscopic products that can be derived from CNTs, together with their classification and main characteristics. Particular attention is devoted to the challenges associated with scaling CNTs into macroscopic assemblies and to the techniques developed to align, bundle, and spin them into continuous fibers. The transition from individual nanotubes to CNT-based fibers is thus introduced, establishing the motivation and framework for the present doctoral research.

Chapter 3 – A model for the effective tensile stiffness of CNTF

This chapter presents a micromechanical model to evaluate the tensile stiffness of CNTFs composed of monodispersed Carbon NanoTubes arranged in a periodic square lattice. The CNTs are assumed to be axially misaligned and interact through lateral van der Waals forces and cross-links, modeled as distributed linear springs. CNTs are treated as elastic bars with defined axial stiffness, and under the hypothesis of periodicity, the governing equations reduce to a delayed-advanced differential formulation. A finite difference approach is employed to solve the equations and compute the effective axial stiffness of the fiber. The model predicts the influence of key parameters such as CNT length, offset, and stiffness on the fiber-level response, and its predictions are compared against existing literature to validate its accuracy.

Chapter 4 – Geometry and mechanics of twisted yarns: an experimental rubber model for the study of CNTFs

This chapter contributes to the theoretical foundations for the mechanical modeling of twisted fibers and yarns. It introduces the necessary differential geometric framework (Frenet-Serret and Darboux frames) to describe the curvature and torsion of helicoidal paths. The mechanics of twisted rods is discussed in the context of cable structures, with attention to internal contact and friction effects. A simplified model is derived for the axial stiffness of yarns composed of two helically wrapped filaments. To validate the analytical models, an experimental study is conducted using two-ply yarns composed of elastic rubber filaments. The objective is to understand the role of prestress and intrinsic eigenstresses in the final mechanical performance. Tensile tests are used to calibrate and verify the predictive capacity of the theoretical models, providing valuable insights into how twisting angle, number of plies, and yarn geometry influence the axial stiffness and failure behavior.

Chapter 5 – Manufacturing optimization of CNTF Yarns

This chapter uses the previous theoretical and experimental findings for the manufacturing optimization of CNTF-based yarns. Analytical and empirical models are proposed to describe the mechanical behavior of bundles and yarns composed of multiple CNTFs, including their sensitivity to twisting angle, ply number, and helical geometry. A manufacturing mechanism model was developed and implemented to make yarns from CNTFs, enabling experimental campaigns for tensile and creep testing. The optimization of the final yarn geometry was guided by both the analytical models and the collected experimental data, targeting high strength and compliance with structural applications. All the steps of this work have been finally collected into a software that takes into account the different parameters and calculates the best set up for the yarn-maker machine, in order to obtain a strong balanced yarn.

Chapter 6 – Effect of torsion on the mechanical properties of CNTFs and multi-fiber structures

This chapter focuses on the impact of torsional loading on the mechanical response of individual CNTFs and their assemblies. It includes both analytical modeling and experimental assessment of how the imposed twist affects tensile stiffness, failure strain, and structural stability. The study covers CNTFs composed of sub CNTF clusters (fibrils), highlighting the interplay between internal torsion, interfacial interactions, and global performance. This chapter examines the effect of pre-twist on the mechanical behavior of individual CNTFs, an aspect less explored compared to wound CNT yarns. Controlled pre-twisting experiments reveal a clear mechanical trade-off: a marked increase in ductility accompanied by reduced stiffness and strength. SEM observations show that pre-twist reorganizes the internal fibrillar structure into a helical arrangement. A mechanical model based on axial strain mismatch and enhanced inter-fibril confinement is proposed and validated using a macroscopic nylon analogue. The study provides a mechanistic understanding of twist-induced behavior and offers design guidelines for tailoring CNTF properties through controlled pre-twist.

Chapter 7 – Integration of CNTFs into carbon fiber composites for enhanced anti-intrusion performance

This chapter explores the hybridization of Carbon Fiber laminates through the introduction of CNTF-based interlayers, aiming to improve the performance of advanced composites under puncture and intrusion loading. Experimental tests were performed to quantify the benefits of CNTF interleaves on laminate punching strength and damage tolerance. A data-driven approach was adopted to optimize the configuration of the multilayer structure as a function of various geometric and material parameters.

Chapter 8 - Conclusions

The main outcomes of the dissertation are reported, providing a concise overview of the work carried out, highlighting the key aspects of each stage and their interconnections, while also outlining possible directions for future developments.

Chapter 2

From Carbon NanoTubes to CNT-based materials

Carbon NanoTubes (CNTs) are cylindrical nanoscopic structures formed by one or more rolled-up graphene layers, with a diameter of the order of 1 nm and typical length of 1–5 μm [7]. They are recognized as complete molecules consisting entirely of carbon atoms that form ordered cylindrical structures closed at the ends (Figure 2.1). Due to their distinctive physical, thermal and electrical properties [9–11], such as high strength, low density, high conductivity and biological compatibility, they represent a promising material for applications in nanoengineering [12, 13], electronics [14, 15], as well as in the biomedical field [16, 17]. Despite their small size and discrete molecular structure, CNTs were found to behave similarly to continuum structures with tensile and bending capacities, with a notably high Young's modulus up to 1 TPa [18, 19], and tensile strength up to 50 GPa [11].

A primary challenge in materials science has been the translation of these remarkable nanoscale properties to macroscopic structural elements. Initial approaches focused on incorporating CNTs as reinforcement within host polymeric matrices to form nanocomposite polymers [20–22]. The efficacy of this method, however, depends heavily on achieving high concentration, dispersion, and alignment of the CNTs within the matrix [23, 24].

A more direct pathway involves assembling the discrete nanotubes into continuous, matrix-free hierarchical structures, such as clusters or macroscopic fibers. In these assemblies, the mechanical behavior is governed by the interactions between weakly interacting tubes, primarily through van der Waals forces [25] and potential cross-linking [26, 27], which allow for compliant mobility associated with their relative longitudinal sliding.

2.1 Carbon NanoTubes

The discovery of CNTs represents a complex journey of scientific progress, characterized by multiple observations, theoretical predictions, and definitive characterizations

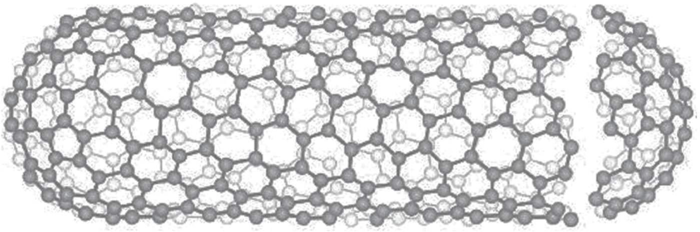

Figure 2.1. Carbon nanotube [28].

across several decades and continents. While Japanese physicist Sumio Iijima, portrayed in Figure 2.2 with a model of the atomic structure of a CNT, is widely recognized for his systematic discovery and characterization in 1991, the historical record reveals significant groundwork laid by earlier researchers.

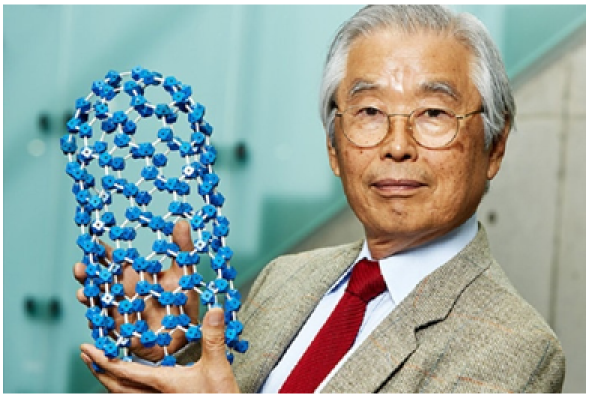

Figure 2.2. Sumio Iijima, whose 1991 Nature paper first conclusively characterized Multi-Walled carbon nanotubes using high-resolution transmission electron microscopy [28].

2.1.1 Discovery and early history of CNTs

The earliest documented evidence of nanotube-like structures dates back to 1952, when Soviet scientists Radushkevich and Lukyanovich published transmission electron micrographs (TEM) showing hollow carbon fibers with 50 nm diameters in the Zhurnal Fizicheskoi Khimii [29]. Due to Cold War-era limited circulation and language barriers, this pioneering work remained largely unknown to Western researchers for decades. An electron micrograph image from their 1952 paper (Fig. 2.3) clearly shows tubular carbon structures, now recognized as Multi-Walled Carbon NanoTubes (MWCNTs).

Further pre-Iijima observations include:

1960: Bollmann and Spreadborough observed "scroll-like" carbon structures, publishing high-resolution transmission electron microscopy (HRTEM) images showing Single-Walled NanoTube (SWCNT) like features while studying graphite layers [30].

1976: Morinobu Endo and colleagues observed "graphitic whiskers" during benzene pyrolysis experiments [31]. Independently, Oberlin, Endo, and Koyama also reported

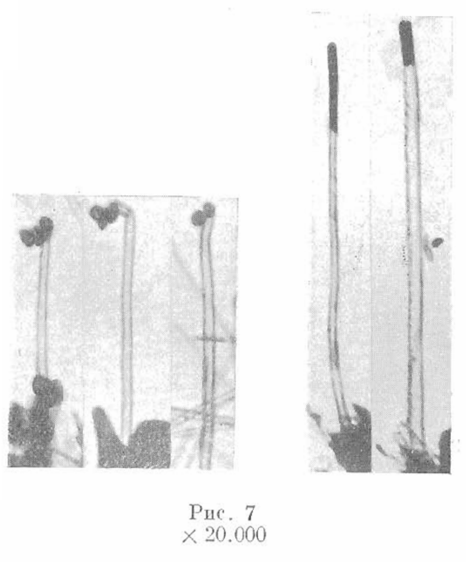

Figure 2.3. Electron micrograph from Radushkevich and Lukyanovich's 1952 paper, showing what now is recognized as Multi-Walled Carbon NanoTubes [29].

hollow carbon fibers with nanometer-scale diameters produced via vapor-phase growth [32]. These structures are now recognized as MWCNTs but were not systematically characterized at the time.

1979: Abrahamson documented tubular carbon formations during arc-discharge experiments [33].

A crucial theoretical foundation for understanding new carbon allotropes emerged in 1985 with Richard Smalley's discovery of C_{60} buckminsterfullerene [34], for which he shared the 1996 Nobel Prize in Chemistry with Robert Curl and Harold Kroto. This breakthrough demonstrated carbon's ability to form closed-cage structures. Adding to the theoretical insights, Soviet scientists Bochvar and Gal'pern had theoretically predicted, in 1981, the existence of SWCNTs through quantum chemical calculations [35], in which they described what are now recognized as (n,n) armchair nanotubes.

The modern era of CNT research began in 1991 with Sumio Iijima's pivotal experiment at NEC Corporation. Using HRTEM, Iijima conclusively characterized MWCNTs formed by vaporizing graphite electrodes [28]. These nested cylindrical graphene sheets, with diameters of 4–30 nm and lengths up to 1 μm, exhibited notable regularity and high mechanical properties, including an estimated tensile strength of 150 GPa and elastic modulus approaching 1 TPa. Iijima noted their potential for "opening a new door to nanosize science of carbon materials".

Iijima's 1991 discovery quickly sparked global interest, leading to rapid advancements:

In 1992, Ebbesen and Ajayan demonstrated gram-scale production of MWCNTs, making systematic studies possible [36]. Also in 1992, Mintmire, Dunlap, and White theoretically predicted CNTs' distinctive electronic properties, showing they could behave as either metals or semiconductors depending on their chirality [37].

In 1993, Iijima and Toshinari Ichihashi [38], and independently Donald Bethune's group at IBM [39], reported the successful synthesis of SWCNTs using metal catalyst particles.

The full recognition of CNTs' potential came through subsequent work by multiple research groups, including the Rice University team led by Smalley, who developed the high-pressure carbon monoxide (HiPCO) process for SWCNT production in 1996 [40]. These parallel discoveries underscore the collaborative nature of nanoscience advancement.

Table 2.1 summarizes these key milestones in the discovery and early characterization of CNTs:

Year	Contribution	Researchers
1952	First TEM images of hollow carbon fibers	Radushkevich and Lukyanovich
1976	Observation of graphitic whiskers	Endo et al.
1981	Theoretical prediction of SWCNTs	Bochvar and Gal'pern
1985	Discovery of C_{60} fullerene	Smalley, Kroto, Curl
1991	Definitive characterization of MWCNTs	Iijima
1993	Synthesis of SWCNTs	Iijima and Ichihashi

Table 2.1. Key milestones in CNT discovery

This complex history illustrates how scientific discovery often involves multiple contributors across time and geography. While Iijima's work provided the definitive foundation for modern CNT science, earlier researchers laid important groundwork, and subsequent theorists and experimentalists collectively revealed the vast potential of CNTs across various applications.

2.1.2 CNTs geometry: chirality and SW-, DW-, MW- configurations

The body of a CNT is formed by carbon atoms arranged in hexagonal lattices, while its closure caps contain both hexagonal and pentagonal rings, as seen in Figure 2.4; this structure is why CNTs can be considered a type of large fullerene. Due to this conformation, nanotubes often have structural defects or imperfections that deform the cylinder.

The diameter of an unsupported SWCNT ranges from 0.4 nm to 6 nm [41]. The extremely high length-to-diameter ratio (on the order of 10^4) allows them to be considered virtually one-dimensional nanostructures and imparts distinctive properties to these molecules [42].

The properties of CNTs depend strongly on their geometry, particularly their diameter, length, and chirality. The chirality, i.e., the angle at which the carbon sheet is oriented relative to the tube axis, strongly influences their electronic properties. Specifically, CNTs can be classified by geometry into three types of structures, i.e., zig-zag, armchair, or chiral (Figure 2.5) and by the number of graphene sheets rolled

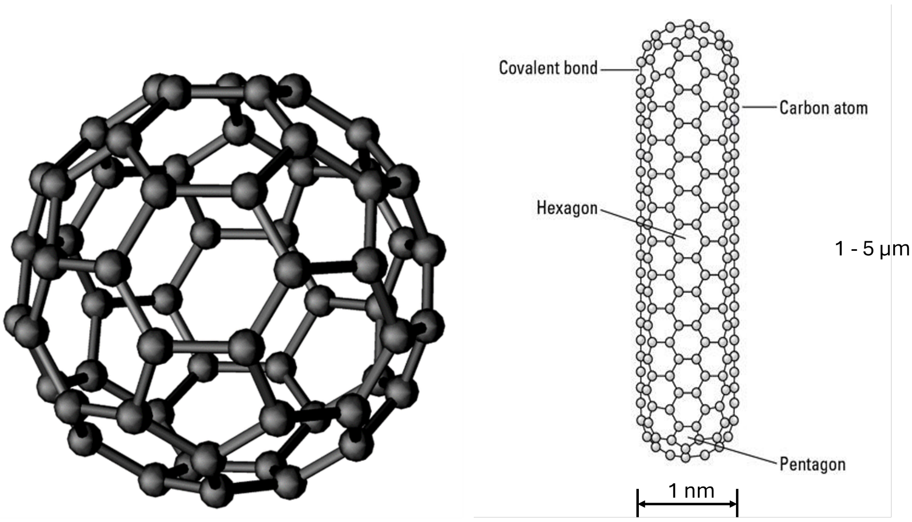

(a) (b)

Figure 2.4. (a) fullerene and (b) CNT structures [9].

concentrically into Single-Walled (SWCNT), Double-Walled (DWCNT), Few-Walled (FWCNT) or Multi-Walled (MWCNT) configurations (Figure 2.6).

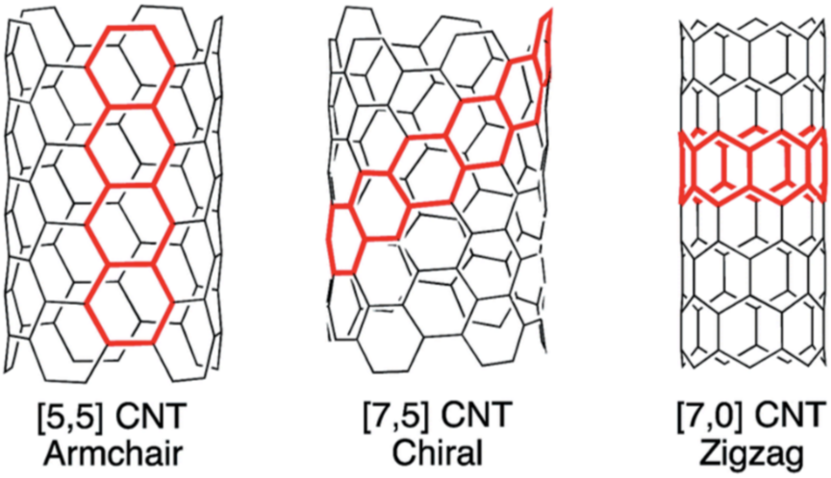

Figure 2.5. Chirality: armchair, chiral and zig-zag nanotube geometries [9].

A SWCNT can be seen as a sheet of graphene that has been rolled into a tube, as represented in Figure 2.7. A MWCNT instead consists of concentric graphitic cylinders with closed caps on both ends, where the graphitic layer spacing is about 0.34 nm [43].

Unlike diamond, which assumes a 3-D crystalline structure with each carbon atom having its four nearest atoms arranged in a tetrahedron, as shown in Figures 2.8(a) and 2.8(c), graphite takes the form of a 2-D sheet of carbon atoms arranged in a

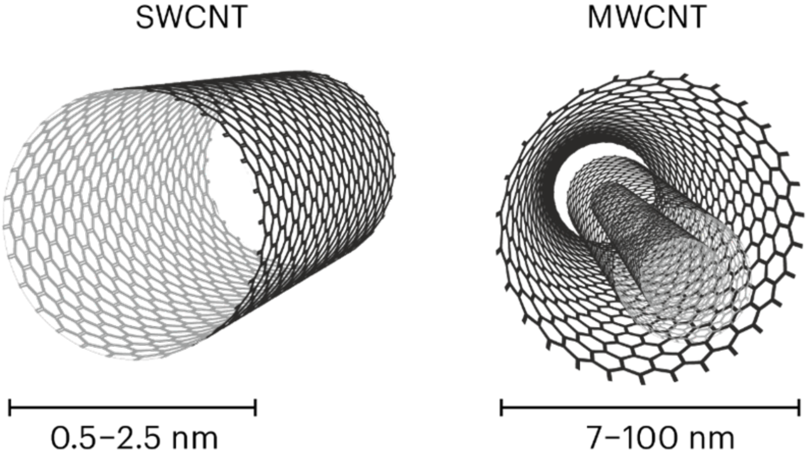

Figure 2.6. Representation of a SWCNT and a MWCNT [43].

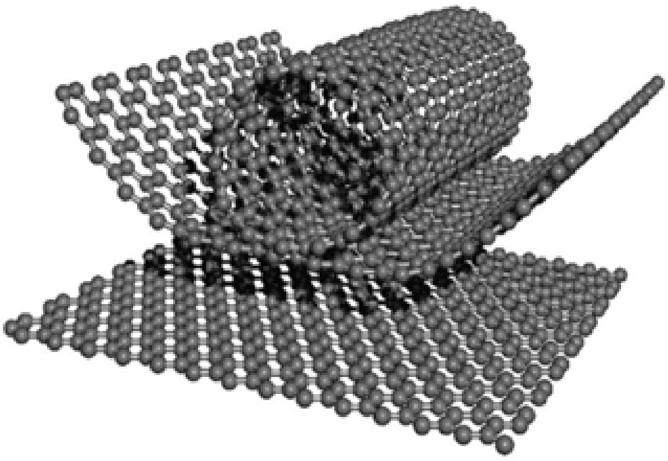

Figure 2.7. Wrapping a single graphene layer into an SWCNT [44].

hexagonal matrix, as shown in Figures 2.8(b) and 2.8(e). In this case, as well as for the CNT shown in Figure 2.8(f), each carbon atom has three neighboring atoms.

CNTs can form following three different patterns based on the preferred winding direction, as illustrated in Figure 2.9. Although every CNT has the same constituents (carbon atoms arranged in a hexagonal lattice), various properties, such as conductivity level, vary with chirality. The growth of SWCNTs with a specific desired chirality has so far been achieved only in laboratory, but not at an industrial level [43, 45].

From the perspective of molecular mechanics, a CNT can be considered as a large molecule consisting of carbon atoms, where the atomic nuclei can be considered as material points. Their movements are governed by a force field, which is generated by electron-nucleus interactions and nucleus-nucleus interactions [44]. Usually, the force field is expressed in the form of steric potential energy and depends exclusively on the relative positions of the nuclei that constitute the molecule.

When carbon is bonded to four other atoms, the hybridization is sp^3, and the

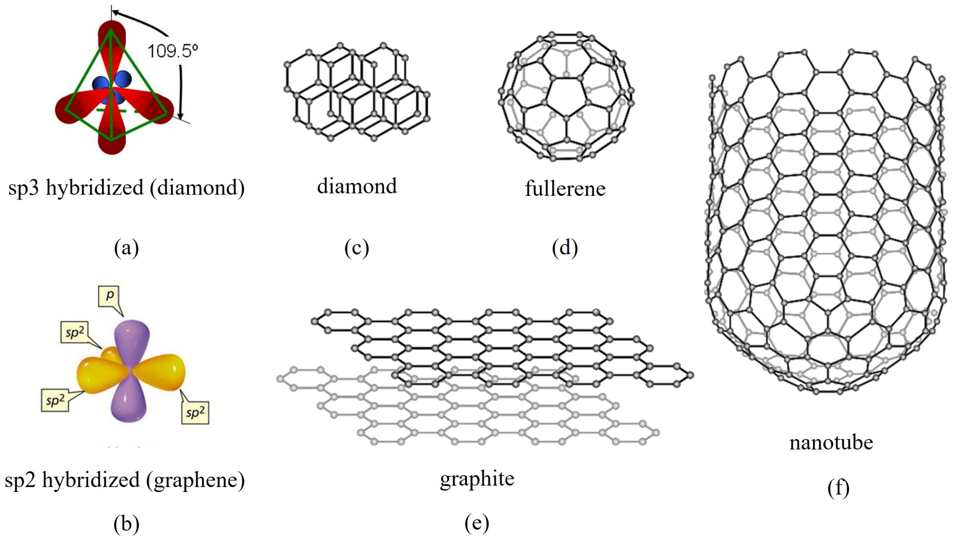

sp3 hybridized (diamond)

(a)

diamond

(c)

fullerene

(d)

sp2 hybridized (graphene)

(b)

graphite

(e)

nanotube

(f)

Figure 2.8. (a) Hybridization sp3; (b) Hybridization sp2; (c) Diamond structure; (d) Fullerene C60 structure; (e) Graphite structure; (f) End of a CNT [43].

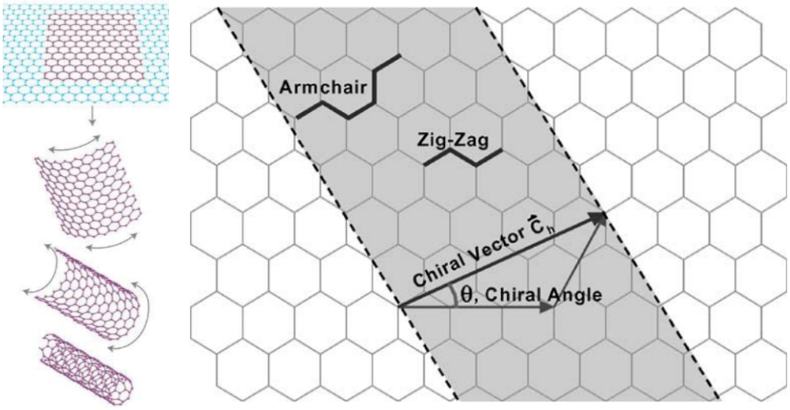

Figure 2.9. Wrapping of a hexagonal graphene sheet and resulting chiralities [9, 42].

atomic arrangement is tetrahedral, as shown in Figure 2.8(a). A carbon atom bonded to three other atoms is instead sp^2 hybridized, forming a planar trigonal configuration with 120° bond angles, as illustrated in Figure 2.8(b). This configuration also gives rise to π bonds, which originate from the overlap of two unhybridized p orbitals.

In CNTs, the atomic configuration is primarily sp^2, with strong σ bonds forming along the tube surface and π bonds oriented perpendicularly to it. However, due to the inherent curvature of the nanotube wall, the trigonal arrangement of the carbon atoms is no longer perfectly planar, as schematically represented in Figure 2.10(a). This curvature causes an asymmetry between the inner and outer π bonds, resulting in a slightly stronger π interaction on the external surface (Figure 2.10(b)). Such an effect can promote lateral bonding or interaction between adjacent CNTs. It must be noted, however, that this is a simplified representation, intended only to illustrate the bonding principle, without accounting for more complex phenomena such as dispersion forces or ionic effects.

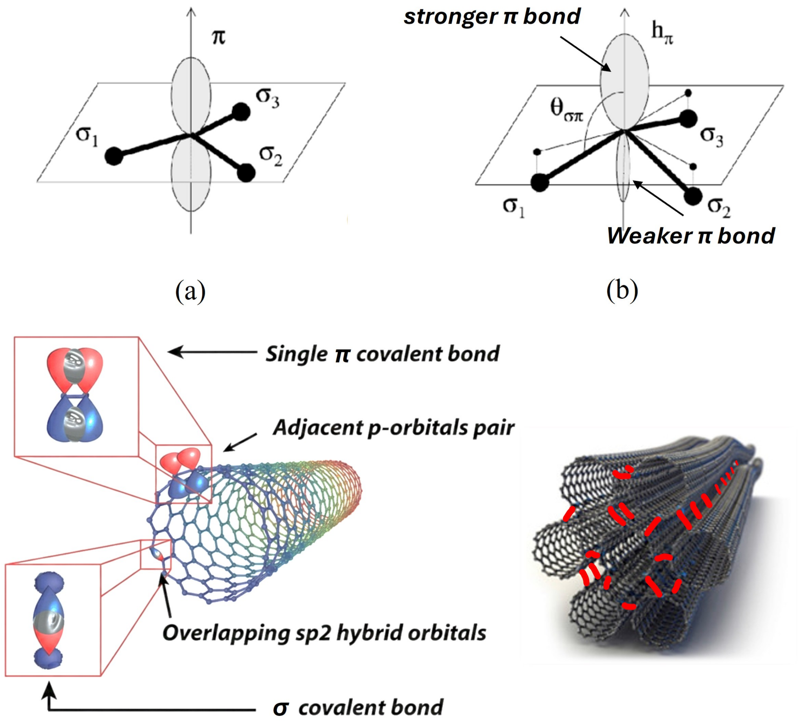

(a) (b)

(c) (d)

Figure 2.10. Representation of the CNTF bonding: (a) graphene structure sp2 hybridized; (b) bonding mutation in bending graphene sheet; (c) representation of bonds of the CNT; (d) forming CNT Clusters [46].

Within the CNT structure, carbon atoms are covalently bonded to one another, forming a network of hexagons on the tube wall, as shown in Figure 2.10(c). These covalent bonds exhibit specific bond lengths and angles in three-dimensional space. When a nanotube is subjected to external loads, the motion of each atom is constrained by its neighboring bonds, and the overall deformation of the nanotube results from the collective response of these atomic interactions [47]. Considering each covalent bond as a connecting element between carbon atoms, the nanotube can be modeled as a space truss-like structure, where carbon atoms act as the nodes of the truss [44].

2.1.3 CNTs physical and mechanical characteristics

Based on simulations and experimental results, CNTs have been recognized as among the strongest materials known [48]. Graphite has an in-plane Young's modulus of 1.06 TPa [18], and due to their sp^2 carbon-carbon bonding, CNTs are expected to show similar stiffness. Consequently, numerous studies have focused on the feasibility of using CNTs as reinforcement, to obtain strong and lightweight materials. Despite experimental difficulties, there have been many reports on the mechanical properties of CNTs. Earlier experimental measurements were performed using a mechanical loading stage integrated within a scanning electron microscope, enabling the first in situ tensile tests on individual SWCNTs and MWCNTs [49]. Reported values for SWCNTs indicated tensile strengths between 13 and 52 GPa and Young's moduli ranging from 320 to 1470 GPa. For MWCNTs, the outer shell strength varied from 11 to 63 GPa, with corresponding moduli between 270 and 950 GPa, and an average bending strength of approximately 14 GPa. More recent measurements on SWCNTs report Young's modulus values between 1.24 and 2.17 TPa [50], and tensile strengths in the range of 25–66 GPa [51].

Additional theoretical studies have also addressed the mechanical properties of CNTs, with some showing agreement with experimental observations. It has emerged that SWCNTs show sliding between tubes within clusters, and due to their weak interlayer bonding, MWCNTs are inefficient at transferring load to their inner shells [52].

The electrical behavior of CNTs arises from their one-dimensional (1D) electronic structure derived from graphene [14]. SWCNTs can be metallic or semiconducting depending on their chiral vector (n, m), with approximately one-third metallic and two-thirds semiconducting [15]. MWCNTs, owing to inter-shell coupling, behave as highly conductive quasi-1D systems, capable of sustaining current densities above 10^9 A/cm^2 [53, 54].

Thermal transport in CNTs is phonon-dominated, with predicted axial conductivities up to 6000 W/(m · K) for SWCNTs and measured values above 3000 W/(m · K) for MWCNTs [55, 56]. They also exhibit high thermal stability up to about 2800°C in vacuum [57].

2.1.4 CNTs applications

Nanotubes can be synthesized using various techniques, through both carbon vaporization and laser use. What all processes have in common is the result: a large fraction of the produced nanotubes have imperfections that make them practically unusable. This creates the need to purify the product. There are numerous purification systems, but they all share the problem of being unable to separate target nanotubes without damaging them. Indeed, extensive purification can lead to significant loss of produced nanotubes and can seriously damage their initial morphology (some techniques have rejection levels exceeding 90%) [58]. All this results in extremely high production costs that limit research to major study and development centers.

CNTs have been the subject of extensive research aimed at understanding and exploiting their notable physical, chemical, and mechanical properties. Depending on their chirality and diameter, CNTs can exhibit either metallic or semiconducting behavior, thus enabling innovative approaches in nanoelectronics, where smaller and faster devices can be fabricated [59]. For instance, semiconducting SWCNTs have been used to produce high-performance field-effect transistors (FETs) with high on/off ratios and carrier mobility, while metallic SWCNTs have been employed in conductive nanocomposites and transparent conductive coatings [60].

The versatility of CNTs has led to a broad spectrum of potential applications across different technological fields. In optoelectronics, they are used in light-emitting diodes (LEDs), solar cells, and transparent electrodes [61]. Their electromechanical response has also been exploited to develop CNT-based actuators, using paper-like or bimorph configurations [62]. At the Massachusetts Institute of Technology, batteries based on CNTs are under development [63], while researchers at Case Western Reserve University are exploring self-assembling nanotube structures. Similarly, the Department of Chemistry and Environmental Sciences at the New Jersey Institute of Technology reported promising results suggesting the feasibility of low-cost CNT-based photovoltaic cells.

CNTs are also finding applications in advanced materials and structural engineering. The English company Surrey NanoSystems developed *Vantablack* (Figure 2.11), a CNT-based coating recognized as one of the darkest materials produced, capable of absorbing 99.965% of visible light [64]. At a nanoscopic scale, IBM researchers demonstrated a 9-nanometer CNT transistor, proving that CNT-based devices can outperform silicon transistors even below the 10-nanometer threshold [15]. Furthermore, within the European NaPhoD project, several universities have collaborated to encapsulate photoactive organic molecules inside CNTs, opening new opportunities in photonic and hybrid nanomaterials research [65].

CNTs have attracted growing attention also in the biomedical field, thanks to their combination of electrical conductivity, mechanical strength, and biocompatibility. Recent research has demonstrated that CNTs can serve as effective platforms for drug delivery, tissue regeneration, and bioelectronic interfaces.

In neuro-engineering, MWCNT substrates have been shown to promote neuronal adhesion and enhance electrical signaling. For instance, mouse hippocampal neurons cultured on MWCNT layers directly grew [66] on supporting surfaces exhibiting significantly improved neuronal activity and network connectivity compared to control substrates. The CNT–neuron interface was found to facilitate signal propagation and synaptic plasticity, highlighting the potential of CNTs in neural interfacing and neuroprosthetic technologies.

Cardiac tissue engineering has also benefited from the integration of CNT-based materials. CNT-infused scaffolds have demonstrated the ability to enhance cardiomyocyte proliferation, differentiation, and functional maturation. In particular, [67] showed that neonatal rat ventricular myocytes cultured on CNT-coated substrates developed more physiologically mature syncytia, characterized by improved sarcomeric organization, enhanced electrophysiological properties, and upregulation of cardiac-specific genes. The incorporation of CNTs within the scaffold provided an electrically conductive microenvironment that promoted synchronous contraction and efficient electrical coupling among cardiomyocytes.

Single-walled CNTs incorporated into collagen substrates were utilized [68] as growth supports for neonatal cardiomyocytes, which enhanced cardiomyocyte adhesion and maturation. Furthermore, through the use of immunohistochemical staining, western blotting, transmission electron microscopy, and intracellular calcium transient measurement, it was discovered that the addition of CNTs remarkably increased ID-related protein expression and enhanced ID assembly and functionality.

A broader overview of these advances is presented by [69], where recent developments in CNT-based scaffolds for myocardial tissue regeneration are reviewed. The authors emphasized that CNT nanocomposites, due to their tunable conductivity and biocompatibility, represent promising candidates for next-generation cardiac patches and implantable bioelectronic devices. Their multifunctionality allows simultaneous mechanical reinforcement, electrical conduction, and biomolecular interaction, which are key to guiding cell behavior and improving tissue regeneration outcomes.

In diagnostics, functionalized MWCNTs have been tested in vitro and in vivo as ultrasound contrast agents, demonstrating prolonged echogenicity and low cytotoxicity [70].

Overall, the versatility of CNTs, from electronics to medicine, continues to drive research toward their integration in next-generation technologies, where their structural, electrical, and multifunctional properties can be fully exploited.

Figure 2.11. Vantablack: one of the darkest materials produced [71].

An important issue concerns the toxicity of CNTs. Research in this field is still in its early stages, and numerous studies are currently underway to assess potential health risks associated with ingestion or inhalation of CNTs. Preliminary results highlight the challenges in evaluating the toxicity of this heterogeneous material. It has been shown that certain CNTs can bypass the body's natural defenses, translocate to organs, and trigger inflammatory and fibrotic reactions. Inhalation exposure to MWCNTs, for example, results in lung deposition and persistent inflammation, with activation of alveolar macrophages and interstitial fibrosis lasting for months after exposure [72–74]. Similarly, SWCNTs have been reported to provoke robust inflammatory responses and early-onset fibrosis in mouse lung tissue following aspiration or inhalation [75]. Overall, exposure to respirable CNTs, regardless of synthesis method or metal impurities, has been consistently associated with inflammatory, fibrotic, and sometimes granulomatous lung lesions [73, 76, 77].

Under certain conditions, CNTs can penetrate the cytoplasm and induce apoptosis (cell death) [78]. Moreover, rodent studies have shown that CNT exposure can lead to epithelioid granulomas, fibrosis, and alterations in lung biochemical and toxicological function. The needle-like shape of CNTs resembles that of asbestos fibers, leading to the hypothesis that, like asbestos, CNTs may induce mesothelioma and pleural diseases, particularly when long, rigid, and biopersistent fibers are involved [79–81].

Environmental applications have emerged as another growth area. CNT-based water filtration membranes demonstrate removal efficiencies exceeding 99% for heavy metals, while agricultural applications show 30–50% improved nutrient uptake efficiency [82]. Composite materials incorporating CNTs exhibit fracture toughness improvements of 200–400% compared to baseline materials [83], with thermal management composites achieving conductivities exceeding 400 $\mathrm{W/m \cdot K}$ [84].

Given the novelty of these technologies, these studies naturally require further investigation, and it remains to be verified whether such effects evolve into cancerous forms [42].

2.2 CNT-based materials

The mechanical properties of CNTs make them suitable candidates for structural applications [85].

Although CNTs have high structural capacity, their dimensions are very small, with diameters on the order of 1 nm and lengths of 1–5 μm. The problem thus arises of how to organize CNTs into structural elements for large-scale applications. When assembled within a matrix, their strength is compromised by defects, impurities, random orientations, discontinuous lengths, and weakness of the matrix itself.

A large number of CNTs aggregated together allows the creation of structures at larger dimensional scale that partially inherit the properties of CNTs.

CNTs can be dispersed in a polymer matrix to create CNT-based composites (Figure 2.12(a)) for different applications. CNT clusters (Figure 2.12(b)), produced and studied mainly during the 1990s and the early 2000s, are composed of a limited number of CNTs (of the order of $10 \div 10^2$), and have diameter of about $10 \div 20$ nm. On the other hand, CNT Fibers (Figure 2.12(c)) with diameter of the order of $10 \div 100$ μm, composed of a larger number of CNTs, are obtained by means of different techniques, which can be divided into “liquid” methods (wet spinning [5, 86]), where CNTs are dispersed into a liquid and solution-spun into fibers, and “solid” methods (dry spinning [87, 88]), where CNTs are directly spun yarn-like fibers. However, these processes yield fibers whose properties do not yet approach optimal values [89, 90].

In the literature, there is often a significant degree of inconsistency and overlap in the terminology used to describe CNT-based assemblies. This confusion arises mainly from the wide variety of fabrication routes, hierarchical structures, and scales involved in CNT materials. For instance, the term CNT Fiber is sometimes employed to describe what are, in fact, bundles of CNTs, while bundle itself may refer

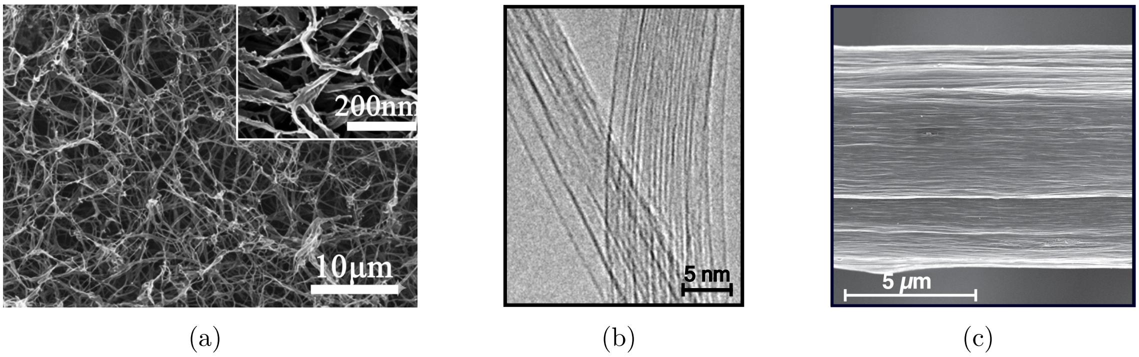

(a) (b) (c)

Figure 2.12. (a) SEM observations of Poly-L-lactic acid (PLLA) nanofibrous scaffolds containing MWCNTs [91]; (b) High-resolution TEM image of pristine Single-Walled CNT clusters [92]; (c) SEM image of the surface morphology of a CNT Fiber [6].

to small agglomerates of nanotubes or subunits within a larger fiber structure. Moreover, the term CNT Yarn (CNTY) is occasionally used interchangeably with CNT Fiber, particularly to denote fibers produced through the dry-spinning process. Such nomenclature can lead to misinterpretations when comparing mechanical properties or processing methods across different studies.

To ensure clarity and consistency throughout this work, the following well-defined terminology is adopted:

- **CNT:** Carbon NanoTube - the basic building block.
- **CNT Composite:** composite of CNTs dissolved in a polymer matrix.
- **CNT Cluster:** a small cross-sectional area and limited length agglomerate of CNTs.
- **CNT Fiber (CNTF):** a larger, aligned assembly of CNTs (possibly formed by CNT clusters), characterized by significant cross-sectional area and length. (Note: CNTF is used as the primary acronym for this assembly hereafter).
- **CNTF Bundle:** an arrangement of several parallel CNT Fibers.
- **CNTF Yarn:** a twisted assembly composed of CNTF bundles.
- **CNTF Cable and Rope:** an assembly composed of CNTF bundles or CNTF Yarns.
- **CNTF Fabric:** woven fabric of CNTF bundles or CNTF Yarns.
- **CNTF Composite:** Laminated composite of CNTF Fabric into polymer matrix.

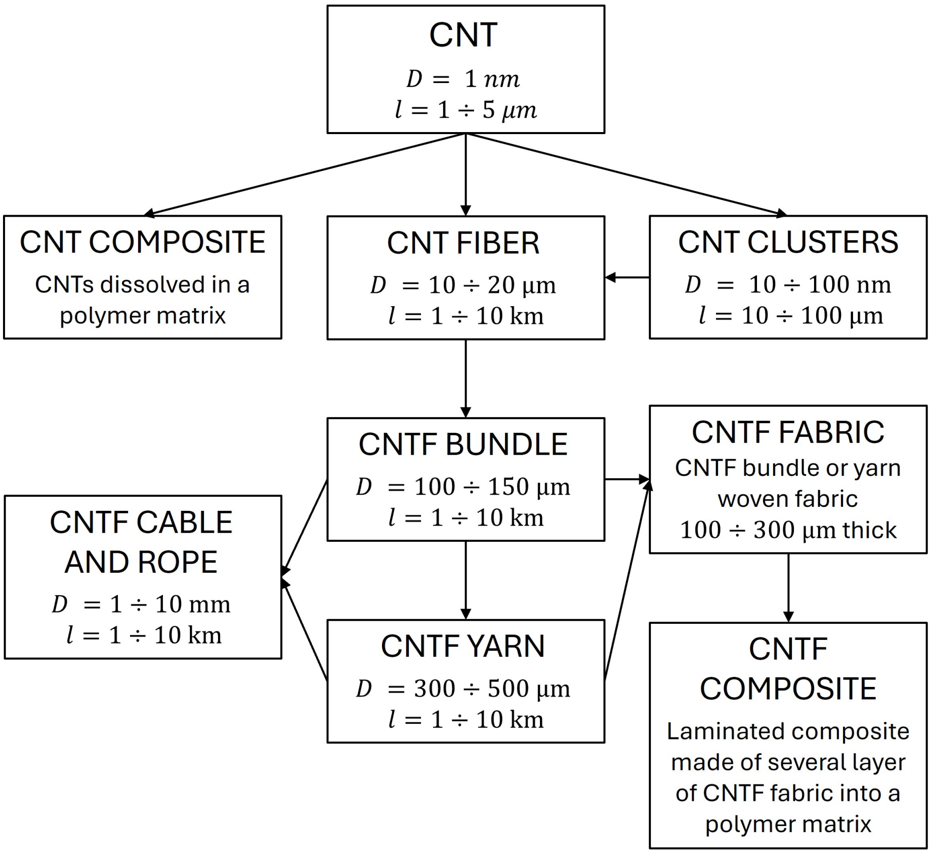

Figure 2.13. Various CNTs assemblies: CNT, CNT Composite, CNT Cluster, CNT Fiber, CNTF Bundle, CNTF Yarn, CNTF Cable and Rope, CNTF Fabric and CNTF Composite

A schematic representation of the different assemblies that can be obtained is reported in Figure 2.13. The following Sections will explore these elements in detail, while CNTF Fabrics and Composites will be discussed extensively in Chapter 7.

2.3 CNT-based composites

A composite material is defined as a system comprising two or more distinct phases that maintain their individual identities while interacting through an interface. This synergistic combination yields properties that cannot be achieved by any constituent phase alone [43, 93]. The fundamental architecture typically consists of a reinforcement phase, which provides mechanical or functional performance, embedded within a continuous matrix that ensures structural cohesion and facilitates load transfer.

While conventional fiber-reinforced composites have approached their practical optimization limits at the microscale [94], the development of nanocomposites has emerged as a viable pathway for further advancement. Initial nanocomposite systems utilized fillers such as carbon black or silica in polymeric matrices [95]. However, the introduction of CNTs has opened new avenues due to their high aspect ratio and intrinsic multifunctionality. Consequently, CNT-polymer nanocomposites have become a principal research focus, enabling the enhancement of polymer properties with the distinctive electrical, thermal, and mechanical characteristics of CNTs [20].

Their fabrication primarily relies on three approaches: solution processing, melt processing, and in situ polymerization. In *solution processing* (Figure 2.14), CNTs are dispersed in a solvent and mixed with a soluble polymer matrix using mechanical stirring or sonication. *Melt processing* (Figure 2.15) is mainly employed for thermoplastic matrices, providing scalability and industrial relevance. *In situ polymerization* (Figure 2.16) allows integration within thermally unstable or insoluble polymers, yielding strong CNT–matrix interfacial bonding.

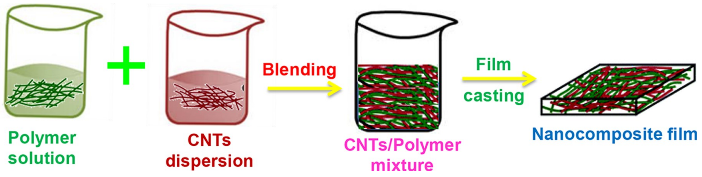

Figure 2.14. Schematic image of the "solution" process [94].

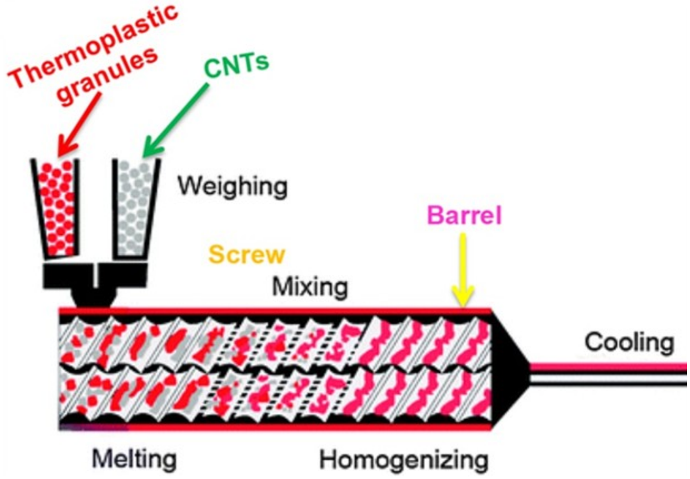

Figure 2.15. Schematic representation of a twin-screw extruder for melt-phase mixing of CNTs with thermoplastic matrices [96].

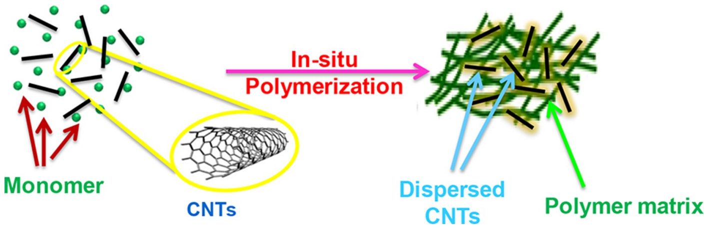

Figure 2.16. Schematic representation of the in situ polymerization process [97].

The performance of CNT-polymer nanocomposites depends strongly on CNT dispersion, alignment, and interfacial adhesion [43, 97]. While stiffness and strength generally increase with CNT loading, excessive content or poor dispersion can lead to agglomeration and mechanical degradation. Surface functionalization of CNTs improves compatibility with polymer matrices and enhances interfacial load transfer. Alignment [43] also plays a crucial role: oriented CNTs significantly improve anisotropic mechanical and electrical properties compared to randomly distributed ones.

CNT-based composites find applications in multifunctional materials for electromagnetic interference (EMI) shielding, thermal management, energy storage, and lightweight structural components. Despite these advances, key challenges remain, notably achieving homogeneous dispersion and controlled orientation of CNTs without compromising their intrinsic properties. Further progress in functionalization and processing techniques is required to fully exploit CNTs within high-performance structural composites [94].

2.4 CNT Clusters

In general, production techniques yield CNT aggregates in weakly interacting clusters (Figure 2.17) with compliant mobility associated with their relative sliding along longitudinal contact regions. Their collective mechanical behavior originates not only from the covalent bonds between atoms within each CNT, but also from the weak van der Waals interactions, which connect the different CNTs [8, 25, 98]. In general, the mechanical properties of CNT aggregates are strongly influenced by their micro- and macro-structure, which is dictated by manufacturing methods and processing techniques, because the arrangement of CNTs and their interactions depend significantly on the manufacturing process. During the 1990s and early 2000s, CNT clusters with diameters of 10–20 nm, composed of a limited number of CNTs (of the order of 10–100) with uncontrolled microstructure, were produced and studied.

The transfer of shear forces between adjacent CNTs, which greatly influences the mechanical properties of the cluster, has been studied by several authors, mainly using molecular models [101–103] and corroborated by experiments [49, 104]. The stiffness of clusters can be increased by cross-linking the constituent CNTs (Figure 2.18), using electron beams [48, 105], ion irradiation [106], cycloaddition reactions [107] and other techniques [26]. The bonding between adjacent nanotubes increases the shear transfer capacity and, therefore, improves the effective mechanical properties of the cluster [7].

The bending of microscopic CNT clusters (composed of a limited number of CNTs) has been characterized both theoretically and experimentally [108–110] but the works that specifically consider the flexural stiffness of macroscopic fibers composed of a large number of CNTs (typically on the order of 10^6–10^8 on the fiber section) are significantly fewer [7]. Some authors have exploited the theory of layered sandwich beams [111, 112] to propose simplified models, but these are characterized by very restrictive assumptions. Through gas flow synthesis, it has been possible to manufacture CNT Clusters with tensile strength greater than 80 GPa [85], but their length remains

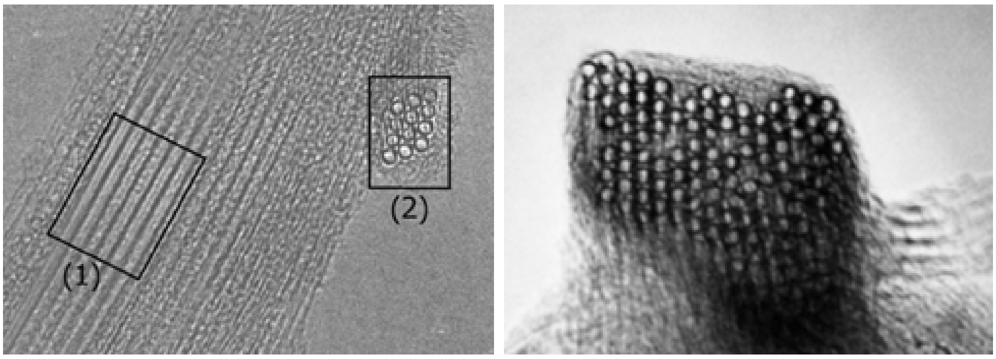

(a) (b)

Figure 2.17. (a) High-resolution TEM image of a Single-Walled CNT cluster with electron beam perpendicular (1) or parallel (2) to the cluster axis [99]; (b) High-resolution TEM image of a CNT clusters [100].

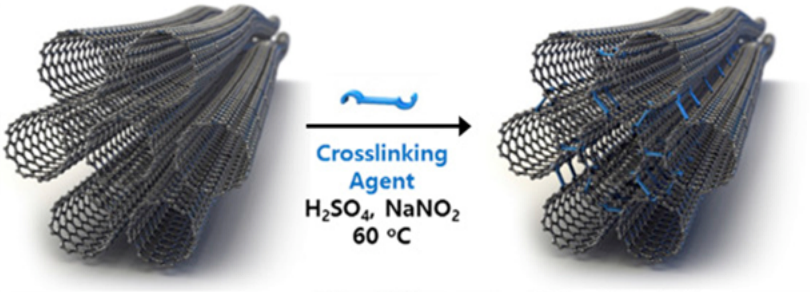

Figure 2.18. Cross-link between CNTs [27].

limited to a few centimeters.

2.5 CNT Fibers

In the last decade, new production techniques [5, 86, 113, 114] have made it possible to obtain macroscopic continuous fibers, composed of a large number of well-organized CNTs. CNTFs, with a diameter of 10–100 μm and a substantially continuous length (tens of meters and more), are suitable for high-value applications in the electronic, aerospace, and biomedical fields, and, thanks to their flexibility, can evolve into engineered materials [7]. Figure 2.19 shows SEM images of the surface morphology of a fiber.

CNTFs are promising for large-scale components as they exhibit mechanical and electrical properties capable of competing with both high electrical resistance fibers (such as aramid or Carbon Fibers) and conductive fibers. Following the significant introduction of aqueous suspension spinning by Poulin's group [117], the solution-spinning process has proven effective for the production of CNTFs with highly aligned densely packed microstructures of short CNTs (below 10 μm), hereinafter referred to

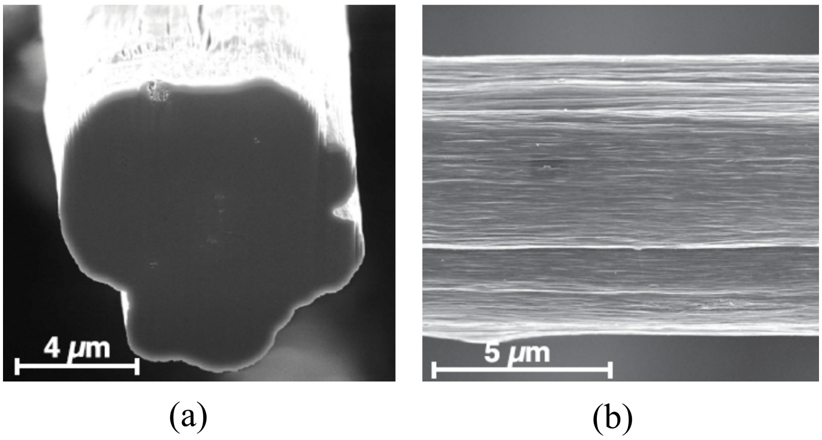

Figure 2.19. (a) SEM image of the fiber surface morphology; (b) fiber section obtained by focused ion beam milling. The fiber is not perfectly round, indicating imperfect coagulation; however, it shows few voids, indicating a densely packed structure, as in previous reports [115, 116].

as solution-spun CNTFs (SS-CNTFs). In current times high-throughput wet spinning procedures [6, 54] have allowed to obtain macroscopic continuous SS-CNTFs, composed of highly oriented and well-packed CNTs, with diameter up to 500 μm, and, in principle, no limit in terms of length. Remarkably, fibers obtained from helically coiled CNTs exhibit more tunable mechanical properties than those with straight ones and hold great potential for a wide range of applications [118, 119]. Since there is no matrix that incorporates CNTFs (unlike classic Carbon Fibers), their macroscopic properties could resemble those of the constituent CNTs. This achievement remains a major goal that is still difficult to attain; however, thanks to advances in production technologies, significant progress has been made over the past two decades [120]. State-of-the-art CNTFs now exhibit mechanical properties that are competitive with traditional Carbon and Aramid Fibers [121–123], often coupled with high flexibility and toughness [124, 125], as well as electrical properties comparable with metallic conductors [6, 126].

To the touch, CNTFs are very similar to a cotton thread: they are lightweight, highly flexible, more conductive than stainless steel, and much stronger than copper. Experiments have shown that their high axial stiffness dominates over flexural stiffness [125]. This is a consequence of the particular microstructural organization of the fibers, which bind to each other along their lateral surface using van der Waals forces. It has been theoretically demonstrated that the tensile and flexural capabilities of the fibers are dictated, more than by the properties of the CNTs [7], by the compliance of the lateral bond and, in particular, by the offset between adjacent CNTs. Therefore, it is expected that improvements in production techniques will allow for a denser packing of longer CNTs with optimal offset, increasing the strength of the lateral bond to achieve mechanical properties close to those of CNT clusters [127]. The availability of long CNTFs can enable the production of structural elements with capabilities that significantly exceed those of their metallic competitors.

Regarding studies on the characterization of the mechanical properties of CNTFs, it has been observed that their flexural response is determined by the shear coupling of the CNTs that compose them, but its analytical treatment becomes very complicated [128].

2.5.1 CNTFs production process

Among the several methods to obtain continuous fibers from CNTs the *direct-spinning method* has received significant attention because of its relative simplicity in producing high-performance materials without apparent limitations in size. CNTFs and films fabricated by this approach have demonstrated notable properties and opened new areas of research and commercial development. Since its introduction more than a decade ago, this method has not only provided valuable insights into the fundamental science of nanomaterials but also enabled the creation of the first prototypes with significant potential for practical applications. As a result, research activity on CNTF spinning has expanded rapidly, with numerous contributions from groups worldwide.

A central challenge in fabricating high-performance CNTFs lies in aligning the individual CNTs along the fiber axis and producing a continuous filament. The four primary spinning methods established to date are *dry spinning*, *array spinning* (Figure 2.20(a)), *direct spinning* (Figure 2.20(c)) and *wet spinning* (Figure 2.20(b)). Below these methods are discussed in detail.

Twisting or rolling from CNT films (*solid-state* or *dry spinning*)

In this technique, CNTFs are obtained by twisting or rolling continuous CNT sheets or ribbons drawn from a forest or produced via filtration as shown in Figure 2.21(a). The process is entirely carried out in the solid state, without the use of solvents. A CNT film, typically composed of aligned or partially aligned nanotubes, is continuously drawn and twisted along its axis to form a compact yarn-like structure. The mechanical integrity of the fiber is primarily achieved through van der Waals interactions and frictional forces between adjacent CNTs. The degree of twist plays a crucial role in determining the final properties: a moderate twist enhances load transfer and tensile strength, while excessive twist may lead to misalignment and a reduction in stiffness. Post-treatments such as densification with organic solvents (e.g., acetone or ethanol) or thermal annealing can further improve packing density and mechanical performance. This approach is particularly suitable for producing fibers with highly aligned CNTs and minimal structural damage. Nanoscale fibers drawn from MWCNTs such as the one shown in Figure 2.21(b) exhibit strengths comparable to spider silk. Replacing conventional metal wires in electronic textiles with these high-strength yarns could enable new functionalities, such as actuation (as artificial muscles [130–132]) and energy storage (as fiber-based supercapacitors or batteries [133]).

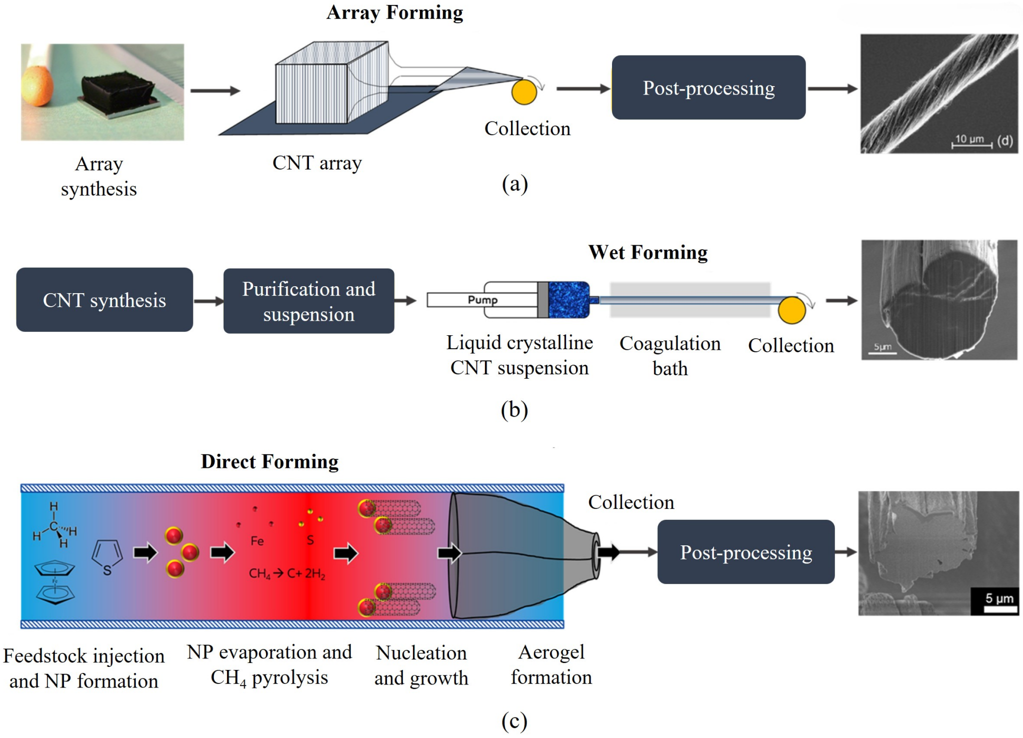

Figure 2.20. (a) Schematic of the array forming process from CNT forests. Left to right: as-synthesized CNT array, array forming, post processing (stretching, micro–combing, polymer infiltration, densification, twisting, etc.), and an array spun yarn; (b) Schematic of the wet forming process. Left to right: CNT synthesis (any synthetic approach), purification and suspension in super-acid, schematic of wet-spinning of a yarn from liquid crystalline CNT dope, SEM image of a dense super-acid spun fiber cross-section; (c) Schematic of the dry forming process. Left to right: floating catalyst CVD process and CNT article collection, post-processing (stretching, densification, infiltration), SEM image of a wet-stretched direct spun CNT yarn cross-section [129].

Spinning from vertically aligned CNT arrays grown on a substrate

Analogous to drawing silk threads from a cocoon, CNTFs can be obtained directly from vertically aligned CNT arrays, often referred to as “CNT forests.” In 2002, Jiang et al. [87] reported the spinning of a 30 cm long CNTF from an array with a height of 100 μm. Since then, extensive research has focused on optimizing this method to enhance fiber properties. The spinnability of CNT arrays depends strongly on their morphology, alignment, and density. Well-aligned, densely packed CNTs with minimal amorphous carbon content enable continuous drawing of cohesive fibers. During spinning, van der Waals forces and mechanical entanglement allow CNTs to be pulled from the array, forming a continuous thread. The resulting fibers can be twisted, densified, or infiltrated with polymers to improve mechanical and electrical properties. This method enables precise control of alignment and purity, but is limited by the scalability and cost of producing large, uniform arrays.

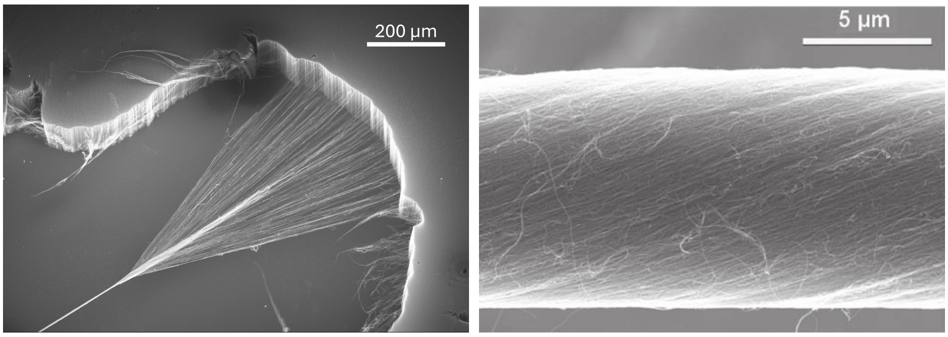

(a) (b)

Figure 2.21. (a) SEM image of dry spinning process of CNT. The fiber shown has a diameter of approximately 1 μm, while the individual nanotubes from which it is composed are about 10 nm in diameter [134]; (b) Dry spun CNTF made of MWCNTs [135]

Spinning from CNT aerogels formed in a chemical vapor deposition reactor

Another route for CNTF fabrication relies on direct assembly from the synthesis environment. Instead of post-processing CNTs from arrays or solutions, fibers can be formed directly inside a CVD furnace. Zhu et al. [88] first demonstrated the continuous synthesis of long, aligned CNT strands using a floating-catalyst CVD process in a vertical furnace. In this method, CNTs are generated in the gas phase and entangle to form a continuous aerogel, a low-density CNT network that flows with the carrier gas. The aerogel is continuously drawn from the reactor outlet, condensed, and wound onto a spool, forming a CNTF. Post-spinning treatments such as twisting, solvent densification, or polymer impregnation can be applied to enhance alignment and packing density. This “direct spinning” technique is among the most scalable routes for CNTF production, allowing continuous synthesis and spinning in a single step.

Spinning from CNT solutions (***solution-state*** or ***wet spinning***)

Wet spinning was one of the first methods developed for the production of CNTFs [86], and it remains one of the most widely employed and versatile approaches to obtain continuous CNTFs. Coagulation spinning, originally developed for the production of high-performance fibers such as Kevlar, acrylic, and poly(acrylonitrile) (PAN), has been successfully adapted to CNTs. In this process, a CNT or CNT–polymer dispersion is extruded through a spinneret into a coagulation bath containing a liquid in which the solvent is soluble but the CNTs or polymer are not. The sudden change in solvent environment induces aggregation and alignment of CNTs, leading to the formation of a continuous filament. This process is schematically represented in Figure 2.22.

The quality of the dispersion, often stabilized by surfactants, polymer wrapping, or chemical functionalization, determines the degree of CNT alignment and the resulting fiber performance. Stretching during coagulation or post-drawing can further enhance alignment, tensile strength, and toughness. Over the past two decades, several variations of coagulation spinning have been developed to produce both pure CNTFs and CNT–polymer composite fibers with high flexibility and multifunctionality.

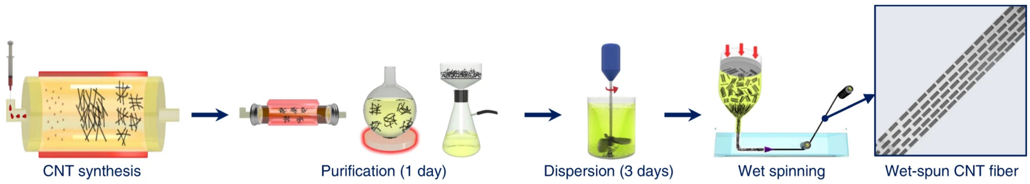

Figure 2.22. Schematic representation of the wet spinning process for CNT Fibers: CNT syntesis, purification, dispersion, extrusion through the spinneret in coagulation bath and collection [136].

The fibers on which this work mainly focuses are Solution-Spun CNT Fibers produced via a *solution-spinning* method known as *wet spinning* developed at the Rice University in Houston, TX by the group of R.E. Smalley [5] and now supervised by M. Pasquali. This technique decouples CNT synthesis from fiber formation, a significant advantage that allows for independent optimization of CNT characteristics, such as aspect ratio, purity, defect density, and wall number, and assembly conditions, including the potential for CNT purification prior to spinning [129]. Depending on the medium and process parameters, two main approaches can be identified:

Wet forming. In this method, CNTs are first suspended in a fluid medium and then consolidated into macroscopic structures. The suspending medium may be removed by evaporation or vacuum filtration, resulting in planar isotropic CNT networks known as *buckypapers* [129]. Alternatively, the CNT suspension can be injected through a fine capillary into an anti-solvent or coagulant, where shear-induced alignment promotes the anisotropic assembly of CNTs into fibers or yarns [129]. The degree of alignment depends on factors such as CNT concentration, viscosity of the dope, and shear rate during extrusion. The alignment can be further improved by mechanical stretching during or after coagulation.

Acid dissolution and liquid crystalline wet spinning. A significant advancement in CNT wet spinning has been the introduction of *superacids*, such as chlorosulfonic acid, which act as true solvents for CNTs [13, 137, 138]. These acids enable stable CNT dispersions at relatively high concentrations (2–6 wt%), where CNTs form *nematic liquid crystal* phases [54, 129]. This intrinsic liquid crystalline order facilitates axial alignment during extrusion, leading to densely packed and highly anisotropic fibers. An important variation of the original wet spinning method apart from the use of acid as a solvent is the use of water as coagulants [5]. This acid-based method simplifies the original wet spinning process by avoiding surfactants in the CNT dispersion and eliminating polymer from the coagulation bath, and has so far produced the most highly ordered and dense CNTFs [5].

In a typical process, high-quality CNTs are dissolved in chlorosulfonic acid (Figure 2.23(b)), filtered to remove impurities (Figure 2.23(d)), and extruded through a die (Figure 2.23(e)) of diameter between 65 and 130 μm, into a coagulant such as acetone or water [139] to remove the acid [54] as shown in Figure 2.23(e) . The forming filament is continuously collected on a winding drum rotating faster than the extrusion rate, ensuring uniaxial stretching and alignment of the CNTs as shown in Figure 2.23(g). The fibers are subsequently washed in water and dried at 100–120°C.

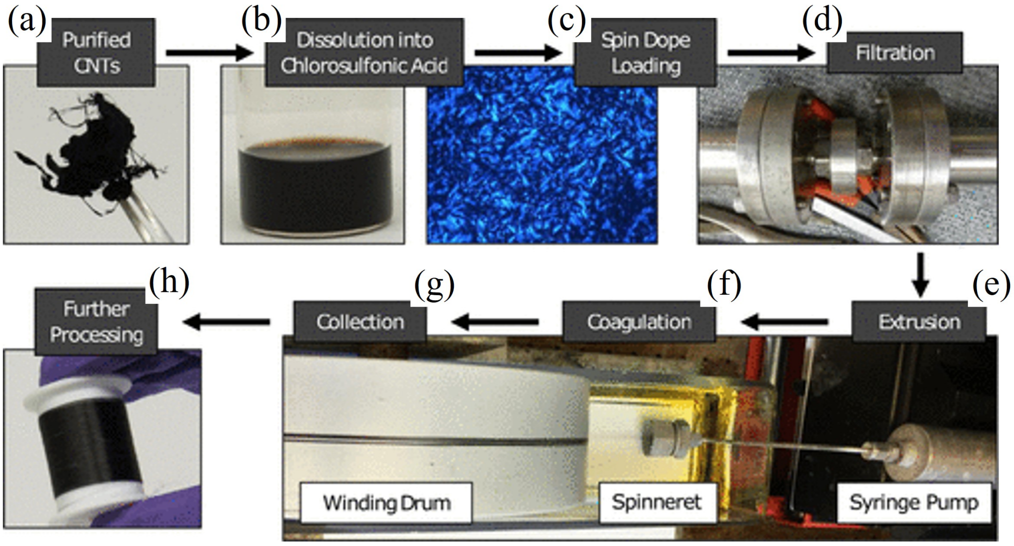

Figure 2.23. (a) Purified CNTs; (b) Dissolution into chlorosulfonic (acid liquid crystalline mixture); (c) Dope loading; (d) Filtration; (e) extrusion and spinning; (f) Coagulation; (g) Winding drums with collected fibers; (h) Further processing [140].

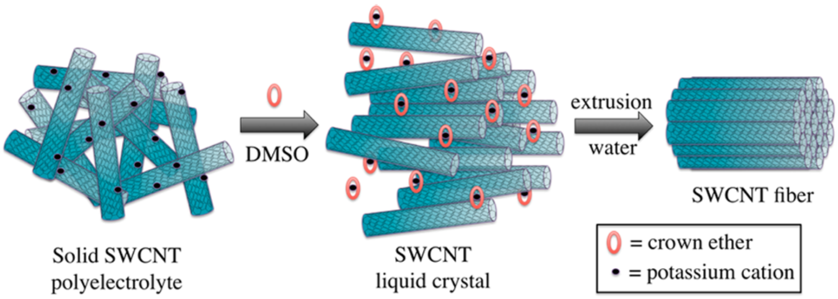

Figure 2.24. Schematic representation of CNT alignment during wet spinning. Shear flow in the spinneret and stretching during collection promote uniaxial orientation of CNTs, enhancing mechanical and electrical properties [139].

Wet spinning is highly scalable, similar to the industrial processes used for high-performance fibers such as Kevlar, Twaron, or PAN-based Carbon Fibers [141]. Moreover, this approach enables the formation of parallel CNT arrays bonded via van der

Waals interactions [8, 25, 98, 142], leading to long and structurally robust fibers or yarns. The resulting microstructure is typically dense and highly aligned [6]. This stands in contrast to other techniques, such as direct spinning, which produce fibers based on much longer CNTs (that can be up to 1 mm [143]) but often with lower alignment and packing density. Wet-spinning technologies allow for the production of continuous fibers with lengths on the order of meters [6] with a morphology shown in Figure 2.25.

Figure 2.25. Low-magnification SEM image showing the typical morphology of Wet-Spun CNT Fibers [54].

Despite the superior structural order achievable with acid spinning, this method faces important limitations. The hazardous nature of superacids complicates large-scale implementation, and dissolution requires CNTs of very high purity and narrow diameter distribution, often necessitating additional purification steps [129]. Furthermore, inadequate CNT length has been a historical challenge. Early acid-spun fibers used very short CNTs, which was presumed to be the culprit for their initially disappointing mechanical properties [89]. This led to a perception in the literature that wet spinning was inappropriate for handling long CNTs. However, recent developments have countered this notion, demonstrating that even with CNTs of moderate length (around 5 μm), optimized wet spinning methods can effectively aggregate them into high-performance, multifunctional fibers with high mechanical and electrical properties [54]. Recent studies have demonstrated that solution-spun CNTFs can be fully and easily recycled without any loss of their original properties, regardless of the characteristics of the constituent CNTs [144]. This recyclability provides a distinct advantage over conventional Carbon Fibers, which cannot be reprocessed without significant degradation of their mechanical and functional performance. The possibility of recovering and reusing CNTFs without compromising their quality not only enhances their economic attractiveness but also aligns with the growing demand for sustainable and circular-material technologies in high-performance applications.

2.5.2 CNTFs mechanical and physical properties

The mechanical, electrical, and thermal properties of wet-spun CNTFs are typically characterized by testing individual macroscopic filaments (e.g. 20 mm gauge length) of diameter between 10 and 30 μm cut from wound spools (100–500 m) [140]. The stress is computed as the applied force divided by the cross-sectional area, which is determined via scanning electron microscopy (SEM), optical microscopy or indirectly estimated from the linear density knowing the fiber density. As CNTFs are frequently investigated and considered in the context of textile engineering, tensile properties are typically expressed in terms of specific strength or specific modulus, with units of N/tex[1].

Studies on wet-spun CNTFs [54] reported notable mechanical properties such as an average tensile strength of 1.0 GPa, a Young's modulus of 120 GPa, and a density around 1.3 g/cm^3. In contrast, fibers produced by direct or array spinning can reach significantly higher values: for example, Lee et al. [136] achieved 4.88 GPa tensile strength and 214.5 GPa modulus, with knot efficiency of 48 ± 15 % but lower electrical properties. Koziol et al. [145] reported up to 9 GPa strength and 350 GPa stiffness for the CNTF spun directly and continuously from gas phase as an aerogel used in their work. More recently, Zhang et al. [146] reported CNTFs with a "dynamic strength" of 14 GPa, attributing such performance to enhanced inter-tube interactions, densification, and improved alignment, especially under high strain-rate loading [146]. Wet-spun CNTFs used in the present work, showed an average tensile strength of 2.2 GPa, modulus 136 GPa, knot efficiency 70%, elongation at break 1.4%, and density 1.3 g/cm^3.

Wet-Spun CNTFs also display substantial electrical and thermal performance. Their baseline electrical conductivity at room temperature is 2.9 MS/m; doping with iodine increased this to 5 MS/m, a level that remained stable over one year and under thermal cycling to 200 °C for 24 h. Thermally, the average conductivity was measured at 380 W/(m · K) on short (1.5 mm) samples; iodine doping boosted this to 635 W/(m · K) and slightly increased density (from 1.3 to 1.4 g/cm^3). Notably, the thermal conductivity remained stable even after annealing at 600 °C, though electrical conductivity dropped an order of magnitude (to 0.4 MS/m) [54].

These combined properties are notable when compared to those of other high-performance materials. In Chapter 3, it will be explored in more detail how these properties are correlated. Table 2.2 reports a comparison between the mechanical properties of different laboratory produced CNTFs [6, 124, 136] and common materials as prestressed concrete (PSC), copper, iron, aluminum, titanium, a structural steel (A36), and a high-strength martensitic steel (MS) and commercial fibers such as Carbon Fibers, Kevlar, Zylon, Dyneema, glass [6, 147–160] and a reference CNT (CNT-R) whose mechanical properties are based on theoretical arguments also considered in other works [48, 85] also reported for the sake of comparison.

---

[1] The *tex* is a unit of linear density for textiles, equal to 1 gram per 1000 meters of material.

GROUP	MATERIAL	DENSITY (g/cm^3)	SPEC. MODULUS (N/tex)	MODULUS (GPa)	SPEC. STRENGTH (N/tex)	STRENGTH (GPa)
COMMON	Concrete (PSC)	2.55	11.77	30.00	0.00	0.01
	Copper	8.96	11.16	100.00	0.02	0.20
	Aluminum	2.70	22.21	60.00	0.04	0.10
	Titanium	4.52	24.36	110.00	0.04	0.20
	Iron	7.86	24.18	190.00	0.07	0.55
	Steel A36	7.85	14.01	110.00	0.07	0.55
	Steel MS	7.85	26.75	210.00	0.23	1.80
CNTF	CINA-UK	2.00	65.00	130.00	2.30	4.60
	SS-CNTF	1.79	167.44	300.00	2.40	4.30
	KIST	1.10	195.00	214.50	4.44	4.88
CARBON FIBER	M55J	1.91	282.72	540.00	2.10	4.02
	M40X	1.79	210.61	377.00	3.07	5.50
	T800	1.80	163.33	294.00	3.27	5.88
	T1100	1.79	181.01	324.00	3.91	7.00
KEVLAR	K29	1.44	48.96	70.50	2.03	2.92
	K49	1.44	78.06	112.40	2.08	3.00
ZYLON	Z HM	1.56	173.08	270.00	3.72	5.80
	Z AS	1.54	116.88	180.00	3.77	5.80
DYNEEMA	SK60	0.99	105.34	104.00	3.14	3.10
	SK99	0.96	160.67	155.00	4.25	4.10
GLASS	V E	2.60	27.85	72.40	0.92	2.40
	V S2	2.48	35.08	87.00	1.85	4.60
CNT	CNT-R	1.27	784.80	1000.00	78.48	100.00

Table 2.2. Comparison of density, modulus, specific modulus, strength, and specific strength for CNTFs, Carbon Fibers, Kevlar, Zylon, Dyneema, glass, CNTs, and common materials (prestessed concrete (PSC), copper, iron, aluminum, titanium, a structural steel (A36), and a high-strength martensitic steel (MS)) [6, 124, 136, 147–160].

It is important to note that fibers produced via other methods (e.g. array spinning or direct CVD spinning) may exhibit different performance profiles: they can offer longer CNT lengths, potentially lower defect densities or higher process throughput, but sometimes at the cost of reduced alignment or packing density relative to the best Wet-Spun Fibers. In Chapter 3, the interdependence between CNT length, alignment, wall number, purity, and graphitic quality will be explored in depth to rationalize these performance differences.

2.5.3 CNTF Bundles, Yarns, Cables and Ropes

Aligned CNTFs (Figure 2.26(a)) can assemble into CNTF bundles (Figure 2.26(b)) , which in turn can be twisted (Figure 2.26(c)) or joined together (in this case every bundle is a ply) to form a macroscopic yarns (Figure 2.26(d)), ropes (Figure 2.26(e)), or cables [127, 161]. These hierarchical structures exhibit significant strength and multifunctionality, making them suitable for structural and functional applications across various engineering sectors. Furthermore, increasing the torque applied to the ends of a cable with one or more concentric layers of wounded yarns increases its strength acting also as a safety factor, because the friction between the fibers generated by the twisting keeps them compact even if one breaks [162].

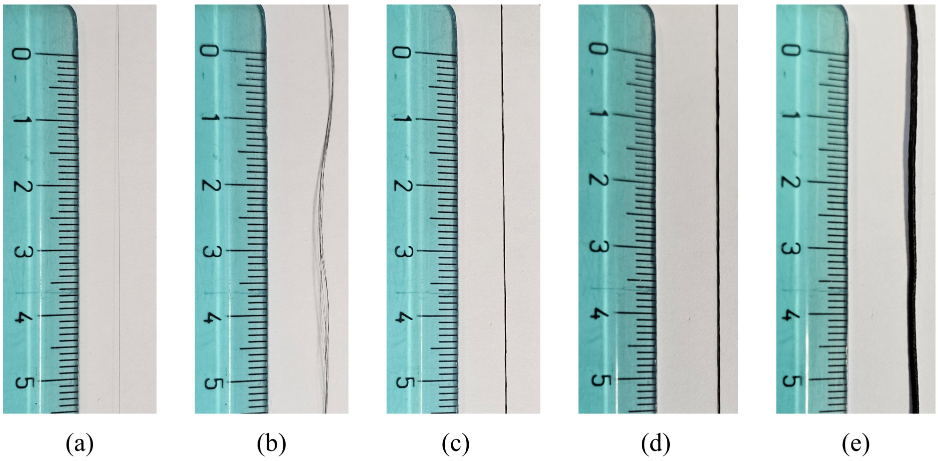

Figure 2.26. (a) CNTF; (b) untwisted CNTF bundle; (c) twisted CNTF bundle; (d) 3 ply CNTF yarn; (e) 4x4 CNTF rope

An important analytical topic in structural engineering is the specific behavior of axial stiffness versus the tensile strength of the cable as a function of the surface twist angle β of the bundle, which is 90° when the fibers in the bundle are untwisted, straight and parallel, while decreasing with the increasing twist rate. The bundle axial stiffness decreases with increasing twist, while the tensile strength of the cable increases. An optimization problem concerns the intersection point of the two functions, in order to satisfy both requirements [127].

Finally, CNTF bundles and yarns can be woven into fabrics, which may serve as reinforcement layers in epoxy-based laminated composites, while unidirectional epoxy-based composites can be produced directly from aligned CNTF bundles.

2.5.4 Applications of CNT Fibers

The distinctive properties of CNTFs have enabled new applications across diverse fields.

Biomedical applications

In biomedical engineering, CNTFs have demonstrated capabilities that challenge conventional materials. Recent advances have shown particular promise in neurological applications, where CNTF-based neural electrodes exhibit higher charge injection capacity compared to traditional platinum electrodes [163] (Figure 2.27(a)). The development of electrically conductive bio-compatible CNTF-based sutures for arrhythmia treatment (Figure 2.27(b)) has created new possibilities in postoperative care, combining wound closure with real-time electrophysiological monitoring [164]. In [165] the bio- and immune-compatibility profiles of CNTF were systematically evaluated at cellular, organ, and systemic levels. In vitro, CNTF showed good cytocompatibility with cell-lines like HEK-293, SH-SY5Y, as well as primary cardiomyocytes and macrophages. Ex vivo, CNTF showed no impact on blood parameters or functionality of key immune cells. In vivo, intraperitoneal injections of leachates from CNTF production revealed no evidence of toxicity suggesting no leachable or residual degradable byproducts. In addition, as the first multiscale toxicological evaluation of a CNT macrostructure, it was demonstrated that CNT macrostructures should be evaluated as their standalone class of carbon material, separately from individualized CNTs and unstructured CNT agglomerates.

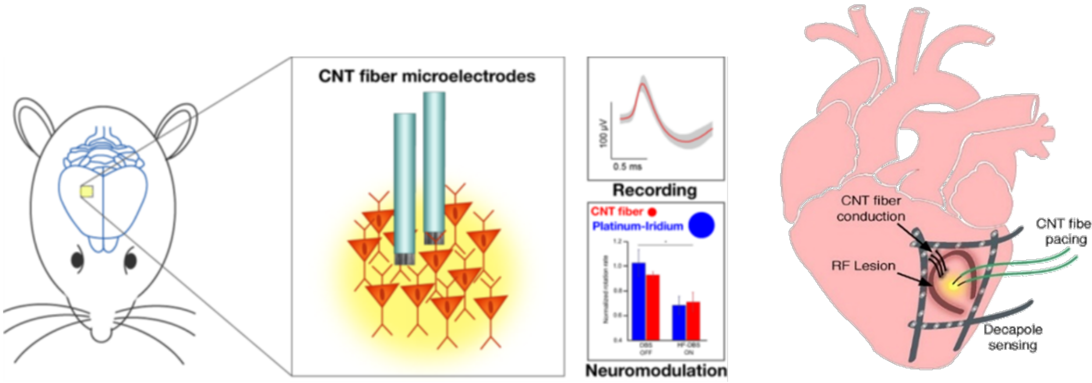

(a) (b)

Figure 2.27. Biomedical applications of CNTFs: (a) Neural electrode array for deep brain stimulation showing seamless integration with neural tissue [163]; (b) Conductive sutures for arrhythmia treatment demonstrating mechanical flexibility comparable to surgical thread while maintaining electrical conductivity [164].

Electronic applications

The development of CNTF-based conductors offers a viable route to significantly reduce the mass of electrical wiring in automotive and aerospace systems. Their combination of low density, high mechanical strength, and excellent electrical conductivity enables significant efficiency gains when replacing conventional metallic cables.

The electronics industry has increasingly embraced CNTFs due to their combination of conductivity, flexibility, and durability [168]. These materials enable the fabrication of smart textiles with embedded sensors and ultra-lightweight wiring networks. Recent advances have demonstrated that neat CNT Threads (CNTTs) made from SS-CNTFs can function as sewable electrodes and signal transmission fibers, combining metal-like conductivity with textile softness and durability [166]. These CNTF threads exhibit low interfacial impedance with skin, enabling high-quality electrocardiogram (EKG) monitoring comparable to commercial electrodes. Moreover, they maintain stable electrical performance after repeated stretching and machine washing, enabling

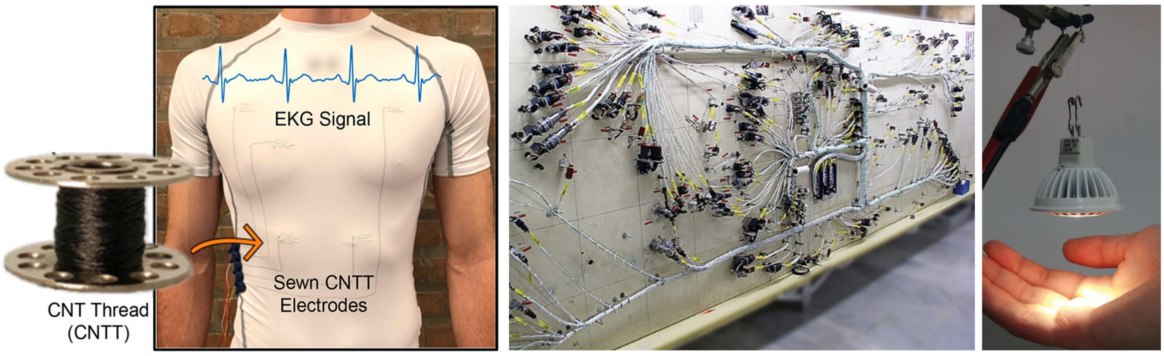

(a) (b) (c)

Figure 2.28. Multifunctional CNTF applications: (a) Shirt with integrated CNTF sensors for continuous vital sign monitoring [166]; (b) CNTF wiring achieving remarkable mass savings compared to conventional cabling [167]; (c) A 46 g light-emitting diode lit and suspended by two 24 μm thick CNT Fibers [54].

scalable, biocompatible, and flexible electronic garments that can be manufactured using conventional textile processes, a practical application where CNTF sensors for continuous vital sign monitoring are integrated in a sport-shirt is shown in Figure 2.28(a).

Transparent conductive films based on CNTF networks have achieved sheet resistances below 100 Ω/sq with over 90% optical transparency, competing with indium tin oxide in display technologies [169]. In flexible electronics, CNTF-based circuits maintain stable electrical operation under bending radii below 1 mm, allowing the realization of foldable and deformable devices.

As alternatives to traditional metallic conductors in electrical and structural wiring systems, CNTFs provide a unique balance between weight and multifunctionality. The very low density of CNTFs (approximately 1.3–1.4 g/cm^3) compared to copper (8.9 g/cm^3) enables significant mass reduction without compromising either mechanical integrity or electrical performance. This feature makes CNTFs particularly suitable for aerospace, automotive, and portable electronic applications, where weight reduction directly translates into energy efficiency and design flexibility.

In [54] it was demonstrated the multifunctional properties of SS-CNTFs by supporting and wiring a light-emitting diode (LED) weighing 46 g shown in Figure 2.28(c) and by fabricating cold electron-emitting cathodes. The LED was supported by two CNTFs of 24 ± 1 μm of diameter. The stress in each fiber was $\sim$500 MPa, well above the breaking strength of copper wires, but the filament resistance was low enough to run 30-mA current (6.6×10^3 A/cm^2 current density) and light the device.

Recent research has demonstrated the development of lightweight copper–CNT core–shell Fibers, in which CNTs act as a conductive core coated with a thin copper layer [170]. These composite wires achieved up to a sixteen-fold reduction in weight compared to pure copper while maintaining comparable conductivity on a gravimetric basis. Similarly, Park *et al.* [171] reported hybrid CNT/Cu/graphene wires with enhanced electrical, thermal, and mechanical performance, highlighting the potential of CNTFs as both reinforcement and conductive elements in lightweight cabling systems.

Beyond laboratory-scale fabrication, the U.S. National Nanotechnology Initiative reported the realization of CNTF-based wiring harnesses capable of replacing conventional coaxial and signal cables in aerospace platforms [167]. These CNTF harnesses demonstrated up to a two-thirds reduction in total cable mass while preserving signal integrity and power transmission capability, representing a significant step toward deployable lightweight wiring architectures and indicating strong potential for future integration into next-generation automotive wiring systems (Figure 2.28(b)).

Efforts to eliminate metallic components entirely have also been reported. Ryu *et al.* [172] developed fully metal-free core–sheath composite cables composed of CNTFs and flexible polymeric insulators. These CNTF-based conductors exhibited high electrical conductivity, low weight, and strong flexibility, rendering them suitable for use in lightweight electric motors and wearable electronics.

Furthermore, scalable manufacturing methods such as flow coating have enabled the production of continuous, flexible CNTF cables with competitive conductivity and excellent fatigue resistance [173]. These fibers and cables represent a new class of multifunctional conductors that combine low mass, high electrical efficiency, mechanical robustness, and potential for energy storage or actuation functionalities.

In parallel, energy storage technologies have greatly benefited from CNTF integration. CNTF-based supercapacitors have achieved high energy densities of 30–50 Wh/kg while maintaining power densities exceeding 10 kW/kg [174]. These characteristics have enabled the fabrication of flexible energy-storage devices seamlessly integrated into wearable textiles [175].

Using the same wet-spinning method, CNT films or tapes may be produced, expanding the application spectrum (e.g. electromagnetic shielding). Figure 2.29 presents a SEM image and commercial CNTF tapes from DexMat.

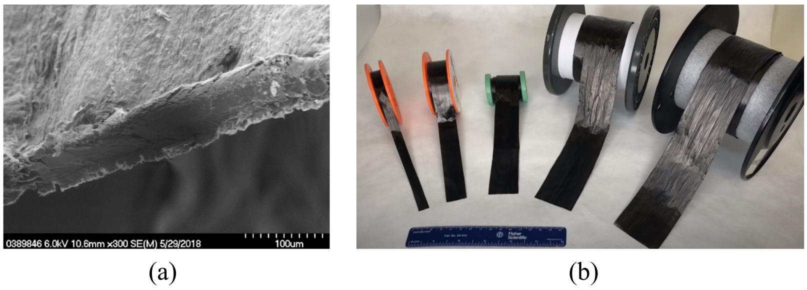

(a)

(b)

Figure 2.29. (a) SEM image of "Galvron CNT tape"; (b) Windings of "Galvron tape" [161].

CNTF-based wiring technologies therefore represent a new approach to reducing cable mass while enhancing multifunctionality. Their combination of low density, high tensile strength, flexibility, and tunable conductivity positions CNTFs as a promising material platform for next-generation lightweight electrical and electronic systems.

Structural applications

If in aerospace applications weight reduction is of paramount importance, in large-scale civil structures, such as long-span suspension bridges, there is a limit size dictated by material properties, beyond which the structure would collapse under its own weight [176, 177]. As already noted by Galileo [178], the scaling laws governing load-bearing systems do not follow the simple geometric proportion: as dimensions increase, structural weight grows faster than load-carrying capacity, leading to a reduction in both strength and effective stiffness [120, 127].

The ratio between tensile strength σ_R and specific weight ρg, referred to as specific strength $\sigma_R/\rho g$, is a material property of critical importance in structural engineering, not only in the design of efficient light-weight aerospace structures, but even more so for the construction of large buildings and bridges, which are close to the limit of collapse under their own weight [177]. To have a better physical understanding of this quantity specific strength can be interpreted as the so-called *characteristic length*, e.g. the maximum length of a vertical column of constant cross-section, which can suspend its own weight when supported only at the top end [127].

In general, materials for structural applications must be selected based on their strength, stiffness, and specific weight. In this regard, CNTFs represent a promising foundation for designing next-generation engineering structures, owing to their combination of high specific tensile strength and stiffness, and notable flexibility in bending [7, 179]. These properties stem from their unique nanostructure and hierarchical assembly.

Structural applications can therefore exploit the high strength and stiffness of CNTFs, which exceed those of high-grade steel by factors of 25–50. Such characteristics enable the design of load-bearing systems far beyond the limits of conventional materials, paving the way for future developments in civil, marine, and aerospace engineering.

The high specific strength of CNTFs enables bridge designs with spans exceeding the limits of steel cables, which are constrained due to self-weight limitations [127]. Feasibility studies for the Strait of Messina Bridge (3.3 km span) indicate that CNTF cables could reduce mass while maintaining safety factors [127].

Analyses show CNTF systems could increase maximum spans by up to three times compared to steel [180, 181]. For instance, replacing cables in the Akashi-Kaikyo Bridge with CNTFs could extend its span from 1.99 km to 6.30 km. Theoretical estimations suggest CNTF cables could enable spans up to 185 km with current materials, and several thousand kilometers approaching ideal CNT performance [127].

Multiscale simulations predict practical CNTF cables could achieve $\sim$10 GPa tensile strength [181]. Additionally, CNTFs maintain structural stiffness over long spans better than steel and can mitigate dynamic instabilities through supplementary strands [181].

CNTFs present advantages for submerged floating tunnels (SFTs), where structural stability depends on tensioned anchoring systems. In these applications, conventional steel cables experience significant stiffness degradation with increasing length due to

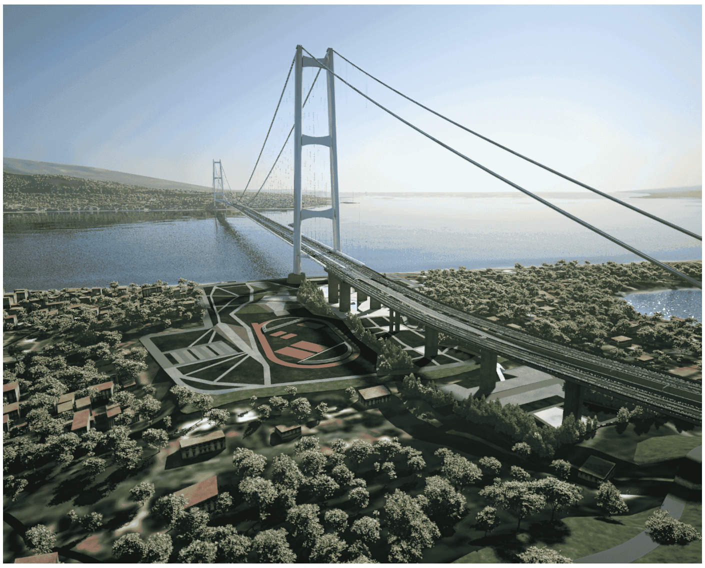

Figure 2.30. Engineering rendering of the Strait of Messina bridge (3.3 km main span) [182].

self-weight effects, limiting their effectiveness in deep water.

CNTFs mitigate these limitations through their combination of low density, high tensile strength, and corrosion resistance, enabling stable anchorage systems at depths exceeding 1 km [127, 183]. Their high specific stiffness reduces dynamic amplification under ocean currents and wave loads.

Applied studies, including investigations by the Norwegian Public Roads Administration for fjord crossings along the E39 coastal highway, demonstrate the feasibility of SFTs in deep-water environments [184]. Hydrodynamic and structural analyses have examined motion, stability, and fatigue response under marine loading conditions [185, 186].

Preliminary designs indicate CNTF cables, such as the Rice 2020 type [6], can support multi-kilometer tunnels while maintaining stability under dynamic ocean conditions. The high buoyancy-to-weight ratio of CNTFs also enables inclined anchorage configurations that improve tunnel stability [183].

The space elevator represents a theoretical application of CNTFs, consisting of a tether anchored to Earth and extending beyond geostationary orbit to enable payload transport without rockets [188]. The system maintains tension through centrifugal force acting on the upper portion, balanced against Earth's gravitational pull on the lower segment.

The critical design requirement is a tether material with specific strength ($\sigma_R/\rho g$) exceeding 5,000 km [190]. While conventional materials such as high-strength steel (60 km) and Kevlar (200 km) fall short, CNTFs theoretically meet this requirement due to their combination of high tensile strength and low density [190].

Current limitations include defects that persist even at synthesis temperatures of 2000–4000 K, limiting macroscopic strength to below 45 GPa [192]. Quantized fracture

Figure 2.31. Conceptual design of the “Archimedes Bridge” [187].

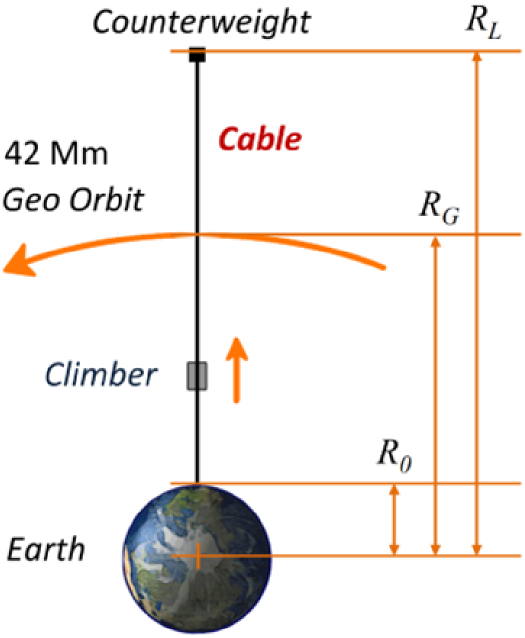

Figure 2.32. Operational schematic of a space elevator system [189].

models are needed to describe strength scaling from nanoscale to macroscopic cables. Tapered tether geometries may provide sufficient safety margins with current CNTF strengths [193], though challenges remain in large-scale manufacturing, radiation resistance, and dynamic stability [194].

CNTFs have also been proposed as structural tendons in modular *flextegrity* architectures for lunar base construction [195]. In these concepts, rigid segments fabricated in situ from molten regolith, valued for its compressive strength and abrasion resistance [196], are held together by prestressed CNTF strands produced on Earth. Thanks to their specific strength, CNTFs enable a substantial reduction in launched

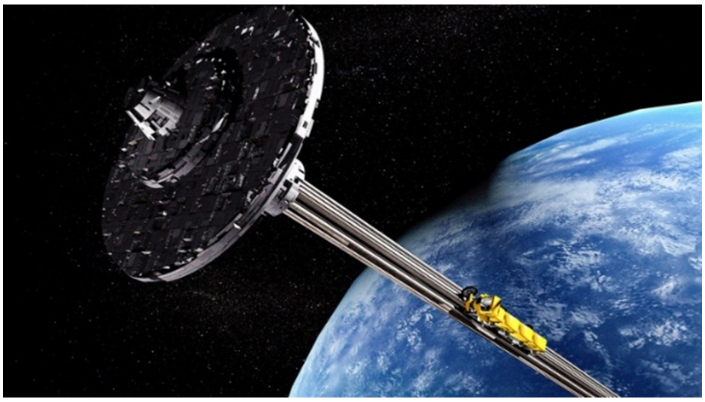

Figure 2.33. Space elevator concept [191].

mass compared to conventional materials such as steel, making them an attractive solution for lightweight, deployable extraterrestrial structures.

The advent of CNTFs as structural materials marks a significant change in engineering design. As synthesis techniques progress, their high specific strength, stiffness, and durability may enable applications and megastructures, ranging from kilometer-scale civil works like bridges and deep-sea tunnels to space-based infrastructures and seamless human-machine interfaces, continually expanding the boundaries of materials science and engineering.

Chapter 3

A model for the effective tensile stiffness of CNTF

The proper assessment of the *effective* mechanical properties of CNT Fibers is of paramount importance for their possible use in macroscopic structural elements.

As discussed in [7], the macroscopic tensile stiffness of CNT Fibers is dictated by the compliance of the lateral bond between adjacent CNTs, dependent on their aspect ratio, arrangement and cross-link density and, in particular, by their overlapping length [7]. The latter is often neglected in analytical approaches (see, among the others, [197, 198], considering CNTs running along the entire fiber length), or taken into account as a random variable in molecular mechanic simulations [53, 199]. In literature models based on solid mechanics [200, 201], one of the main simplifying assumption consists in neglecting the axial deformation of the CNTs composing the Cluster/Fiber, i.e., the constituent CNTs are modelled as axially rigid bars [7, 202]. This usually leads to an overestimation of the macroscopic stiffness of the fiber.

This is why, in the refined model here proposed, the CNTs are modelled as deformable bars, with given axial stiffness. The considered model problem is that of a fiber composed by CNTs with length much shorter than the fiber length, and connected along their lateral surfaces by means of distributed shear springs. CNTs are considered to be arranged in a square lattice in the fiber cross-section, of arbitrary shape, while in the axial direction they are offset of a given quantity with respect to the adjacent ones. These assumptions are similar to that adopted in [7], but in that article the CNTs were assumed to be axially rigid, and hence the fiber elongation was due to their axial displacement only. On the contrary, here they are modeled as deformable bars, whose axial compliance is accounted for, and consequently the fiber elongation results into two different-in-kind deformation mechanisms, occurring at the nanoscopic level: the axial displacement of the CNTs, and their elongation.

3.1 Traction response of a CNTF

To investigate the tensile response of the CNT Fiber, an approach similar to that adopted in [7] is used, i.e., a macroscopic elongation is prescribed to the whole fiber, and the correspondent axial force is evaluated *a posteriori*. In the aforementioned work, the constituent CNTs were assumed to be axially rigid, and hence the fiber elongation was given by the axial displacement of the CNTs. Here, the axial compliance of the CNTs is accounted for, and hence the macroscopic elongation results into two different-in-kind deformation mechanisms, occurring at the nanoscopic level, that will be detailed in the sequel: *i)* the displacement of the CNTs composing the fiber in the axial direction and *ii)* the (possibly non-uniform) stretch of the individual CNTs.

3.1.1 The model problem

The considered model problem is that of a fiber of length L, with cross-section of arbitrary shape, with size of the order of 10÷100 μm, as shown in Figure 3.1. The fiber is composed of monodisperse CNTs, arranged in a regular square lattice in the cross-section (Figure 3.1), with diameter d of the order of 1 nm and length $l \ll L$ of the order of 1÷10 μm, so that the CNT aspect ratio is $l/d = 10^3 \div 10^4$. Here, *compliant* single-walled[1] CNTs are considered, with axial stiffness EA, where A is the cross-sectional area and E the Young's modulus.

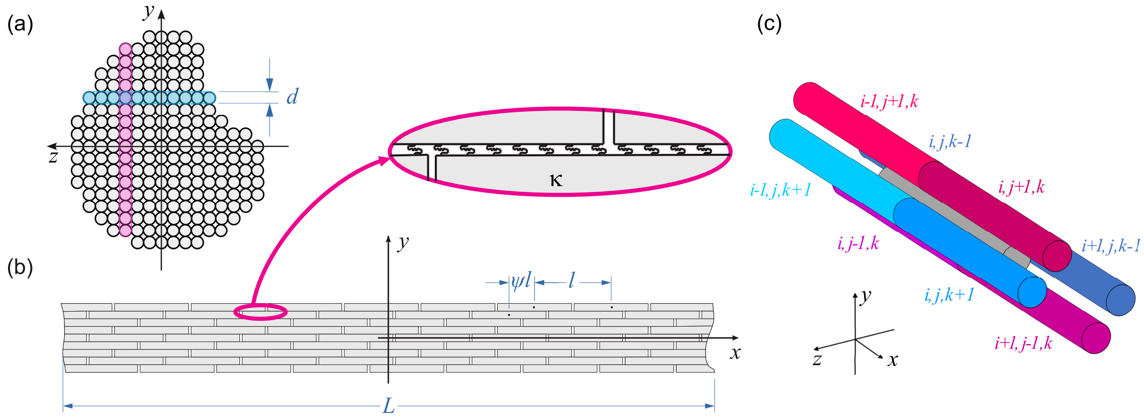

Figure 3.1. Geometry of the considered CNT fiber, (a) cross and (b) longitudinal sections; (c) shear coupling of the (i, j, k) CNT.

The offset between the caps of CNTs placed on the same longitudinal line allows their mobility in the longitudinal direction, and their interaction is negligible [98]. The shear coupling of adjacent CNTs on their lateral surface is due to the presence of van der Walls forces, and may be increased by cross-link [26, 27]. Since the scale of the

---

[1] The model can be easily extended to double-walled and multi-walled CNTs simply by correctly account for their cross area.

interaction is at the atomistic level, this may be modelled, from the mechanical point of view, by means of a soft thin interface layer [200, 203], or with shear springs *à la* Winkler [7, 204].In the present model, the distributed shear springs illustrated in the magnified view of Figure 3.1(b) are employed, assuming a linear response[2] with a stiffness per unit length denoted by κ.

With reference to Figure 3.1, introduce the reference system (x, y, z) with x on the direction of the fiber axis and y, z parallel to the lattice directions. In the cross-section, each $y-$"column" ($z-$"row", respectively) is constituted by a number of CNTs dependent on the z (y, respectively) coordinate. Following [7], the random axial misalignment of each CNT with respect to those belonging to adjacent lines is interpreted in an average way: when moving in the increasing y (respectively, z) direction, each CNT is offset (in the x direction) of ψl, with $\psi \in [0,1]$, with respect to the "previous" one. The non-dimensional parameter ψ will be referred to as *offset parameter*. According to this spatial distribution, each CNT is connected to those composing the four adjacent "lines" in the $y-$column and $z-$row direction. Therefore, as emphasized in Figure 3.1(c), each nanotube is connected with eight CNTs.

3.1.2 Kinematics and loading state

Assuming that the CNTs are deformable bodies, when the CNT Fiber undergoes a macroscopic deformation ϵ, this will produce two different mechanisms, namely: the axial displacement of the individual CNTs, moving apart from one another, and their elongation due to the forces transmitted by the springs, providing a traction load on the CNT itself. Due to the initial spacing between the CNT caps, and to their axial displacement increasing the distance of their centroids, the CNT elongation does not affect the macroscopic stretch of the fiber. Hence, it can be assumed that distance increase between the centroids of nanotubes belonging to the same line is homogeneous, and proportional to ϵ. As detailed in Section 3.2, this allows evaluating the CNTs position in the deformed configuration and, consequently, the relative displacement between points lying on adjacent CNTs.

A key point of the proposed model is that, due to the periodicity of the considered geometry, each CNT will be subjected to the same actions[3], transmitted by the shear springs. Hence, the axial displacement field, hereafter referred to as $u(\xi)$, will be the same on all the CNTs composing the fiber[4]. The shear forces (per unit length)

---

[2] More generally, the interaction between adjacent CNTs can be represented using non-linear springs [205].

[3] This is not true for CNTs lying on the fiber surface, that are connected with less than 8 adjacent CNTs. However, since the cross-sectional area of the fiber is in general 4 (or even 5) orders of magnitude higher than that of CNTs, the contribution of the external CNTs may be considered to be negligible.

[4] Notice that other models proposed by the literature, based on similar approaches [200, 201], consider the interaction between only two adjacent CNTs, so neglecting both the complex mutual

transmitted by the springs, of stiffness κ, connecting the CNT to the adjacent ones are derived in Section 3.2, and may be written as

$$
\begin{aligned}
&t_{i,j+1,k}(\xi) = t_{i,j,k+1}(\xi) = \kappa\left[\psi l \epsilon + u(\xi - \psi l) - u(\xi)\right] ,\\
&t_{i-1,j+1,k}(\xi) = t_{i-1,j,k+1}(\xi) = \kappa\left[-(1-\psi) l \epsilon + u(\xi + (1-\psi) l) - u(\xi)\right] ,\\
&t_{i,j-1,k}(\xi) = t_{i,j,k-1}(\xi) = \kappa\left[-\psi l \epsilon + u(\xi + \psi l) - u(\xi)\right] ,\\
&t_{i+1,j-1,k}(\xi) = t_{i+1,j,k-1}(\xi) = \kappa\left[(1-\psi) l \epsilon + u(\xi - (1-\psi) l) - u(\xi)\right] ,
\end{aligned}
\tag{3.1.1}
$$

where pedex follow the notation of Figure 3.1(c).

As schematically indicated in Figure 3.2(a), the (i, j, k)th CNT can be divided in three regions[5], where it is connected with different adjacent CNTs, namely: region A, with $\xi \in [-l/2, l(\psi - 1/2)]$; region B, with $\xi \in [l(\psi - 1/2), l(1/2 - \psi)]$; region C, with $\xi \in [l(1/2 - \psi), l/2]$.

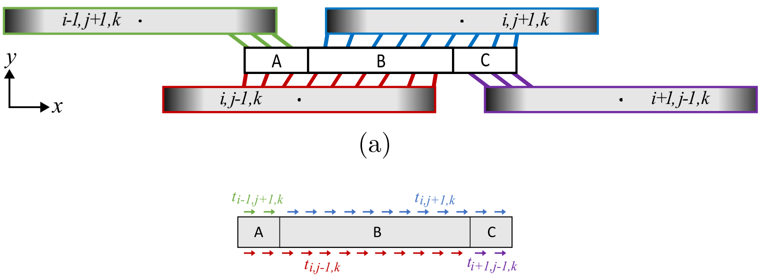

(a)

(b)

Figure 3.2. (a) Different regions defined on the (i, j, k)th CNT, and (b) forces transmitted by CNTs acting on the (i, j, k)th CNT, on the (x, y) plane.

The total force transmitted by the shear springs on the lateral surface of the CNT, hereafter denoted to as $t_{tot}(\xi)$, is the sum of the forces transmitted by the adjacent CNTs. Hence, on the diverse regions it takes different expressions, that are recorded in Section 3.2.

3.1.3 Evaluation of axial force and displacement

The axial force $N(\xi)$ acting on the (i, j, k)-th CNT is related to the axial displacement by

---

interaction between the CNT lattice, and the periodicity of the considered problem. Roughly speaking, these models do not consider that the axial displacement/strain/stress fields must be the same on *all* the CNTs composing the fiber.

[5] Obviously, for $\psi = 0.5$ (i.e., for CNTs offset by exactly half their own length) the end of region A (at $\xi = 0$) coincides with the beginning of region C, while the length of region B is nil.

$$N(\xi) = EAu'(\xi) \tag{3.1.2}$$

where E is the CNT Young's modulus, of the order of 1 TPa [18, 19, 44], while A is the cross-sectional area of the CNT. This may be evaluated as the area of the annulus (see, among the others, [98, 206]) having mean diameter d, and thickness s, corresponding to the thickness of the graphite layer, assumed equal to the interlayer spacing of graphite, i.e., 0.34 nm [47, 207]. The axial force is related to the total shear forces transmitted by the distributed springs (3.2.12) by the axial equilibrium of the CNTs, providing the differential relation

$$N'(\xi) = EAu''(\xi) = -t_{tot}(\xi)\,, \tag{3.1.3}$$

taking different form in the different regions. In particular,

$$\begin{cases} EAu''(\xi) = 2\kappa\,[-\epsilon l + u(\xi + (1-\psi)l)) + u(\xi + \psi l) - 2u(\xi)] & \text{in region } A\,, \\ EAu''(\xi) = 2\kappa\,[u(\xi - \psi l)) + u(\xi + \psi l) - 2u(\xi)] & \text{in region } B\,, \\ EAu''(\xi) = 2\kappa\,[\epsilon l + u(\xi - (1-\psi l)) + u(\xi - \psi l) - 2u(\xi)] & \text{in region } C\,. \end{cases} \tag{3.1.4}$$

Continuity condition on both $u(\xi)$ and $N(\xi) = EAu'(\xi)$ should be required at the interfaces between adjacent regions. Furthermore, since the axial force is null at the ends of the CNTs, boundary conditions are

$$N(\xi)|_{\xi=-l/2} = EAu'(\xi)|_{\xi=-l/2} = 0\,, \quad N(\xi)|_{\xi=l/2} = EAu'(\xi)|_{\xi=l/2} = 0\,. \tag{3.1.5}$$

Eq. (3.1.4) is a *delayed-advanced* differential equation, where the derivative of the unknown function at a certain coordinate (ξ) depends on the function at other coordinates, with both a negative and a positive shift. Qualitatively, this stems from the fact that the value of $u(\xi)$ at a generic point ξ of the CNT depends on what happens at the "correspondent" points (i.e., points with the same axial *global* coordinate x) of adjacent CNTs, having a diverse *local* coordinate ξ. Due the symmetry of the problem (which causes the axial strain and stress field to be the same on each of the CNTs constituting the fiber), this value of $u(\xi)$ therefore depends on the value of the same function at different points on the same CNT.

This kind of equation is most frequently encountered when dealing with time evolution problems, where a time-dependent function depends on both the current state and the previous and subsequent states. Applications can be found in electronic, physics, biology, and economy fields [208, 209], as well as in non-local elasticity [210, 211] and in peridynamic theory [212–214]. The exact solution of this class of equations is a very difficult task [215], and it is usually found by means of numerical techniques (see, among the others, [208, 216, 217]).

3.2 Analytical evaluation of the shear forces in CNTF and numerical implementation

By considering the generic (i,j,k)th nanotube, whose centroid has axial coordinate $x_{G;i,j,k}$, the axial coordinates of the centroids of the adjacent CNTs on the (x,y) plane, shown in Figure 3.3(a), are

$$\begin{aligned} x_{G;i,j+1,k} &= x_{G;i,j,k} + \psi l\,, \qquad & x_{G;i-1,j+1,k} &= x_{G;i,j,k} - (1-\psi)l\,, \\ x_{G;i,j-1,k} &= x_{G;i,j,k} - \psi l\,, \qquad & x_{G;i+1,j-1,k} &= x_{G;i,j,k} + (1-\psi)l\,. \end{aligned} \tag{3.2.6}$$

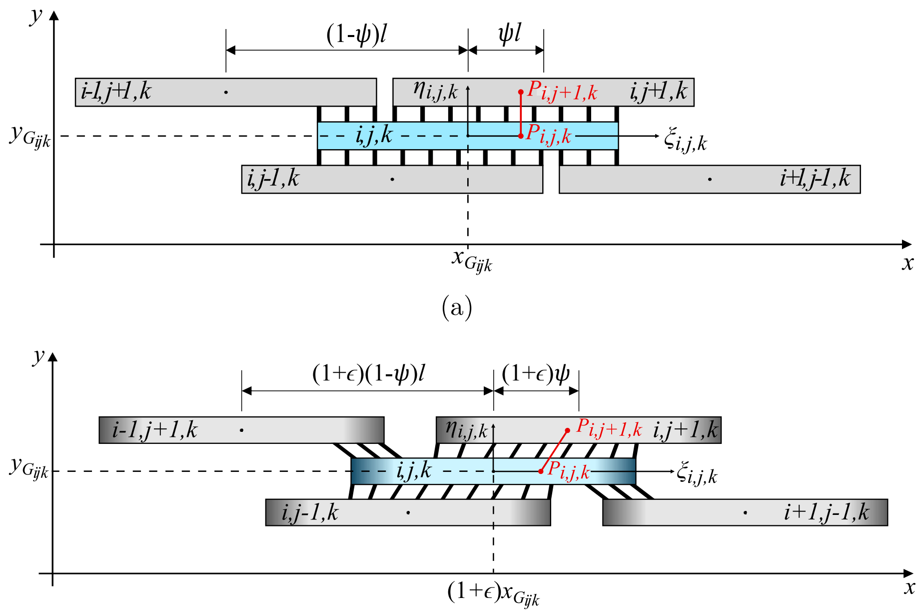

(a)

(b)

Figure 3.3. (a) Undeformed and (b) deformed configuration of adjacent CNTs, on the (x,y) plane, highlighting the axial displacement of the individual CNTs, and their axial strain.

Consequently, by denoting by ξ the local axial coordinate defined on the (i,j,k)th CNT (Figure 3.3(a)), the local coordinates defined on the four adjacent CNTs are

$$\begin{aligned} \xi_{i,j+1,k} &= \xi - \psi l\,, \qquad & \xi_{i-1,j+1,k} &= \xi + (1-\psi)l\,, \\ \xi_{i,j-1,k} &= \xi + \psi l\,, \qquad & \xi_{i+1,j-1,k} &= \xi - (1-\psi)l\,. \end{aligned} \tag{3.2.7}$$

Since the CNTs distribution on the (x,y) and on the (x,z) planes is the same, due to the symmetry of the problem (Figure 3.1), relations analogue to (3.2.7) may be written by considering CNTs adjacent to the (i,j,k)th one, lying on the (x,z) plane.

As discussed in Section 3.1.2, the mesoscopic deformation of the fiber produces the two mechanisms schematized in Figure 3.3(b), i.e., the CNT elongation (highlighted by the darker regions in Figure 3.3(b)), due to the forces transmitted by the springs, and their axial displacement. The latter is proportional to the macroscopic stretch ϵ prescribed to the fiber, and consequently the position of the centroid of the (i,j,k)th CNT in the deformed configuration is $x_{G;i,j,k}(1+\epsilon)$, as shown in Figure 3.3(b).

To evaluate the relative slip between adjacent CNTs, consider first the arrangement on the (x,y) plane, as indicated in Figure 3.3(b). Consider the generic points P_0 and P_1, belonging to the (i,j,k)-th and $(i,j+1,k)$-th CNTs, respectively, and initially having the same axial position, as shown in Figure 3.3(a). By denoting by $u(\xi)$ the axial displacement at the local coordinate ξ, the position of P_0 after the deformation will be $x_{G;i,j,k}(1+\epsilon)+\xi+u(\xi)$. Since, as discussed in Section 3.1.2, the axial displacement field $u(\xi)$ is the same on each CNT, the axial position of P_1 after the deformation will be $(x_{G;i,j,k}+\psi l)(1+\epsilon)+(\xi-\psi l)+u(\xi-\psi l)$ (Figure 3.3(b)). The reciprocal sliding between P_0 and P_1 may be evaluated simply as the difference between their final positions, and reads

$$\delta_{i,j+1,k}(\xi) = \psi l\epsilon + u(\xi-\psi l) - u(\xi)\,, \tag{3.2.8}$$

while, analogously, the relative slip of the (i,j,k)th CNT with the other adjacent CNTs are

$$\begin{aligned}
\delta_{i-1,j+1,k}(\xi) &= -(1-\psi)l\epsilon + u(\xi+(1-\psi)l) - u(\xi)\,,\\
\delta_{i,j-1,k}(\xi) &= -\psi l\epsilon + u(\xi+\psi l) - u(\xi)\,,\\
\delta_{i+1,j-1,k}(\xi) &= (1-\psi)l\epsilon + u(\xi-(1-\psi)l) - u(\xi)\,.
\end{aligned} \tag{3.2.9}$$

Consequently, the forces (per unit length) transmitted by the springs, of stiffness κ, connecting the CNT to the adjacent ones, on the (x,y) plane, may be written as

$$\begin{aligned}
t_{i,j+1,k}(\xi) &= \kappa\ \delta_{i,j+1,k}(\xi) = \kappa\left[\psi l\epsilon + u(\xi-\psi l) - u(\xi)\right]\,,\\
t_{i-1,j+1,k}(\xi) &= \kappa\ \delta_{i-1,j+1,k}(\xi) = \kappa\left[-(1-\psi)l\epsilon + u(\xi+(1-\psi)l) - u(\xi)\right]\,,\\
t_{i,j-1,k}(\xi) &= \kappa\ \delta_{i,j-1,k}(\xi) = \kappa\left[-\psi l\epsilon + u(\xi+\psi l) - u(\xi)\right]\,,\\
t_{i+1,j-1,k}(\xi) &= \kappa\ \delta_{i+1,j-1,k}(\xi) = \kappa\left[(1-\psi)l\epsilon + u(\xi-(1-\psi)l) - u(\xi)\right]\,.
\end{aligned} \tag{3.2.10}$$

The forces transmitted by CNTs connected to the (i,j,k)th nanotube on the (x,z) plane are analogue to that on the (x,y) plane, and read

$$\begin{aligned}
t_{i,j,k+1}(\xi) &= \kappa\left[\psi l\epsilon + u(\xi-\psi l) - u(\xi)\right]\,,\\
t_{i-1,j,k+1}(\xi) &= \kappa\left[-(1-\psi)l\epsilon + u(\xi+(1-\psi)l) - u(\xi)\right]\,,\\
t_{i,j,k-1}(\xi) &= \kappa\left[-\psi l\epsilon + u(\xi+\psi l) - u(\xi)\right]\,,\\
t_{i+1,j,k-1}(\xi) &= \kappa\left[(1-\psi)l\epsilon + u(\xi-(1-\psi)l) - u(\xi)\right]\,.
\end{aligned} \tag{3.2.11}$$

In the three regions schematically indicated in Figure 3.2(a), the (i,j,k)th is connected with different adjacent CNTs, namely:
- region A: $(i-1,j+1,k)$, $(i,j-1,k)$, $(i-1,j,k+1)$, $(i,j,k-1)$ CNTs;
- region B: $(i,j+1,k)$, $(i,j-1,k)$, $(i,j,k+1)$, $(i,j,k-1)$ CNTs;
- region C: $(i,j+1,k)$, $(i+1,j-1,k)$, $(i,j,k+1)$, $(i+1,j,k-1)$ CNTs.

Hence, the total force transmitted by the shear springs on the lateral surface of the CNT may be defined, in the three regions, as

$$t_{tot}(\xi)=\begin{cases} t_{i-1,j+1,k}(\xi)+t_{i,j-1,k}(\xi)+t_{i-1,j,k+1}(\xi)+t_{i,j,k-1}(\xi) & \text{in region } A\,,\\ t_{i,j+1,k}(\xi)+t_{i,j-1,k}(\xi)+t_{i,j,k+1}(\xi)+t_{i,j,k-1}(\xi) & \text{in region } B\,,\\ t_{i,j+1,k}(\xi)+t_{i+1,j-1,k}(\xi)+t_{i,j,k+1}(\xi)+t_{i+1,j,k-1}(\xi) & \text{in region } C\,. \end{cases} \tag{3.2.12}$$

3.2.1 Analytical comparison with the case of rigid CNTs

If the CNTs composing the fiber are assumed to be rigid, as in [7], the governing equations turn out to be strongly simplified. Indeed, when the axial stiffness of the CNTs is assumed to be $EA\to\infty$, the axial displacement field $u(\xi)$ is identically nil, and the expressions for the shear forces transmitted by the distributed springs ((3.2.10) and (3.2.11)) may be simplified as follows:

$$\begin{aligned} &t_{i,j+1,k}=t_{i,j,k+1}=\kappa\psi l\epsilon\,,\\ &t_{i-1,j+1,k}=t_{i-1,j,k+1}=-\kappa(1-\psi)l\epsilon\,,\\ &t_{i,j-1,k}=t_{i,j,k-1}=-\kappa\psi l\epsilon\,,\\ &t_{i+1,j-1,k}=t_{i+1,j,k-1}=\kappa(1-\psi)l\epsilon\,, \end{aligned} \tag{3.2.13}$$

that coincide with expressions recorded in [7]. This allows to evaluate the total force transmitted on the lateral surface of the CNT, according to (3.2.12).

The axial force in each CNT may be evaluated by means of equilibrium relation (3.1.3), with boundary conditions (3.1.5) (null axial force at the CNT's ends), and by requiring continuity of $N(\xi)$ at the interfaces between adjacent regions. It may be verified that it takes the following expression:

$$\begin{cases} N(\xi)=\kappa\epsilon l(l+2\xi) & \text{in region } A\,,\\ N(\xi)=2\kappa\epsilon\psi l^2 & \text{in region } B\,,\\ N(\xi)=\kappa\epsilon l(l-2\xi) & \text{in region } C\,. \end{cases} \tag{3.2.14}$$

It has been numerically verified that the obtained solution, in terms of $N(\xi)$, coincide with this closed form expression, when a very high value for the axial stiffness of the individual CNTs is set, i.e., for $EA\to\infty$.

If the constituent CNTs are assumed to be rigid, as in [7], their axial force $N(\xi)$ cannot be found from their constitutive law (3.1.2). This is why in [7] the axial force in the whole fiber is evaluated as the resultant of the shear interactions, by performing a "step-cut" of the fiber, not intersecting the CNTs. However, as discussed in Section 3.2.1, $N(\xi)$ may be recovered from the equilibrium of the individual CNTs, and it turns out to be in the form (3.2.14). The proposed approach hence allows to calculate N_f as the resultant of the axial forces on the individual CNTs by means of Eq. (3.3.8), providing the following expression:

$$N_f = 2\ A_f \kappa \epsilon\ \frac{l^2}{d^2} \psi(1-\psi)\,. \tag{3.2.15}$$

The stiffness of the CNT Fiber may be obtained by means of Eq. (3.3.1), providing an expression that coincide with (3.3.11) obtained in [7].

3.2.2 Implementation of the finite difference model

The determination of the axial displacement field in the CNTs composing the fiber is governed by the "delayed advanced differential equation" (3.1.4), i.e., a differential equation in which the unknown function and its derivatives at a given point in the domain depend on the values taken by the function itself at "previous" and "subsequent" points, in terms of the axial coordinate. Because of the high complexity, these kinds of equations are usually solved by numerical techniques [208].

Here, the solution is found by implementing (3.1.4) with a finite difference technique. The considered CNT is discretized by dividing it into $n_e = n - 1$ elements, where n is the number of nodes[6], of the same length b. To treat Neumann boundary conditions (3.1.5) in an accurate way, it is necessary to add two "ghost nodes" (see, among the others, [218, 219]) outside of the domain and next to the boundaries, as shown in Figure 3.4. This obviously results in a total number of $n + 2$ nodes.

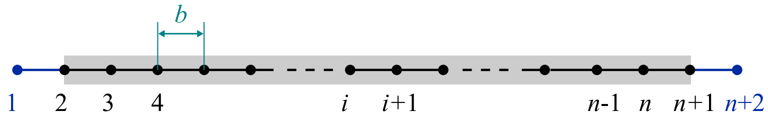

Figure 3.4. CNT discretization, with evidence of the “ghost nodes”.

The displacement field in the CNT is described by a vector $\mathbf{u}$, whose components are denoted in the sequel as u_i, $i = 1 \ldots n + 2$. Notice that this choice ensure the continuity of the axial displacement at the interfaces between the different regions. In the interior of the computational domain the second derivative is defined by using the “second central difference” scheme, i.e.,

$$u''(\xi)\ \Rightarrow \frac{u_{(i+1)} - 2u_i + u_{(i-1)}}{b^2}\,, \tag{3.2.16}$$

while boundary conditions (3.1.5) are prescribed by using the “backward difference” and “forward difference” schemes at the two ends of the domain, respectively, i.e.,

---

[6] To have a symmetrical configuration with respect to the central node, n is chosen to be an odd number.

$$\frac{u_2 - u_1}{b} = 0\,, \quad \frac{u_{(n+2)} - u_{(n+1)}}{b} = 0\,. \tag{3.2.17}$$

The numbers of elements in region A, n_A, and B, n_B, are respectively given by

$$n_A = \psi\ n_e \quad n_B = (1 - 2\psi)\ n_e. \tag{3.2.18}$$

Hence, the boundary nodes between regions A and B, and between B and C, are located at $i_{AB} = n_A + 2$ and $i_{BC} = n_A + n_B + 2$, as schematized in Figure 3.5. Obviously, for $\psi = 0.5$ the end of region A coincides with the beginning of region C, while the length of region B is nil. Henceforth, in the numerical code $i_{AB} = i_{BC}$.

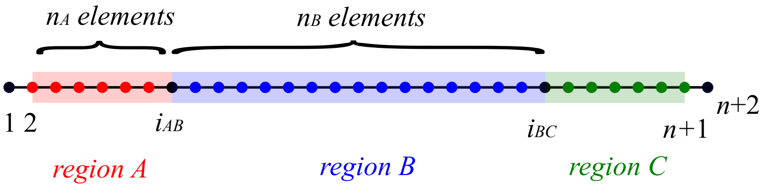

Figure 3.5. Discretization of CNT regions.

To avoid ambiguities, the continuity of the axial force $N(\xi)$, i.e., the equality between the backward and the forward first derivative of $u(\xi)$, is prescribed at the interface nodes i_{AB} and i_{BC}, in the form

$$\frac{u_i - u_{(i-1)}}{b} = \frac{u_{(i+1)} - u_i}{b} \qquad i = i_{AB},\ i_{BC}\,, \tag{3.2.19}$$

while the field equations (3.1.4) are prescribed on the three regions in the form

$$\begin{cases} EA\frac{u_{(i+1)}-2u_i+u_{(i-1)}}{b^2} = 2k(\varepsilon l - u_{(i+n_A)} - u_{(i+n_A+n_B)} + 2\ u_i) & \forall i \in [2, i_{AB} - 1] \\ EA\frac{u_{(i+1)}-2u_i+u_{(i-1)}}{b^2} = 2k(u_{(i+n_A)} - u_{(i-n_A)} + 2\ u_i) & \forall i \in [i_{AB} + 1, i_{BC} - 1] \\ EA\frac{u_{(i+1)}-2u_i+u_{(i-1)}}{b^2} = -2k(\varepsilon l - u_{(i-n_A-n_B)} - u_{(i-n_A)} + 2\ u_i), & \forall \in [i_{BC} + 1, n + 1]\,. \end{cases} \tag{3.2.20}$$

To avoid rigid body displacements, the displacement of the central node has been set equal to zero. Equation (3.2.20) may be rearranged in a matrix form as $\mathbf{Ku} = \mathbf{b}$, where $\mathbf{K}$ is the matrix of coefficients, $\mathbf{u}$ is the vector of unknown nodal displacements, and $\mathbf{b}$ is the vector of known terms. It may be verified that $\mathbf{K}$ is a banded matrix.

3.2.3 Influence of model parameters

The delayed-advanced differential equation (3.1.4) is numerically solved by means of the finite difference technique, allowing to evaluate both the axial displacement $u(\xi)$ and the axial force $N(\xi)$. The details of the implementation may be found in Section 3.2.2. This allows to evaluate *a posteriori* the relative slips between adjacent CNTs (Eq.s (3.2.8) and (3.2.9)) and the shear forces transmitted by the distributed springs.

In Section 3.2.1, the results are analytically compared with the closed-form solution obtained in [7] for the case of fiber composed by rigid CNTs. In the sequel, the influence on the displacement field of the CNT length and offset is studied.

Results in terms of axial displacement and axial force

By numerically solving the delayed-advanced differential equation (3.1.4), it is possible to evaluate the displacement field $u(\xi)$ on the CNT. Consider, as a reference example, a fiber composed of SW-CNTs with diameter $d = 1$ nm, and Young modulus $E = 10^6$ MPa. The axial stiffness of the individual CNTs is, hence, $EA = 1.068\ 10^{-6}$ N. According to [7], the stiffness of the shear springs[7] connecting the adjacent CNTs is assumed to be $\kappa = 0.1$ MPa. For these parameters, Figure 3.6(a) shows the arrangement of the reference (i, j, k)th CNT and of its neighboring ones, for CNT lenght $l = 2$ μm and offset parameter $\psi = 0.2$, in the undeformed (reference) configuration, while Figure 3.6(b) shows CNTs arrangement and deformation due to a prescribed macroscopic fiber deformation $\epsilon = 10\%$.

It may be noticed from Figure 3.6(b) that the CNTs not only move away from each other, but also elongate. To clearly appreciate the extent of this deformation in the figure, the representation of the CNTs with initial length (shown with light colors) is superimposed on that of the actually deformed CNTs (shown with darker colors). The axial strain $\varepsilon(\xi) = u'(\xi)$ in the (i, j, k)th CNT is plotted, with colorbar, on the same figure. Notice that the CNT is not uniformly strained, i.e., $\varepsilon(\xi)$ is higher in the central part of the CNT, while being null at its ends.

To investigate the influence on the CNT axial strain of the offset parameter ψ, now the case $\psi = 0.5$ is considered. Figure 3.7 shows the arrangement of CNTs, with $l = 2$ μm and $\psi = 0.5$, before and after the deformation.

For the cases $\psi = 0.2$ and $\psi = 0.5$, Figure 3.8(a) shows the axial displacement $u(\xi)$ of the CNT (to avoid rigid body displacement, here $u(\xi)|_{\xi=0} = 0$ has been set). As expected, due to the symmetry of the considered problem, the displacement field is anti-symmetric. Graph in Figure 3.8(b) records the axial force $N(\xi) = EAu'(\xi)$, varying along the axial coordinate of the CNT. Figure 3.8(c) show the trend of the total shear force $t_{tot}(\xi)$ (3.2.12) transmitted by the adjacent CNTs.

It may be observed that, for $\psi = 0.2$, $t_{tot}(\xi)$ is approximately constant in region A and C, while being almost nil in the central region B. Noticeably, this solution is qualitatively very similar to that obtained by adopting the assumption of rigid CNTs (see also Section 3.2.1). On the other hand, for $\psi = 0.5$, the variation of the total force $t_{tot}(\xi)$ along the ξ coordinate is more relevant than that recorded for $\psi = 0.2$.

---

[7] Unfortunately, the scientific literature does not provide univoque values for the shear stiffness of van der Waals bonding, that is highly dependent on several chemical and geometrical parameters, as, for example, the CNT chirality [220, 221] and the spacing between adjacent CNTs [200]. Furthermore, the shear stiffness of the bonding can be consistently increased by means of cross-links (see, among the others, [53, 201, 222]). Hence, in order to compare the proposed analytical model with that of [7], the same value κ=0.1 MPa recorded in that paper is used.

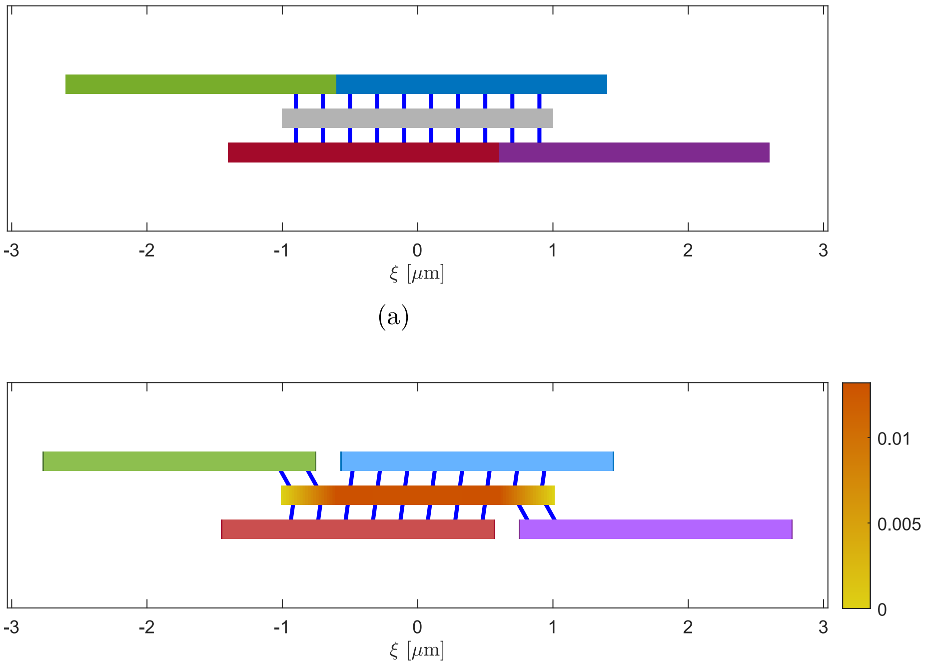

(a)

(b)

Figure 3.6. Case $l = 2$ μm, $\psi = 0.2$. (a) Undeformed and (b) deformed configuration of the (i, j, k)-th CNT and of its neighboring CNTs, on the (x, y) plane, with plot of the axial strain $\varepsilon(\xi)$ on the (i, j, k)-th CNT.

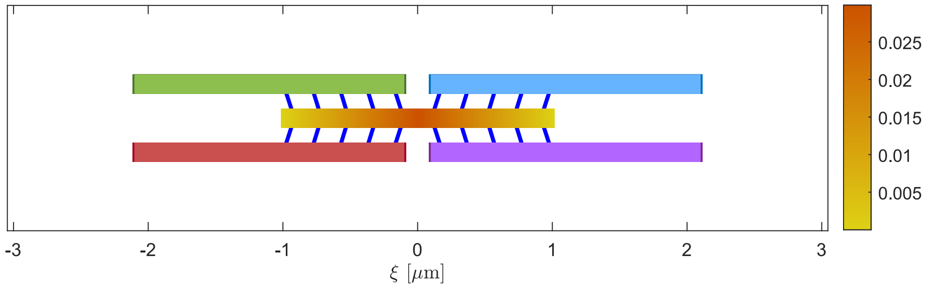

Figure 3.7. Case $l = 2$ μm, $\psi = 0.5$. Deformed configuration of the (i, j, k)th CNT and of its neighboring CNTs, on the (x, y) plane, with plot of the axial strain $\varepsilon(\xi)$ on the (i, j, k)th CNT.

This indicates that the deformability of the individual CNTs plays a more important role for high values of axial offset. It may also be noticed that, for $\psi = 0.5$, $N(\xi)$ takes high values in the central region of the CNT, hence resulting in a high value of strain in proximity of $\xi = 0$.

To investigate the influence of the CNT length on its axial displacement field, now a fiber composed by CNT 5 μm long is considered, while leaving unchanged the other relevant parameters. Figures 3.9(a) and 3.9(b) show the arrangement of CNTs, for the cases $\psi = 0.2$ and $\psi = 0.5$, respectively. For the same cases, Figure 3.10 shows the

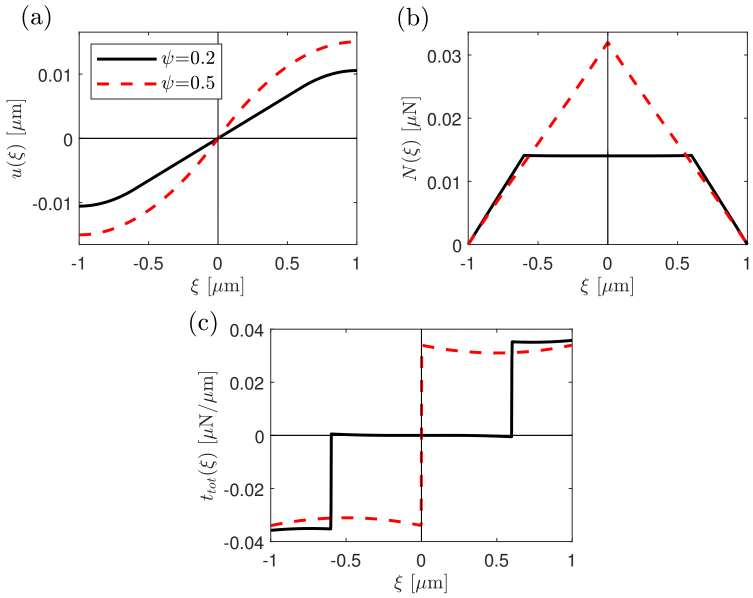

Figure 3.8. Case $l = 2$ μm. (a) Axial displacement field $u(\xi)$, (b) axial force $N(\xi)$, c) total shear force $t_{tot}(\xi)$.

axial distribution of the axial displacement and of the axial force in each CNT, as well as the total shear forces.

It may be noticed from Figure 3.9 that, in this case, the elongation of the individual CNTs is consistently higher than that observed in Figures 3.6(b) and 3.7. Furthermore, by comparing Figure 3.10 with its counterpart for CNTs 2 μm long (Figure 3.8), it may be observed that, for longer CNTs, the (non-linear) variation of the total force along the ξ axis is much more relevant. Notice, in particular, that for the case $\psi = 0.5$ the axial strain tends to localize in the neighbouring of the interface between the two regions, i.e., at $\xi = 0$. It may be verified that this phenomenon is even more relevant for higher values of l (graphs are not recorded here for the sake of brevity). This is because, for very high CNT length (or, equivalently, for very low axial stiffness of the CNTs, or for high stiffness of the distributed springs), the forces exerted by the springs tend to concentrate at the interface between region A and C, tending to become dipoles. Correspondingly, the axial force $N(\xi)$ tends to become constant along ξ, with a Dirac delta arising at $\xi = 0$. Obviously, this kind of response cannot be captured by the simpler model of [7].

The particular case of null axial offset ($\psi = 0$) corresponds to a configuration with vertically stacked CNTs. As already observed in [7], in this case the fiber is underconstrained and cannot bear axial loads, because the stacks can move independently one another. Therefore, both the displacement and strain fields are nil, as well as the forces transmitted by the (not-deformed) shear distributed springs.

For all the considered cases, the numerical model allows to evaluate the resultant of the shear forces acting, on the (x, y) plane, on the lower part of the CNT (i.e., in

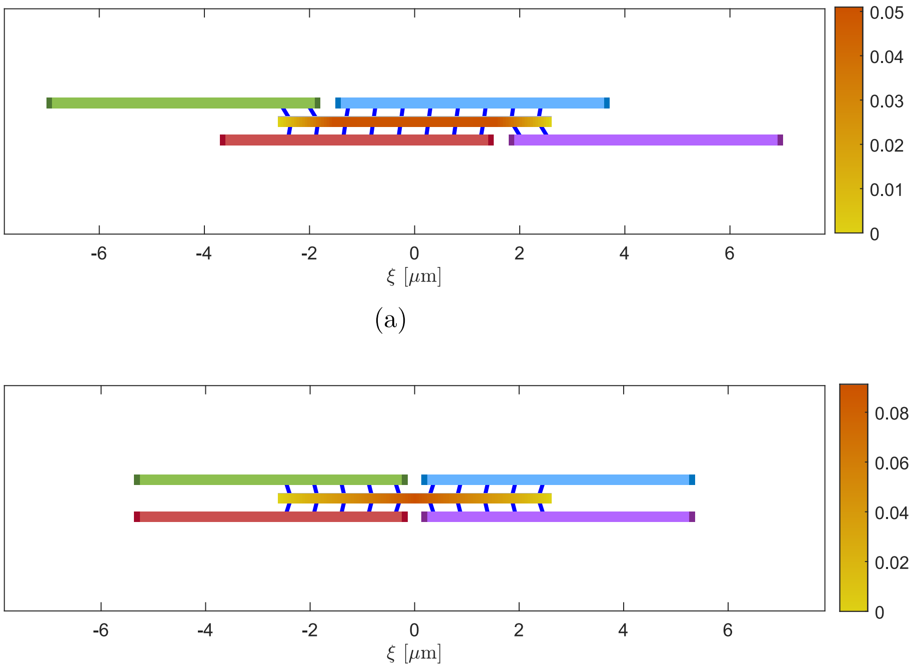

(a)

(b)

Figure 3.9. Case $l = 5$ μm. Deformed configuration of the (i, j, k)th CNT and of its neighboring CNTs, on the (x, y) plane, with plot of the axial strain $\varepsilon(\xi)$ on the (i, j, k)th CNT. Cases (a) $\psi = 0.2$ and (b) $\psi = 0.5$.

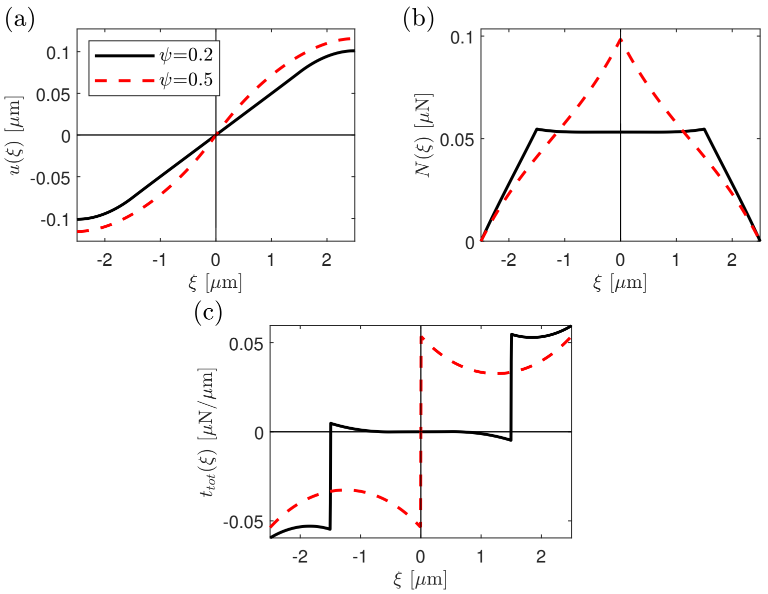

Figure 3.10. Case $l = 5$ μm. (a) Axial displacement field $u(\xi)$, (b) axial force $N(\xi)$, c) total shear force $t_{tot}(\xi)$.

the direction of decreasing y), and on its upper (direction of increasing y) part, i.e.,

$$\begin{aligned} T_{y^-} &= \int_{-l/2}^{l(1/2-\psi)} t_{i,j-1,k}(\xi)\ d\xi + \int_{l(1/2-\psi)}^{l/2} t_{i+1,j-1,k}(\xi)\ d\xi\,, \\ T_{y^+} &= \int_{-l/2}^{l(\psi-1/2)} t_{i-1,j+1,k}(\xi)\ d\xi + \int_{l(\psi-1/2)}^{l/2} t_{i,j+1,k}(\xi)\ d\xi\,. \end{aligned} \tag{3.2.21}$$

Obviously, due to the symmetry of the problem, on the (x,z) plane the resultants will be $T_{z^-} = T_{y^-}$ and $T_{z^+} = T_{y^+}$. To satisfy the rotational equilibrium about the y and z axes, all the resultants must be nil (so to not give rise to couples), i.e.,

$$T_{z^-} = T_{y^-} = T_{z^+} = T_{y^+} = 0\,. \tag{3.2.22}$$

This obviously satisfies also the equilibrium in the axial direction. Condition (3.2.22) has been numerically verified, confirming the accuracy of the obtained solution. Remarkably, this will be useful for the evaluation of the effective tensile stiffness of the CNT Fiber, as it will be discussed in Section 3.3.2.

CNT relative elongation and strain energy

The results presented in the previous Subsection suggest that the axial strain of the CNTs is higher for long CNTs, and for high values of axial offset. To deeply investigate this phenomenon, consider the strain energy of the single CNTs, correspondent to the energy "spent" to deform the individual CNTs, defined as

$$\mathcal{E}_{CNT} = \frac{1}{2}\int_{-l/2}^{l/2} N(\xi)u'(\xi)\ d\xi = \frac{EA}{2}\int_{-l/2}^{l/2} \left[u'(\xi)\right]^2\ d\xi\,. \tag{3.2.23}$$

In Figure 3.11(a), $\mathcal{E}_{CNT}$ is plotted as a function of the offset parameter ψ, for different values of the CNT's length ($l = 2,\ 5,\ 7\ \mu$m). Obviously, the graph is symmetric, because the case $\psi \in [0.5,1]$ may be treated by considering, instead of ψ, the value $1-\psi$. Obviously, for the stacked configuration ($\psi = 0,\ 1$), the strain energy is null. Figure 3.11(b) is the counterpart of Figure 3.11(a), showing $\mathcal{E}_{CNT}$ as a function of l, for different values of ψ.

It is evident that the strain energy is strongly dependent upon the CNT length and offset, being higher for long and highly coupled CNTs (i.e., for high values of ψ). Figure 3.11(b) highlights how the dependence of $\mathcal{E}_{CNT}$ on the CNT length is superlinear.

Consider now the relative elongation of the individual CNTs, $\Delta l/l$, that is strongly dependent on their axial stiffness, and on the stiffness κ of the distributed springs. By defining a coefficient $\beta := EA/\kappa$, the following non-dimensional quantity may be defined

$$\phi(\beta,l,\psi) := \frac{\Delta l}{\epsilon l} = \frac{1}{\epsilon l}\int_{-l/2}^{l/2} u'(\xi)\ d\xi\,, \tag{3.2.24}$$

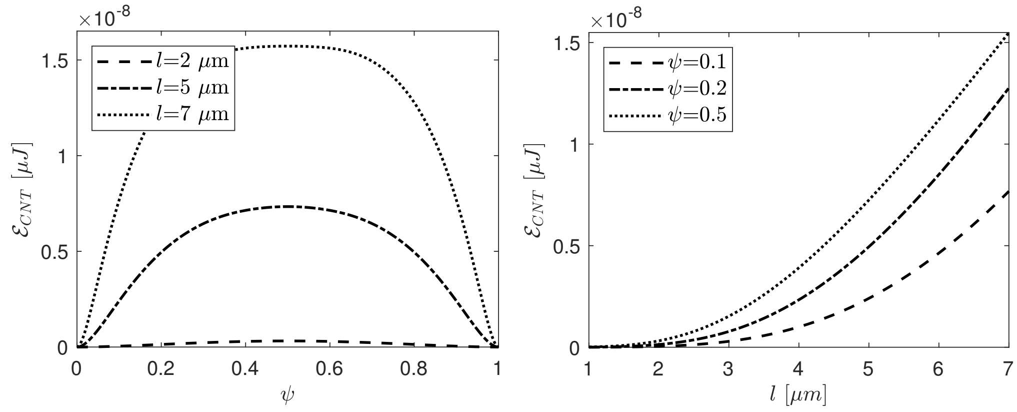

(a) (b)

Figure 3.11. Strain energy of the individual CNT (a) as a function of ψ, for different values of l and (b) as a function of l, for different values of ψ.

correspondent to the ratio between the relative elongation of the individual CNTs and the prescribed macroscopic deformation ϵ, correspondent to the displacement of their centroids along the fiber axis (independent of l and ψ, as discussed in Section 3.1.2). It may be verified that, due to the linearity of the considered problem, $\phi(\beta, l, \psi)$ is independent of ϵ. It is expected to vary between 0 (when the CNTs are rigid and hence $\Delta l = 0$, and when they are stackered), and 1 (when the CNTs are very deformable with respect to the shear springs, and hence all the prescribed deformation results in an elongation of the individual CNTs). Indeed, in the latter case, the axial displacement may be evaluated by requiring that the relative displacement of adjacent CNTs is null, and turns out to be in the form $u(\xi) = \epsilon\xi$, hence providing $\Delta l = \epsilon l$ and, consequently, $\phi(\beta, l, \psi) \to 1$. Hence, $\phi(\beta, l, \psi)$ may be regarded as a "measure" of the relevance of the two deformation mechanisms described at the beginning of Section 3.1. This will be discussed more in detail in Section 3.3.3.

Figure 3.12(a) shows $\phi(\beta, l, \psi)$ plotted as a function of the offset parameter ψ, for the same values of l considered in Figure 3.11(a). Figure 3.12(b) is the counterpart of Figure 3.12(a), showing $\Delta l/l$ as a function of l, for different values of ψ.

As expected from previous results, the relative elongation of the CNTs increases as their length and offset increase. With reference to the two deformation mechanisms described at the beginning of Section 3.1, this means that the stretch of the individual CNTs becomes more relevant, with respect to the displacement of their centroids along the fiber axis, for long and highly offset CNTs.

Notice that, for low values of l, the dependence on the offset parameter ψ is approximately parabolic, while for higher values of l it takes a more complicated dependence on ψ. In particular, in the latter case, $\phi(\beta, l, \psi)$ is almost constant for a wide range of values of ψ, taking lower values for $\psi \simeq 0.5$. This is because, as discussed in Section 3.2.3, in this case the strain tends to concentrate only in the central region of the CNTs. It may be verified that this phenomenon is even more relevant for higher

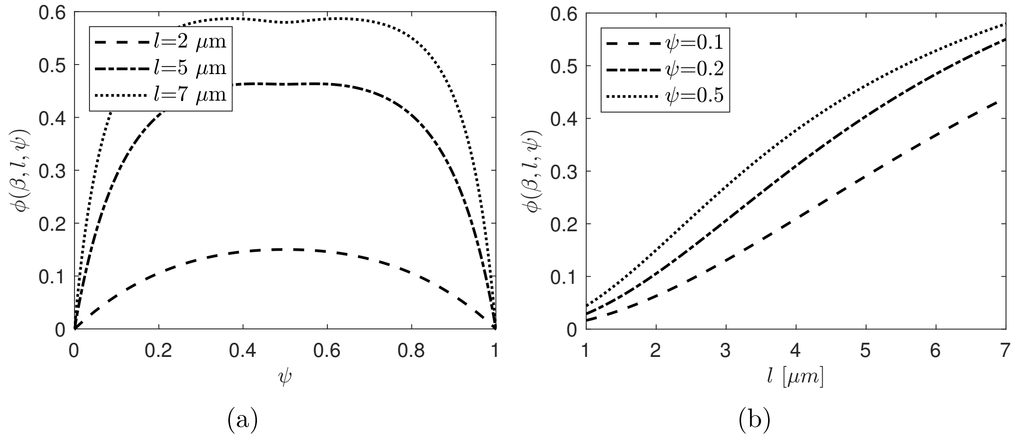

(a) (b)

Figure 3.12. Non-dimensional function $\phi(\beta, l, \psi)$ (a) as a function of ψ, for different values of l and (b) as a function of l, for different values of ψ.

values of l.

3.3 Effective tensile stiffness

The displacement field determined in Section 3.1 allows to evaluate the macroscopic stiffness of the whole CNT Fiber. This may be done by considering the fiber as an equivalent homogeneous beam, subjected to a macroscopic deformation ϵ, whose *effective Young's modulus* E_f can be defined as

$$E_f = \frac{N_f}{A_f \epsilon}, \tag{3.3.1}$$

where A_f is the cross-sectional area of the fiber, of arbitrary shape, while N_f is the total axial force acting on the fiber itself, that may be evaluated as the sum of the axial forces acting on the individual CNTs. To calculate N_f, it is important to proper account for the CNTs distribution in the fiber cross-section.

In the sequel, first the simple case where the fiber may be considered as formed by "bunches" composed by a integer number of CNTs is considered, for the sake of explanation, and hence the more general case is treated.

3.3.1 Simple case

Consider first the simple case where $\psi = 1/n_b$, being n_b a natural number. Recall that, as discussed in Section 3.1, the CNTs are assumed to be arranged in the fiber cross-section according to a square matrix, allowing their distribution to be the same on the (x, y) and (x, z) planes. Since the distribution of CNTs on each row/column repeats periodically every n_b CNTs, it is possible to identify "bunches" composed by n_b CNTs on each row/column composing the fiber cross-section. Due to the periodicity, the bunches are equal one to each other, and repeat on each row/column (i.e., on both the (x, y) and the (x, z) planes). This kind of subdivision is illustrated in Figure 3.13, referring to a fiber[8] composed by CNTs offset in the axial direction of 1/5 of their length (i.e., $\psi = 0.2$), where "bunches" of 5 CNTs may be identified on both the y and z directions. In the following, for simplicity, reference is made to bunches lying on the (x, y) plane.

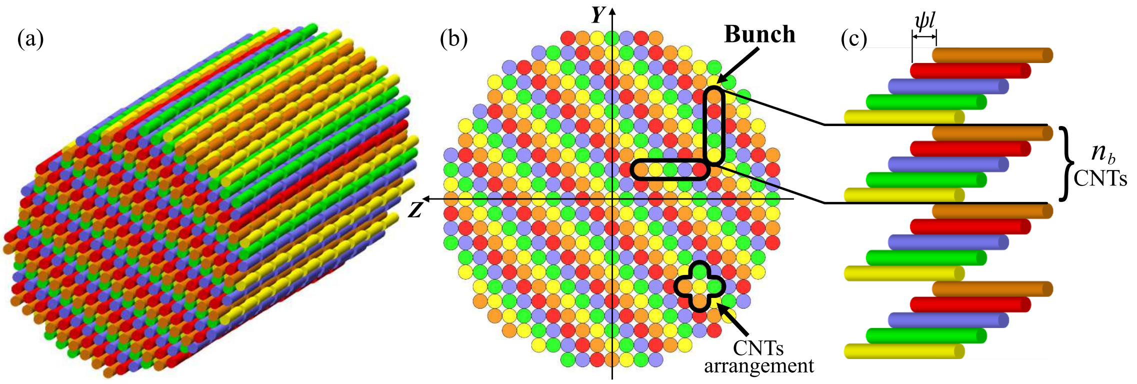

Figure 3.13. Section of the CNT Fiber: (a) 3D and (b) 2D view, and (c) detail of the CNT bunch. Different colors indicate different axial position of the CNTs.

Due to the periodicity of the considered structure, each bunch carries the same axial load, hereafter denoted to as N_b. This may be evaluated by sectioning the bunch as shown in Figure 3.14, at a generic distance αl, with $\alpha < \psi$, from the left end of the first CNT.

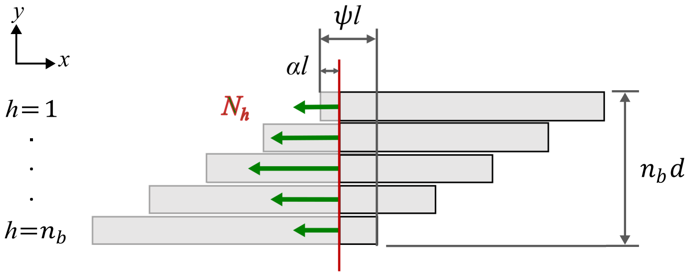

Figure 3.14. Sectioning the bunch.

Notice that this correspond to section each CNT composing the bunch at a different coordinate ξ. Consequently, by numbering the CNTs composing the bunch with the pedex $h = 1 \ldots n_b$ as in Figure 3.14, the axial force acting on the hth CNT may be evaluated as

$$N_h = N(\xi)\big|_{\xi=-\frac{l}{2}+\alpha l+(h-1)\psi l} \,. \tag{3.3.2}$$

---

[8] For the sake of example, without loss of generality, in Figure 3.13 a CNT Fiber with circular cross-section is shown. However, the proposed approach can be used for any shape of the cross section.

Consequently, the normal force on the whole bunch is given by

$$N_b = \sum_{h=1}^{n_b} N_h = \sum_{h=1}^{n_b} N\left(-\frac{l}{2} + \alpha l + (h-1)\psi l\right) . \tag{3.3.3}$$

It has been numerically verified that N_b is independent of the parameter α. This is a noteworthy result, confirming that, even if the axial force on the individual CNTs is highly variable along their axis (see Figures 3.8 and 3.10), their resultant on the bunch is uniform. Once N_b is known, the total force acting on the fiber may be evaluated by summing the contributions of all the bunches. Observing that the "area of competence" of each bunch is

$$A_b = n_b d^2 = \frac{d^2}{\psi} , \tag{3.3.4}$$

and consequently the total force N_f may be evaluated as

$$N_f = \frac{A_f}{A_b} N_b = \frac{\psi A_f}{d^2} N_b . \tag{3.3.5}$$

3.3.2 General case

The approach proposed in Section 3.3.1 can be used only if the bunch is composed by an integer number $n_b = 1/\psi$ of CNTs, while the case where ψ is a generic real number may be treated in a more general way. To illustrate it, consider the CNT bunch of Figure 3.13, sectioned with $\alpha = 0$, as shown in Figure 3.15(a). Consider also the cut with "saw-toothed profile" indicated with dashed line in the same Figure, formed by n_b inclined cuts with slope $-\psi l/d$.

Consider the equilibrium in the axial direction of the portion comprised between these two "cuts", as shown in Figure 3.15(b). As schematized in the same Figure, on the l.h.s. each CNT, of diameter d, is subjected to the axial forces N_h (3.3.2), while on the inclined cut the force $\frac{N(\xi)}{d} d\eta$ arise on the infinitesimal $-d\eta$. Furthermore, the portion of bunch is also subjected to the shear forces[9] acting on the lower part of the CNTs, correspondent to $t_{i,j-1,k}(\xi)$ (in regions A and B) and $t_{i+1,j-1,k}(\xi)$ (in region C, see also Figure 3.2(a)).

The equilibrium of this portion of the bunch may be evaluated in a very simple way. Indeed, by "translating" each CNT of ψl in the axial direction, as shown in Figure 3.16, it is evident that the inclined cut covers all the CNT length.

Recalling that the slope is $-\psi l/d$, and hence $-d\eta = \frac{d}{\psi l}\, d\xi$, the axial equilibrium of the portion of the bunch between the cuts reads

---

[9] Recall that, due to the periodicity of the problem, each CNT is subjected to the same action configuration.

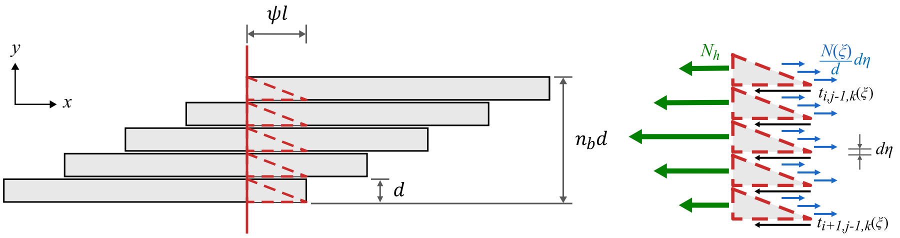

(a) (b)

Figure 3.15. (a) Cut with "saw-toothed profile"; (b) Equilibrium of the portion between the cuts.

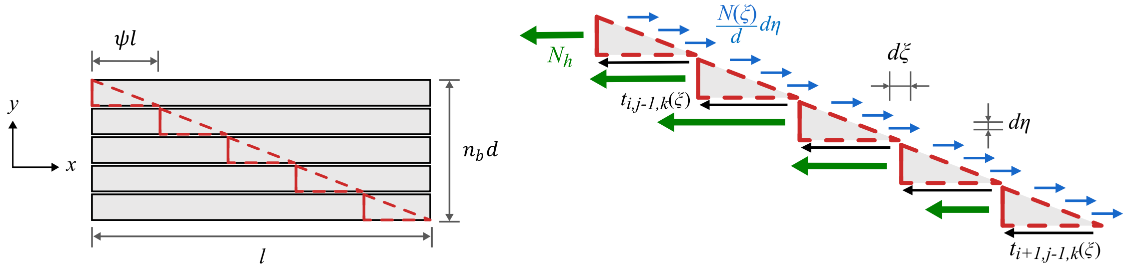

(a) (b)

Figure 3.16. (a) "Translating" each CNT of ψl in the axial direction; (b) The inclined cut covers all the CNT length.

$$-\sum_{h=1}^{n_b} N_h + \frac{1}{\psi l}\int_{-l/2}^{l/2} N(\xi)\ d\xi - \int_{-l/2}^{l(1/2-\psi)} t_{i,j-1,k}(\xi)\ d\xi + \int_{l(1/2-\psi)}^{l/2} t_{i+1,j-1,k}(\xi)\ d\xi = 0\,. \tag{3.3.6}$$

Observe now that the latter two terms of (3.3.6) correspond to the resultant of the shear forces acting on the lower part of the CNT, i.e., T_{y^-} of Eq. (3.2.21), that is nil as per Eq. (3.2.22). This allows to evaluate the axial force on the bunch as

$$N_b = \sum_{h=1}^{n_b} N_h = \frac{1}{\psi l}\int_{-l/2}^{l/2} N(\xi)\ d\xi\,. \tag{3.3.7}$$

Equation (3.3.7) may be regarded a generalization of Eq. (3.3.3), allowing to evaluate the axial force N_b acting on the bunch as the integral of the axial force $N(\xi)$ acting on the whole length of the constituent CNTs.

Remarkably, this expression can be used for arbitrary values of ψ. However, in this case, unless $1/\psi$ is an integer, it is obviously not possible to define a bunch composed by an integer number of CNTs. Consequently, N_b may be interpreted as the resulting axial force on a fiber portion, lying on the (x, y) plane, of height d/ψ and "thickness" d (in the z direction). Henceforth, its "area of competence" is again given by (3.3.4). Consequently, the total force on the whole fiber may be evaluated with an expression analogue to (3.3.5), i.e.,

$$N_f = \frac{A_f}{ld^2} \int_{-l/2}^{l/2} N(\xi)\ d\xi \tag{3.3.8}$$

while the effective Young's modulus of the fiber (3.3.1) may be evaluated as

$$E_f = \frac{1}{\epsilon l d^2} \int_{-l/2}^{l/2} N(\xi)\ d\xi\,. \tag{3.3.9}$$

This confirms that, as expected, the effective Young's modulus is independent on size and shape of the fiber cross-section, being dependent only on the geometrical and mechanical properties of the constituent CNTs, and on their lateral bond.

3.3.3 Results and comparisons

Once the axial strain and the axial load on the individual CNTs has been numerically evaluated as detailed in Section 3.1, the effective Young's modulus of the fiber can be calculated by means of Eq. (3.3.9). Here, the obtained results are compared with those obtained by using the simplified model of [7], assuming rigid CNTs, as well as with experimental data from literature.

Influence of mechanical and geometric parameters

To evaluate the influence of the diverse geometric and mechanical parameters, observe that, by recalling that $\int_{-l/2}^{l/2} N(\xi)\ d\xi = EA \int_{-l/2}^{l/2} u'(\xi)\ d\xi = EA\Delta l$, Eq. (3.3.9) may be rearranged as

$$E_f = \frac{\kappa\beta}{d^2}\ \phi(\beta, l, \psi)\,. \tag{3.3.10}$$

where, again, $\beta = EA/\kappa$, and the non-dimensional function $\phi(\beta, l, \psi)$ is given by Eq. (3.2.24). It may be verified that the fiber axial modulus is intermediate between the following limits:

- when the CNTs are rigid ($EA \to \infty$), $\beta \to \infty$ and $\phi(\beta, l, \psi) \to 0$. In this case, it may be verified that

  $$\beta\ \phi(\beta, l, \psi) \to 2\psi(1-\psi)l^2 \qquad \Rightarrow \qquad \lim_{\beta\to\infty} E_f = 2\kappa\psi(1-\psi)\frac{l^2}{d^2}\,, \tag{3.3.11}$$

  that coincides with the expression recorded in [7]. The details of the calculation are recorded in Section 3.2.1.

- when the shear springs are rigid, i.e., $\kappa \to \infty$, $\beta \to 0$. In this case, as discussed in section 3.2.3, $\phi(\beta, l, \psi) \to 1$ and

  $$\lim_{\beta\to 0} E_f = \frac{EA}{d^2}\,. \tag{3.3.12}$$

Notice that, since the quantity A/d^2 is the ratio between the CNTs cross sectional area and its "area of competence" in the cross-section of the fiber, the effective fiber stiffness simply corresponds to the sum of the axial stiffness of the (fully coupled) individual CNTs.

In Figure 3.17, the non-dimensional function $\phi(\beta, l, \psi)$ is plotted, as a function of β, for different values of ψ. The different graphs correspond to different CNT length. It is evident that $\phi(\beta, l, \psi) \to 1$ for low values of β, also dependently on the values of ψ and l. As expected, the ratio between the axial stiffness EA of the individual CNTs, and the stiffness κ of the distributed springs, plays a definite role on the fiber response. When the CNTs are bonded by means of cross-link, κ may be evaluated as a function of the cross-link density [53, 201]. Remarkably, graphs in Figure 3.17 may represent a practical tool to evaluate the effective stiffness of CNT Fibers. Indeed, if the geometric (l, ψ) and mechanical (E, A, κ) parameters are known, these allow to evaluate the non-dimensional function $\phi(\beta, l, \psi)$ and, consequently, E_f through Eq. (3.3.10).

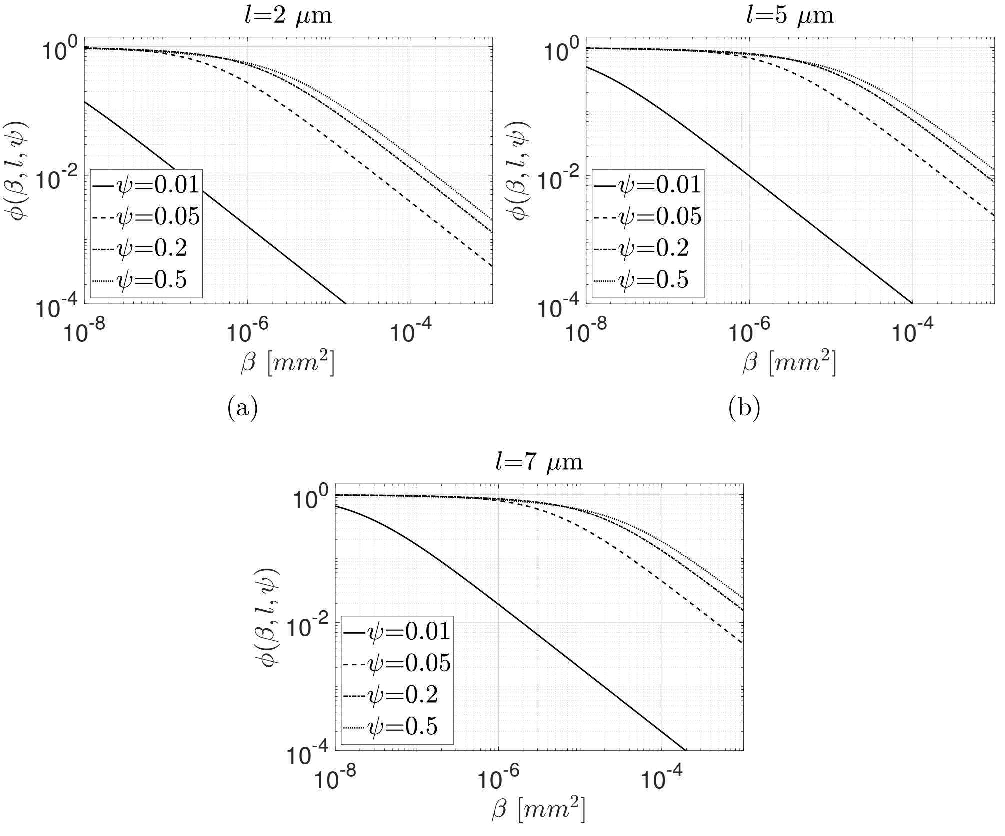

(a) (b)

(c)

Figure 3.17. Evaluation of $\phi(\beta, l, \psi)$, as a function of $\beta = EA/\kappa$, for different values of ψ, for CNT length of (a) 2 μm, (b) 5 μm and (c) 7 μm.

Comparison with the results obtained for the case of rigid CNTs

Here, the effective Young's modulus (3.3.9) is numerically evaluated for CNT Fiber with the same geometric and mechanical parameters considered in Section 3.2.3, i.e., $d = 1$ nm, $s = 0.34$ nm, $E = 10^6$ MPa, $\kappa = 0.1$ MPa, and variable l and ψ. According to Eq. (3.3.9), the size of the fiber cross-section does not affect its effective modulus.

Figure 3.18(a) shows the effective Young's modulus E_f (plotted with thick black lines), on a logarithmic scale, as a function of the CNT length l. The different curves correspond to different values of the offset parameter ψ. To highlight the influence on the overall tensile response of the compliance of the CNTs, the results are compared with those obtained by by assuming, as done in [7], the constituent CNTs to be rigid (3.3.11) (thin red curves).

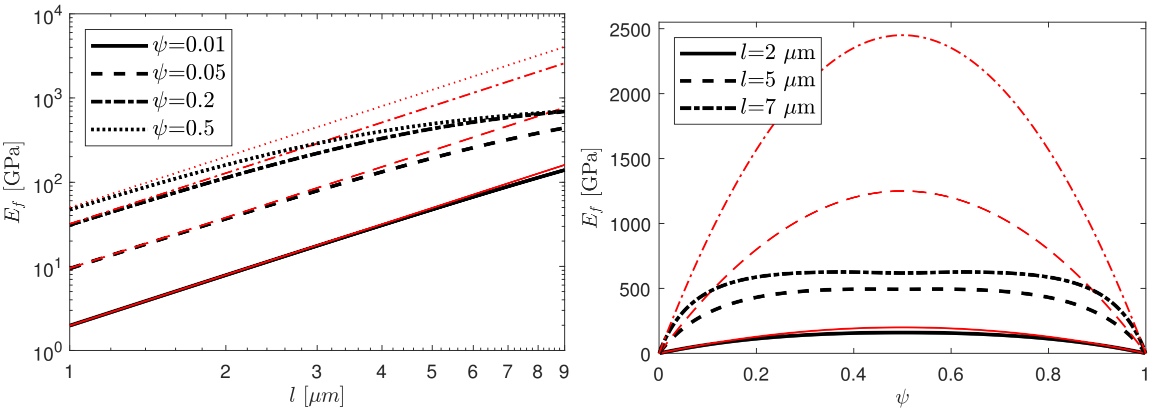

(a) (b)

Figure 3.18. Effective Young's modulus E_f of the CNT Fiber (a) as a function of l, for different ψ, and (b) as a function of ψ, for different l: proposed model (thick black curves) and model by [7] (thin red curves).

As expected, when the offset parameter ψ increases, the coupling between the different CNTs increases, so providing an increase of macroscopic stiffness of the CNT Fiber.

Notice that the model [7] provides an effective modulus directly proportional to the square of the length of the constituent CNTs, according to Eq. (3.3.11), so resulting in straight curves on the logarithmic plane. As may be noticed from Figure 3.18(a), for low values of l, the proposed model provides results that in practice coincide with those of [7]. This is because, when the constituent CNTs are "short", their strain is very low (see also plot in Figure 3.12(b)) and it does not affect the macroscopic stiffness. When l increases, the contribution of the deformability of the individual CNTs becomes more relevant, leading to a decrease of the overall axial stiffness of the fiber, with respect to that predicted by the model [7]. This results in a decrease of the slope of the curves in Figure 3.18(a), that is more relevant for high values of the offset parameter ψ.

It can also be verified that, for very high values of the length l of the CNTs (dependently on the offset parameter, of the order of 10-20 μm, a value that cannot be obtained with the current technology), E_f settles to a constant value, independent on ψ. This means that when the CNTs are very long, they are "well coupled" because of their length, regardless of the offset, which becomes irrelevant under these conditions. This behavior is qualitatively similar to that observed [7] for the *bending* response of CNT Fibers.

Figure 3.18(b) shows the effective Young's modulus E_f of the CNT Fiber, plotted as a function of the offset parameter ψ, for various lengths l of the CNTs composing the fiber. Again, also the result obtained by assuming rigid CNTs are plotted for the sake of comparison. When CNTs are rigid, Eq. (3.3.11) provides a quadratic dependence of E_f on the offset parameter, with $E_f = 0$ for $\psi = 0{,}1$ (configuration with stacked CNTs). The proposed model (Eq. (3.3.9)) provides a qualitatively different trend of E_f: the stiffness is still null for $\psi = 0{,}1$, but the middle part of the graph is more "flattened". This behavior suggests that also values of ψ quite distant from 0.5 are sufficient to impart to the fiber an high coupling. This phenomenon is more marked for high values of l, confirming the conclusions drawn from Figure 3.18(a).

It may be noticed that, since E_f is proportional to $\int_{-l/2}^{l/2} N(\xi)\, d\xi$, it has the same qualitative dependence on ψ and l of the function $\phi(\beta, l, \psi)$ plotted in Figure 3.12(a). In particular, for higher values of l, E_f has a slight decrease for $\psi = 0.5$. This is because, as discussed in Section 3.2.3, for $\psi = 0.5$ the central region of the CNT is ovestrained, so resulting in a decrease of the effective stiffness.

Comparison with experimental results

The obtained results are now compared with those recorded in the technical literature. Usually, experimental papers report measures of the effective axial stiffness of CNT Fibers, sometimes indicating the (mean) values of d and l, but with no consideration of the offset parameter ψ. Indeed, real fibers are composed of CNTs with different lengths, randomly aggregated. The proposed model interprets this random phenomenon by the parameter ψ, which can be varied to obtain a range of values for the effective Young's modulus, within which the experimental results should fall.

In the sequel, reference is made to the accurate experimental results recorded in [125]. These refer to tensile tests, performed with a rheometer, on 3 cm long fibers, with circular cross-section of diameter 10 μm, composed of SW-CNTs with $d \simeq$1.5 nm and different values of (mean) length l, i.e., 2.21 μm, 4.17 μm and 6.28 μm. Results presented in the sequel have been evaluated by considering a shear stiffness[10] of the lateral bonding $\kappa = 0.1$ Mpa, and a thickness of the graphite layer $s = 0.34$ nm. Figure 3.19 shows the comparison between the effective modulus E_f (3.3.9) and the experimental results recorded in [125].

The proposed model seems to correctly capture not only the order of magnitude of the experimental results (the experimental data fall within the band of values provided

---

[10] Again, since no precise data on the shear stiffness of the bonding are available, the value for κ recorded in [7] is here considered.

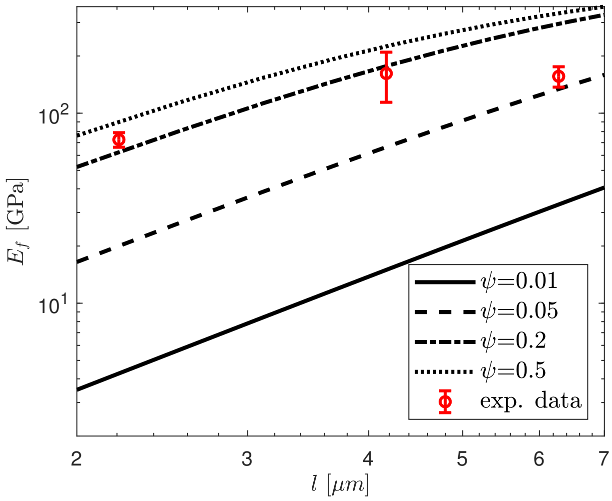

Figure 3.19. Effective Young's modulus E_f of the CNT Fiber as a function of l, for different ψ: comparison among the proposed model and experimental data from [125].

by the proposed model), but also the decrease in the curve slope for increasing CNTs length. It may be noticed that, for 2.21 μm and 4.17 μm long CNTs, the offset parameter is near to 0.2, while it decreases with increasing length. As observed in [7], this theoretical prediction may be justified by the particular production process [54], in which long CNTs, having a limited mobility with respect to short CNTs, may tend to gather in bunches. It may be easily verified, by comparing Figure 3.19 with Figure 3.18(a), that the proposed model provides a better fit of the experimental data, with respect to the model assuming rigid CNTs [7], in particular for high values of l. This confirms that, when CNTs are "long", their axial strain becomes more relevant, and to neglect it leads to an underestimation of the macroscopic stiffness of the fiber.

3.4 Discussion

The chapter presents an analytical-numerical micromechanical model for the evaluation of the tensile stiffness of Carbon NanoTube (CNT) Fibers, accounting for the coupling occurring on their lateral surfaces, thanks to Van der Waals forces and to cross-links. CNTs are modeled as bars with a given axial compliance, a factor neglected in most models previously proposed by the literature. The proposed model is based on the consideration that, due to the periodicity of the considered geometry, the same loading state is defined on each CNT composing the fiber, hence resulting in the same axial strain/stress field. It is demonstrated that these are governed by a delayed-advanced differential equation, here solved with finite difference technique. An analytical procedure has been presented to evaluate the resultant, on the whole fiber, of the axial forces on the individual CNTs, allowing to define the *macroscopic (effective) stiffness* of the fiber. It is demonstrated that this increases with the length of the CNTs and their axial offset, reaching its highest values when the latter is near to the half of the CNTs length. Graphs allowing to evaluate the effective stiffness of CNT Fibers, as a function of geometric and mechanical parameters, are recorded.

The obtained results are in good agreement with the literature experimental data [125]. The accuracy of the model is found to be higher than that obtained by neglecting the axial compliance of the CNTs [7]. Thus, this represents an important step forward in the study of CNT Fibers response, of particular importance in view of their use to produce cables for large-scale structural purposes. In particular, as technology is moving toward the production of longer CNTs, it is of particular importance to correctly account for the CNTs compliance. Further developments can consider more complex arrangements of CNTs, and the non-linear response of the connection between adjacent CNTs. With minor modifications, the proposed model could be suitable for the description of other structures composed of aligned nano-components, as for example boron nitride NTs [223].

The results of this work were summarized in [128].

Chapter 4

Geometry and mechanics of twisted yarns: an experimental rubber model for the study of CNTFs

Propaedeutical to a better understanding of the mechanics of CNTF yarns an more in general cables, with potential applications in material science and biology, tensile tests were performed on two-ply yarns made of rubber rods, manufactured by transforming the twist on two adjacent straight rods into tortuosity for the resulting double-helix shape.

4.1 Background on twisted rods

The mechanics of ropes subjected to tensile loads, and in particular the simplest case of two-ply yarns, has been the subject of numerous studies [224] and it is today considered a well consolidated topic [225]. Structural theories mainly focus on macroscopic applications, such as steel strands and hemp/nylon ropes. Apparently little attention has been paid to possible eigenstress states that can be present already in the reference configuration, when no tensile loads are applied, because they are not important for such applications. In steel cables, e.g., plastic deformation can annihilate the internal forces that are generated when the initially-straight wires are bent and twisted to form the cable. The eigenstress can be eliminated after manufacturing by heat treatment in metals, and mitigated by viscosity in materials such as nylon or plastics. Supported by an experimental campaign on two-ply yarns made up of hyperelastic rubber rods, it is experimentally and theoretically investigated the possible states of eigenstress that can occur in the constituent filaments, supposedly elastic and straight in the undistorted natural configuration, when these are helically wound around one another. How such eigenstress states can influence the gross tensile response of the yarn is shown, especially when the winding is very tight.

In helically wound structures, often encountered in engineering and biology, eigenstress states may potentially give rise to unexpected effects, due to the interaction with peculiar material properties and size effects. In recent years there has been growing interest in high-performance ultra-thin braids and yarns manufactured with CNTFs [6] that can be weaved and braided. CNT-Fiber yarns can be analyzed as classical helical-wire cables [226], but residual stresses cannot be removed by plasticity or annealing treatments, as for steel, and should not be neglected, at least in principle, when modeling their tensile response. In biology, the most studied structure is certainly represented by DNA, characterized by a double-helix architecture made with two phosphate-sugar chains [227]. Even if the shape of DNA, as well as that of other coiled biological macromolecules, is governed by complex mechanical and electro-chemical interactions, starting from the seminal work by Coleman and Swigon [228], many authors [228–236] have successfully contributed to explain the mechanism of formation of the helices by using Kirchhoff's theory of rods. This mechanism might be affected as well by the presence of an eigenstress state.

In the reference balanced configuration, in absence of external applied loads, the two threads (filaments) forming a two-ply yarn are mutually wound one another, forming a double helix of defined radius and pitch. The manufacturing process providing this configuration consists in transforming the artfully imposed twist on the straight threads into tortuosity for the helix: it can be obtained [230, 237] by first pre-twisting the two threads, placing them in longitudinal contact and releasing them, while constraining the relative rotation of their ends. It is energetically favorable to transform the pre-twist into tortuosity, causing each thread to become a helix thanks to the symmetry of the longitudinal contact with the neighboring thread. The tensile response of the yarn, starting from this configuration, can be studied by assuming that each thread is a Kirchhoff rod: if the wound threads are pulled, they will arrange themselves according to a new double helix, with radius and pitch compatible with the new deformed state. From the constitutive relations, it is then possible to find the internal forces in each thread and, consequently, evaluate their resultant at the ends, which balances the applied external forces. In many cases, the bending and torsional stiffness of each thread is so small that it can be neglected compared to the extensional contribution [120], an assumption which provides noteworthy simplifications.

The goal is to better understand the mechanics of twisted yarns, with particular attention at the effects of possible eigenstress states on their gross tensile properties. However, using extremely thin threads for the yarn would make experimental observation difficult. This is why an experimental campaign was carried out for two-ply yarns made of Nitrile Butadiene Rubber (NBR). This is a synthetic rubber [238] derived from acrylonitrile and butadiene, used in the automotive, aeronautical and nuclear industry to make fuel and oil handling hoses, grommets, seals and gaskets. For short duration loads the material can be approximately considered hyperelastic, with elongation at fracture of the order of 600 %. The yarns were made of two helically wound NBR rods with circular cross-section with undistorted diameter of 5 mm. Samples of yarns formed by helices with various pitch were manufactured with the procedure mentioned above and their tensile response successively measured.

Although the structure is very simple and its theoretical modeling well established, a very poor agreement between the theoretical predictions and the test results was found, the discrepancy being the more evident the closer the slope of the helices was to the angle $\pi/4$ (closely packed rods).

This discrepancy between theory and experiments represented the motivation for this research.

By examining the distorted yarns, particularly through measurements of the rubber rod diameter variation and the twist, it was observed that they experienced significant internal stresses even in the nominally balanced reference configuration, despite the absence of any external load.

Many studies such as [239, 240], to mentioned but a few, have considered cables formed by $n-$ply yarns and determined the internal actions in the constituting filaments. Renewed interest for the mechanics of twisted rods was motivated by the modeling of DNA and protein-protein interactions. The mechanism of formation of two-ply yarns from pre-twisted rods was carefully analyzed in [230]. A comprehensive theory of equilibria for two elastic rods, winding around each other and in continuous contact, was presented in [235]. The elastic effects on coiled coils were analyzed in [232]. Instabilities and self-contact phenomena were experimentally and theoretically discussed in [241]. Credit for a systematic analysis, which clearly evidenced the eigenstress state in uniform balanced n-ply yarns made of elastic Kirchhoff rods, has to be given to Neukirch and van der Heijden [237]. However, the specific effect of the eigenstress state on the tensile properties of the ply does not appear to have been sufficiently appreciated, probably because it was not essential for applications in biology, for which the main interest is in the formation of the double-helical structure, rather than for the load-bearing capacity. Here, it is demonstrated, through theory and experiments, that this eigenstress state has noteworthy effects on the tensile stiffness the yarn and, hence, on the failure load. This is of paramount importance for structural rods and cables, typically designed to withstand high tensile loads. Nevertheless, although the interest here is not specifically in biology (DNA, proteins) but in engineering structures (ropes, cables), the conclusions of this work, corroborated by the experimental evidence, may potentially find an application, yet to be investigated, in the vast field of biological macro-molecules.

The state of eigenstress in each rod of the yarn, represented by bending and twisting moments as well as by tensile and shear forces, is here characterized through simple balance equations, independently of the constitutive properties of the material, by considering the equilibrium of segments of various shapes. In general, the axial force and bending moments are small, whereas the twist is dominant. Its value can be easily evaluated, because it depends only on the geometry of the double helix appearing in the equilibrium equations, which can be directly observed and measured in the prototyped yarns. Assuming, in a successive step, the constitutive equations for a Kirchhoff rod, it is demonstrated that the residual twist is also related to the ratio between torsional and bending stiffnesses, which can approach a finite value even when both numerator and denominator are very small. Remarkably, direct tensile tests on highly-twisted straight rods demonstrated that the axial stiffness can be highly increased with respect to an un-twisted rod. This effect is captured by non-linear elasticity theory, assuming a standard form of the strain energy compatible with the molecular theory of rubber [242–244].

The major contribution of this work is the following. Only by considering the stiffening effect from the twist, already present in the reference configuration, one can find an excellent agreement with the results of tensile experiments on the yarn, whatever the slope of the double helix is. In other words a standard model where the threads are Kichhoff rods is accurate, only if their axial stiffness is corrected by the amount due to the twist, already present in the balanced reference configuration. Evidence is given to the crucial role of the twist-stretch coupling by means of precision tensile experiments on a large sample of macroscopic yarns with different slope angles, by finding an excellent agreement with theory. The measurements also evidenced that, if the constitutive equations are assumed as for a Kirchhoff rod, the torsional to bending stiffness ratio shall remain constant whatever the helix slope angle, although this constant is slightly different from what expected from linear theory of rods with circular cross-section.

4.2 Theoretical preliminaries

Classical Kirchhoff's theory is now applied to model the tensile response of two-ply yarns made with elastic rods, with emphasis on the manufacturing process and the classification of possible states of eigenstress. Although there have been substantial developments [245], even in recent years [230, 237], the derivation of this work is distinguishable because based on pure equilibrium considerations. It will be followed the approach originally proposed by Love in the first edition [246] of his classical *Treatise on the Mathematical Theory of Elasticity* for its insightful appeal, although Love's notation from the fourth edition of the treatise [247] will be borrowed, because it is considered simpler.

4.2.1 Kinematics of stretched, bent and twisted rods

Consider a rod, straight and prismatic in the initial undistorted state. A local right-handed *material frame* $\{x, y, z\}$, with corresponding unit vectors $\{\boldsymbol{e}_x, \boldsymbol{e}_y, \boldsymbol{e}_z\}$, is defined at each point P of the centerline, such that $\boldsymbol{e}_x$ and $\boldsymbol{e}_y$ identify the principal axes of inertia of the rod cross-section, whereas $\boldsymbol{e}_z$ follows the axis of the rod centerline. An abscissa s along the axis of the rod is introduced, increasing in the same direction of $\boldsymbol{e}_z$. In the deformed state, represented in Figure 4.1(a), $\boldsymbol{e}_z$ will become tangent to the tortuous curve described by the centerline of the rod, whereas $\boldsymbol{e}_x$ and $\boldsymbol{e}_y$ will remain aligned with the principal flexure planes. The (infinitesimal) length $\mathrm{d}s$ between any two neighboring points P and P' on the rod centerline becomes $\mathrm{d}\bar{s} = (1+\varepsilon_r)\,\mathrm{d}s$, being ε_r the axial strain of the rod at P. However, when the rods are only mildly-stretched, the engineering approximation $\mathrm{d}\bar{s} \simeq \mathrm{d}s$ can be made.

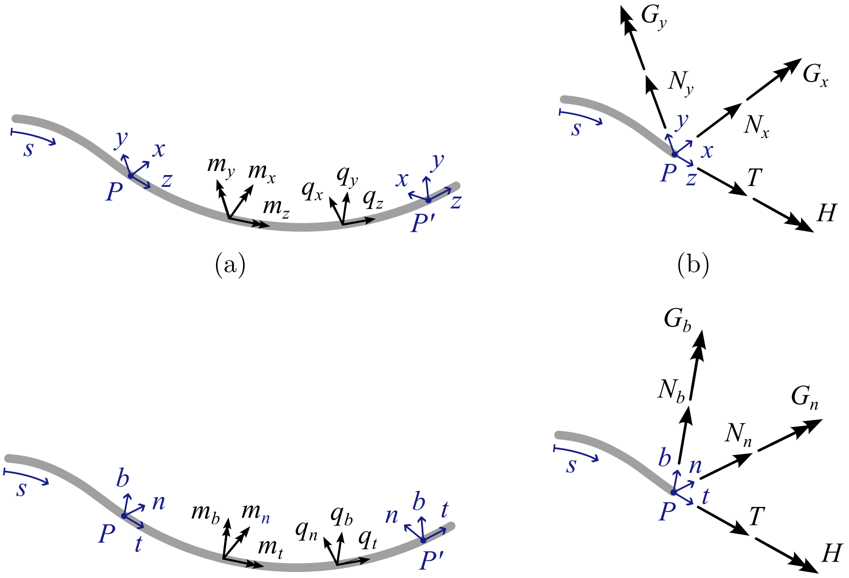

(a) (b)

(c) (d)

Figure 4.1. Schematic representation of the deformed rod: (a) material frame $\{x, y, z\}$ and corresponding components of external forces (q_x, q_y, q_z) and couples (m_x, m_y, m_z) per unit length; (b) components of internal forces (T, N_x, N_y) and couples (H, G_x, G_y), referred to the material frame at point P; (c) Frenet frame $\{n, b, t\}$ and corresponding components of external forces (q_n, q_b, q_t) and couples (m_n, m_b, m_t) per unit length; (d) components of internal forces (T, N_n, N_b) and couples (H, G_n, G_b) in the Frenet frame.

It is useful to consider also the right-handed *Frenet frame* $\{n, b, t\}$, indicated in Figure 4.1(c), with corresponding versors $\boldsymbol{e}_n$ along the normal, $\boldsymbol{e}_b$ along the binormal, and $\boldsymbol{e}_t$ along the tangent to the curve identified by the deformed centerline of the rod. Clearly $\boldsymbol{e}_t$ coincides with $\boldsymbol{e}_z$.

Name $\delta\vartheta_x$, $\delta\vartheta_y$, $\delta\vartheta_z$ the rotations along the axes x, y, z, respectively, that make the versors of the material frame at P to be aligned to the corresponding versors at P'. With respect to the material frame $\{x, y, z\}$, bending and twisting is characterized by [246, 248] the components of curvature $\kappa = \delta\vartheta_x/\mathrm{d}\bar{s}$ and $\lambda = \delta\vartheta_y/\mathrm{d}\bar{s}$, and by the *twist* $\tau = \delta\vartheta_z/\mathrm{d}\bar{s}$. In the Frenet frame $\{n, b, t\}$, the $n-t$ plane coincides with the osculating plane: the rod is bent in this plane, with principal curvature $1/\rho$. Obviously, one has

$$\frac{1}{\rho} = \sqrt{\kappa^2 + \lambda^2}\,. \tag{4.2.1}$$

On the other hand, the rotation of the Frenet frame about the axis t over the length $\mathrm{d}\bar{s}$ defines the *tortuosity* $1/\Sigma$. This is the Frenet torsion, which only depends on the shape of the curve.

An expression of paramount importance is the correlation between twist and tortuosity ([247], Art. 253)

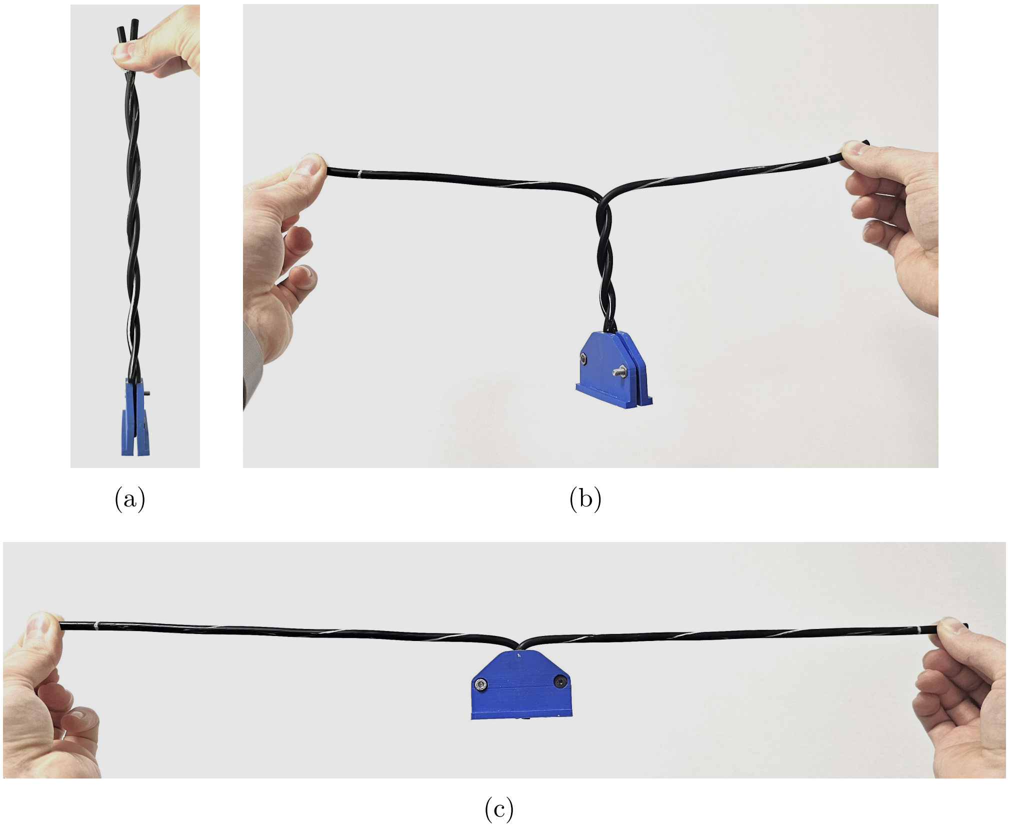

Figure 4.2. Simple unbending of a two-ply yarn: (a) double helix initial configuration of the yarn; (b) straightening of the rod, preventing the rotation of the upper ends; (c) final configuration of straight and twisted rods.

$$\tau = \frac{\mathrm{d}f}{\mathrm{d}\bar{s}} + \frac{1}{\Sigma}\,, \tag{4.2.2}$$

where $\frac{1}{2}\pi - f$ is the angle that, in the strained state, the $x - z$ plane makes with the normal n at point P. From vectorial composition of curvatures [247], one can demonstrate that $f = \tan^{-1}(-\lambda/\kappa)$.

Love [246] provides an insightful interpretation of f. If the tortuous deformed centerline of the rod were *simply unbent*, by turning each portion $\mathrm{d}\bar{s}$ through the angle of contingence in the osculating plane, and each osculating plane through the (Frenet) angle of torsion about the tangent, the rod would be found twisted, with twist rate equal to $\tau_0 = \mathrm{d}f/\mathrm{d}\bar{s}$. In rough terms, it may be added that τ_0 represents the amount of twist of the rod that “sums up” with the Frenet torsion. While the Frenet torsion can be evaluated by observing the deformed centerline only, because it is dictated by the geometry of the curve, the evaluation of τ_0 requires measuring the distortion of the material that forms the rod.

An example may be useful. Consider the two-ply yarn of Figure 4.2(a), made up of two initially-straight cylindrical rods wrapped in a double helix. The two rods can be unbent by pulling apart their upper ends while preventing their rotation, as shown in Figure 4.2(b). Observe that the blue clamp at the bottom is free to rotate, but constrains the relative rotation of the lower ends of the rods. This procedure corresponds to the *simple unbending*, in the meaning by Love [246]. In fact, the applied forces straighten the curve, by turning each portion of the rod through the angle of contingence in the osculating plane, whereas by constraining the relative rotation of the rod ends only the Frenet torsion is annihilated (each osculating plane is turned through the angle of torsion about the tangent). Once the two rods have been unwrapped, as per Figure 4.2(c), one observes the residual twist τ_0. Therefore, the twist τ in the curved state of the rod can be obtained from Eq. (4.2.2), since the tortuosity $1/\Sigma$ is calculated from differential geometry.

4.2.2 Equilibrium equations

Following as much as possible Love's notation [247], the rod in the deformed state is subjected to internal forces equipollent, at each cross-section, to the torsion moment $\boldsymbol{H}$, the bending moment $\boldsymbol{G}$, the tensile force $\boldsymbol{T}$ and the shear force $\boldsymbol{N}$. External forces per unit length $\boldsymbol{q}$ and the external couples per unit length $\boldsymbol{m}$ are also applied along the rod centerline. Body forces of special type, such as those due to mass or electro-magmatic attraction [249] are not considered. The force/moment components can be expressed either in the material frame $\{x, y, z\}$, as indicated in Figure 4.1(b), or in the Frenet frame $\{n, b, t\}$, as per Figure 4.1(d), i.e.,

$$\boldsymbol{H} = H\,\boldsymbol{e}_z = H\,\boldsymbol{e}_t\,, \tag{4.2.3a}$$

$$\boldsymbol{G} = G_x\,\boldsymbol{e}_x + G_y\,\boldsymbol{e}_y = G_n\,\boldsymbol{e}_n + G_b\,\boldsymbol{e}_b\,, \tag{4.2.3b}$$

$$\boldsymbol{T} = T\,\boldsymbol{e}_z = T\,\boldsymbol{e}_t\,, \tag{4.2.3c}$$

$$\boldsymbol{N} = N_x\,\boldsymbol{e}_x + N_y\,\boldsymbol{e}_y = N_n\,\boldsymbol{e}_n + N_b\,\boldsymbol{e}_b\,, \tag{4.2.3d}$$

$$\boldsymbol{q} = q_x\,\boldsymbol{e}_x + q_y\,\boldsymbol{e}_y + q_z\,\boldsymbol{e}_z = q_n\,\boldsymbol{e}_n + q_b\,\boldsymbol{e}_b + q_t\,\boldsymbol{e}_t\,, \tag{4.2.3e}$$

$$\boldsymbol{m} = m_x\,\boldsymbol{e}_x + m_y\,\boldsymbol{e}_y + m_z\,\boldsymbol{e}_z = m_n\,\boldsymbol{e}_n + m_b\,\boldsymbol{e}_b + m_t\,\boldsymbol{e}_t\,. \tag{4.2.3f}$$

For a prismatic rod whose centerline is held deformed into a tortuous curve, the equilibrium equations in the material frame $\{x, y, z\}$, read [247]

$$\frac{\mathrm{d}N_x}{\mathrm{d}\bar{s}} - N_y\tau + T\lambda + q_x = 0\,, \tag{4.2.4a}$$

$$\frac{\mathrm{d}N_y}{\mathrm{d}\bar{s}} - T\kappa + N_x\tau + q_y = 0\,, \tag{4.2.4b}$$

$$\frac{\mathrm{d}T}{\mathrm{d}\bar{s}} - N_x\lambda + N_y\kappa + q_z = 0\,, \tag{4.2.4c}$$

$$\frac{\mathrm{d}G_x}{\mathrm{d}\bar{s}} - G_y\tau + H\lambda - N_y + m_x = 0\,, \tag{4.2.4d}$$

$$\frac{\mathrm{d}G_y}{\mathrm{d}\bar{s}} - H\kappa + G_x\tau + N_x + m_y = 0\,, \tag{4.2.4e}$$

$$\frac{\mathrm{d}H}{\mathrm{d}\bar{s}} - G_x\lambda + G_y\kappa + m_z = 0\,. \tag{4.2.4f}$$

For this analysis, it is convenient to use the Frenet frame $\{n, b, t\}$. Following the same argument of [246], Art. 234, one can write

$$\frac{\mathrm{d}N_n}{\mathrm{d}\bar{s}} - N_b\,\frac{1}{\Sigma} + T\,\frac{1}{\rho} + q_n = 0\,, \tag{4.2.5a}$$

$$\frac{\mathrm{d}N_b}{\mathrm{d}\bar{s}} + N_n\,\frac{1}{\Sigma} + q_b = 0\,, \tag{4.2.5b}$$

$$\frac{\mathrm{d}T}{\mathrm{d}\bar{s}} - N_n\,\frac{1}{\rho} + q_t = 0\,, \tag{4.2.5c}$$

$$\frac{\mathrm{d}G_n}{\mathrm{d}\bar{s}} - G_b\,\frac{1}{\Sigma} + H\,\frac{1}{\rho} - N_b + m_n = 0\,, \tag{4.2.5d}$$

$$\frac{\mathrm{d}G_b}{\mathrm{d}\bar{s}} + G_n\,\frac{1}{\Sigma} + N_n + m_b = 0\,, \tag{4.2.5e}$$

$$\frac{\mathrm{d}H}{\mathrm{d}\bar{s}} - G_n\,\frac{1}{\rho} + m_t = 0\,. \tag{4.2.5f}$$

It can be demonstrated [120, 237] that, when pre-twisted rods are in bilateral contact with a frictionless cylinder of given radius, the configurations corresponding to energy minimizers are helices of constant radius, say r, and constant pitch, say $2\pi r \tan\alpha$. The two-ply yarn of Figure 4.3(a) represents a particular case of the cylinder degenerating into a straight line.

For any given helix of radius r and slope angle α, one finds from differential geometry that the tortuosity is given by [250]

$$\frac{1}{\Sigma} = \frac{\sin\alpha\,\cos\alpha}{r}\,, \tag{4.2.6}$$

while the principal bending curvature is

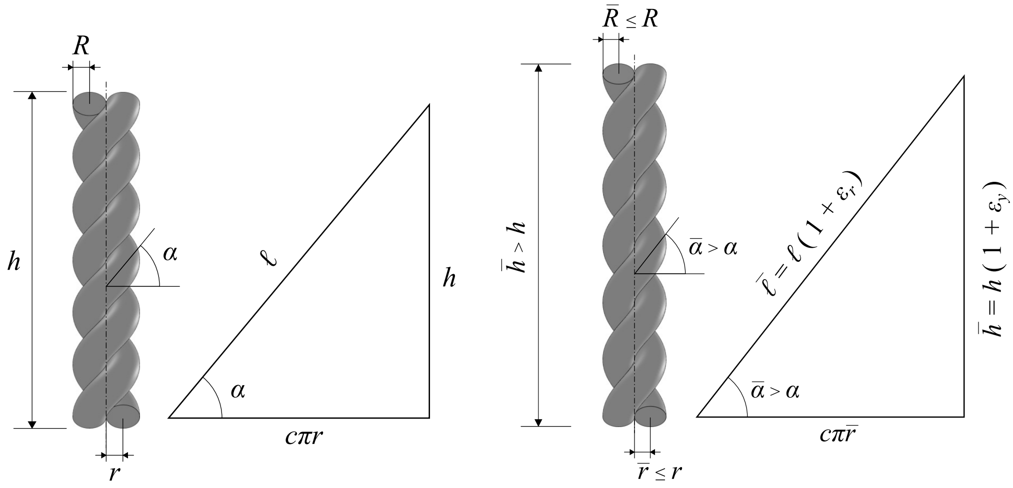

(a) (b)

Figure 4.3. Schematic representation of a two-ply yarn in the (a) reference state, with no applied external end forces or moments and (b) the stretched state, after the application of end forces and moments. The hypotenuse of the triangle aside indicates the centerline of the rod on the cylinder containing the helix, after that is has been cut along a generatrix and made flat.

$$\frac{1}{\rho} = \frac{\cos^2 \alpha}{r}\,, \tag{4.2.7}$$

Observe that the only possible equilibrium states compatible with the symmetry of the problem require [246, 250] that the twist rate τ is constant. Since the tortuosity is also constant, it follows that $\mathrm{d}f/\mathrm{d}\bar{s}$ is constant as well. An experimental verification of this result is detailed in the Appendix 4.4.4.

4.2.3 Eigenstress states in a two-ply yarn

The presence of eigenstress states in uniform balanced n-ply yarns was theoretically demonstrated in [237]. The derivation of this work are recorded here because it is pursued exclusively with balance laws, independently of the constitutive material properties, by considering particular subdivisions of the body that isolate segments of various shapes.

Consider the two-ply yarn whose reference configuration, when no external forces or moments are applied, is schematically represented in Figure 4.3(a). It is made of elastic rods with circular cross-section of radius R, straight and prismatic in the undistorted state, which have been twisted and bent to form a double helix. Figure 4.4(a) represents a segment of the two-ply yarn, obtained with two slicing planes parallel one another and orthogonal to the axis of the yarn, indicated with a dash-dot line in Figure 4.3(a). Although no external action is applied, the rods are bent and twisted and remain in equilibrium: there shall be a state of *eigenstress* in the yarn.

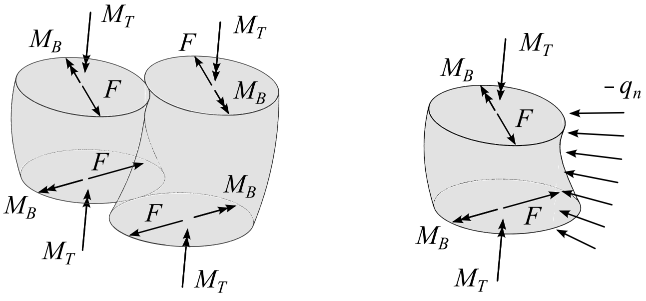

(a) (b)

Figure 4.4. Schematic representation of a segment of the two-ply yarn in the reference state (no applied external forces or moments), obtained with two parallel slicing planes, orthogonal to the yarn axis. (a) Self-equilibrated internal actions in the coupled rods; (b) free-body diagram of one rod, with indication of the compression contact forces.

In the Frenet reference frame $\{n, b, t\}$, the internal actions are represented by the forces (T, N_n, N_b) and the couples (H, G_n, G_b), as per Figure 4.1(d). Such actions shall provide zero resultant and zero moment resultant on each one of the two faces of the segment. Observe that $G_n = 0$ since the cross-section is circular and that $N_n = 0$ thanks to geometric symmetry. Exploiting again the geometric symmetry of the problem, the only possibility is represented by the free-body-diagram of Figure 4.4(a), where the moments M_T are parallel to the yarn axis and the moments M_B are orthogonal to the helix radius and at right angle with the yarn axis. Equilibrium requires that the couple formed by the two forces F, again orthogonal to the helix radius and at right angle with the yarn axis, annihilates the effects of the two moments M_T. If α denotes the helix angle, supposing that the radius R is much smaller than the length of the yarn, one can write

$$M_B = -H\cos\alpha + G_b \sin\alpha\,, \tag{4.2.8a}$$

$$M_T = -H\sin\alpha - G_b \cos\alpha\,. \tag{4.2.8b}$$

Moreover, equilibrium requires

$$T\sin\alpha + N_b\cos\alpha = 0\,, \tag{4.2.9a}$$

$$T\cos\alpha - N_b\sin\alpha = F = \frac{M_T}{r}\,. \tag{4.2.9b}$$

If one consider the equilibrium of one single rod, as indicated in Figure 4.4(b), the contact forces with the neighboring rod have to be added. These can be schematized as a force per unit length q_n, orthogonal to the yarn axis and passing through it. In fact, from geometric symmetry one has $q_b = q_t = 0$ and $m_b = m_t = 0$. In principle, one could have $m_n \neq 0$, but this contribution would be associated with internal contact

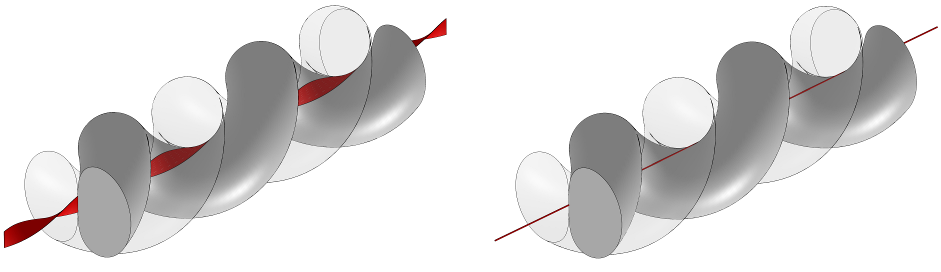
(a) (b)

Figure 4.5. Contact zone between the two rods forming the yarn: (a) ruled thin strip (ribbon) defined by the flattened zone due to Hertzian contact; (b) limit case in which the strip reduces to a line coinciding with the yarn axis.

micro-couples. It is expected that the effect of Hertzian contact would be that of flattening the contact region between the rods, as indicated in [251]. However, thanks to symmetry, it was deduced that the contact region takes the shape of a ruled thin strip, swept by a segment of line passing through the yarn axis and orthogonal to it, translating and rotating with the same pitch of the helix. This is the ribbon surface shown in Figure 4.5(a). The micro-couples m_n shall be associated with the inter-rod adhesion/frictional forces, with a lever arm of the same order of the width of the contact strip, but, unless an unrealistically high friction coefficient is considered, this effect is found to be negligible. Hence, the analysis refers directly to the limiting condition in which the contact surface reduces to a line, coinciding with the yarn axis, as shown in Figure 4.5(b): this implies that $m_n = 0$. In conclusion, the equilibrium equations provide

$$q_n = -\frac{F}{r}\cos\alpha = -\frac{M_T}{r^2}\cos\alpha\,. \tag{4.2.10}$$

Combining Eqs. (4.2.8), (4.2.9) and (4.2.10), one can express the non-null internal actions in the yarn as a function of the torsion H, in the form

$$G_b = -\frac{H}{2}\Big(\tan\alpha - \cot\alpha\Big)\,, \tag{4.2.11a}$$

$$T = -\frac{H}{r}\frac{\cot\alpha}{2}\,, \tag{4.2.11b}$$

$$N_b = \frac{H}{2r}\,, \tag{4.2.11c}$$

$$q_n = \frac{H}{r^2}\frac{\cot\alpha}{2}\,. \tag{4.2.11d}$$

which verify all the equilibrium equations (4.2.5). These expressions characterize all possible states of eigenstress in the reference configuration.

Observe that Eqs. (4.2.11) come from pure equilibrium laws and no hypothesis is made about the constitutive equations of the material. However, it was implicitly assumed that the rod is homogeneous: since the principal curvature, the tortuosity and the twist are constant in value along the rod, in order to respect the helical symmetry, also the corresponding internal actions shall enjoy the same property.

Further conclusions can be reached by introducing the constitutive equations for an elastic Kirchhoff rod. The twist moment can be written as the product between the torsional stiffness A and the twist angle per unit length τ, that is $H = A\,\tau$; the bending moment is $G_b = B/\rho = B\cos^2\alpha/r$, where B is the bending stiffness and $1/\rho = \cos^2\alpha/r$ the bending curvature. Hence, from Eq. (4.2.11a), one obtains

$$\frac{B}{A} = -\frac{\tau}{2}\,\frac{\tan\alpha - \cot\alpha}{\cos^2\alpha}\,r\,. \tag{4.2.12}$$

This result recovers formula (42) of [237], and provides a non-linear relationship of paramount importance between the twist rate τ and the helix slope angle α.

In words, a state of eingenstress exists in the rods, characterized by a twist angle per unit length τ which is uniquely determined by the helix angle α, according to Eq. (4.2.12). It should be observed that such an eigenstress is determined by the ratio B/A between the bending and the torsional stiffness of the rod. *Although in most cases both B and A are so small to be considered negligible quantities, their ratio may achieve a significant value.*

From Eq. (4.2.11a), two limit conditions can be identified. The first one corresponds to $\alpha \to \pi/2^-$, for which $(\tan\alpha - \cot\alpha) \to +\infty$, while $G_b = 0$, since the rod is straight. The only possible eigenstress in a pair of (parallel) rods is that in which $H = 0$.

The second limit case is for $\alpha \to \pi/4^+$. Now, $(\tan\alpha - \cot\alpha) \to 0^+$, and $G_b \neq 0$, because the rod forms a tortuous curve. Hence, in order to have a finite value of G_b, it is necessary that $H \to -\infty$. This suggests that helix angles approaching $\pi/4$ are not physically attainable, because this would require an infinite twist for any finite value of the rod bending stiffness.

The condition $\alpha = \pi/4$ is not only a limit case from equilibrium, but it also results from pure geometry, as already mentioned in [237]. To demonstrate, consider a cross-section of the yarn, obtained with a slicing plane orthogonal to the yarn axis. With respect to a two-dimensional reference frame $\{\xi, \eta\}$, coinciding with the axes of geometric symmetry of the cross-section, the parametric representation of the contours of the rod is provided by

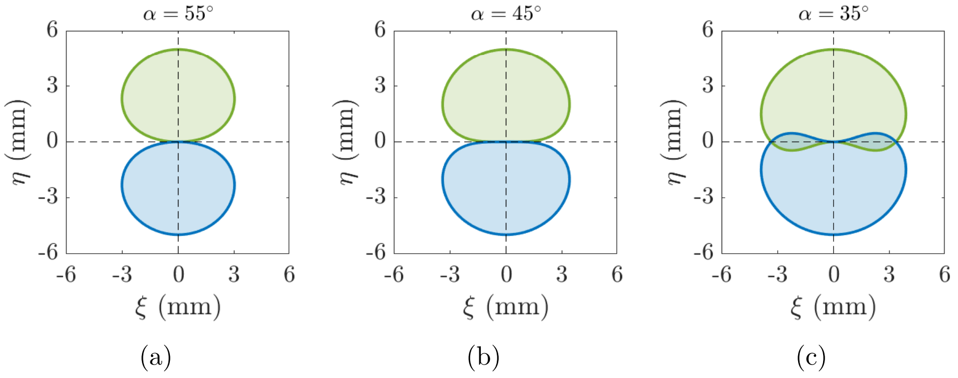

Figure 4.6. Section of the two-ply yarn, obtained with a slicing plane orthogonal to the yarn axis, for varying helix angle and $R = r = 2.5\,\text{mm}$: (a) $\alpha = 55°$, (b) $\alpha = 45°$, and (c) $\alpha = 35°$.

$$\begin{aligned}\xi = (r + R\cos\theta)\cos\left(\frac{j\pi}{2} - \frac{R\sin\theta\cos\alpha}{r\tan\alpha}\right)\\ + R\sin\theta\sin\alpha\sin\left(\frac{j\pi}{2} - \frac{R\sin\theta\cos\alpha}{r\tan\alpha}\right),\end{aligned} \tag{4.2.13a}$$

$$\begin{aligned}\eta = (r + R\cos\theta)\sin\left(\frac{j\pi}{2} - \frac{R\sin\theta\cos\alpha}{r\tan\alpha}\right)\\ - R\sin\theta\sin\alpha\cos\left(\frac{j\pi}{2} - \frac{R\sin\theta\cos\alpha}{r\tan\alpha}\right),\end{aligned} \tag{4.2.13b}$$

where $\theta \in [0,2\pi]$ is the parameter of the representation, R the radius of the rod and r the radius of the helix, whereas $j = 1$ or $j = 3$ identify one or the other rod of the couple.

The curves (4.2.13) are plotted in Figure 4.6 for three different values of the helix angle α and $R = r = 2.5\,\text{mm}$. Observe that, as the helix angle α is reduced, the concavity at the contact point ($\theta = \pi$) changes its sign. At $\alpha = 55°$ the contour of both rods is convex, as shown in Figure 4.6(a), but at $\alpha = 35°$ both rods have a concave contour, as per Figure 4.6(c). In the latter case, the cross-sections would partially overlap, with unrealistic material interpenetrations. The limit condition corresponds to $\alpha = 45°$, for which curvature of the profiles at the contact point is null, as indicated in Figure 4.6(b). In fact, one has

$$\left.\frac{\partial^2\eta}{\partial\theta^2}\right|_{\theta=180°} = 1 - \frac{2}{1+\tan^2\alpha}, \tag{4.2.14}$$

which is zero for $\alpha = 45°$.

4.2.4 Tensile response of a two-ply yarn

The contribution to the strain energy provided by the axial stiffness of the constituent rods is usually dominant with respect to that associated with the bending and torsional stiffness, as for the case at hand, in which the rods are made of rubber. Consequently, only the tensile properties of the constituent rods may be taken in account while estimating the gross tensile properties of a yarn. However, as demonstrated in the next Section 4.4, it is important to consider, in the tensile response of each rod, the stiffening effect from the twist. This may be non-negligible in the reference configuration because, as detailed in Section 4.2.3, it does not depend on the raw values of the bending and torsional stiffness of the rod, but on their ratio. Therefore, as input datum, it will be necessary to consider the constitutive equation $T = T(\varepsilon_r, \tau)$, being ε_r the axial (engineering) strain and τ the twist angle per unit length of each rod forming the yarn.

Suppose that the yarn of length h, whose reference state is a double helix of angle α and radius r as per Figure 4.3(a), is stretched uniaxially by end forces. Thanks to geometric symmetry, the two constituent rods will assume again a double helix configuration, characterized by the new length $\bar{h}$, angle $\bar{\alpha}$ and radius $\bar{r}$. Hence, the strain of the rod ε_r and the strain of the yarn ε_y can be written as

$$\varepsilon_y = \frac{\bar{h} - h}{h}\,, \tag{4.2.15a}$$

$$\varepsilon_r = \frac{\bar{\ell} - \ell}{\ell} = \frac{\bar{h}}{h}\,\frac{\sin\alpha}{\sin\bar{\alpha}} - 1\,. \tag{4.2.15b}$$

For a two-ply yarn, one can assume that the radius R of the rod approximately coincide with the radius r of the helix described by the rod inside the yarn; the same holds for the actual values in the stretched yarn, i.e., $\bar{r} \simeq \bar{R}$. If the material is elastic, then $\bar{R} = R\,(1 - \nu\varepsilon_r)$; for a rubber material, the Poisson ratio is approximately $\nu = 0.5$.

If the yarn is stretched without relatively rotating its extremities, according to the schematic of Figure 4.3, then one has

$$c\,\pi\,r = h/\tan\alpha\,, \tag{4.2.16a}$$

$$c\,\pi\,\bar{r} = c\,\pi\,r(1 - \nu\varepsilon_r) = \bar{h}/\tan\bar{\alpha}\,, \tag{4.2.16b}$$

where $c\,\pi$ ($c \in \mathbb{R}$) represents the number of revolutions of the rod inside the helix. From Eqs. (4.2.15) and (4.2.16), one obtains

$$\varepsilon_y = \left(1 + \frac{\cos\alpha - \cos\bar{\alpha}}{\nu\,\cos\alpha + \cos\bar{\alpha}}\right)\frac{\sin\bar{\alpha}}{\sin\alpha} - 1\,, \tag{4.2.17a}$$

$$\varepsilon_r = \frac{\cos\alpha - \cos\bar{\alpha}}{\nu\,\cos\alpha + \cos\bar{\alpha}}\,, \tag{4.2.17b}$$

which give the deformation of the yarn and of the two rods inside the yarn for any given couple of helix angles $(\alpha, \bar{\alpha})$.

Once ε_r is found, the axial force T in the rods can be calculated from the constitutive equation $T = T(\varepsilon_r, \tau)$. The value of τ should be that in the deformed state, and there would be no problem in calculating that from equilibrium. However, there is a small variation of this parameter when passing from the reference to the deformed state, especially when the yarn is moderately stretched, i.e., $\alpha \simeq \bar{\alpha}$. Consequently, one may evaluate τ from Eq. (4.2.12) for the reference configuration at rest, and assume this value as a constant when the yarn is moderately stretched starting from this configuration.

Clearly, the force Q required to axially stretch the yarn reads

$$Q = 2\,T \sin\bar{\alpha}\,. \tag{4.2.18}$$

Observe that, to prevent the rotation at the exterminates, the torque of magnitude $2\bar{r}\,T\cos\bar{\alpha}$ has also to be applied about the yarn axis.

4.3 Experimental set-up

The procedure used for manufacturing of the two-ply yarn samples is now presented. This is based on transforming an initial pre-twist applied to straight rods into tortuosity of the resulting helix [230, 237]. The experimental setup and the geometry of the tested specimens are then detailed.

4.3.1 Two-ply yarn fabrication

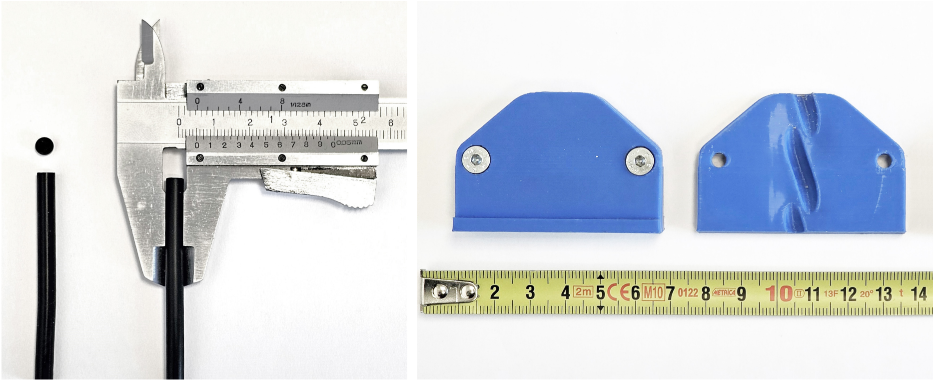
(a) (b)

Figure 4.7. Rubber rod and clamping device: (a) photograph of the Nitrile Butadiene rubber rod used to fabricate the yarns, with indication of the circular cross-section; (b) 3D-printed clamp made of blue polylactide.

The rubber rods used to prepare the yarns are made of Nitrile Butadiene rubber (NBR or Buna rubber). They are straight and prismatic in the undistorted state, with circular cross-section of radius 2.5 mm, with a mass per unit length of 0.024 kg/m. Figure 4.7(a) shows a photograph of the rods, whose diameter was preliminary checked with a Vernier caliper.

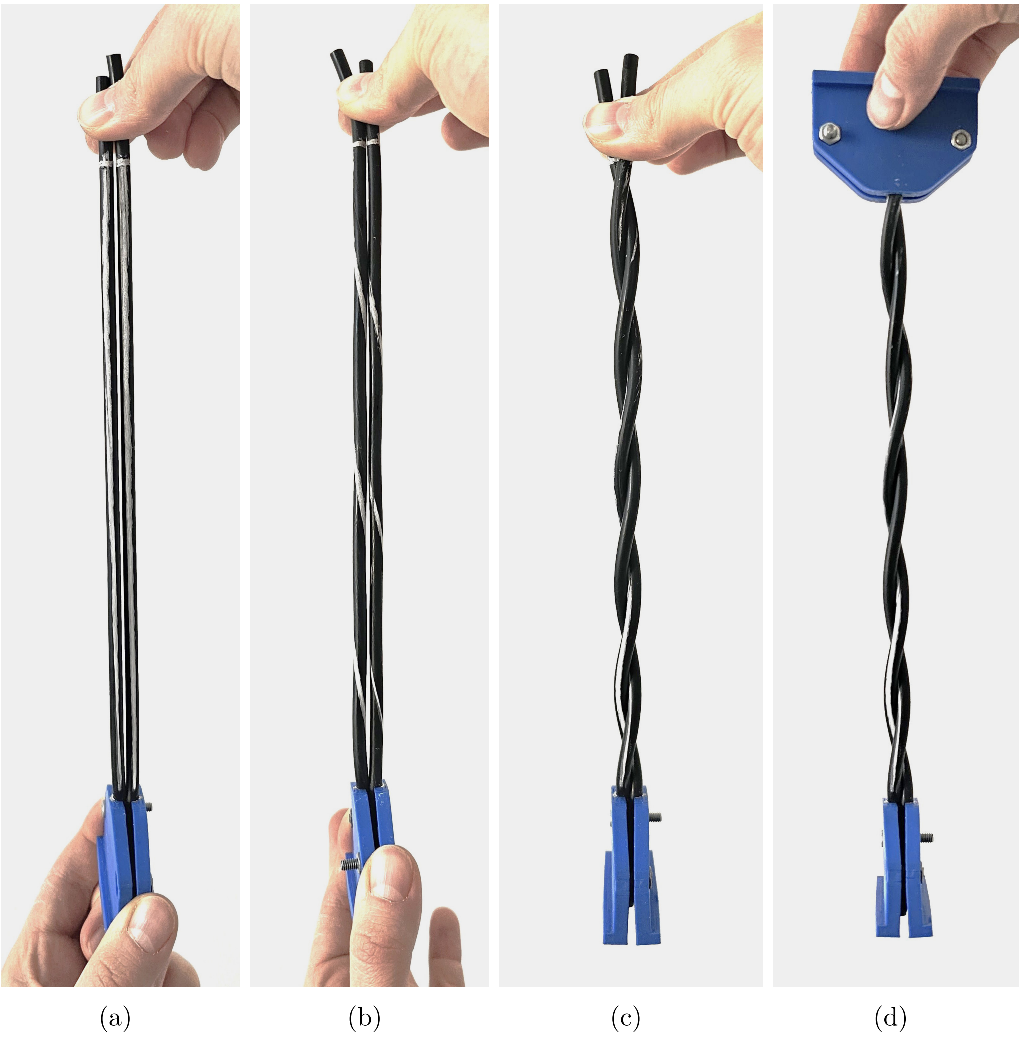

Figure 4.8. Fabrication of the two-ply yarn: (a) initial state with two straight undistorted parallel rods, clamped together at the bottom; (b) the rods are pre-twisted while keeping them straight and parallel, preventing the rotation of the clamped ends; (c) after releasing the clamp, twist is transformed into tortuosity; (d) final yarn after that also the upper ends have been clamped.

To fabricate the two-ply yarn, two rods are first aligned side by side and clamped together at one extremity, as indicated in Figure 4.8(a). A longitudinal white line was drawn on the surface of each rod for reference. The clamp was 3D printed in blue polylactide, and it consists of two portions bolted together; each one of the two portions has a groove inside to accommodate the helically wound rods, as displayed in Figure 4.7(b). The clamp is externally held fast to prevent its rotation. Subsequently, each rod is pre-twisted of the same angle per unit length τ_0 at the free ends and stretched axially so as to keep it straight, as evidenced in Figure 4.8(b). Here, the pre-twist is evidenced by the helix formed by the initially-straight white line. Then, the rotation restraint at the lower clamp is released, so that one rod naturally wraps around the other[1], transforming part of the initial twist into tortuosity, as shown in Figure 4.8(c). Finally, the upper ends of the rods are clamped together, obtaining the two-ply yarn specimen of Figure 4.8(d).

Observe that the manufacturing technique just described is exactly the reverse of the *simple unbending*, in the meaning by Love [246], discussed in Section 4.2.1. Hence, one can readily calculate the twist τ from formula (4.2.2). In particular, also considering Eq. (4.2.6), one has that $\tau = \tau_0 + \sin\alpha\cos\alpha/r$.

This technique has been known for centuries. As a curiosity, Leonardo da Vinci himself designed two machines to manufacture strands and ropes following, in practice, the process indicated above. The two devices used either 15 or 3 spindles, as respectively indicated in Figures 4.9(a) and 4.9(b), taken from the Codex Atlanticus [253].

For the specimen of Figure 4.8, the height of the yarn is $h = 214\,\mathrm{mm}$ and the radius of the helix is $r \simeq R = 2.5\,\mathrm{mm}$. Each straight rod was pre-twisted of the angle $\tau_0 \simeq -5.0°/\mathrm{mm}$ (3 turns of the free end in clockwise direction according to right-hand rule) and the resulting helix angle is $\alpha = 78.6°$; hence the twist of the rods forming the yarn is $\tau \simeq -0.6°/\mathrm{mm}$.

Clearly, by changing the initial pre-twist τ_0, it is possible to manufacture yarns with different helix angle α.

It is worth mentioning that the eigenstress state embedded in the yarn was first detected by simple visual inspection: an appreciable modification of the diameter of the rubber rod was observed after fabrication. For example the rod diameter, measured with a Vernier caliper, changed from being 5.0 mm in the undistorted state to the new value 4.6 mm inside the yarn, when the helix slope angle was $\alpha \simeq 60°$. The observed distortion was higher the lower the slope of the helix. Recall that the state of eigenstress is characterized by the Eqs. (4.2.11), derived from pure equilibrium, which involve the angle α: this can be measured on the prototyped yarns. Consequently, following the procedure detailed in Section 4.4.2, it was possible to characterize the eigenstress state experimentally.

---

[1] It should be mentioned that, for an isolated highly-twisted rod, a configuration with straight axis is not stable [252]: the rod tends to coil up at localized sections. However, since here there are two equally-twisted rods in parallel, the reciprocal contact guides the propagation of such instability and the final result is a double helix with uniform twist and tortuosity.

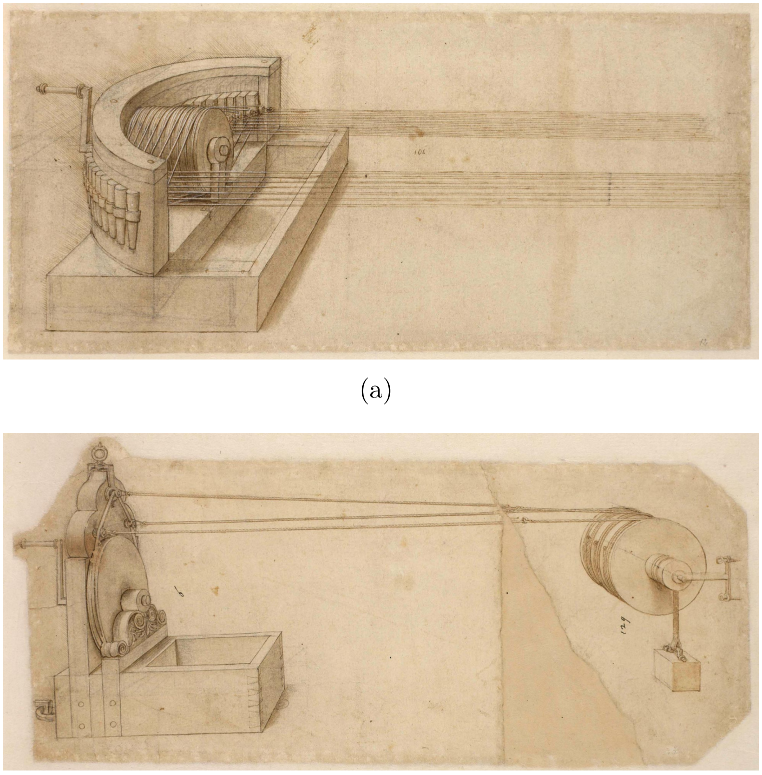
(a)

(b)

Figure 4.9. Drawings by Leonardo da Vinci for rope-making machines, taken from Codex Atlanticus [253]. (a) 15-spindle machine for twisting strands, from page 12 recto; (b) 3-spindle rope machine, from page 13 recto.

4.3.2 Testing apparatus

All tensile tests were performed with a Chatillon TCD225 Series Force Measurement System, equipped with a TLC-0200 load sensor. The testing machine is shown in Figure 4.10(a). This is equipped with aluminum grippers in which the clamps of Figure 4.7(b) perfectly fit. The grippers are fixed to the cross-heads in such a way that the specimens are stretched, but the ends cannot rotate.

Preliminary tensile tests were carried out on the undistorted straight rubber rod, as indicated in Figure 4.10(b), to determine the force-elongation curve. In order to measure the stiffening effect of the twist on the tensile response, further tests were made on pre-twisted straight rods, as per Figure 4.10(c), with various angles of twist. Figure 4.10(d) shows the final testing of the two-ply yarns. The rods forming the yarns were lubricated with soap, so to reduce the effects of parasitic friction at the points of reciprocal contact.

All the tests were strain driven, imposing the speed of the relative displacement of the cross-heads, equal to 100 mm/min.

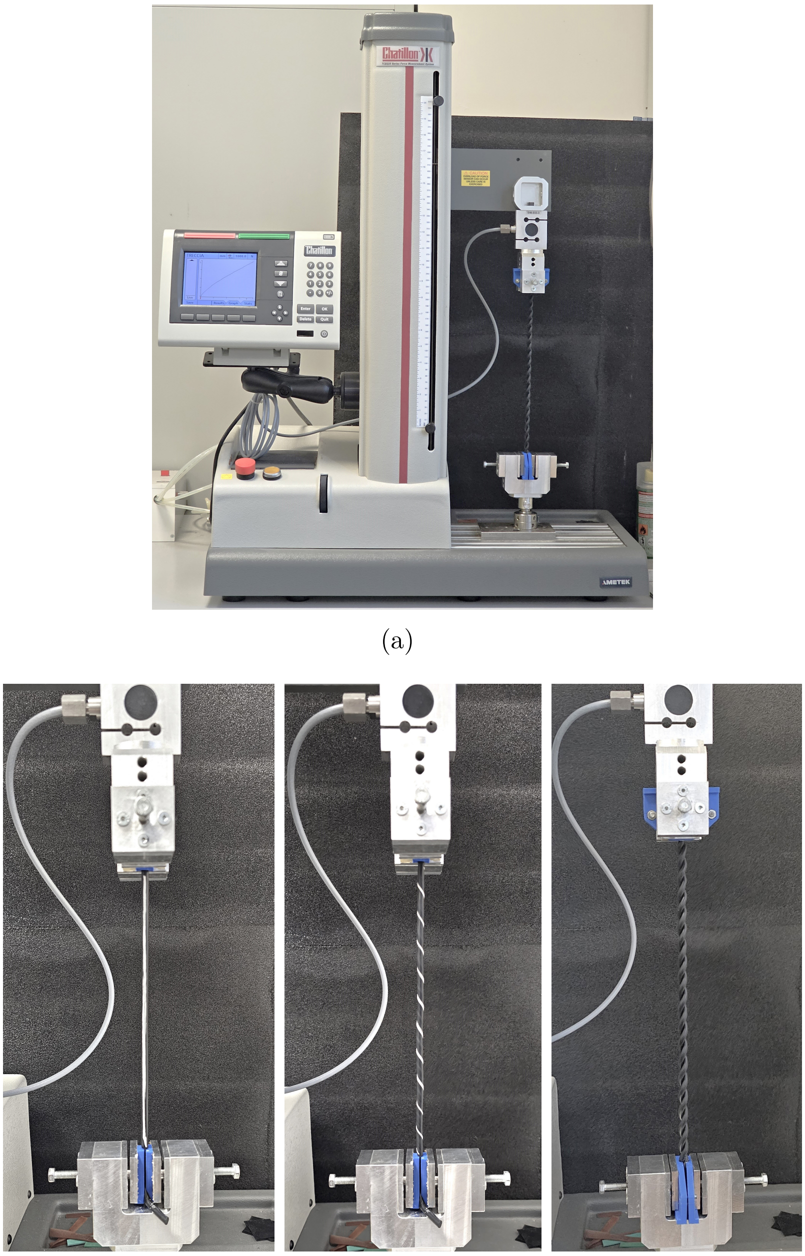

(a)

(b) (c) (d)

Figure 4.10. Testing machine and specimens. (a) Chatillon TCD225 Series Force Measurement System; (b) undistorted rod, (c) pre-twisted rod and (d) two-ply yarn, subjected to tensile load.

4.4 Experimental results and their interpretation

The results from tensile tests on two-ply yarns with various geometries are now analyzed and discussed. To obtain agreement with the theoretical predictions from the model of Section 4.2, it is necessary to consider that the a twisted rod is axially stiffer

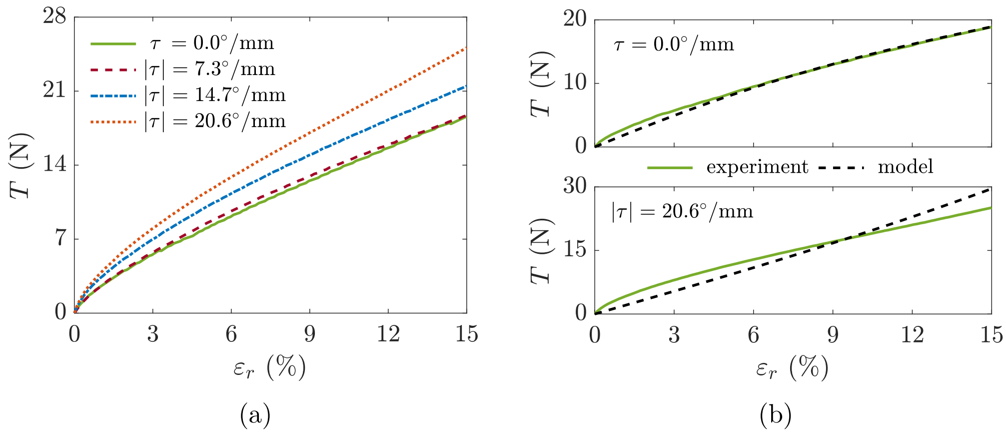

Figure 4.11. Tensile response of the rubber rod: (a) experimentally-measured tensile force vs. engineering strain curves, for varying values of the pre-twist τ; (b) comparison of the experimental results with the theoretical predictions from non-linear elasticity theory.

than a non-twisted one. This is why the twist-stretch coupling, confirmed by non-linear elasticity models based on the molecular theories of rubber [242–244], is first measured experimentally on a single straight rod; the results are then incorporated in the two-ply yarn model. It is showed that if this effect is not considered, it will not be possible to reproduce the tensile experiments on the yarn when the helix slope angle α is less than 70°.

4.4.1 Tensile properties of the twisted rod

Preliminary tests on single rods were carried out, aiming at measuring the tensile constitutive properties. Remarkably, it was observed that a pre-twist has a strong stiffening effect. Various degree of twist were considered, in order to experimentally define the constitutive equation $T = T(\varepsilon_r, \tau)$, mentioned in Section 4.2.4.

Figure 4.11(a) reports the experimentally-measured force-strain curves for various values of the twist τ of the rod. Here, ε_r is the engineering strain, obtained by dividing the incremental relative displacement of the cross-heads by their initial reciprocal distance. The stiffening effect of the pre-twist is negligible as long as $|\tau| < 7°/\text{mm}$: the curve corresponding to $|\tau| = 7.3°/\text{mm}$ overlaps in practice with that corresponding to $\tau = 0.0°/\text{mm}$. Further increasing τ, it is evident that the slope of the curves increases.

The fact that the twist increases the axial stiffness of rubber rods is in agreement with molecular theories of rubber elasticity [242, 243]. In fact, the molecular chains are non-linearly and progressively stretched and untangled by any relative rotation of the rod cross-sections, and thus become stiffer. This fact is captured by macroscopic models in non-linear elasticity theory. Rivlin [244] considered a rubber cylinder under simultaneous extension and torsion. It was found that a good agreement with experiments could be obtained by considering the strain-invariant energy function proposed by Davies et al. [254]

$$W = \frac{\mathcal{A}}{2(1-n/2)}(I_1 - 3 + \mathcal{C}^2)^{1-n/2} + \mathcal{K}(I_1 - 3)^2 \,, \tag{4.4.1}$$

where, for the case at hand, it was set $\mathcal{A} = 0.43778\,\mathrm{N/mm^2}$, $\mathcal{C} = 0.40465$, $\mathcal{K} = 1.46845\,\mathrm{N/mm^2}$, $n = 2.09414$, while I_1 represents the first strain invariant of the (right) Cauchy-Green strain tensor. For the case of uniaxial stretching of a cylindrical rubber rod, supposing the material incompressible, this reads

$$I_1 = (1+\varepsilon_r)^2 + \frac{2}{(1+\varepsilon_r)} + \tau^2\rho^2(1+\varepsilon_r)\,, \tag{4.4.2}$$

being $(1+\varepsilon_r)$ the axial stretch, τ the torsion angle per unit length and $\rho \in [0, R]$ the polar distance of each point of the cross-section of the rod from its centroid.

One obtains [244] that the axial force at the extremities of the cylindrical rubber rod under simultaneous extension and torsion is given by

$$T = 4\pi\left[(1+\varepsilon_r) - \frac{1}{(1+\varepsilon_r)^2}\right]\int_0^R \rho\frac{\partial W}{\partial I_1}\,\mathrm{d}\rho - 2\pi\tau^2\int_0^R \rho^3\frac{\partial W}{\partial I_1}\,\mathrm{d}\rho\,. \tag{4.4.3}$$

Observe that for a twisted rod ($\tau \neq 0$), one has that $T = 0$ corresponds to an axial strain $\varepsilon_r > 0$: the rod elongates according to the well-known Poynting effect [255]. If one is interested in the incremental deformation beyond this configuration, as for the case at hand, in the $T - \varepsilon_r$ plane the theoretical curve shall be shifted leftwards of the pre-strain to make it pass through the origin. In this way, it is possible to compare the tensile response of rods incorporating different levels of twist in the balanced state.

The two cases $\tau = 0.0°/\mathrm{mm}$ and $|\tau| = 20.6°/\mathrm{mm}$ are shown in Figure 4.11(b): the twist clearly make the force-strain curve steeper. The experimental curves are also juxtaposed in the same plot. For the untwisted rod, the invariant-based model by Davies et al. [254] accurately reproduces the measured tensile response. For the twisted rod, the predicted force-strain law is in fair agreement with the tests. In fact, despite a difference in the concavity of the two curves, the quantitative difference is limited even for high values of the axial strain.

The non-linear elastic model by Davies et al. justifies the stiffening effect of the twist, and provides results that are certainly valid at least at the qualitative level. A more refined model could be calibrated for a more precise interpretation of the experimental results on this specific material, but this goes beyond the scope of the present work. In order to interpret the results of the tests on the two-ply yarns, it will be considered the experimentally measured constitutive relationship $T = T(\varepsilon_r, \tau)$, already shown in Figure 4.11(a). This will represent the input datum for the model detailed in Section 4.2.4.

It should be remarked that the Poynting effect does not influence the axial force in the rods forming the yarn. In fact, in the reference balanced state (no end actions), the rod axial force is dictated by pure equilibrium, as shown in Section 4.2.3. The axial strain, whatever it is, produces only a modification of the length of the rods: since the yarn ends are not constrained, a uniform elongation of the rods is compatible with the helical symmetry, and produces a modification of the yarn length without introducing additional stresses. On the other hand, the twist-stretch coupling in the constituent rods becomes of paramount importance when, starting from the reference balanced configuration, the yarn is pulled, because the axial stiffness is strongly affected by the twist already embedded in the rods.

4.4.2 Tensile response of two-ply yarns

Measured tensile force vs. engineering strain curves for the two-ply yarns are shown in Figure 4.12. Yarns with different helix angle α in the range $59.4° \div 77.3°$ were considered. For each case, the pre-twist τ incorporated as an eigenstress in the reference configuration was considered in the constitutive equation $T = T(\varepsilon_r, \tau)$ for each rod. Observing that the tortuosity $1/\Sigma$ can be calculated from Eq. (4.2.6) since the helix angle α is known, to determine τ one has to estimate the quantity $\mathrm{d}f/\mathrm{d}\bar{s}$ that appears in the expression (4.2.2). The value of τ can be estimated in three different ways.

i. According to the *simple unbending* procedure described in Figure 4.2, after the test, the clamping at one end was removed and the two rods straightened, in order to measure the residual $\mathrm{d}f/\mathrm{d}\bar{s}$.

ii. In the manufacturing process shown in Figure 4.8, $\mathrm{d}f/\mathrm{d}\bar{s}$ corresponds to the imposed initial twist applied to each straight rod, detailed in Figure 4.8(b).

iii. The twist τ was directly checked on the assembled yarn of Figure 4.8(d), by measuring the relative rotation of two neighboring sections of the rods, taking as reference two pin markers inserted at these sections and on the initially straight white line, represented in Figure 4.8(a).

For helix angles $\alpha \geq 69.0°$ it was found that the stiffening effect of the twist was negligible; therefore, the measured force-strain curve for the untwisted rod can be used in the model. For $\alpha = 67.3°$, $\alpha = 60.3°$ and $\alpha = 59.4°$, the curves respectively corresponding to $|\tau| = 7.3°/\mathrm{mm}$, $|\tau| = 14.7°/\mathrm{mm}$ and $|\tau| = 20.6°/\mathrm{mm}$, already represented in Figure 4.11(a), were considered. The theoretical response of the yarns, derived from the simple model illustrated in Section 4.2.4, is represented in Figure 4.12 by means of black dots juxtaposed to the experimental curves. Despite its simplicity and all the approximations made, the experimental findings are very accurately reproduced. It is worth remarking that if the stiffening effect from the twist were not considered, there would be a drastic discrepancy between theory and experiments, which becomes very evident as the helix angle is reduced. This is evidenced in Figure 4.12 by the blue cross markers, representing the theoretical curve if the twist-induced stiffening were neglected.

Other attempts were made to reproduce the experimental results. In particular, referring to the notation of Section 4.2.3, it was considered the effects of micro-couples

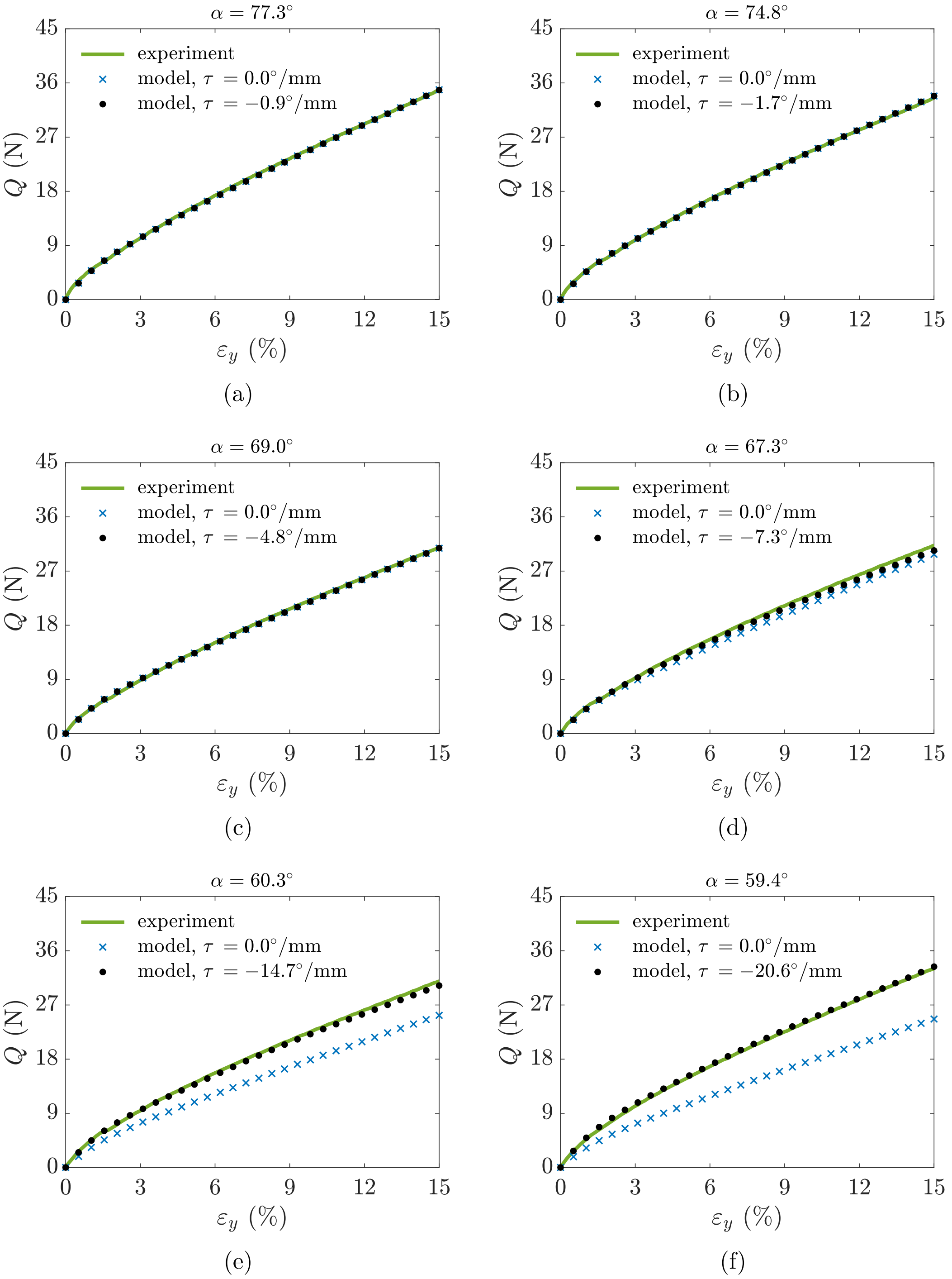

Figure 4.12. Tensile response of the yarns made with two twisted rubber rods. Comparison between the model (black dots) and the experiments (solid line) for different values of the helix angle: (a) $\alpha = 77.3°$, (b) $\alpha = 74.8°$, (c) $\alpha = 69.0°$, (d) $\alpha = 67.3°$, (e) $\alpha = 60.3°$ and (f) $\alpha = 59.4°$. The blue cross markers represent the theoretical curve if the twist-induced stiffening were neglected.

m_n, produced by inter-rod adhesion/frictional forces, which can be associated with a scissoring mode of deformation [225]. However, an estimate of the width of the contact strip region obtained via Hertz theory, as per Figure 4.4(a), demonstrated that it was so small that unrealistic values of adhesion or friction had to be taken into account. Nor the discrepancy could be justified by considering a viscoelastic component in the deformation of the rods. In fact, the measured tensile response of the yarns with low helix angles was much stiffer than that theoretical derived from the model of Section 4.2.4, considering the tensile response of the untwisted rod: viscosity would have increased the compliance of the rods, and therefore the theoretical stiffness of the yarn would have become even smaller.

The only possibility to match the experimental findings was to consider the stiffening effect on the tensile response from the twist. This required the characterization of the eigenstress state, present in the reference configuration of the yarn. No evidence of this effect has been reported in the technical literature to date.

4.4.3 The role of bending and torsional stiffness

Figure 4.13(a) shows the non-linear relationship between helix angle α and twist angle per unit length τ (the negative value of τ is just a sign convention). Here, the dots indicate the experimental data: τ was measured as discussed in Section 4.4.2, and α was estimated directly from the geometry of the yarn. Observe that $|\tau|$ steeply increases with decreasing α, confirming that an infinite twist would be needed to reach the limit angle $\alpha = 45°$. Indeed, during manufacturing or at early stages of testing, the material often experienced failures, attributable to torsion due to the conformation of the fracture surfaces, when the helix slope angle was less than 60°. The twist-induced stiffening of the rods has a remarkable effect on the macroscopic response of the yarn. In fact, observe from Eq. (4.2.18) that, kept fixed the tensile force T in each rod, the force Q in the yarn decreases with decreasing helix-angle α: the yarn should become more compliant. However, comparing the graphs of Figure 4.12, the gross stiffness of the yarn seems to be only mildly affected by α. This is because there is the competing effect of the twist-induced stiffening of the rods: the amount of twist increases as α is reduced. Therefore, by diminishing α, on the one hand the helix geometry renders the yarn more compliant; on the other hand, the higher twist makes the rods stiffer. The two effects almost compensate one another.

Based on the model of Section 4.2.3, the non-linear relationship between the twist τ and the helix angle α is provided by Eq. (4.2.12), and depends upon the ratio between the bending stiffness B of the rod and its torsional stiffness A. Since the rod is made of soft rubber, it is expected that B and A may be affected by the amplitude of the deformation, and that the rod cross-section may distort from the initial circular shape due to inter-rod contact. If de Saint Venant's theory was assumed to be valid, denoting with E and ν respectively the Young modulus and Poisson ratio, one would have

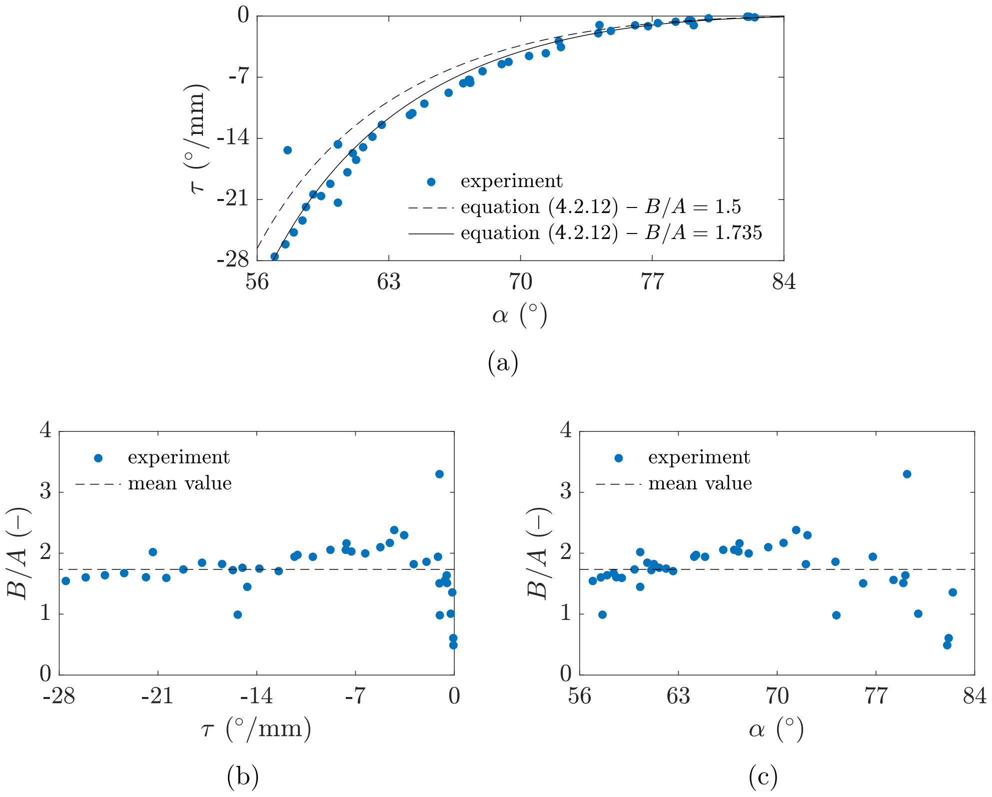

(a)

(b)

(c)

Figure 4.13. Twist in a two-ply yarn in the reference state: experimental points and theoretical predictions. (a) Relationship between the twist angle τ and the helix angle α. Bending to torsion stiffness ratio B/A for a rod of the yarn, plotted against (b) the twist angle τ and (c) the helix angle α.

$$A = \frac{E}{2(1+\nu)}\,\pi\frac{R^4}{2}\,, \qquad B = E\,\pi\frac{R^4}{4}\,. \tag{4.4.4}$$

Since for an incompressible material like rubber $\nu = 0.5$, one would find $B/A = 1.5$. For the sake of comparison, the dashed curve also represented in Figure 4.13(a) shows the expected dependence from Eq. (4.2.12), for $B/A = 1.5$ and for $r = 2.5\,\mathrm{mm}$ (initial radius of the undistorted rod). The agreement with the experimental point is quite satisfactory.

The experimental data, which relate each value of α to a corresponding τ, allow the determination of the ratio B/A through expression (4.2.12). This is shown in Figures 4.13(b) and 4.13(c), respectively as a function of τ and α, for the actual value of r measured on the yarn. There is some scatter, which is more evident for $\tau \to 0$ and $\alpha \to 90°$, because the measurement error increases here, where the quantity to be measured is small. Anyway, for meaningful values of τ and α, the points tend to cluster around the line $B/A = 1.735$. This finding is in agreement with the theory developed in Section 4.2.3, but suggests that the estimate $B/A = 1.5$, obtained via linear elasticity theory for a rod of circular cross-section, is not extremely accurate.

Indeed, the Euler-Bernoulli hypothesis that plane sections remain plane after deformation is questionable for beams under bending, twisting and shear force, especially when the curvature and twist rate are so high that the radius of curvature and the helix pitch become comparable with the radius of the rod cross-section. In addition, the circular cross-sections are certainly subjected to some flattening and distortion due to the reciprocal contact of the rods forming the yarn. All these aspects, as well as non-linear constitutive effects, should be taken into account for a better estimate of the ratio B/A, but this goes beyond the scope of the present work. In this case, the value of B/A was fitted based on the experimental results.

If one uses the value $B/A = 1.735$ in the expression (4.2.12), the solid-line curve in Figure 4.13(a) is obtained. Now, the agreement between theory and experiments is excellent. It should be remarked that, despite all the uncertainties and errors in the experimental measurements, it is found that the ratio $B/A = 1.735$ should be constant and quite close to the value predicted by linear rod theory.

4.4.4 Competition between twist and tortuosity in two-ply yarns

Here an experimental verification of the two expressions that are at the base of theory is recorded. The first one is represented by Eq. (4.2.2) which provides [247] the relationship between the twist τ, the tortuosity $1/\Sigma$ and the variation of the angle f; recall that $\frac{1}{2}\pi - f$ is the angle that, in the strained state, the $x - z$ material plane makes with the normal n at any point of centerline of the bent and twisted rod. The second one is the expression (4.2.12), which correlates the helix angle α, its radius r and the twist τ, with the ratio between the bending stiffness B and the torsional stiffness A.

As indicated in Figure 4.14(a), a white reference longitudinal line was drawn on the lateral surface of the unstrained straight rod. At each point, the material frame is such that z is in the direction of the axis of the rod, whereas x is orthogonal to it, and passes through the aforementioned line; the axis y renders $\{x, y, z\}$ a right-handed frame. When the rod is bent and twisted according to a helix to form a yarn, the reference line is transformed into a tortuous curve , wrapping around the external surface of the rod, as displayed in Figure 4.14(b). The radius of the helix was found to coincide with the radius of the rod in the unstrained state $r = 2.5\,\text{mm}$. The helix angle of the yarn of Figure 4.14(b) was measured to be $\alpha = 77.8°$.

The value $B/A = 1.735$ was estimated from experimental results, as detailed in Section 4.4.3. Hence, from Eq. (4.2.12), one has $\tau = -0.81°/\text{mm}$ and, from Eq. (4.2.2), $\mathrm{d}f/\mathrm{d}\bar{s} = \text{const.} = -5.54°\,\text{mm}$. Consequently, after integration, one has

$$f = \int \frac{\mathrm{d}f}{\mathrm{d}\bar{s}}\,\mathrm{d}\bar{s} = \frac{\mathrm{d}f}{\mathrm{d}\bar{s}}\,\Delta\bar{s} + C_1\,, \tag{4.4.5}$$

where C_1 is the constant of integration and $\Delta\bar{s} \in [0, \ell]$ is the length of any finite portion of the rod starting from the bottom clamped end, being ℓ the length of the

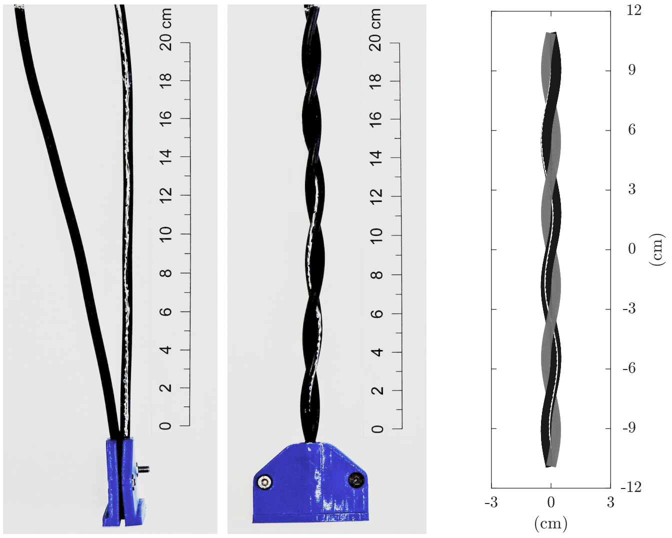

(a) (b) (c)

Figure 4.14. Experimental verification of the role of the angle f that appears in the expression (4.2.2). (a) Straight reference white line, drawn on the lateral surface of the unstrained rod; (b) the reference line is transformed into a tortuous curve when the rod is bent and twisted to form a yarn; (c) the location of the reference line as reproduced analytically from the model, taking into account tortuosity and the angle f.

centeriline of the rod in the curved state.

At any point of the rod centerline, the Frenet frame can be found from differential geometry. Consider a line element that is aligned to the normal n, starts on the rod centerline and points towards the center of curvature of the rod inside the yarn. According to Eq. (4.2.2), if this line element is rotated along the tangent of the quantity $-\frac{1}{2}\pi + f$, it will be aligned to the $x-$axis of the material frame, thus intercepting the external surface of the rod at a point belonging to the reference line of Figure 4.14(b).

This construction is analytically reproduced. The calculated shape of the reference line, obtained in Matlab®, is shown in Figure 4.14(c). The agreement with the manufactured rod is excellent when the constant of integration is set to $C_1 = 0.8\,\pi$. This value takes into account the rotation of the bottom clamp, which makes the two rods integral at the clamped portion, as well as possible sliding of the rubber rods inside the clamp.

4.5 Discussion

This study was motivated by the discrepancy found between the measured tensile response of two-ply yarns and the theoretical predictions from standard models based on Kirchhoff's rod theory. Nitrile Butadiene rubber rods with circular cross-section were pre-twisted and then released, letting them wrap one another by transforming twist into tortuosity for the resulting double-helix configuration, with variable slope angle α dictated by the pre-twist level. The material is hyperelastic and, since the diameter of the rods is small, the energetic contribution from bending and torsion can be neglected with respect to tensile stiffness. Considering the elongation of each rod when the yarn is uniformly axially stretched, the constitutive equations indicate the forces to be applied at the ends. However, the yarns were found much stiffer than expected, especially when α approached the limit value $\alpha = \pi/4$, below which there would be material interpenetration in the constituent rods. Any effect related to the cohesive-frictional contact of the wires, limited in any case by lubrication, could not justify the stiffness increase.

It was experimentally verified that the rubber rods formed a double helix both in the reference and in the stressed configuration. If modeled as Kirchhoff rods, the bending and torsional stiffness of each rod were found to have only a marginal influence on the overall tensile stiffness of the yarn [256]. A certain degree of viscoelasticity, as well as distortion of the rod cross-section due to lateral contact, was considered; however, none of these effects could explain the discrepancy between theory and experiment. Since the yarn assumes a double-helical geometry even after deformation, no axial slip or relative twist occurs between the rods: the only possible frictional interaction would be associated with a scissoring mode of deformation [225]. Yet, even accounting for this effect did not reconcile theoretical predictions with experimental results.

Examination of the distorted yarns, specifically through measurements of changes in the rubber rod diameter and twist, revealed that the rods were significantly stressed even in the nominally balanced reference configuration, despite the absence of any external load. The internal stress increases progressively as the helix slope decreases, becoming theoretically infinite as α approaches $\pi/4$. This value represents a physical limit, corresponding to the onset of geometric interpenetration between the constituent rods, as previously noted by [237]. Experimentally, it was confirmed that manufacturing two-ply yarns with slope angles smaller than $\pi/4$ was not feasible, as the material underwent torsional failure when $\alpha \to \pi/4$.

It was therefore recognized that the helically wound rods, although stable in the absence of external forces, are subjected to a state of intrinsic or eigenstress arising from their nonzero curvature and twist rate. Kirchhoff's rod theory predicts that the twist depends on the ratio between the flexural stiffness B and torsional stiffness A, increasing markedly as α decreases. Even though both B and A are small for such rubber rods, their ratio B/A remains significant, making the twist non-negligible. The model thus predicts a lower-bound helix angle $\alpha = \pi/4$, at which the twist becomes infinite, coinciding with the limit dictated by material interpenetration. This eigenstress state was directly evaluated on the manufactured yarns with various helix angles α, showing good agreement with theoretical predictions. The observed twist substantially increases the effective tensile stiffness of each rod, as confirmed by nonlinear elasticity theory and experimental testing. By incorporating this twist-induced stiffening into the theoretical model, excellent agreement between predictions and measurements was achieved.

This study focused on two-ply yarns, which certainly represented the simplest configuration, but can be readily extended to cables and ropes made up of multiple helically wound cables. Considering rods bent and twisted to form braids or ropes, possibly hierarchically arranged from thinner sub-elements, certainly requires to take into account the complex cohesion/frictional contact forces between the rods, which instead play a negligible role in the considered problem. In these experiments, rubber rods with circular cross-section of considerable diameter were used. This certainly facilitated the experimental observation, but if the yarns were made of very thin filaments, for example Carbon NanoTube Fibers, it would be much more difficult to measure the twist rate and detect possible states of pre-stress. The use of Kirchhoff's rod theory in the modeling of biological double-helical structures, such as DNA, still represents an open field of investigation. More in general, the effects of the eigenstress state on the gross bending and torsional properties of wound rods is the subject of ongoing research.

Anyway, despite all its limitations, the contribution of this study consists in the systematic experimental campaign, whose results are corroborated by a simple theoretical model. In particular, it is reputed that the proposed example of the two-ply yarn can highlight the importance of the eigenstress states on coiled structures due to their effects on macroscopic properties. If residual stresses can be removed by plasticity or annealing in steel cables, this may not be the case for nanomaterials or biological structures, where self-stress states can interact with constitutive material properties and size effects, giving rise to phenomena yet to be fully discovered and appreciated.

The results of this study, summarized in [257], represent an important step toward a comprehensive understanding of the mechanical behavior of twisted yarns, providing insights and methodologies that are directly applicable to CNTF yarns. Their specific implementation and implications for Carbon NanoTube Fiber structures will be discussed in the following chapter.

Chapter 5

Manufacturing optimization of CNTF Yarns

Following the fundamental insights obtained in Chapter 4, a geometric–kinematic model is now introduced to describe the mechanical behavior of twisted CNTF yarns and to support the optimization of their manufacturing process aiming to enhance their mechanical properties. Mechanical testing was conducted on CNTF bundles and yarns supplied by DexMat Inc., to investigate yarn formation mechanics and the impact of twist rate on bundle strength. It was demonstrated how twisted bundles improve load distribution among individual CNTFs. Higher twist rates led to an initial increase in strength, reaching a peak before declining at excessive twist levels [162], leading to the identification of an optimal twist value for maximizing CNTF bundle's mechanical performance. A helical geometric model was developed to describe the yarn structure. The model was designed to ensure that the final geometry of the produced yarn would grant an optimal twist to the internal CNTF bundles, based on the hypothesis that such an optimal configuration at the bundle level leads to superior mechanical properties for the yarn as a whole. The model was successfully applied to CNTF yarns, yielding a solid increase respect to previous registered tensile properties. A software tool was created to simulate and predict yarn configurations providing the operational parameters for industrial yarn production machinery in order to consistently achieve yarns with peak mechanical performance.

5.1 Background on yarns and ropes

In 2020, the discovery in France of a rope fragment attributed to Neanderthal craftsmanship and dated to approximately 52,000 years ago (Figure 5.1) provided the earliest known evidence of rope-making [258]. This remarkable finding pushed back the origin of fiber technology far beyond previous estimates, as the oldest known examples before this discovery were only about 8,000 years old. The technique of twisting individual fibers into bundles and then assembling these bundles into stronger, more functional yarns and ropes is further evidenced by historical artifacts such as the Papyrus Fiber

Rope from Amarna (Figure 5.2) [259]. Such evidence indicates that the ability to intertwine fibers into load-bearing cords long predates the emergence of the great ancient civilizations [260], underscoring the deep evolutionary origins of this mechanical principle, which continues to inspire the design of modern materials and structures.

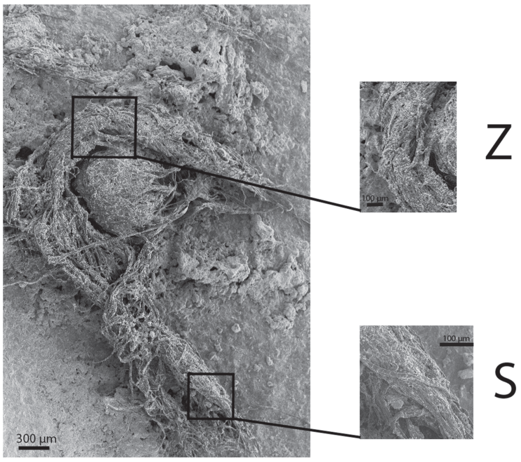

Figure 5.1. SEM photo of 3-ply cord rope used by Neanderthal man fifty-two thousand years ago. First closeup shows Z-twist of strands (image rotated 90° counter-clockwise for clarity); 2nd closeup shows S-twist of fibres within a single strand [258].

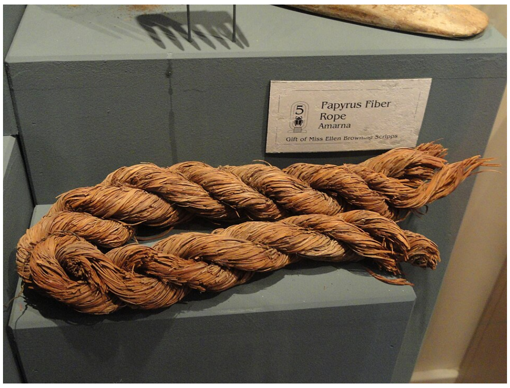

Figure 5.2. Papyrus Fiber Rope from Amarna, Exhibit in the San Diego Museum of Man, San Diego, California, USA. This artwork is old enough so that it is in the public domain. Photography was permitted in the museum without restriction [259].

Despite the fact that great past civilizations made extensive use of this technology, efficient production developed only in recent centuries, a transformation driven by the Industrial Revolution.

A natural question arises: *why use a yarn instead of a single large fiber?* Depending on the scale and nature of the application, a yarn, when compared to a monofilament of equivalent tensile strength, offers several advantages. These include increased flexibility, improved stress distribution, and enhanced damage tolerance [261]. In fact, due to internal friction or interlacing (e.g., twisting or braiding), the failure of a single filament within a yarn typically affects only a short segment of the structure (on the order of a meter), preventing catastrophic failure and allowing the remaining filaments to continue bearing the load. Moreover, this failure is usually confined to an isolated filament and does not affect the entire cross-section, unlike the initiation and propagation of a crack, which tends to grow under repeated or cyclic loading, potentially leading to sudden and complete failure of the material [262]. This hierarchical structure promotes efficient load sharing and increased mechanical resilience [175, 263]. However, the overall tensile strength of a yarn is generally lower than the theoretical sum of the individual strengths of its constituent filaments [264]. This phenomenon, often referred to as *loss of stranding*, arises due to several factors: slight variations in load distribution among filaments, differences in orientation with respect to the yarn axis, and unequal contact pressure between neighboring filaments. As a result, yarns typically exhibit a reduction in ultimate load capacity by approximately 10–15% compared to the ideal sum of the strengths of their components [265, 266].

In addition, rope-like assemblies often display substantial ductility, as they undergo gradual damage accumulation through fiber breakage, fraying, or local yielding rather than sudden brittle failure. Such progressive deterioration produces perceptible changes, such as visible abrasion, slackening, or fiber pull-out, that can serve as warning signals [267]. The progressive degradation of outer filaments acts as an early indicator of impending rupture, thereby enhancing operational safety. Finally, yarn-based ropes can reach lengths of several kilometers by joining multiple segments through specialized splicing or knotting techniques, which, when properly executed, do not significantly compromise their mechanical performance or increase the structural cross-section [268, 269].

5.2 Yarn structure and mechanics

Understanding the hierarchical structure of a yarn is fundamental to interpreting its mechanical behavior: the smallest structural element is the fiber, multiple fibers are then assembled into bundles and during yarn formation, these bundles are twisted and wound together under controlled tension and specific helical angles, yielding a cohesive, torque-balanced yarn as illustrated in Figure 5.3.

The resulting yarn geometry depends on several parameters, including the number of constituent bundles, their cross-sectional diameter and the imposed twist level. Variations in these parameters lead to distinct hierarchical configurations, ranging from few-ply cords to highly compact multi-ply yarns, each characterized by different porosity, packing density, and load-transfer efficiency. The simplest configuration to analyze is the 2-ply yarn made by only two bundle wrapped around, but theoretical considerations extend naturally to 3, 4, or more plies. When the number of bundles exceeds four, it is necessary to introduce a central ply to fill the geometric void at the core of the yarn and prevent structural collapse towards the center, stabilizing the geometry as shown in Figure 5.4.

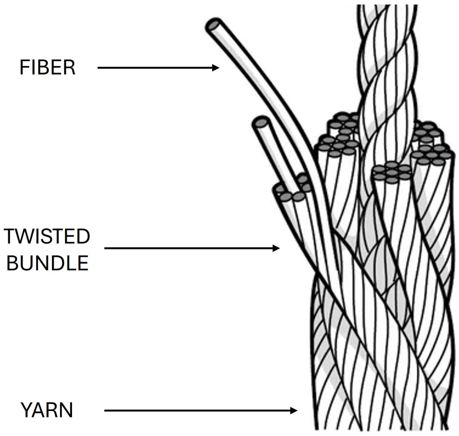

Figure 5.3. Yarn structure: the base element is a fiber, several fibers wounded together form a twisted bundle, several bundles from a yarn [270].

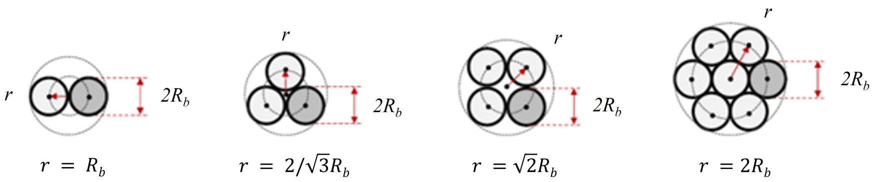

Figure 5.4. Schematic cross-sectional view of n-ply yarn, where r_b represent the ply radius and r the corresponding radius for the helical configuration [127].

This study specifically focuses on carbon-based threads, where the hierarchical organization, from CNTs to fibers, bundles, and finally yarns, plays a crucial role in determining the overall mechanical response of the structure.

Therefore, a key research objective is to establish a clear relationship between the mechanical behavior of a yarn and that of its constituent bundles analyzing the yarn-forming process and using the insights gained to optimize the final structure by tuning geometrical and processing parameters.

The structural unit of a CNTF yarn is not a single homogeneous cylindrical rod but a multifilament bundle whose tensile response is strongly influenced by the applied twist. This configuration is inherently more complex than that of a yarn composed of uniform elastic rods. In principle, the mechanics of a twisted bundle could be described by extending the 2-ply model developed in Chapter 4 to a larger number of plies, each corresponding to an individual CNTF. Furthermore, Chapter 4 provides essential insight into the interplay between twist and tortuosity, a key aspect in understanding the yarn manufacturing process. The theoretical framework established therein thus constitutes a valuable foundation for generalization, serving as a first-order approximation of the mechanical behavior of a twisted CNTF yarn, provided that suitable modifications are introduced to account for the multifilament nature of each ply.

5.2.1 Helix geometry

As discussed in Chapter 4, the fundamental geometry of a ply within a twisted yarn can be described as a helical structure. The key parameters defining this geometry, illustrated in Figure 5.5 are: the yarn helix angle α, which represents the inclination of the helical path of a ply with respect to a plane normal to the yarn axis; the pitch b, corresponding to the axial length of one complete turn of the helix; the number of turns n_y made by the helix around the yarn axis; and the helix radius r.

The relationship between these parameters is given by the equation for the helix angle:

$$\alpha = \arctan\left(\frac{b}{2\pi r}\right) . \tag{5.2.1}$$

For a yarn with total axial length $h = n_y b$, each ply follows a helical path of length $l = n_y\sqrt{b^2 + (2\pi r)^2}$, while its projection onto the plane normal to the yarn axis is equal to $2\pi n_y r$.

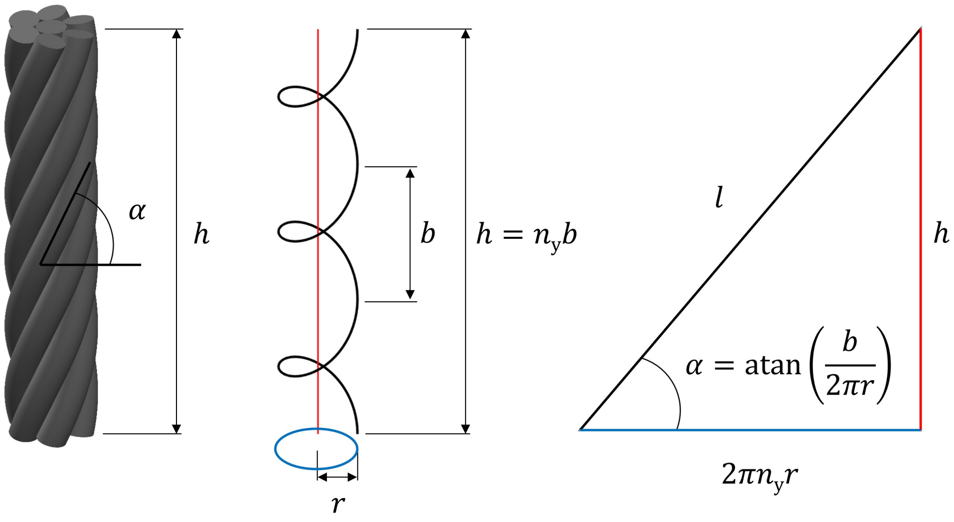

Figure 5.5. Helix geometry.

Among these, the helix angle has been shown in several studies to be the most critical factor: yarns composed by the same amount of plies with similar helix angles often display similar mechanical performance, even when pitch or radius differ to some extent [162, 271–273].

While the Twist Per Inch (TPI) is often used as a reference in textile processing, it can be misleading when comparing yarns with different structural configurations. It should be noted that TPI does not uniquely determine the yarn geometry: In fact, two yarns with the same TPI may exhibit different helix angles and, consequently, distinct mechanical behaviors [273], since the geometric parameters of the helix do not scale exclusively with TPI. Variations in yarn radius or packing density affect the actual fiber orientation, making TPI an insufficient descriptor of the yarn geometry and its mechanical response. Conversely, yarns with different TPIs but the same helix angle often show similar mechanical responses, because α scales with the yarn geometry as shown in Figure 5.6. Therefore, the helix angle is a more reliable and physically meaningful descriptor for mechanical modeling and comparison of twisted structures.

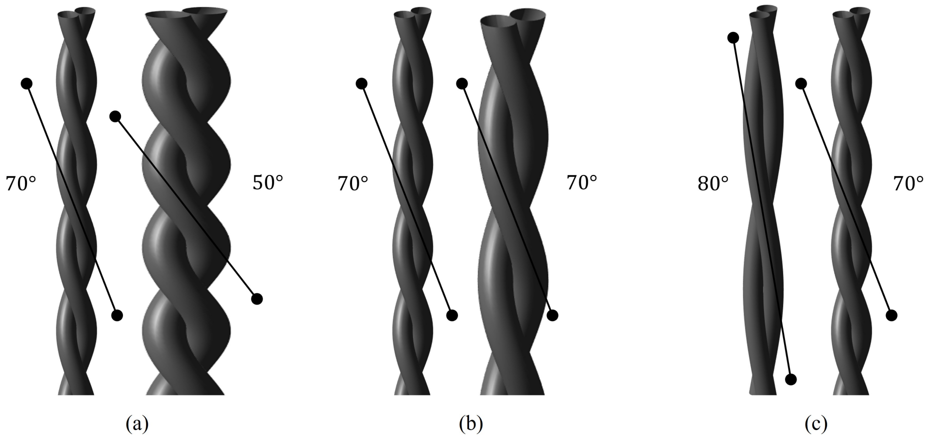

Figure 5.6. Influence of TPI, ply radius and helix angle: (a) same TPI, different angle, different radius give different mechanical behavior; (b) different TPI, same angle, different radius give same mechanical behavior; (c) different TPI, different angle, same radius give different mechanical behavior

Generally, lower helix angles are associated with more compliant and extensible yarns [162], since a larger portion of the applied load is accommodated through geometric deformation rather than direct fiber elongation. In this configuration, the yarn behaves similarly to a spring, where the load–extension response is governed by untwisting and helical reconfiguration effects rather than by the intrinsic axial stiffness of the constituent fibers. However, this geometric compliance results in a reduction in tensile strength, as the fibers become increasingly misaligned with the load direction and the effective load-bearing component of their stiffness decreases [162]. Conversely, higher helix angles, meaning fibers more closely aligned with the yarn axis, lead to stiffer but less extensible structures, resulting in higher tensile strength but lower strain capacity [271, 273], too high angles, however, can cause sliding and insufficient homogeneous load sharing [274].

Effect like inter-fiber friction, and the efficiency of load transfer among neighboring filaments become critical in determining the overall stiffness and strength of the yarn, particularly when bundle cohesion is weak and slippage or interfacial shear influence the deformation behavior.

These considerations underscore the importance of precise geometric control in the yarn manufacturing process to tailor the final mechanical properties for specific applications.

5.2.2 Twist kinematics

The geometry of a single twisted ply is illustrated in Figure 5.7. The ply is modeled as a cylinder with a length l and a base radius R_b. The *total twist angle* Φ, expressed in radians, represents the total rotational displacement applied from one end of the ply to the other over the length l and can be expressed as

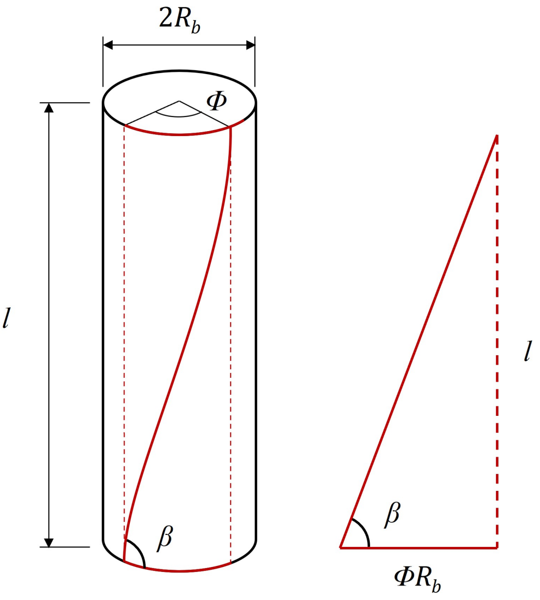

Figure 5.7. Geometrical parameters of a twisted ply: length l, ply radius R_b, total twist angle Φ, and surface helix angle β.

$$\Phi = 2\pi n_b \tag{5.2.2}$$

where n_b is the number of revolutions n_b applied over the ply length l. The *surface twist angle* β is defined as

$$\beta = -\arctan\left(\frac{l}{\Phi R_b}\right), \tag{5.2.3}$$

where the negative sign account for the fact that Φ is a clockwise rotation. It indicates the inclination of the outermost fibers, represented by the helical red line on the cylinder's surface, with respect to the circumferential direction and quantifies the degree of twisting within the ply.

The relationship between these geometric parameters is clarified by "unrolling" the cylindrical surface into a planar right-angled triangle, as depicted on the right side of Figure 5.7. In this triangle, the vertical cathetus corresponds to the ply length l, while the horizontal cathetus represents the arc length traced by the twist angle, given by the product ΦR_b.

To characterize the mechanical behavior of twisted yarns, it is essential to describe the evolution of the ply geometry under varying boundary conditions. The initial configuration is assumed to be a straight ply, as shown in Figure 5.8(a). An *initial twist* is then prescribed, resulting in the geometry depicted in Figure 5.8(b). This twist is quantified by the angle per unit length, τ_0, defined as:

$$\tau_0 = -\frac{\Phi_0}{l}\,, \tag{5.2.4}$$

where Φ_0 is the corresponding *initial twist angle.* During this phase, the ply ends are maintained under axial tension. If the tension is subsequently released, allowing the structure to reach its natural minimum-energy configuration as shown in Figure 5.8(c), the ply adopts a helical or tortuous helical shape characterized by a specific helix angle and helix radius.

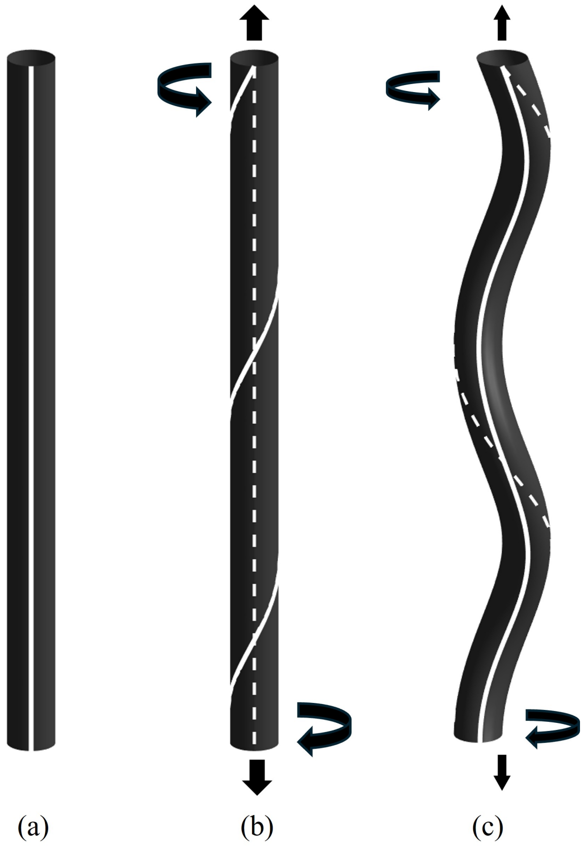

Figure 5.8. Ply torsion: (a) straight untensioned ply; (b) straight, tensioned and twisted ply; (c) tortuous ply after the reduction of axial load. The dotted line represents the initial untwisted state, while the solid line depicts the evolution under applied twist.

A key parameter describing this geometry is the *tortuosity*, defined as $1/\Sigma = \sin(\alpha)\cos(\alpha)/r$, which serves as an index of the ply helix angle and reflects how tightly or loosely the yarn is wound.

As discussed in Chapter 4, during yarn formation not all of the initial twist τ_0 is converted into geometric tortuosity $1/\Sigma$; a fraction remains stored within the ply as *residual twist* τ. This concept is schematically illustrated in Figure 5.9, where the dotted line represents the initial untwisted configuration and the continuous line shows the evolution of twist in the ply. Starting from three parallel and untwisted plies (Figure 5.9(a), where solid and dotted lines overlap), the same twist τ_0 is applied to each element (Figure 5.9(b), with the solid line indicating the surface twist). Once the ends are fixed and the applied torque is released, the plies adopt a helical configuration, converting part of the imposed twist τ_0 into tortuosity (Figure 5.9(c)). In this final configuration, the solid line tends to realign with the original dotted orientation but does not completely recover it; the resulting angular offset quantifies the residual twist τ.

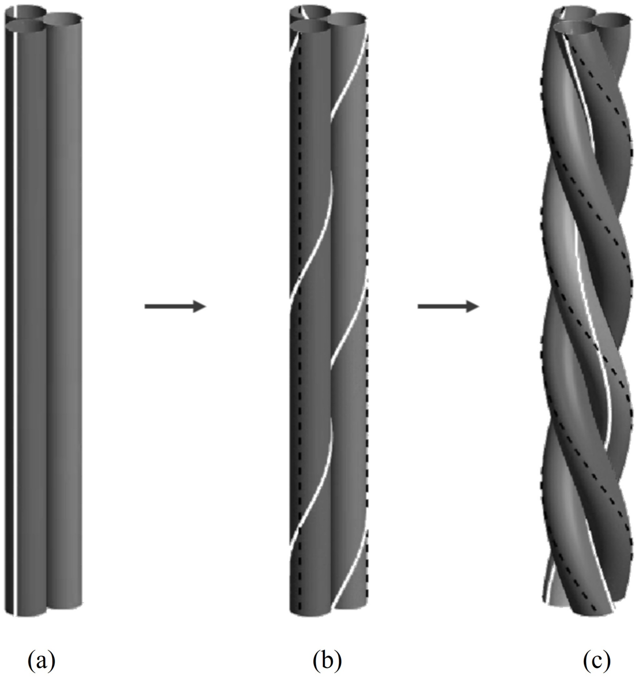

Figure 5.9. (a) 3 parallel untwisted ply (b) parallel twisted ply (c) 3-ply yarn showing residual twist. Dotted line represents the initial untwisted configuration and solid line represent the evolution of the twist in the ply.

When plies are twisted forming a yarn, their final state is determined by a balance of initial twist, tortuosity, and residual twist. The relationship between these quantities is described by Love's formula (Eq. (4.2.2)) already discussed in Chapter 4 and here reported for convenience

$$\tau = \frac{\mathrm{d}f}{\mathrm{d}\bar{s}} + \frac{1}{\Sigma}\,, \tag{5.2.5}$$

where $\frac{\mathrm{d}f}{\mathrm{d}\bar{s}}$ represent the initial twist imparted to the bundle that here was indicated as τ_0.

Rewriting (5.2.3) in function of the twist τ and defining β_0 as the *initial surface twist angle* as follow

$$\beta = -\arctan\left(\frac{1}{R_b\tau}\right), \tag{5.2.6}$$

$$\beta_0 = -\arctan\left(\frac{1}{R_b\tau_0}\right). \tag{5.2.7}$$

Eq. (5.2.5) can be rewritten in the form

$$\frac{1}{R_b \tan\beta} = \frac{1}{R_b \tan\beta_0} - \frac{\sin\alpha\cos\alpha}{r}, \tag{5.2.8}$$

In particular for the case of a 2-ply yarn in which $r = R_b$, Eq. (5.2.8) simplify in

$$\frac{1}{\tan\beta} = \frac{1}{\tan\beta_0} - \sin\alpha\cos\alpha, \tag{5.2.9}$$

that shows a direct correlation between the surface twist angles β and β_0 of the ply and the helix angle α of the yarn that the two plies forms in the hypothesis that R_b and r remain constant during the yarn formation process.

As established in Chapter 4, Love's formulation (5.2.5) describes how the twist in a ply evolves as a function of the initial twist imparted to it and the helical shape it subsequently assumes in the yarn. These quantities do not vary arbitrarily; rather, a natural equilibrium exists between them, governed by the material properties and, in particular, by the ratio between the bending stiffness B and the torsional stiffness A of the ply [257]. This ratio, which reflects the coupling between bending and twisting deformations, can be determined experimentally.

5.3 Experimental investigation on CNTF bundles

A shown in Figure 5.10, in the case of a CNTF yarn, each ply is not a homogeneous elastic rod but as a CNTF bundle, a multifilament and microstructured system rather than a continuous isotropic material. As a result, its mechanical response involves additional mechanisms and requires specific modeling approaches that differ from those used for simple elastic rods [275].

5.3.1 Optimal twist rate in a CNTF bundle

The presence of residual twist τ plays a crucial mechanical role in a CNTF bundle: the twist not only holds the fibers tight together but also promotes a more uniform distribution of tensile load across the bundle itself. It is very unlikely that the filaments in a bundle are stretched unevenly, so in the absence of twist, the shortest fibers would carry a disproportionately portion of the load, leading to premature cascading failure [264]. Residual twist mitigates this effect by engaging friction and mechanical coupling between filaments, enabling more efficient load sharing and enhancing the

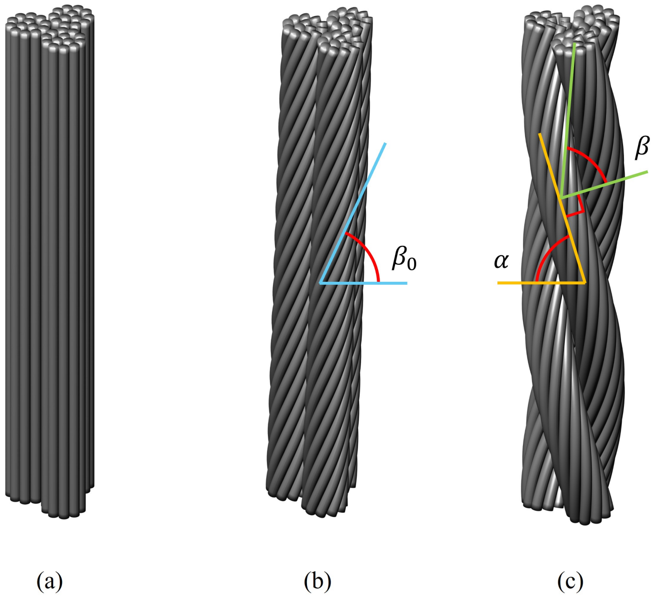

Figure 5.10. (a) 3 parallel untwisted bundles (b) parallel twisted bundles (c) 3-ply yarn.

overall mechanical performance of the bundle. For the CNTF bundle, the surface twist angle β corresponds to the helix angle of the helical path traced by the outermost fibers. This correspondence is illustrated in Figure 5.10, which, for clarity, also labels the previously discussed angles β_0, β, and α.

The key hypothesis is that an optimal amount of twist ensures efficient stress transfer between fibers. At low twist levels, when the angle β is close to 90°, fiber sliding and insufficient homogeneous load sharing occur [274]. Conversely, at high twist levels, as β decreases, the resulting radial pressure within the bundle increases. This promotes more rapid stress recovery in fibers adjacent to breaks, leading to an overall strengthening effect. However, if β is too low, obliquity effects in the fibers become dominant, since the fiber stress component contributing to the bundle strength is proportional to the square of the sine of the helix angle of the fiber path (5.3.11) [264]. Consequently, at excessively low values of β, the reduction in the total axial stress component creates a detrimental internal state of stress [264].

Due to these two competing mechanisms, the beneficial increase in radial pressure and the detrimental reduction in the axial stress component, there exists an optimal twist level, corresponding to an angle β_{opt}, at which the bundle strength is maximized.

The experimental campaign was conducted on CNTF bundles composed of 10, 20, and 40 continuous aligned CNTFs produced by wet solution spinning from a chlorosulfonic acid (CSA) solution containing a blend of Single- and Few-Walled CNTs with a high aspect ratio ($L/D > 4.5 \times 10^3$). The superacidic solvent enables true dissolution without the need for surfactants or sonication, thereby preserving nanotube length and minimizing structural damage. Owing to their high aspect ratio, the CNTs form a liquid-crystalline phase that promotes excellent alignment during extrusion. The wet spinning process [140] involved extruding the CNT-CSA solution through a spinneret into a coagulation bath, where the filament rapidly solidified. Continuous collection on a rotating drum under controlled tension further enhanced axial alignment and densification of the CNT network. The resulting anthracite-colored continuous filaments exhibited an approximately circular cross-section with a diameter of 24 ± 1 μm and a linear density of 0.65 ± 0.05 tex.

To determine the optimal twist level, samples of CNTF bundles long 34 cm were prepared and their linear density was measured. For each twist level, tensile tests were conducted on five specimens using a Shimadzu EZ-Test Compact Table-Top Universal Tester equipped with pneumatic capstan grips for yarns and cables [276], as shown in Figure 5.11.

(a) (b)

Figure 5.11. (a) Shimadzu EZ Test Compact Table-Top Universal / Tensile Tester (b) Shimadzu Pneumatic Capstan Grips for Yarn and Cables testing machine setup [276].

Pre-twisting was achieved using an electric motor, applying a number of revolutions n_b from 0 to 400. Prior to testing, the diameter of each bundle was measured using a Zumbach 15XY laser micrometer and verified through digital microscopy with a Dino-lite digital microscope, as illustrated in Figure 5.12, which shows an optical micrograph of a representative 10-filament CNTF bundle after twisting.

Number of filaments	**Average diameter (μm)**	**Linear density (tex)**
10	96	6.66
20	110	8.38
40	212	34.02

Table 5.1. Average diameter and linear density of CNTF bundles with different numbers of constituent filaments.

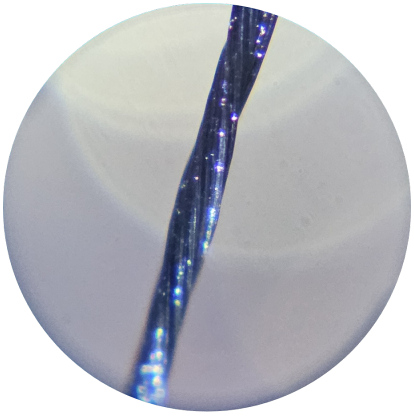

Figure 5.12. Magnification of a twisted 10-filaments CNTF bundle with a diameter of 96 μm.

From these measurements reported in Table 5.1, the corresponding torsion τ and surface twist angle β were calculated.

Each twisted bundle was then clamped between the grips of the testing machine, and uniaxial displacement-driven tensile tests were performed at a speed of 10 mm/min until failure to determine the effect of twist on tensile strength, stiffness, and strain-to-failure.

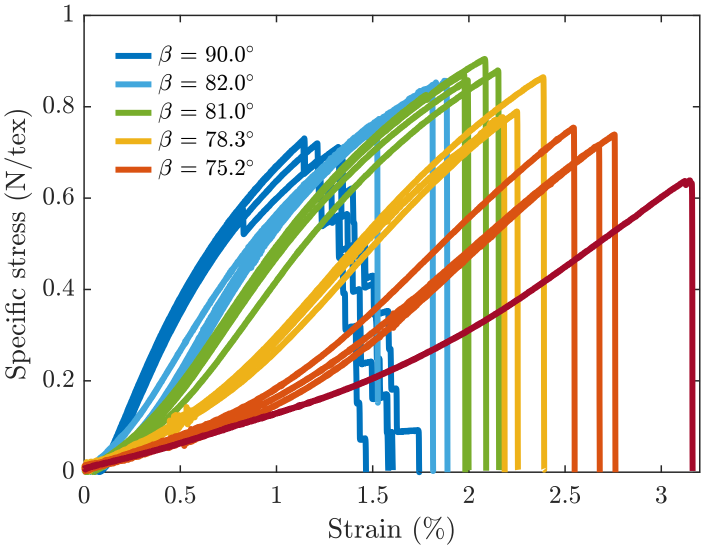

Figure 5.13. Tensile response of 10-filament CNTF bundles with different twist rate.

Figure 5.13 shows the tensile response of 10-filament CNTF bundles subjected to different twist levels. As the twist level increases, an initial and pronounced enhancement in strength is observed, followed by a gradual decline accompanied by a continuous reduction in stiffness. This behavior supports the initial hypothesis that an optimal twist promotes efficient stress sharing among filaments, whereas insufficient twist results in poor load transfer, and excessive twist introduces additional internal stresses that can ultimately degrade the mechanical performance. In particular, for the configuration corresponding to $\beta = 90°$, failure occurs through a cascade-like sequence of filament breaks within the bundle, indicating a highly localized stress redistribution. Furthermore, a concurrent and significant increase in ductility is also observed, an aspect that will be examined in greater detail in Chapter 6.

The experimental data obtained from 10, 20 and 40-filament CNTF bundles, reported in Figure 5.14(a), reveal a characteristic trend: the tensile strength increases with twist, reaches a maximum value, and subsequently decreases. This behavior highlights the existence of an optimal twist level that maximizes the mechanical performance of the bundle. In particular for all of the different bundles, the breaking strength peaks at a range of optima surface twist angle β_{opt} between 77° and 82°, while stiffness decreases progressively beyond this point.

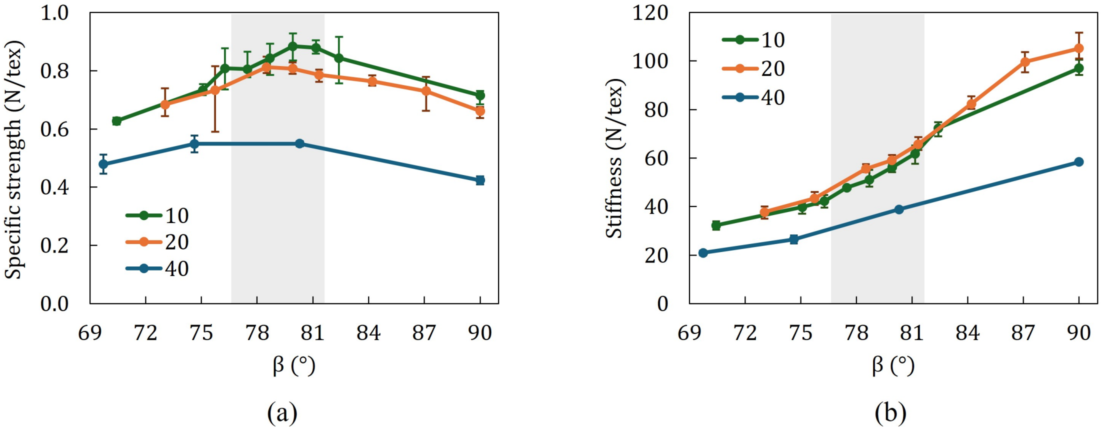

(a)

(b)

Figure 5.14. Test results of 10,20 and 40-filament CNTF bundles with different twist rate: (a) specific strength, (b) stiffness. The range of β with the peak strength is highlighted in gray.

This trend can be compared with a theoretical prediction based solely on geometric considerations and on the average specific strength of the single CNTFs. Tensile test on single CNTFs of 0.495 tex of liner density, taken from the same bundle, shown an average specific strength of 0.84 N/tex. The axial component of the fiber force T is related to the axial force of the bundle Q through the relation:

$$Q = m(R)\,T(R)\,\sin(\beta(R))\,, \tag{5.3.10}$$

where $R = [0, R_b]$ is the radial distance of the fibers from the bundle axis, $m(R)$ is the number of filaments and $\beta(R)$ is the torsion angle of the bundle at the radial distance R.

This correlation can be expressed in terms of specific strength as

$$S_b = S_f(R)\,\sin(\beta(R))^2\,, \tag{5.3.11}$$

Where S_b indicate the specific strength of the bundle, while S_f the one of the fiber. According to this formulation, as the helical angle β decreases, the axial contribution of each fiber diminishes, and consequently, the overall axial strength of the bundle decreases.

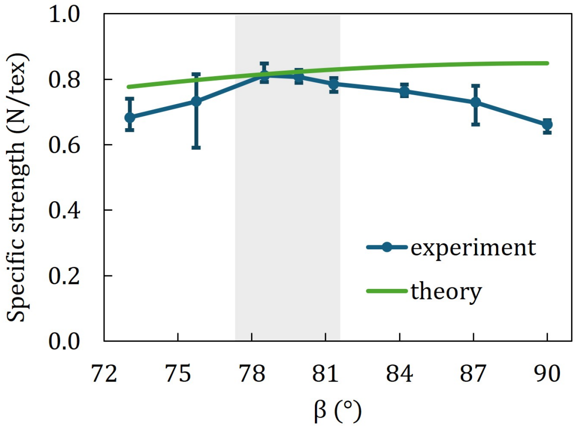

Figure 5.15. Specific strength trend as a function of β for 20-filament CNTF bundles, compared with the theoretical prediction.

Figure 5.15 compares the experimental trend of specific strength as a function of the helical angle β for 20-filament CNTF bundles with the corresponding theoretical prediction. The experimental data deviate from the theoretical curve, a discrepancy that can be attributed to a chain-like failure mechanism. When β approaches 90° and the fibers are nearly parallel, theoretical models predict that the tensile strength of the bundle should equal the average strength of its individual filaments. However, as shown in Figure 5.16, which compares the tensile responses of untwisted 10-filament bundles with those of single CNTFs extracted from the same bundle, the experimental evidence reveals a cascade-type failure process. Although individual fibers exhibit

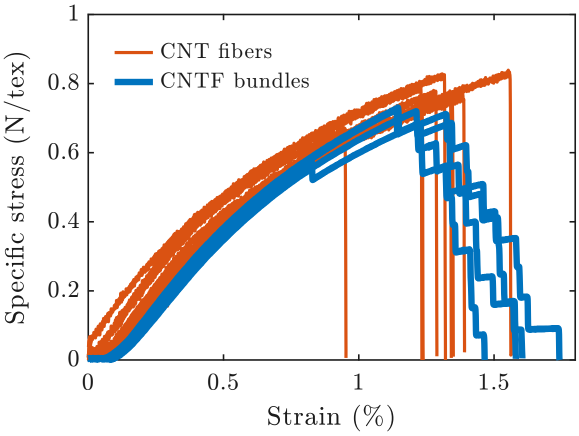

Figure 5.16. Tensile response of untwisted 10-filament CNTF bundles compared with single CNTFs extracted from the same bundle, highlighting the cascade-like failure behavior.

slightly higher specific strength on average, the premature fracture of a single filament within the bundle triggers a rapid sequence of failures in the remaining ones, leading to a lower overall bundle strength. In practice, the average tensile strength measured for the 10 and 20-filament bundles corresponds to approximately 80% of the theoretical maximum.

The reason lies in the premature failure of individual fibers: the breakage of a single filament (the weak link in the chain [277]) reduces the effective load-bearing section, which then initiates a cascade of failures in the neighboring filaments, ultimately causing the collapse of the entire bundle. Figure 5.17 shows the fracture analysis of 20-filament CNTF bundles with an approximate diameter of 150 μm, tested at three different twist levels: 1, 2.5, and 5 rad/mm. At low twist levels, the individual fibers tend to spread and behave rather independently, whereas increasing the twist results in a more compact and cohesive structure, with enhanced inter-fiber confinement.

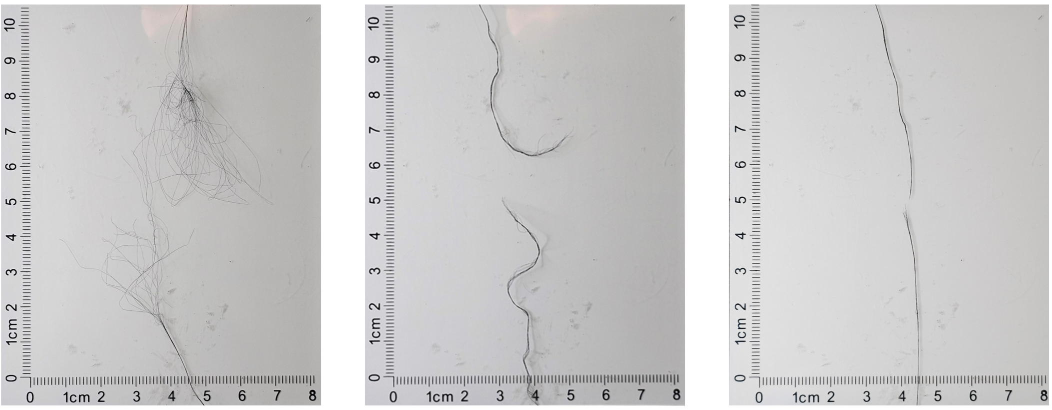

(a) (b) (c)

Figure 5.17. Fracture analysis after tensile test of 20-filament CNTF bundles (diameter ≈150 μm) with different twist levels: (a) 1 rad/mm, (b) 2.5 rad/mm, and (c) 5 rad/mm.

Further insight into the fracture behavior was obtained by analyzing untwisted bundles, which showed that their tensile strength follows a Weibull distribution [277]. This confirms that the *weakest chain model*, commonly used to describe fracture in materials composed of multiple load-bearing elements, is well suited for CNTF bundles. According to this model, the failure of the bundle is governed by its weakest segment: when one critical defect or flaw is activated, it leads to fracture of the whole structure. Consequently, the survival probability of the bundle depends on the probability that all its constituent elements remain unbroken under the applied load.

The Weibull distribution provides a quantitative framework for this statistical variability. Its cumulative failure probability is expressed as:

$$P_f = 1 - \exp\left[-\left(\frac{\sigma}{\sigma_0}\right)^{m_w}\right], \tag{5.3.12}$$

where σ is the applied stress, σ_0 is the scale parameter (characteristic strength), and m_w is the Weibull modulus, which quantifies the scatter of the data. A low m_w indicates high variability in strength due to defect sensitivity, while a higher m_w reflects more uniform failure behavior. Figure 5.18 shows the Weibull distribution on the Weibull plot [277], for a 10-filament CNTF bundle, for which it was obtained $m_w = 21.54$ and $\sigma_0 = 0.8$ N/tex.

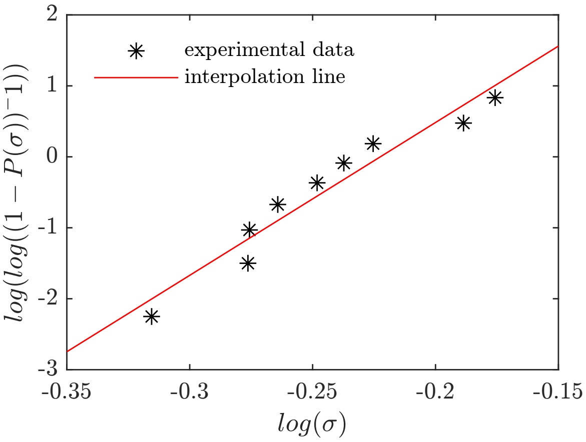

Figure 5.18. Weibull distribution for CNTF bundles.

In the case of CNTF bundles, the distribution of defects and the possible slack between filaments justify the applicability of the weakest chain model. The observed Weibull statistics confirm that bundle strength is primarily controlled by flaw distribution, and reliability analysis is therefore essential to describe their mechanical response.

Finally, the role of twist can be further interpreted in this framework. At low twist levels, fibers are poorly compacted, load sharing is limited, and fracture occurs progressively, preventing the bundle from achieving its theoretical maximum strength. As twist increases, fibers become more compacted and better aligned; through friction and cohesion they share the applied load more effectively, leading to enhanced strength and as evident in Figure 5.15, at an optimal level of twist, the breaking strength attains a value consistent with the theoretical prediction. However, excessive twist introduces significant combined tensile and torsional stresses, once again reducing the overall performance of the bundle.

The underlying assumption is that if the elementary unit (the bundle) exhibits optimal performance, the overall structure (the yarn) will also achieve maximum efficiency. Consequently, it is crucial that each bundle forming the yarn possesses the twist level that maximizes its breaking strength. To this end, it is necessary to quantify the residual torsion τ of the bundle once incorporated into the yarn with a specific helix angle α.

5.3.2 Relationship between twist and tortuosity

To establish the relationship among τ and α in the case of a CNTF bundle, an experimental approach analogous to that described in Sections 4.3.1 and 4.4.2 of Chapter 4 was adopted. In particular, the procedure followed the same steps illustrated in Figure 4.8, which depicted the setup used for a macroscopic rubber rod.

The experimental campaign was conducted on CNTF bundles composed of 10 and 20 CNTFs presented in Section 5.3.1, which avarege measure are reported in Table 5.1. Figure 5.19 shows an image obtained via digital microscopy of a 2-ply yarn fabricated by twisting two 20-filament CNTF bundles.

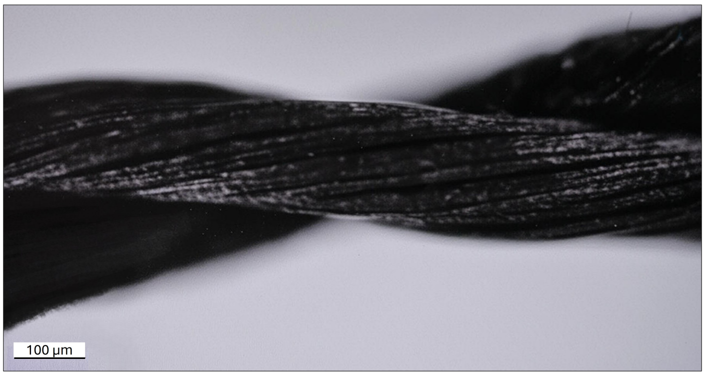

Figure 5.19. Microscopic image of a 2-ply CNTF yarn using a Dino-lite digital microscope. The structure results from the twisting of two 20-filament bundles.

Two bundles, each of a length l of 5 cm, were joined at one end using a clamp consisting of two layers of adhesive tape with a thin layer of cyanoacrylate between them to ensure a solid connection. Both bundles were then twisted by the same number of turns n_y, from which the initial twist per unit length τ_0 and the surface twist angle β_0 were consequently determined after measuring the twisted bundle diameter using Eqs. (5.2.4) and (5.2.7). The free ends of the bundles, held under axial tension, were subsequently brought together and fixed using the same clamping method, as illustrated in Figure 5.20(a). Once the applied tension and torque were released, the structure spontaneously formed a helical configuration, as shown in Figure 5.20(b).

From this natural equilibrium configuration, the helix angle α was measured, allowing the corresponding tortuosity $1/\Sigma$ to be determined empirically. Figure 5.20 highlights the significant shortening observed in a yarn made of 20-fiber bundles with a high twist level ($\alpha = 66.3°$, $\tau_0 = -12.5$ rad/mm) compared to the reference length of 5 cm, which would correspond to the case where the two bundles remained parallel and untwisted.

Assuming that the bundle behaves as a single, continuous structure, the values of the residual twist τ and the corresponding surface twist angle β within the bundle can be obtained by substituting the measured values of τ_0 and $1/\Sigma$ into Eq. (5.2.5). Figure 5.21 reports the experimental measurements of these quantities as a function of the helix angle α for a 10-filament CNTF bundle (Figure 5.21(a)) and for a 20-filament CNTF bundle (Figure 5.21(b)).

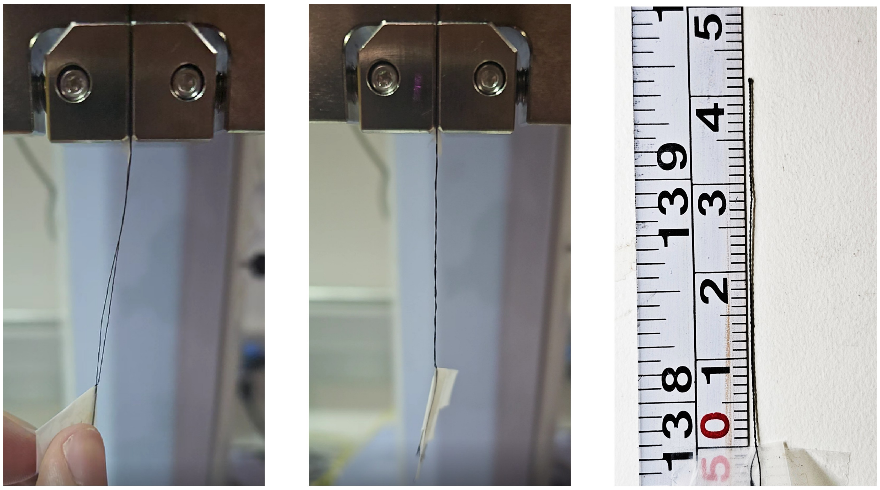

(a) (b) (c)

Figure 5.20. Forming a yarn made of 20-filament CNTF bundles: (a) Two CNTF twisted bundles which ends are fixed together; (b) 2-ply yarn formed after releasing the constraints; (c) detail of the final length of a with a high twist level ($\alpha = 66.3°$, $\tau_0 = -12.5$ rad/mm), showing significant shortening compared to the initial reference length of 5 cm.

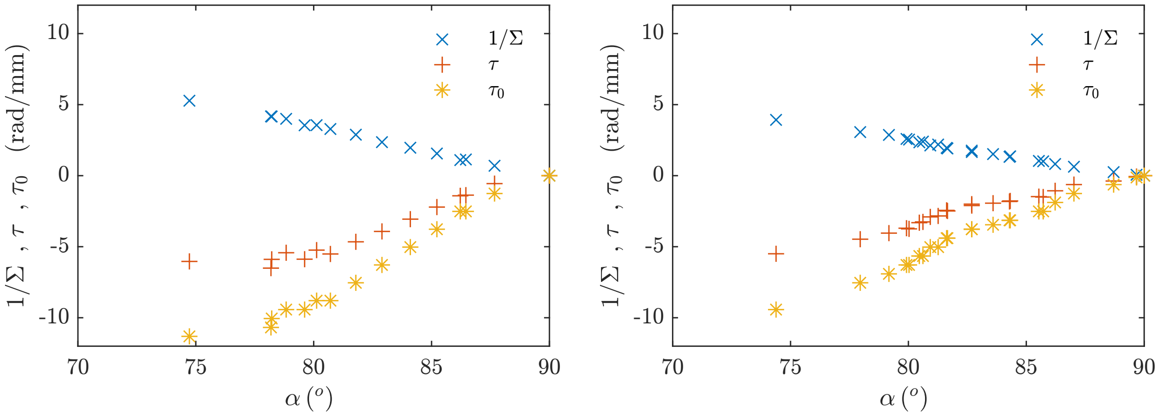

(a) (b)

Figure 5.21. Initial twist τ_0, tortuosity $1/\Sigma$, ad residual twist τ as a function of α (a) for a 10-filament CNTF bundle and (b) for a 20-filament CNTF bundle.

As shown in Figure 5.21, the trends observed for the 10- and 20-filament bundles are not identical, primarily due to geometric effects, particularly the dependence on the bundle diameter. However, as illustrated in Figure 5.22, the experimental data reveal a consistent functional relationship between initial and residual bundle surface twist angle β_0 and β and the helix angle α independently from the geometric parameters (number of fibers and bundle diameter). The relationship between β and α, that will be employed in Section 5.4 for subsequent modeling purposes, has been fitted with the polynomial function

$$\beta = c_1\,\alpha + c_0\,, \tag{5.3.13}$$

which coefficients for least-squares fit are reported in Table 5.2 .

coefficient	value
c_0	-0.5092 rad
c_1	1.3226

Table 5.2. Coefficients of the least-squares fit for the $\beta - \alpha$ relationship.

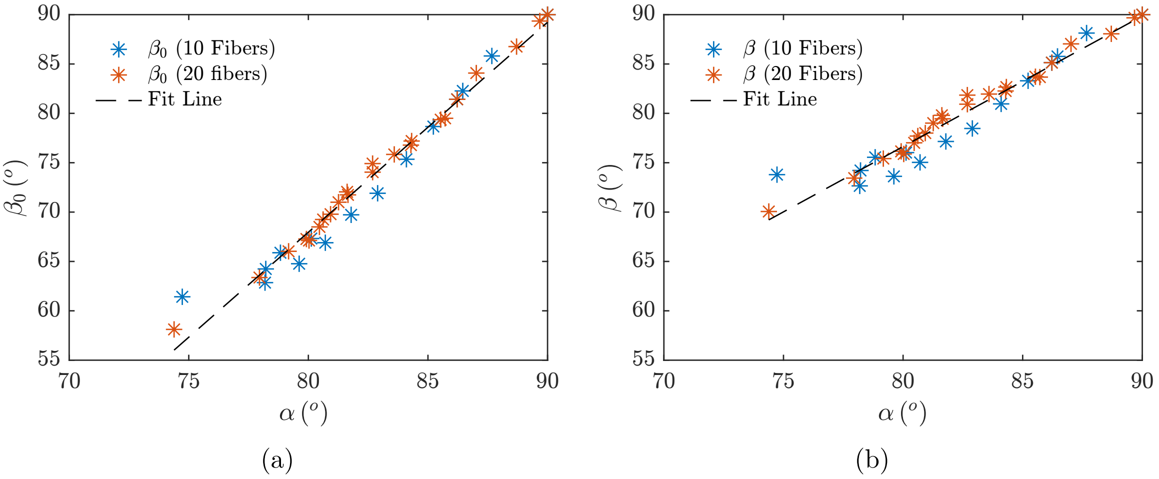

(a)

(b)

Figure 5.22. (a) Initial surface twist angle β_0 of 10- and 20-filament CNTF bundles in the unplied configuration; (b) residual surface twist angle β of 10- and 20-filament CNTF bundles in the yarn configuration.

For qualitative characterization and comparison with a homogeneous and isotropic rod, the CNTF bundle can be assumed to follow a simplified mechanical relationship in which the twist moment is expressed as the product of the equivalent torsional stiffness A_{eq} of the bundle and the twist per unit length τ, namely $H = A_{eq}\,\tau$. Similarly, the bending moment is given by $G_b = \frac{B_{eq}}{\rho}$ where B_{eq} is the equivalent bending stiffness and $1/\rho = \cos^2\alpha/r$ is the curvature associated with bending.

Combining these expressions with Eq. (4.2.11a) ones can rewrite Eq. (4.2.12) of Chapter 4 as

$$\frac{B_{eq}}{A_{eq}} = \frac{1}{2R_b\tan\beta}\,\frac{r}{\sin\alpha\cos\alpha}\,\left(1 - \tan^2\alpha\right)\,. \tag{5.3.14}$$

By substituting the experimental data into this relation, it is found that, in the case of a CNTF bundle, the stiffness ratio B_{eq}/A_{eq} is not constant but varies with the applied twist level and therefore depends on β, α and on r.

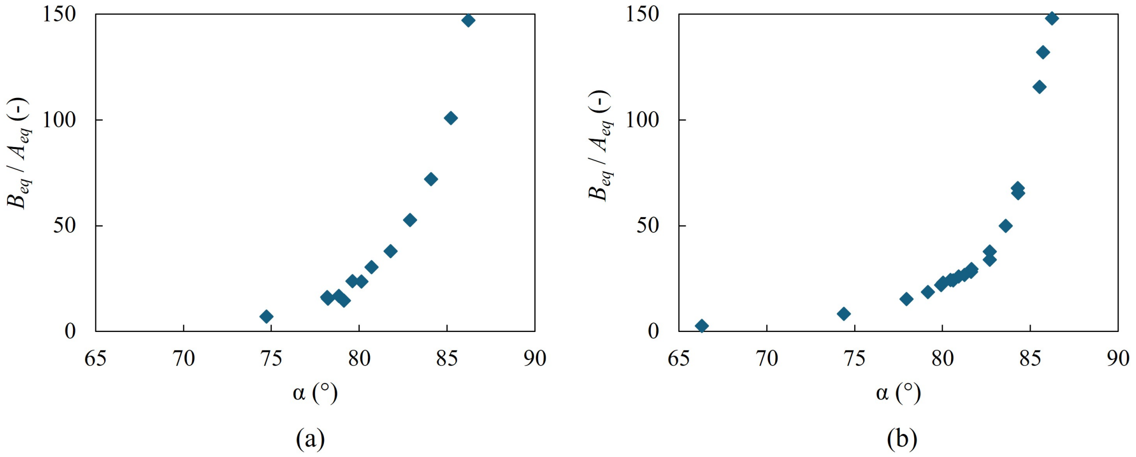

Figure 5.23. Ratio between equivalent bending and torsional stiffness in function of yarn helix angle α for (a) 10-filament and (b) 20-filament CNTF bundle.

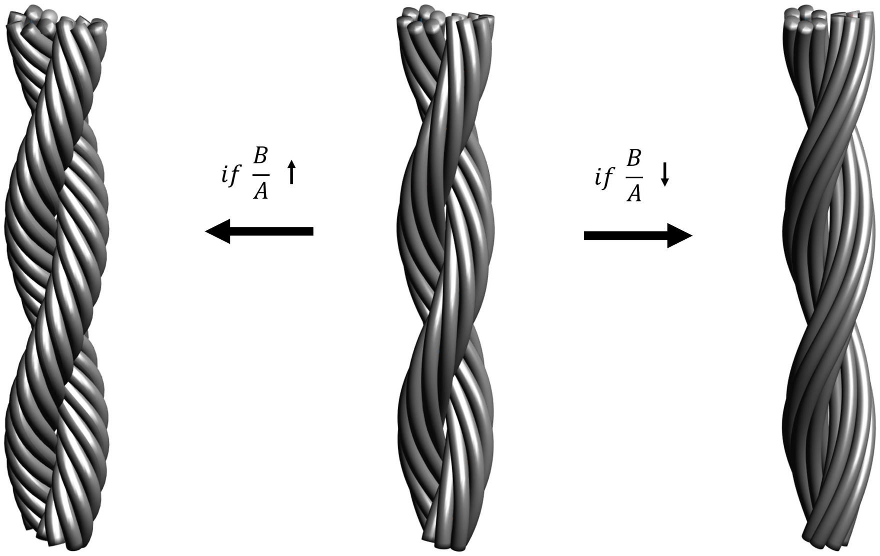

Figure 5.24. Qualitative influence of the stiffness ratio. When the stiffness ratio is high, the bundle favors maintaining its twist, whereas at low ratios it tends to convert twist into tortuosity, as bending becomes energetically preferable.

Experimental results for both the 10- and 20-filament CNTF bundles show that this ratio increases more rapidly as α approaches 90°, as illustrated in Figure 5.23.

This parameter is particularly useful for understanding how the initial twist is distributed between residual torsion and geometric tortuosity. As shown in Figure 5.24, for higher stiffness ratios the bundle tends to remain twisted rather than bending into a tortuous configuration, since the bending stiffness dominates over the torsional one. Conversely, when the stiffness ratio is low, the bundle tends to transform its initial torsion into tortuosity.

5.4 Yarnmaker kinematic

Once the optimal twist value β_{opt} maximizing bundle performance has been identified, it is essential to ensure that the residual twist within the bundles composing the yarn corresponds to this value. Given the yarn geometry and the desired optimal surface twist angle, there exists a specific set of machine parameters that yield an optimized yarn structure.

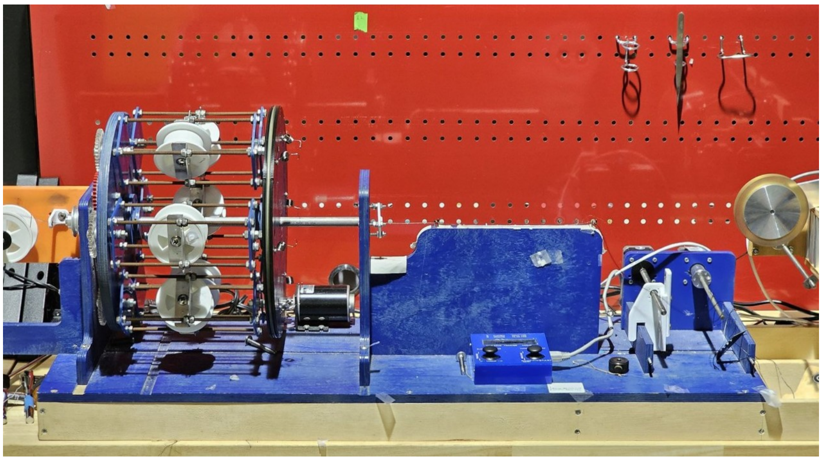

Figure 5.25. Illustration of the Yarnmaker, the machine used to ply CNTF bundles into continuous CNTF yarns.

To control the final properties of the yarn, a kinematic model of the yarn-making process was developed. Figure 5.25 shows the *Yarnmaker*, the machine used to ply CNTF bundles into continuous CNTF yarns through an epicyclic gear mechanism. The corresponding kinematic scheme is illustrated in Figure 5.26, where the following parameters are defined:

- $\omega_c = \dfrac{dn_c}{dt}$: angular velocity of the carrier, corresponding to n_c rotations of the spools (planets) around the central axis (sun) in a time interval and determining the number of windings imparted to the yarn;

- $\omega_s = \dfrac{dn_s}{dt}$: angular velocity of each spool about its own axis, corresponding to n_s revolutions of the spool in a time interval, determining the twisting motion applied to the individual bundles;

- $\xi = \dfrac{dh}{dt}$: linear take-up speed of the yarn, i.e., the rate at which a length h of the twisted yarn is drawn and collected in a time interval.

The interaction among these parameters defines the resulting yarn geometry, particularly the helix angle α.

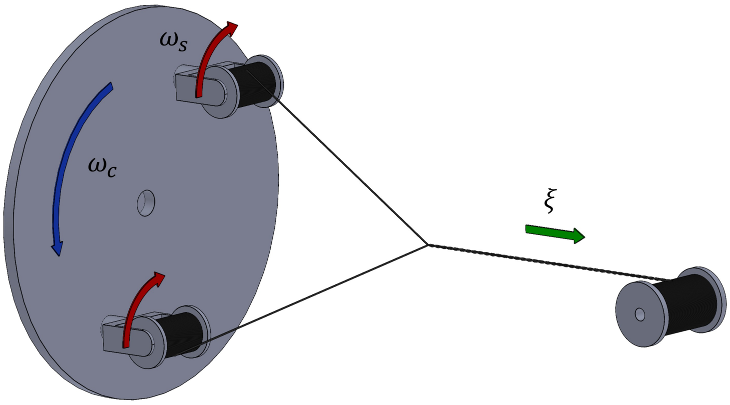

Figure 5.26. Schematic representation of the Yarnmaker kinematics.

The model establishes a relationship between the machine's operational parameters, ω_c, ω_s, and ξ, and the resulting yarn geometry (α, r), as well as the surface twist angle β within the bundles.

In the Yarnmaker, the gear train imposes a fixed ratio of $\omega_s/\omega_c = 2$, while ξ can be adjusted independently. As discussed in Section 5.3.2, the natural relationship between the number of twists imparted to each bundle n_b and the number of windings n_y formed in the resulting yarn expressed by

$$n_b = \frac{l}{2\pi R_b \tan\beta_0}\,, \tag{5.4.15}$$

$$n_y = \frac{h}{2\pi r \tan\alpha}\,. \tag{5.4.16}$$

is governed by the geometric relation between β and α and it is given by the ratio

$$\frac{n_b}{n_y} = \frac{r}{R_b \tan\beta_0 \cos\alpha}. \tag{5.4.17}$$

In contrast, the machine ratio n_s/n_c is the same of ω_s/ω_c and it is fixed by the mechanical gear ratio.

Since these two ratios are generally not identical, the operating conditions of the machine may not coincide with the yarn's natural ones. This mismatch can introduce an over- or under-twisted state within the bundles, which must be properly accounted.

Since the machine parameters are known, the system can be described analytically and solved to identify the optimal combination of the two independent control parameters ω_c and ξ needed to achieve a target surface twist angle β_{opt} in the bundles, thereby optimizing the yarn's mechanical performance.

5.4.1 Mathematical model for CNTF yarn-making

The cross-sectional geometry of the CNTF yarn is defined by m individual bundles helically wound around a common central axis. Depending on the number of bundles, the structure may include either an empty central region or a core bundle. For $m = 2$, the bundles are directly wound around each other and in contact, for $3 \geq m \leq 4$ they form a distinct central empty cylindrical region, whereas for $m > 4$, the geometry allows for the presence of a central bundle that occupies the void space between the external bundles.

Each external bundle of radius R_e follows a helical path characterized by a radius r, measured from the yarn axis to the bundle centerline. To the possible central bundle, or, equivalently, the inscribed empty cylinder defining the inner boundary of the external bundles arrangement, is assigned a radius R_i. These quantities are related to the overall helical geometry through:

$$r = R_i + R_e \,. \tag{5.4.18}$$

Four alternative configurations can be defined for the core region, depending on the desired structural layout:

(i) **Automatic optimal sizing:** the inner radius is computed automatically from the geometric function $R_{i,e}(\alpha, m)$ reported in Appendix A, which depends on the helix angle α and the number of bundles m,

$$R_i = R_e \times R_{i,e}(\alpha, m) \,; \tag{5.4.19}$$

(ii) **Identical sizing:** the central and external bundles are assumed to have equal radii,

$$R_i = R_e \,; \tag{5.4.20}$$

(iii) **Well-compacted configuration:** used to achieve a tight packing arrangement, compensating for the bundle's radial deformation if it occurs,

$$R_i = \begin{cases} 0, & \text{for } m \leq 4, \\ R_e \times R_{i,e}(\alpha, m), & \text{for } m > 4; \end{cases} \tag{5.4.21}$$

(iv) **User-defined configuration:** a fully customizable case in which R_i is directly assigned by the user.

This parametrization allows the model to represent a commonly used range of yarn architectures, from simple multi-ply structures to compact, core-stabilized configurations.

The governing parameter of the model is the bundle surface twist angle β, which selection is determined by the desired final properties of the structure. For instance, to maximize tensile strength, the optimal value β_{opt} found in Section 5.3, should be chosen.

Once the target value for β is established, the yarn helix angle α can be derived from (5.3.13) and the quantities τ,τ_0 and $1/\Sigma$ can be calculated.

Two production configurations are modeled depending on whether the yarn is allowed to rotate after fabrication.

In the *rotation-allowed configuration*, once the yarn is unspooled, it is assumed to be free to rotate around its longitudinal axis. Under these conditions, the yarn spontaneously relaxes toward its natural configuration by releasing the accumulated over-twist. Consequently, the only relevant control parameter is the spool angular velocity ω_s, since, when free to rotate, the yarn self-adjusts to achieve its equilibrium number of windings. The corresponding take-up speed of the Yarnmaker is thus calculated as:

$$\xi = -\frac{2\pi\,\omega_s}{\tau_0}\,\sin(\alpha)\,, \tag{5.4.22}$$

In contrast, in the *rotation-restricted configuration*, the yarn is constrained against rotation after manufacturing, preventing the relaxation of the excess twist. In this case, the machine parameters to achieve a prescribed β can be found by solving Love's equation (5.2.5), expressed in terms of the linear and the angular velocities ξ, ω_c, and ω_s:

$$\frac{1}{R_e\tan\beta} = \frac{2\pi\,\xi\,\omega_c}{\xi^2+4\pi^2\omega_c^2r^2} - \frac{2\pi\,\omega_s}{\sqrt{\xi^2+4\pi^2\omega_c^2r^2}}\,. \tag{5.4.23}$$

Fixing a desired β and one of the angular velocities, the linear take-up speed ξ can be determined to properly configure the Yarnmaker. The resulting helix angle of the yarn α_{rr}, which will differ from the natural one, is then given by:

$$\alpha_{rr} = \arctan\left(\frac{\xi}{2\pi r\,\omega_c}\right)\,. \tag{5.4.24}$$

The final yarn diameter depends on the geometric arrangement of the bundles, which varies with the number of ply m. The maximum and minimum projected diameters of the yarn cross-section $D_{y,\max}$ and $D_{y,\min}$ can be geometrically estimated as follows

$$m=2: \quad D_{y,\max} = 4R_e, \qquad D_{y,\min} = 2R_e, \tag{5.4.25a}$$

$$m=3: \quad D_{y,\max} = 4R_e, \qquad D_{y,\min} = 2R_e + r\sqrt{3}, \tag{5.4.25b}$$

$$m=4: \quad D_{y,\max} = 2R_e + 2r, \qquad D_{y,\min} = 4R_e, \tag{5.4.25c}$$

$$m=5: \quad D_{y,\max} = 2R_e + 2r\frac{\sqrt{10+2\sqrt{5}}}{4}, \qquad D_{y,\min} = 2R_e + r\frac{5+\sqrt{5}}{4}, \tag{5.4.25d}$$

$$m=6: \quad D_{y,\max} = 2R_e + 2r, \qquad D_{y,\min} = 2R_e + \sqrt{3}\,r. \tag{5.4.25e}$$

To obtain a representative single value, the *Root Mean Square (RMS)* diameter of the yarn $D_{y,\mathrm{RMS}}$ is defined as:

$$D_{y,\mathrm{RMS}} = \sqrt{\frac{D_{y,\max}^2 + D_{y,\min}^2}{2}}\,, \tag{5.4.26}$$

which provides an effective average measure of the yarn's cross-sectional dimension, accounting for geometric variations due to bundle arrangement.

The proposed simplified model allows, within reasonable approximations, the estimation of the machine parameters required to achieve the desired yarn performance by controlling the applied twist. Despite its effectiveness, the model presents some inherent limitations, including the dependence on experimentally derived relationships, the assumption of linear elastic behavior, and the neglect of inter-bundle frictional effects. Nevertheless, this comprehensive mathematical framework provides a valuable basis for the optimization of CNTF yarns, as it integrates geometric, mechanical, and manufacturing aspects into a unified system of equations suitable for computational implementation and experimental validation.

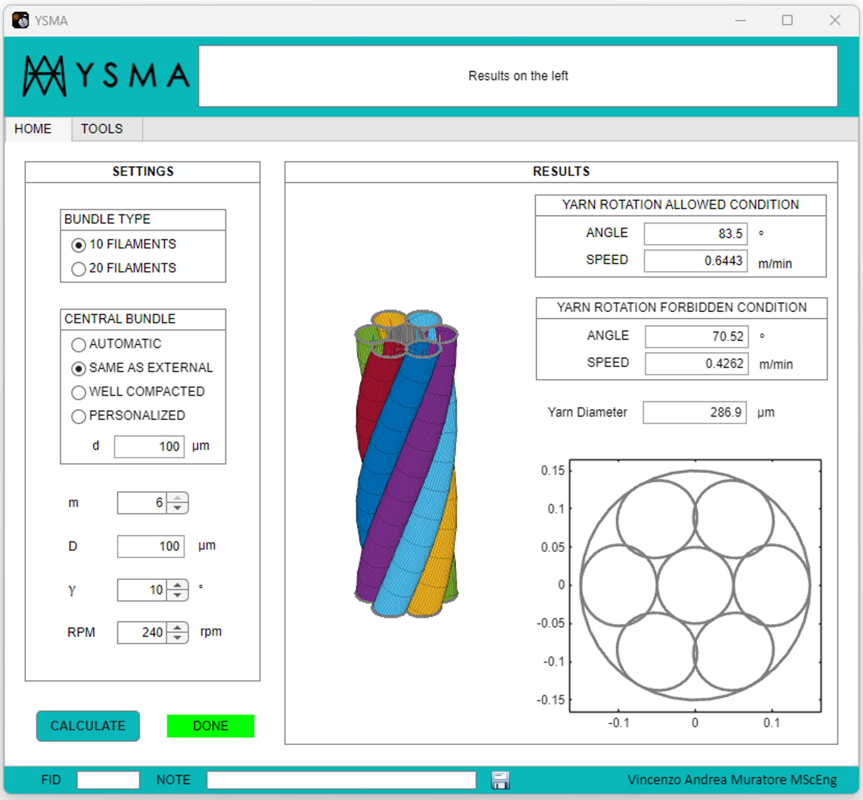

Results on the left

BUNDLE TYPE
● 10 FILAMENTS
○ 20 FILAMENTS

CENTRAL BUNDLE
○ AUTOMATIC
● SAME AS EXTERNAL
○ WELL COMPACTED
○ PERSONALIZED
d 100 µm

m 6
D 100 µm
Y 10 °
RPM 240 rpm

YARN ROTATION ALLOWED CONDITION
ANGLE 83.5 °
SPEED 0.6443 m/min

YARN ROTATION FORBIDDEN CONDITION
ANGLE 70.52 °
SPEED 0.4262 m/min

Yarn Diameter 286.9 µm

Vincenzo Andrea Muratore MScEng

Figure 5.27. Graphical user interface of the Yarn and Strand Maker App (YSMA).

The model was implemented as a computational tool with the MATLAB app designer environment. Its graphical user interface (GUI), shown in Figure 5.27, guides the user through a sequential parameter input process. The left panel enables the selection of the bundle type based on its constituent filament count. Subsequently, the user defines the yarn's geometric configuration by specifying the presence of a central bundle and the expected packing density among the bundles. Then the user can select the number of circumferential bundles (m), their diameter (D), the surface twist angle expressed by $\gamma = \pi/2 - \beta$, and the rotational speed of the carrier (ω_c) in revolutions per minute (RPM).

The model was tested experimentally by producing several yarn configurations and measuring their properties. The results demonstrate significant improvements over yarns manufactured using empirically-derived settings based on historical experimentation. Table 5.3 compares the mean tensile strength from previous experiments with the values obtained from yarns made using the model parameters, specifically for the cases of a 3-ply yarn and a 5+1-ply yarn (comprising 5 external plies and 1 central ply). The implementation of the model's recommended parameters yielded a substantial increase in specific strength. Overall, the application of model-predicted values resulted in an average improvement of 14% in the yarn's mechanical properties relative to previous products.

Yarn	Average Specific Strength (N/Tex)		
Configuration	No Model	Model-Based	Improvement
3-ply	1.277	1.411	(+10.5%)
5+1-ply	1.190	1.408	(+18.3%)

Table 5.3. Comparison of average specific strength for yarns manufactured using empirical methods versus model-predicted parameters.

5.5 Other investigations, future works and final discussion

Following the experimental investigations and the development of a kinematic model, several complementary investigations were pursued to explore other critical aspects of yarn architecture and mechanical properties of CNTF bundles. These parallel research threads were essential to build a more comprehensive understanding of the structure-property relationships in CNTF yarns and to identify practical pathways for performance enhancement beyond twist optimization alone. The findings from these studies are presented herein, alongside a discussion of future research directions.

5.5.1 Yarn architecture and cross-sectional optimization

Within the framework of yarn architecture and cross-sectional optimization, an in-depth analysis of bundle packing was carried out on CNTF yarns featuring concentric ply arrangements. In particular, 2-ply and 3-ply yarns generally exhibit superior mechanical stability compared with more complex configurations, as their constituent bundles experience uniform loading conditions and share the applied stress evenly. In contrast, 4-ply yarns tend to develop internal asymmetries: two opposing bundles may collapse toward the center while the remaining two stay on the periphery, as illustrated in Figure 5.28. This configuration results in heterogeneous stress distributions, as the inner bundles, characterized by smaller helical radii, undergo different strain levels than the outer ones, leading to early failure of the more stressed outer plies.

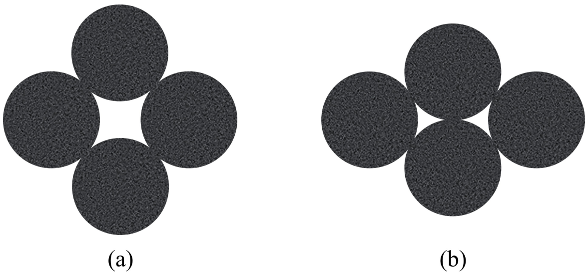

Figure 5.28. (a) Ideal cross-section of a 4-ply yarn; (b) collapsed geometry due to centripetal pressure.

A different non-uniformity occurs in the common 6+1-ply configuration, where six outer bundles surround a central one. The central bundle does not follow the same helical trajectory as the external plies but is primarily subjected to torsion, or may even consist of nearly untwisted parallel fibers. Consequently, it exhibits a distinct stress–strain response, often resulting in localized or non-uniform failure [263].

Figure 5.29 compares the tensile strength of 6+1- and 3-ply CNTF yarns with varying helix angles, each composed of 10-filament CNTF bundles. The 3-ply configuration demonstrates slightly superior performance, reflecting the benefits of structural symmetry and more uniform stress distribution.

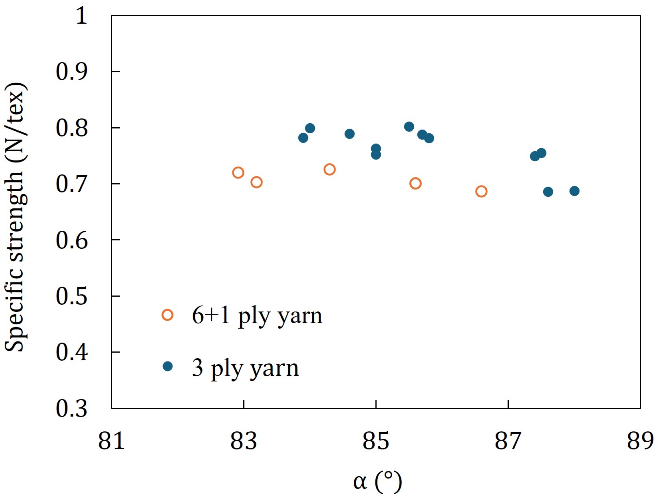

Figure 5.29. Specific strength of 6+1 and 3-ply CNTF yarns with different helix angles, each composed of 10-filament CNTF bundles.

By combining geometric modeling (e.g., fiber-packing simulations and radial angle distribution analysis) with experimental mechanical testing (tensile, fatigue, and cyclic loading), it becomes possible to identify yarn architectures that maximize specific strength, packing efficiency, and dimensional stability while maintaining consistent mechanical performance across all plies.

The geometric configuration also affects the effective and enveloping cross-sectional areas of the yarn. Based on the number of external plies (m), the *effective area* A_{eff}, corresponding to the total cross-sectional area of the CNTF bundles, and the outer *enveloping area* A_{env}, representing the area of the minimal circle enclosing the yarn, can be determined. Their ratio defines the *packing efficiency*, which quantifies the fraction of the cross-section effectively occupied by CNTF material.

From the geometric relationships described in Eq. (5.4.25), the maximum yarn diameter and its corresponding bounding area can be obtained. For configurations with $m > 4$, the area of a central bundle must also be considered in the effective area calculation, leading to:

$$A_{\text{eff}} = \begin{cases} m\pi R_e^2, & \text{for } m \leq 4, \\ m\pi R_e^2 + \pi R_i^2, & \text{for } m > 4, \end{cases} \tag{5.5.27}$$

while the total bounding area is expressed as $A_{\text{env}} = \pi R_y^2$.

The packing efficiency is therefore given by:

$$\eta = \frac{A_{\text{eff}}}{A_{\text{env}}} \times 100\,. \tag{5.5.28}$$

Table 5.4 summarizes the calculated packing efficiencies for configurations with $m = 2$ to $m = 6$.

Number of plies (m)	**Packing efficiency (%)**
2	50.00
3	64.62
4	68.63
5	75.26
6	77.78

Table 5.4. Packing efficiency of CNTF yarns as a function of the number of plies (m).

Despite these limitations, the 6+1-ply configuration achieves the highest packing density and thus maximizes the effective cross-sectional area while minimizing bulk. Moreover, advances in yarn manufacturing could enable the central bundle to be twisted in a controlled manner, improving the uniformity of load sharing and aligning its mechanical response more closely with that of the external bundles.

5.5.2 Post-twist hardening of CNTF bundles

In Section 5.3, it was observed that the application of twist increases the maximum tensile strength of the bundle, but concurrently leads to a reduction in stiffness.

To evaluate whether this drawback could be mitigated, a series of post-twist hardening tests was performed on 20-filament CNTF bundles with average diameter of 110 μm, linear density of 8.38 tex and twist of 3.7 rad/mm (β of 67.9°) that were pre-tensioned at different percentages (from 50 to 95%) of their ultimate tensile load prior to testing. The results illustrated in the histogram of Figure 5.30 were highly encouraging: the bundles recovered approximately 80–90% of the stiffness (N/tex) lost during twisting (Figure 5.30(b)), reaching values comparable to those of untwisted bundles (Figure 5.30(b) reference), while maintaining the same specific strength (N/tex), as illustrated in Figure 5.30(a).

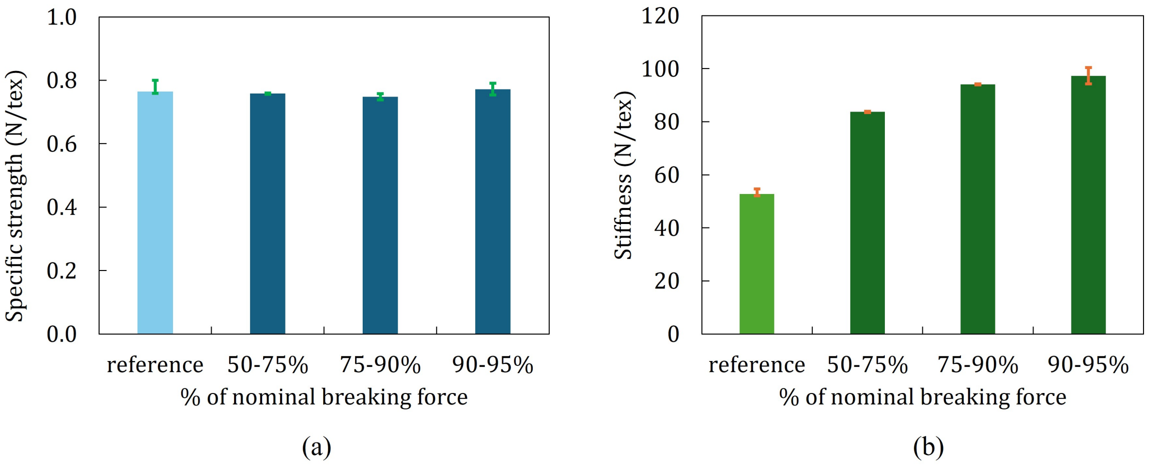

Figure 5.30. (a) Specific strength, (b) recovered stiffness for a 20-filament bundle with average diameter of 110 μm, linear density of 8.38 tex and twist of 3.7 rad/mm ($\beta = 67.9°$).

This improvement can be attributed to fiber rearrangement, enhanced alignment, and increased inter-filament friction promoted by the hardening process, which collectively reduce internal slippage under load. In addition, a small elongation of about 2% of the bundles' initial length was observed, causing a slightly reduction of their linear mass density and resulting in a modest but measurable increase in specific strength.

These findings demonstrate that hardening effectively restores the stiffness lost during twisting while enhancing the overall mechanical efficiency of CNTF bundles, providing a practical means to balance strength and stiffness.

5.5.3 Viscoelastic properties of CNTF bundles

Further tests were carried out on 20-filament CNTF bundles with average diameter of 110 μm, linear density of 8.38 tex and twist of 3.7 rad/mm (β of 67.9°) to investigate their visco-elastic behavior. These experiments were designed with two main objectives. First, to assess the influence of testing speed, ensuring that the strain rate does not affect the measured mechanical properties and, at the same time, to evaluate the response of the fibers under different dynamic loading conditions. Second, to investigate the static resistance of the fibers, i.e., their ability to withstand a sustained load over time, thereby providing both a reference value for static strength and useful data for creep characterization.

As shown in Figure 5.31, varying the testing speed between 50 and 1000 mm/min did not produce any measurable influence on the shape of the tensile response.

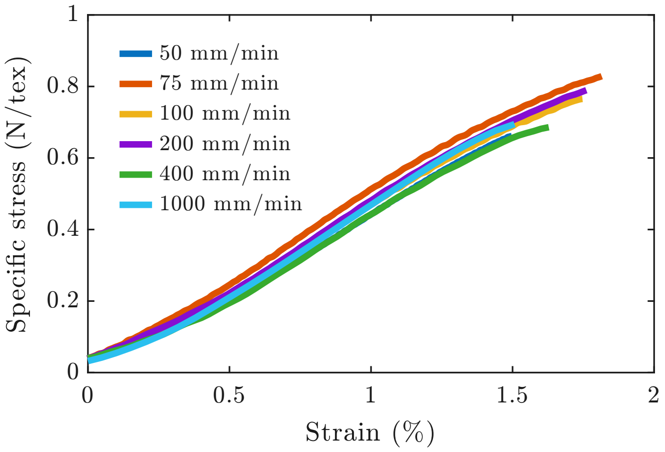

Figure 5.31. Stress-strain diagram for several tests performed at increasing testing speed on 20-filament CNTF bundles with average diameter of 110 μm, linear density of 8.38 tex and twist of 3.7 rad/mm (β of 67.9°).

On the other hand, creep tests performed at different fractions of the ultimate tensile strength (ranging from 83% to 67%) revealed a clear visco-elastic behavior, indicating that the specific strength obtained from standard tensile tests does not accurately represent the long-term performance under sustained loading. Even at stress levels as low as 67% of the ultimate tensile strength, a continuous increase in strain over time was observed. The quantitative results of the creep experiments, including the creep rate coefficient, time to failure, and final strain, are shown in Figure 5.32 and summarized in Table 5.5.

Load %	Sp. stress (N/tex)	Final Strain (-)	Creep Rate (s^{-1})	Time (s)
83	0.59622	0.018751	8.236×10^{-6}	398
75	0.53701	0.018932	1.0545×10^{-7}	26523
72	0.51309	0.015640	3.1654×10^{-8}	62182
67	0.47741	0.016489	1.2238×10^{-8}	no fail $> 10^5$

Table 5.5. Creep test parameters from test performed under static loading conditions at various fractions of the ultimate tensile strength on 20-filament CNTF bundles with average diameter of 110 μm, linear density of 8.38 tex and twist of 3.7 rad/mm (β of 67.9°).

This indicates that more refined investigations are required to determine reliable strength values and safety factors for the practical structural application of CNTFs.

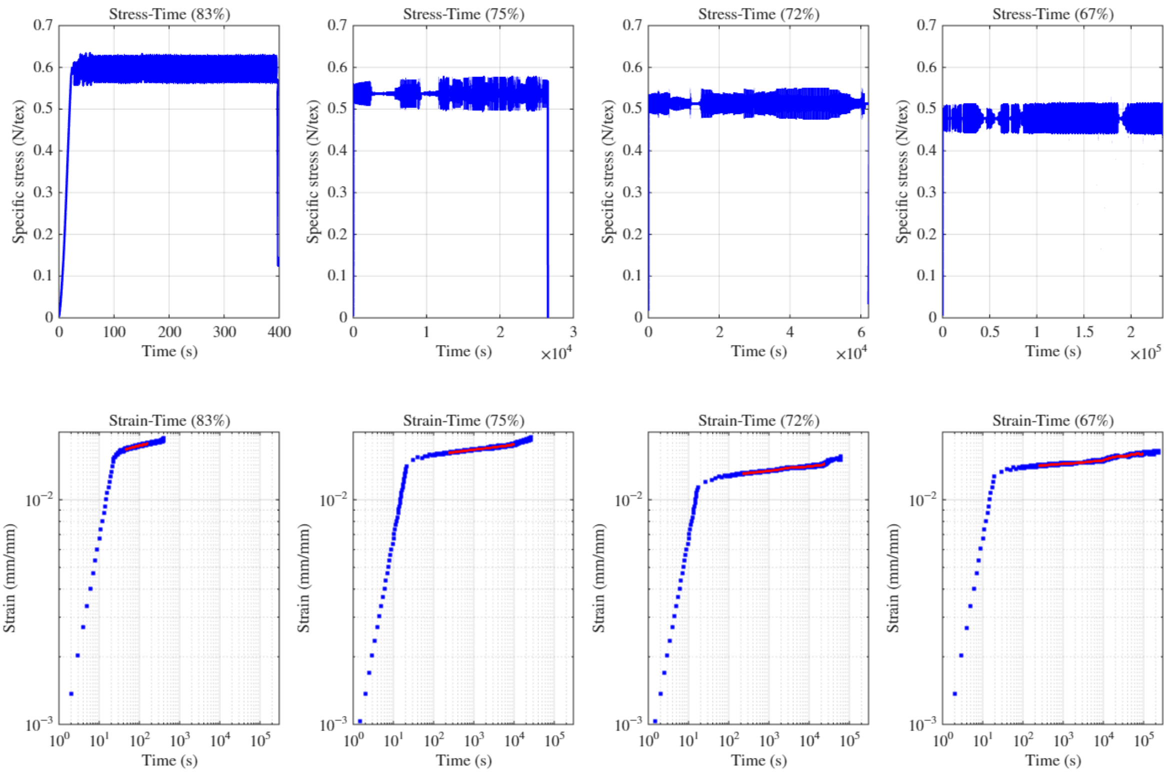

Figure 5.32. Creep response diagrams obtained under static loading conditions at various fractions of the ultimate tensile strength of 20-filament CNTF bundles with average diameter of 110 μm, linear density of 8.38 tex and twist of 3.7 rad/mm (β of 67.9°).

5.5.4 Discussion

The validated model established a direct correlation between the machine's operating parameters, the final yarn geometry, and the residual twist within the constituent bundles. This relationship enabled a systematic investigation of the structure–property relationships in twisted fiber assemblies and provided a comprehensive framework for designing new experimental campaigns with precise control over the geometric and kinematic parameters of the yarn manufacturing process.

The model's implementation as a computational tool demonstrated its practical utility for process optimization, yielding an average improvement of 14% in specific tensile strength. This result confirms the central hypothesis that controlling the residual twist through appropriate kinematic tuning during fabrication is a critical factor for enhancing the mechanical performance of CNTF yarns.

However, this significant outcome was achieved using a simplified model that relies on several approximations, indicating a clear need for further research to refine both the theoretical and experimental aspects of this work. Future studies should focus on:

- Quantifying the torsional and bending stiffness of individual fibers and bundles.
- Incorporating inter-filament frictional effects, viscosity and progressive collapse

into the model.

- Developing a more robust multi-scale model that accurately links single-fiber mechanics to bundle-level behavior.
- Extending mechanical characterization to include long-term durability assessments, such as fatigue, creep tests.
- Developing a refined predictive model for the mechanical response of CNTF yarns.

Addressing these research directions will be essential to enhance the understanding and performance of advanced CNTF-based yarns, paving the way for their successful implementation in next-generation structural and multifunctional applications.

Chapter 6

Effect of torsion on the mechanical properties of CNTFs and multi-fiber structures

While the mechanics of CNTFs wound into yarns have been extensively investigated in Chapter 5, the effect of applying a controlled pre-twist directly to an individual CNT Fiber remains far less explored.

The remarkable increase in ductility observed in twisted bundles, as reported in Section 5.3 and exemplified in Figure 5.13, did not find a direct correspondence with classical models commonly employed for twisted fiber bundles, such as those proposed in [278] or the extended version in [257] for an arbitrary number of filaments. It was therefore hypothesized that this atypical mechanical response originates from the intrinsic behavior of the twisted individual CNTFs composing the bundle, motivating an in-depth investigation into the influence of torsion on the mechanical properties of CNTFs.

This chapter demonstrates through tensile testing that such pre-twisting induces a remarkable mechanical trade-off in a single fiber: a significant enhancement in ductility alongside a reduction in stiffness and strength. This behavior is explained through scanning electron microscopy and a mechanistic model, corroborated by testing a macroscopic analogue. The findings indicate that strategically tailoring the pre-twist can program CNT Fiber properties for superior macroscale structures.

As discussed in Section 2.5.1, CNT Fibers are commonly produced using three main techniques: solution spinning [279, 280], direct spinning from floating-catalyst CVD reactors [281, 282], and dry spinning (from forest or vertically grown CNT arrays) [283, 284]. Despite their different routes, all methods share the same objective of aligning CNTs into a densely packed, cohesive microstructure arising from van der Waals interactions along the extensive lateral surfaces of the CNTs, which, although weak individually, are collectively effective due to the high aspect ratio of the CNTs (length/diameter $> 10^3$).

The present experiments focus on Solution-Spun Fibers, which yield a highly aligned and densely packed microstructure, albeit typically composed of shorter CNTs. Scanning electron microscopy reveals that well-produced fibers have pseudo-circular cross-sections with few voids and diameters of microns. Crucially, this structure is not monolithic; it is hierarchically composed of smaller CNT clusters, also named *fibrils* in the sequel. This multi-filament architecture is central to the present investigation. The bonding within this hierarchy is also multi-scale: the CNTs within a fibril are linked by van der Waals forces, while the bonds between the fibrils appear significantly weaker.

SEM imaging remarkably demonstrates that pre-twisting reorganizes the multi-filament structure of the fiber, transforming the constituent loosely bonded CNT fibrils into a helical architecture. By viewing CNT Fibers as hierarchical yarn-like systems, one can better rationalize the interplay between microscopic interactions, mesoscale rearrangements and macroscopic response, ultimately advancing the predictive modeling of their mechanical performance. Within this framework, the intrinsic multilevel helical organization of fibrils emerges as the key feature modulating stiffness, strength, and deformation, also at the level of the individual CNT Fiber.

Positioning CNT Fibers within the broader category of yarn-like multi-filament materials enables leveraging established knowledge. The assembly of individual filaments into yarns, strands, and cables through twisting is a key manufacturing process, which provides integrity to the assembly [278]. The underlying mechanics is a mature field of study, widely investigated for metallic steel wires. Models, often based on Kirchhoff-Love rod theory, treat the structure as an ensemble of helically arranged filaments to predict its overall tensile and torsional stiffness [234, 237, 256]. The behavior is generally dominated by the axial stiffness of the filaments organized into helices, with pre-twist during manufacturing being the critical parameter that defines the geometric shape and, hence, the gross mechanical properties. The hierarchical helical organization inherent in twisted structures has been recognized as a key feature governing stiffness, strength, and deformation mechanisms [226]. Analyses of twisted yarns have demonstrated how twist-induced internal stress and eigenstress distributions can alter the apparent tensile behavior. In particular, recent experimental studies on two-ply yarns [257] confirmed that these residual stress states can significantly affect strength and stiffness.

Only specific studies have been conducted on CNT assemblies, mainly focused on comparing processing methods with gross properties, to bridge the gap between nanoscale constituents and macroscale tensile [128] or bending response [7]. The effect of twisting on tensile properties has been investigated for dry spun CNTF [285] or clusters [286]. Yarn mechanics provides valuable insights on frictional interactions as the fundamental mechanism governing load transfer and deformation behavior [278, 287–289]. Molecular dynamics has been used [286] to investigate the mesoscale mechanics of twisted CNT clusters with inter-tube interactions, emphasizing the importance of shear interactions and identifying optimal twist angles through pull-out simulations. A multiscale modeling strategy, combining atomistic and coarse-grained molecular dynamics, was applied in [290] to twisted CNT clusters, to demonstrate that twisting enhances intertube shear interactions by increasing contact surface, but excessive twist weakens them due to cross-sectional deformation of individual CNTs.

The effect of pre-twist on the tensile properties of an individual solution-spun CNT fiber has not been previously investigated, to the best of current knowledge. This investigation addresses this effect by modeling the CNTF as a compactly packed structure composed by clusters of nanotubes, idealized as cylindrical elements, arranged in concentric layers within the circular perimeter of the fiber.

The tests conducted have reported a marked enhancement in ductility, exceeding the ultimate strain of untwisted fibers, alongside a reduction in stiffness and strength. To interpret this observation, a mechanical model founded on the following key hypotheses, specific to the single-fiber scale, is proposed.

(i) *Axial strain mismatch.* Pre-twist causes the constituent fibrils in each radial layer to form helices with different pitch angles, leading to a differential projection of their lengths along the fiber axis. This geometry induces a progressive engagement of the fibrils during axial loading: outer layers, being forced into longer helical paths, become prestressed and bear load earlier, while inner clusters remain unstressed until the fiber extends sufficiently, directly explaining the nonlinear tensile response.

(ii) *Enhanced confinement.* The helical shape from the pre-twist induces lateral compression in the fibrils, each composed of aligned CNTs, which promotes their lateral bond and is the reason for the source of increased ductility.

The fact that increasing twist leads to a progressive decrease in strength and stiffness, while markedly enhancing ductility, was already observed in [278, 285, 291] for different fiber yarns.

Here, the mechanism (i) of progressive inter-fibrillar load-transfer is proposed, arising from strain mismatch among helically-arranged fibrils. This non-uniform stress distribution was double-validated experimentally using a counterpart macroscopic physical model composed of twisted nylon filaments arranged in a strand geometry. It is worth mentioning that this rationale is fundamentally distinct from the traditional modeling of wound filaments, which are deliberately cut to different lengths to reduce strain mismatch: here, the mechanism is instead predicated on the strain mismatch generated between fibrils of *identical initial length.*

To account for the significant increase in ductility, hypothesis (ii) posits that the lateral confinement induced by the helical geometry alters the intrinsic tensile response of the fibrils, enhancing their behavior beyond what is observed in a straight configuration. Although the precise micromechanical origin of this effect remains speculative at this stage of the study, a parametric analysis is presented which considers various shapes of “constitutive continuation” for the tensile response of the fibrils, beyond the ultimate strain measured in untwisted fibers. The analysis indicates that plastic-like responses can provide predictions in excellent agreement with experimental results.

Recent studies on ultra-strong CNT clusters [85] and efforts to improve processing-structure-property relationships [6, 292] underline the importance of linking twist-induced architecture with macroscale performance.

The effect of twist on the mechanical response of a CNTF was investigated by modeling it as a compactly packed structure composed by clusters of nanotubes, idealized as cylindrical elements, arranged in concentric layers within the circular perimeter of the fiber. Upon twisting, each radial layer forms helices with different pitch angles. This structure leads to a progressive engagement of CNT clusters during axial loading: outer layers, being forced into longer helical paths, become prestressed and bear load earlier, while inner clusters remain unstressed until the fiber extends sufficiently. This leads to a decreasing of the axial stiffness of the fiber, as showed by experiments. This non-uniform stress distribution was double-validated experimentally using a counterpart macroscopic physical model composed of twisted nylon filaments arranged in a strand geometry. The resulting decrease in effective stiffness is consistent with experimental observations.

By integrating macroscopic testing with theoretical modeling, this work offers a mechanical interpretation of the twist-dependent properties of CNT Fibers, directly linking their macroscopic performance to the deformation of their underlying fibrillar architecture. The findings extend beyond fundamental mechanics, providing a solid foundation for the rational design of advanced hierarchical fiber structures and improving the understanding of the tensile behavior of twisted CNTF bundles, from which this investigation originated.

By tuning pre-twist, the mechanical properties of the fundamental CNT Fiber building block can be programmed, enabling the bottom-up engineering of macroscale materials for structural applications with improved damage tolerance and energy absorption capacity [132, 293].

6.1 Experimental evidence

This section describes the materials and methods for the tensile testing of individual pre-twisted CNT Fibers. The analysis of their multi-filament structure, confirmed by scanning electron microscopy, forms the basis of the present analysis.

6.1.1 Materials

The CNT Fibers examined in this study were fabricated via wet solution spinning. The precursor material consisted of a blend of polydisperse Single-Wall and Few-Walled CNTs, characterized by a high length-to-diameter aspect ratio exceeding 4.5×10^3.

The CNTs were dissolved in chlorosulfonic acid (CSA), a superacid capable of forming true solutions at concentrations up to 5000 ppmw without requiring surfactants or sonication, thereby preserving CNT length and minimizing damage. Due to the high aspect ratio of the CNTs, these solutions exhibit a liquid crystalline behavior, which facilitates excellent alignment during spinning. The wet spinning process [140] involved extruding the CNT-CSA solution through a spinneret into a coagulation bath, where the filament rapidly solidified. Continuous collection on a rotating drum under tension promoted axial alignment and densification of the CNT clusters.

The resulting anthracite-colored continuous filaments exhibited an approximately circular cross-section with a diameter of $24 \pm 1\,\mu$m and a linear density of 0.65 ± 0.05 tex. High-resolution scanning electron microscopy (SEM) and focused ion beam (FIB) cross-section imaging [140] revealed a densely packed internal morphology with minimal voids and a high degree of CNT cluster alignment. This alignment was further confirmed by wide-angle X-ray diffraction (WAXD), which yielded Herman orientation factors up to 0.996.

The solution spinning method employed in this work, utilizing a high-purity CSA-CNT solution, demonstrates significant advantages by decoupling CNT growth from fiber formation. Unlike direct spinning or array spinning methods, which often require specialized synthesis and tolerate lower crystallinity or higher impurity levels, solution spinning allows for the use of a broad range of CNT types, provided they meet stringent crystallinity and aspect ratio requirements [6]. This approach also offers excellent scalability.

Consequently, the fibers investigated are representative of state of the art Solution-Spun Carbon NanoTube Fiber (SS-CNTF) technology.

6.1.2 Tensile response of twisted CNT Fibers

The CNT Fibers were pre-twisted and subjected to tensile testing. The experiments were performed with a TesT 112.2kN Universal Testing Machine, equipped with a TesT 307.100N load cell, displayed in Figure 6.1(a). The pre-twist was applied by subjecting the lower clamp, and hence the fiber, to a controlled number of full rotations by means of a dedicated 3D-printed twisting mechanism, shown in Figure 6.1(b).

In detail, each fiber specimen, of length 350 mm, was first secured in the upper clamp, then the fiber was wrapped three times around a cylindrical guide (indicated by the blue circle in Figure 6.1(b)) and routed downwards toward the lower clamp; the fiber was then wrapped three times around the cylindrical guide of the lower clamp (green circled in Figure 6.1(b)) and finally secured. The distance between the top and bottom guides was fixed at 150 mm. Upon applying the controlled pre-twist, which changed the length of the fiber, care was taken to gradually adjust the position of the upper clamp to ensure a condition in which the axial load was always close to zero. All tests started from the condition of quasi-zero axial load (0.00 ± 0.02 GPa) and the tensile test was displacement-driven, until failure, at a speed of 1 mm/min.

Figure 6.2 shows the experimentally-derived engineering stress σ_f in the fiber as a function of the applied engineering strain ε_f for specimens subjected to increasing levels of pre-twist τ. The untwisted fibers showed an average tensile strength of 1.7 GPa and a tangent Young's modulus up to 110 GPa. The average elongation at break was 1.7%, with corresponding toughness values around 13 kJ/kg. Both tensile strength and stiffness progressively decrease at increasing twist level, while ductility (quantified by the elongation at breakage) increases significantly. For $\tau = 25.1$ rad/mm, the measured average tensile strength was 0.92 GPa, with corresponding ultimate elongation of 3.4% and a tangent Young's modulus at the origin of about 17 GPa. This observed trade-off

(a) (b)

Figure 6.1. Testing apparatus: (a) TesT 112.2kN Universal Testing Machine and (b) detail of the TesT 307.100N load cell and the clamps with the mechanism for application of pre-twist.

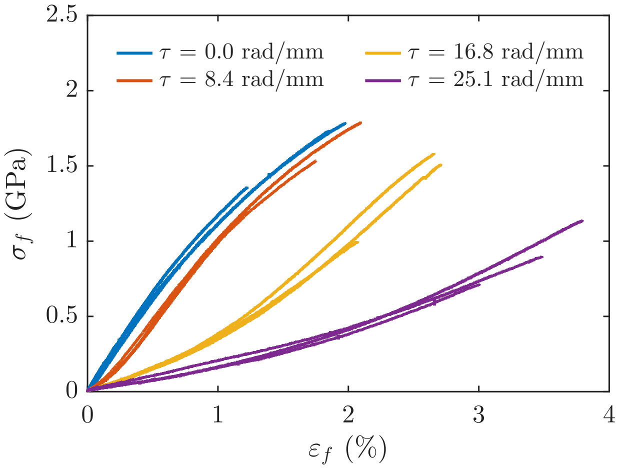

Figure 6.2. Tensile response of twisted CNT Fibers: engineering tensile stress σ_f vs. engineering strain ε_f curves, for varying values of the pre-twist $\tau = 0.0$, 8.4, 16.8, 25.1 rad/mm.

motivated a search for its underlying mechanical origins.

6.1.3 Microscopy

Observations were made with a Jeol JSM-6400 Scanning Electron Microscope. Samples were prepared by mounting straight, twisted and kinked portions of the CNT Fibers

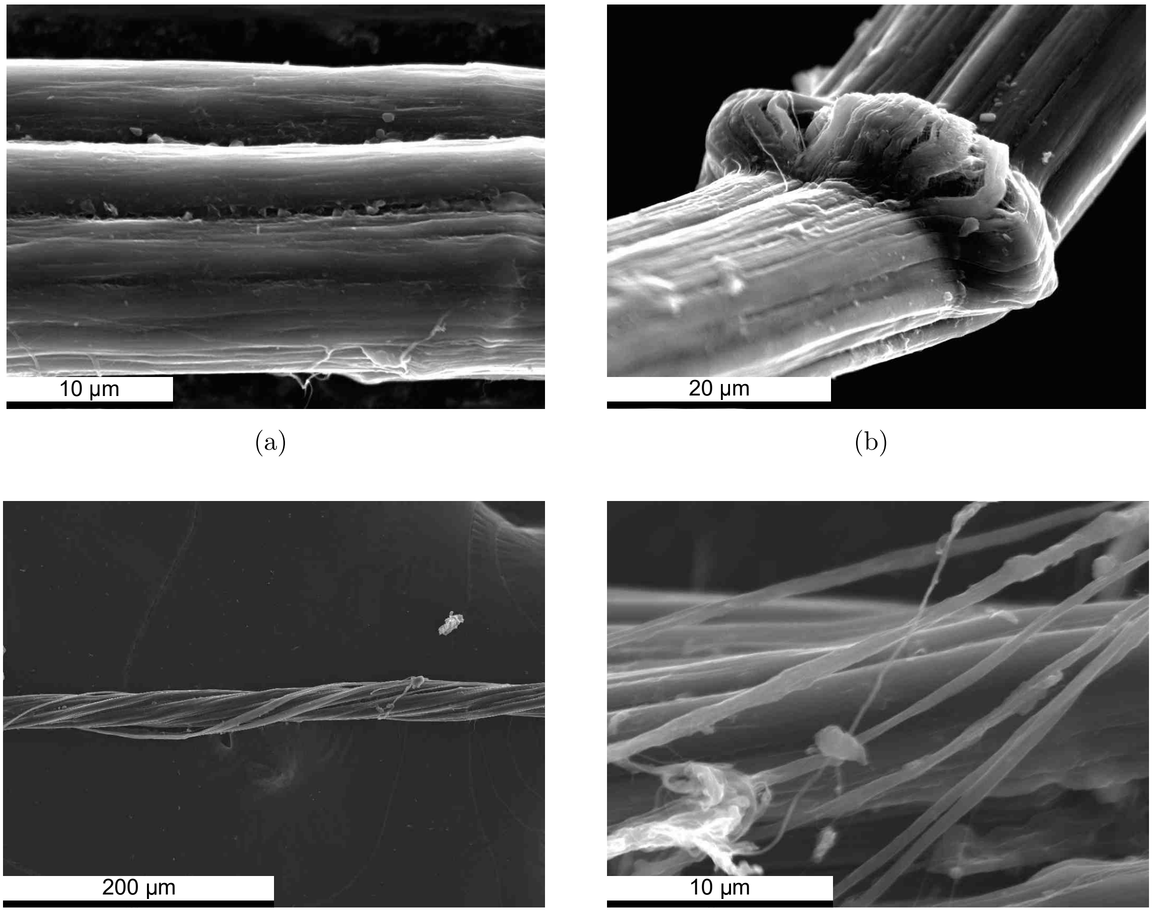

(a) (b)

(c) (d)

Figure 6.3. Scanning electron microscopy images of CNT Fibers: (a) fiber lateral surface morphology in the natural unstressed state; (b) kinked CNT Fiber shows the fibrillar structure; (c) a pre-twisted CNT Fiber ($\tau = 16.2$ rad/mm) shows how the fibrils arrange into helical structures; (d) high magnification image of a twisted CNT Fiber indicates fibrils of diameter comprised between 0.1 μm and 1 μm.

onto a graphite tape substrate. To minimize charging effects, the samples were coated with a thin layer of conductive carbon via vapor deposition.

The micrographs reported in Figure 6.3 reveal key features of the CNT Fiber structure. The lateral surface, shown in Figure 6.3(a), exhibits a textured morphology, indicative of its composition from aligned CNT clusters, called *fibrils* in the sequel. This multi-filament organization becomes more distinct in Figure 6.3(b), representing a kinked portion of the fiber, because the strain localization causes the separation of individual fibrils. The application of a pre-twist, as shown in Figure 6.3(c), reorganizes the multi-filament structure into a well-defined helical architecture. The high-magnification image of Figure 6.3(d) indicates that these fibrils have diameters ranging from approximately 0.1 μm to 1.0 μm, with an average diameter of 0.6 μm.

These observations confirm that the fiber consists of highly-aligned filament-like substructures, consistent with prior literature [6]. The fibrils are weakly bonded, as their assembly can be effectively manipulated and loosened through controlled pre-twist.

6.1.4 Origin of the fibrillar morphology

The formation of the distinct fibrillar microstructure results from nanoscale phenomena that occur during wet spinning, as extensively documented in the literature. Rather than remaining uniformly dispersed throughout the fiber, CNTs tend to aggregate into fibrillar clusters, i.e., densely packed and aligned clusters that serve as the primary load-bearing units of the fiber.

The driving force for this aggregation is the van der Waals interaction between adjacent nanotubes, particularly the π-π stacking between their graphitic walls [140]. CNTs can be temporarily dissolved into a true solution of CSA due to protonation of their walls. However, during coagulation, when CSA is rapidly exchanged with a non-solvent, solubilization is reversed and CNTs reassemble into energetically favorable clustered states. This bundling is thermodynamically favorable because it reduces the interfacial area with the surrounding medium, minimizing the system's free energy [294].

In addition to intermolecular forces, the liquid crystalline nature of CNT-CSA solutions plays a critical role. Given their extremely high aspect ratio and stiffness, CNTs form lyotropic liquid crystalline phases, self-organizing into anisotropic, locally aligned domains. Upon extrusion and drawing, these domains elongate and merge, and lateral association is promoted, driving the formation of well-aligned fibrillar clusters [140].

The kinetics of fiber formation further reinforce this structure. Coagulation is extremely rapid: the bath immediately extracts CSA, causing rapid fiber solidification and preventing nanotubes from redistributing uniformly. As a result, the fibrillar morphology becomes kinetically "frozen" within the fiber. Focused ion beam and scanning electron microscopy analyses of cross-sections confirmed this behavior, showing densely packed yet distinct fibrils [6].

Far from being detrimental, this bundling (fibrillation) is important for achieving high-performance CNT Fibers. Both computational and experimental studies [90, 295] have demonstrated that efficient load transfer requires close contact and high alignment between CNTs, which are naturally achieved within fibrils. This hierarchical arrangement is reminiscent of biological fibrous systems, such as collagen or silk, where fibrillar architectures self-assemble to optimize mechanical properties. The present study investigates a previously unexplored consequence of fibrillation: the change of tensile properties in individual CNT Fibers induced by the application of a pre-twist.

6.2 The model

The proposed model conceptualizes the twisted CNT Fiber as concentric layers of helically-wound cylindrical fibrils, of equal initial length. To validate this conceptual approach, a physical analogue was fabricated and tested.

6.2.1 Theory

The model assumes that fibrils exhibit negligible torsional and bending stiffness compared to axial tensile stiffness, and provide no compression resistance due to slackening. A key hypothesis is that all fibrils share an initial equal length H_0; consequently, pretwist induces a helical shape that creates a differential projection along the fiber axis, leading to a length mismatch under tensile load. This focus on *initial length equality* fundamentally distinguishes the present approach from classical wound filament mechanics.

Let R_f indicate the radius of the CNT Fiber, assumed of circular cross-section and composed of $n \in \mathbb{N}$ concentric layers of mutually identical fibrils, as shown in Figure 6.4(a). Let $i = 0,1,\ldots,n$ be the index that identifies each layer, with $i = 0$ representing the central fibril and $i = n$ the outmost layer. Each layer consists of $m_i \in \mathbb{N}$ fibrils.

The number n of layers is estimated from the average fibril diameter $2R$ and R_f using the geometric relation

$$R = \frac{R_f}{2n+1}\,. \tag{6.2.1}$$

As shown in Figure 6.4(a), each layer i, for $i = 0,1,\ldots,n$, is located at a radial distance $r_i = 2iR$ from the center. The number m_i is calculated by dividing the layer circumference $2\pi r_i$ by the fibril diameter $2R$, and applying the floor function $\lfloor \cdot \rfloor$ to ensure an integer value, i.e.,

$$m_i = \left\lfloor \frac{2\pi r_i}{2R} \right\rfloor . \tag{6.2.2}$$

Since the center of the fiber ($i = 0$) contains a single fibril, m_0 is set to 1.

Let L_i represent the initial length of the fibrils in the layer i at the radial distance r_i. In the untwisted state, the fiber is a bundle of straight parallel fibrils aligned with the fiber axis, all of initial length $L_i = H_0$ for all r_i. Figure 6.4(b) evidences three fibrils at different radial distances. Tensile tests on the untwisted fiber are used to define the constitutive response of the fibrils. Let σ and ε respectively indicate the engineering stress and strain for the tensile-tested fiber, i.e.,

$$\sigma = \frac{F}{\pi R_f^2}\,, \quad \text{and} \quad \varepsilon = \frac{\delta H_0}{H_0}\,, \tag{6.2.3}$$

where δH_0 is the imposed elongation and F the corresponding tensile force. The measured response is fitted with the polynomial

$$\sigma = \sum_{j=0}^{g} p_{g-j}\, \varepsilon^{g-j} \,, \tag{6.2.4}$$

where $g \in \mathbb{N}$ is the polynomial degree and $p_{g-j} \in \mathbb{R}$ are the polynomial coefficients, with $j = 0, 1, \ldots, g$.

The experimental measurement can be extrapolated to obtain the constitutive response of the individual fibril in the layer i. For an untwisted fiber, made of straight fibrils, the elongation δL_i coincides with the fiber elongation δH_0, i.e., $\varepsilon = \delta L_i / L_i = \delta H_0 / H_0$, for $i = 0,1, \ldots, n$. Since the axial force F_i^* on the straight fibril is given by

$$F_i^* = \frac{F}{\sum_{i=0}^{n} m_i} \,, \tag{6.2.5}$$

from Eq. (6.2.4) one obtains

$$F_i^* = \sum_{j=0}^{g} c_{g-j}\, (\delta L_i)^{g-j} \,, \tag{6.2.6}$$

where

$$c_j = \frac{\pi R_f^2\, p_j}{H_0^{4-j} \sum_{i=0}^{n} m_i} \,, \quad \text{for } j = 0, 1, \ldots, g \,. \tag{6.2.7}$$

For a pre-twisted fiber, the helical shapes of the fibrils must be taken into account. If $\varPhi$ is the torsion angle imposed to the fiber, the twist per unit length is $\tau = \varPhi / H_0$. Based on microscopy evidence (Figure 6.3(c)), it is assumed that the fibrils become cylindrical helices, whose pitch is dictated by τ and r_i.

If the fiber length were constrained to remain at H_0 after the pre-twist, the helically-wound fibrils in outer layers ($r_i > 0$) would be forced to elongate to a length greater than H_0, with the fibrils at r_n being the longest. This would generate tensile stress in the fiber. To achieve a stress-free state after pre-twisting, the initial length H_0 of the fiber must be reduced to H, so that outermost fibrils retain their natural length $L_n = H_0$. However, this forces the inner fibrils to become slack since their length would be less than H_0 for $i < n$ and they are assumed unable to withstand compression loads. This scenario is schematically depicted in Figure 6.4(c), where the waviness of the lines corresponding to the inner fibrils indicates that they need to accommodate the fiber length H. The same Figure also reports the unraveled helices: the outermost fibril ($i = n$) forms a right triangle with hypotenuse $L_n = H_0$, while the hypotenuse of inner fibrils ($i < n$) is wavy, indicating their greater length.

The new reference length H, corresponding to the zero axial load condition at the beginning of the test, can be calculated from geometric considerations as

$$H = \sqrt{H_0^2 - (\varPhi R_f)^2} \,. \tag{6.2.8}$$

The axial elongation δH of the twisted fiber induces a variation of the length of the helical path of the fibers in the i-th layer at r_i given by

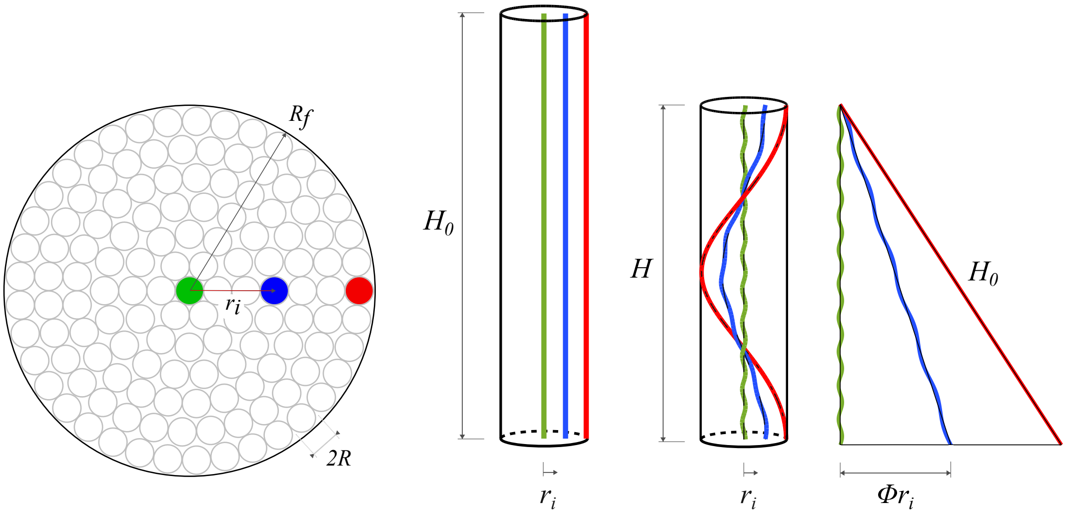

(a) (b) (c)

Figure 6.4. Schematic representation of filament structure of the CNT Fiber: (a) idealized cross-section composed of cylindrical fibrils arranged in concentric layers of radius r_i, around one central fibril; (b) un-twisted initial state, with indication of three different fibrils, co-planar with the axis, at three different distances from the center; (c) stress-free configuration after pre-twist, in which the external fibrils keep their initial length and the inner ones slacken, juxtaposed to the triangular shapes of unraveled helices.

$$\delta L_i = \sqrt{(H+\delta H)^2 + (\Phi r_i)^2} - H_0 \,. \tag{6.2.9}$$

The quantity δL_i can be either positive or negative, depending on the values of radius r_i, fiber elongation δH and twist angle Φ. Consistent with the model assumptions, a fibril only contributes stress when taut, meaning that the force F_i carried by the fibrils of the i-th layer reads

$$F_i = \begin{cases} 0\,, & \text{if} \quad \delta L_i \leq 0\,, \\ F_i^*(\delta L_i)\,, & \text{if} \quad \delta L_i > 0\,, \end{cases} \tag{6.2.10}$$

where $F_i^*(\delta L_i)$ is the constitutive relation for the fibril, defined by the polynomial fit in Eq. (6.2.6).

The helix angle α_i of the taut fibrils in the layer i can be calculated as

$$\alpha_i = \arctan\left(\frac{H+\delta H}{\Phi r_i}\right)\,, \tag{6.2.11}$$

with $\alpha_0 = \pi/2$ for the central fibril $i = 0$. The overall axial force F_f in the twisted fiber can be obtained by summing up the forces carried by all the fibrils. Considering that only the component of F_i on the fiber axis contributes to F_f, one obtains

$$F_f = \sum_{i=0}^{n} m_i \, F_i \, \sin(\alpha_i) \,, \tag{6.2.12}$$

with F_i given by Eq. (6.2.10). Consequently, the stress and strain in the fiber read

$$\sigma_f = \frac{F_f}{\pi R_f^2} \,, \quad \varepsilon_f = \frac{\delta H}{H} \,. \tag{6.2.13}$$

To summarize, once the tensile response of the untwisted fiber has been experimentally determined, the proposed theory allows predicting the tensile response of the twisted fiber in terms of stress σ_f and strain ε_f, based on the observation that the fibrils are progressively engaged from the outer layer towards the center as the fiber is increasingly stretched.

6.2.2 The physical analogue

A macroscopic physical analogue was fabricated and tested to validate strain mismatch between fibrils as a core principle of the theoretical model. In the prototypes, fibrils are made with nylon filaments with a circular cross-section (0.32 mm diameter) and a linear density of 92.5 tex.

The tensile response was first measured on individual filaments. Figure 6.5(a) shows how the nylon filament was secured in custom metallic clamps using cyanoacrylate adhesive. A bundle of parallel nylon filaments (Figure 6.5(b)) was also tested, to represent the macroscopic analogue of the untwisted CNT Fiber.

The bundle was fabricated using the following procedure. Nylon filaments were inserted into a 3D-printed alignment template, i.e., a plate with holes reproducing the fiber's cross-sectional arrangement. One end of the bundle was glued with cyanoacrylate adhesive and secured in a custom 3D-printed clamp. A knot was then tied to compact the bundle of filaments, while the template was carefully slid along the bundle to ensure perfect alignment and prevent tangling, as shown in Figure 6.5(c). The alignment template plate and the clamp, composed of two mating parts, are shown in 6.5(d) and in Figure 6.5(e), respectively. After completing the alignment, the free end was inserted in one half of the clamp (Figure 6.5(f)), glue was poured in, and the second half was placed to complete the assembly. The cross-sectional view of Figure 6.5(g) shows the position of the filaments inside the clamp after the adhesive cured, confirming their arrangement into approximately concentric circular paths.

Application of the theoretical model to this case, as per the scheme in Figure 6.4(a), yields a physical analogue consisting of one central fibril ($i = 0$), a mid-layer ($i = 1$) of six fibrils, and an outer layer ($i = n = 2$) of twelve fibrils.

Tensile tests were conducted using a Chatillon TCD225 Series Force Measurement System with a TLC-0200 load cell, shown in Figure 6.6(a), as the testing machine used for CNT Fiber tests (Figure 6.1(a)) could not accommodate the required higher full scale. All tests were displacement-driven at a speed of 10 mm/min until failure. Pre-twisting was achieved using the method described in Figure 6.1(b), which involved

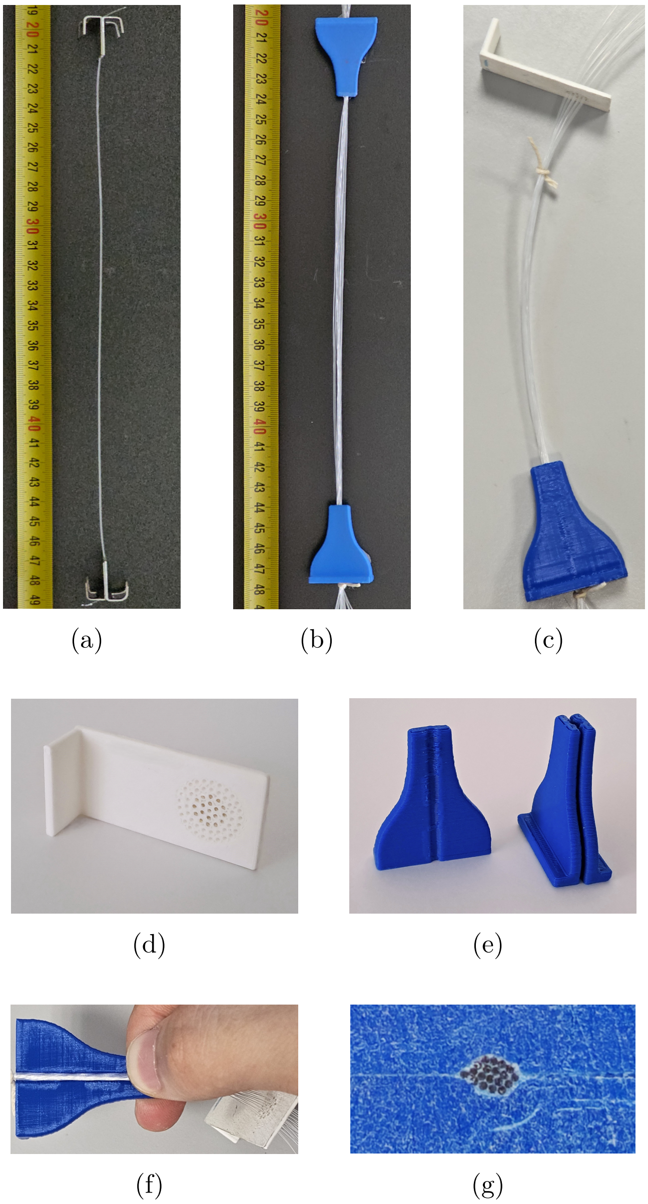

(a) (b) (c)

(d) (e)

(f) (g)

Figure 6.5. The macroscopic physical analogue made of nylon filaments: (a) single filament with custom clamps for tensile testing, and (b) bundle composed of 19 parallel nylon filaments. Preparation of the samples: (c) filaments are inserted into the alignment template, one end is glued and secured with custom clamps, a small knot is tied to compact the bundle while the template is slid to assure alignment; (d) detail of the 3D-printed alignment template; (e) detail ofthe 3D-printed custom clamps composed of two parts; (f) the free ends of the filaments are inserted in one of the mating halves of the clamp and glued; (g) cross-sectional view showing the filaments inside the clamp after glue curing.

applying a prescribed number of turns to the lower clamp. A representative twisted specimen is shown in Figure 6.6(b), with detailed views of its geometry before and after twisting provided in Figure 6.6(c) and 6.6(d), respectively. All tests commenced from a condition of quasi-zero axial load ($0.0 \pm 0.2\,\mathrm{N}$).

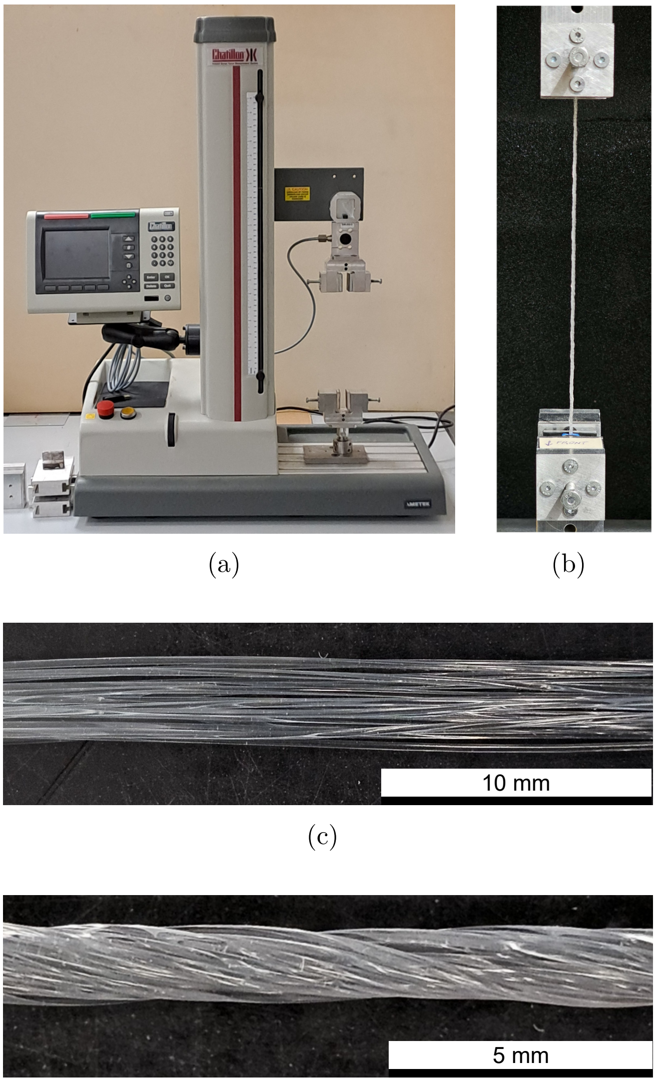

(a) (b)

(c)

(d)

Figure 6.6. Experimental set-up for the physical analogue. (a) Chatillon TCD225 Series Force Measurement System, equipped with a TLC-0200 load cell; (b) a twisted nylon filament bundle mounted in the clamps; close-up view of the bundle in its (c) initial untwisted and (d) final pre-twisted configurations.

The stress-strain response of the untwisted bundle was initially measured. As shown in Figure 6.7(a), the results were highly repeatable and are presented alongside a fifth-degree polynomial approximation of the form given in Eq. (6.2.4). The coefficients for least-squares fit are provided in Table 6.1. Additional tests were conducted on *individual* twisted filaments. Even under an applied twist of $\tau \approx 0.77\,\mathrm{rad/mm}$, comparable to that later applied to the bundle, the curves showed negligible deviation. This result confirms that twist has a minimal effect on the tensile response of the single filament (fibril scale), which can be overlooked.

coefficient	value $\times 10^6$
p_0	0.0000 MPa
p_1	0.0023 MPa
p_2	−0.0328 MPa
p_3	0.3982 MPa
p_4	−1.6240 MPa
p_5	2.4702 MPa

Table 6.1. Coefficients of the least-squares polynomial fitting for the stress-strain curve of the untwisted bundle made of nylon filaments.

Figure 6.7(b) compares the experimentally-measured response of the twisted macroscopic bundle with predictions from the theoretical model presented in Section 6.2.1. The model uses the polynomial approximation of the constitutive law of the nylon filament as input. The excellent agreement between experiments and theory validates the proposed mechanical interpretation of twisted fibers composed of initially parallel filaments.

The macroscopic scale of the physical analogue provided a visual representation of the mechanism of load transfer. During twisting, the filaments form helical arrangements. Under tension, the outer filaments, due to their shorter effective axial length, engage first, while the inner filaments remain slack. The progressive engagement of these inner filaments with increasing axial elongation produces a nonlinear stress-strain response characterized by a gradually increasing tangent elastic modulus.

Notably, macroscopic failure occurred when the filaments in the outermost layer ($i = 2$) reached the failure strain of a single filament. This can be recognized from the comparison of Figure 6.7(b) with Figure 6.7(a).

The successful validation using a nylon-filament analogue demonstrates the effectiveness of the model in Section 6.2.1, supporting its application to pre-twisted CNT Fibers. Interpreting their behavior, however, requires a further step, detailed in the next section.

6.3 Interpretation of experiments on CNT Fibers

The tensile response of pre-twisted CNT Fibers is interpreted using the theoretical model described in Section 6.2. The geometry is defined according to the microscopy observations of Section 6.1.3, with the number of layers set to $n = 20$ and the fibril diameter to 0.6 µm.

The model operates on the premise that fibrils in different layers are progressively engaged under tension. However, while experiments on the nylon-filament analogue

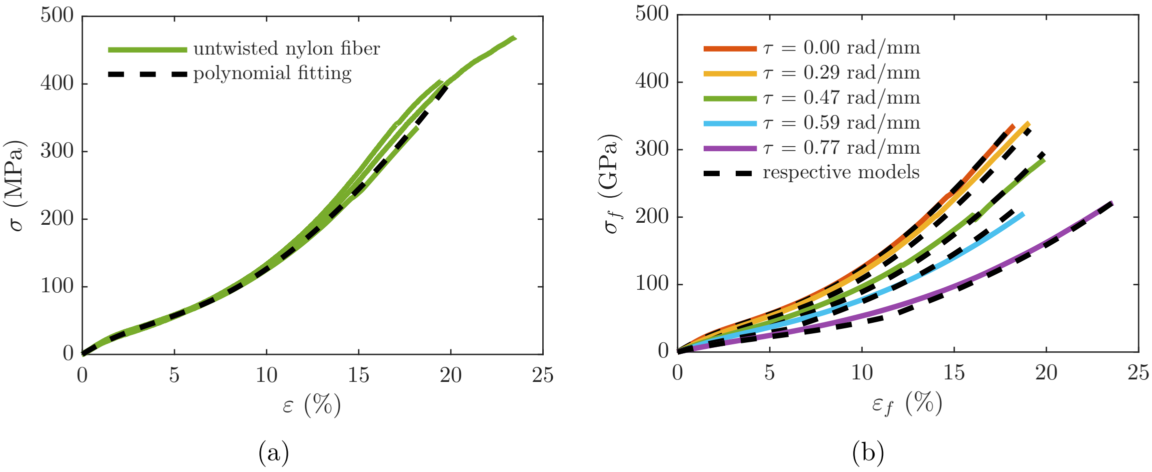

(a) (b)

Figure 6.7. Tensile response of the physical analogue. Experimentally-measured stress-strain curves for (a) the untwisted nylon bundles (experimental data and fifth-degree polynomial best-fit) and (b) the pre-twisted bundles (experimental results and theoretical prediction from the model).

showed that failure occurred once the most-strained outer layers reached the failure strain of a single filament, pre-twisted CNT Fibers exhibit a significantly higher failure strain. The underlying reason for this enhanced ductility remains conjectural at this stage, but it may be attributed to the helical configuration, which promotes lateral confinement as the fiber is pulled. It is well established [7, 296] that CNT Fibers consist of nanotubes in lateral contact, which can be interpreted [297] within the broad paradigm of cohesive-frictional adherence, combined with conservative forces of attraction. It is hypothesized that the centripetal pressure generated by helically wound fibrils during elongation enhances lateral bonding between CNTs, thus increasing the strain capacity. This mechanism improves the ductility of the fibrils, a phenomenon that needs to be taken into account in the model of Section 6.2.1.

Figure 6.8 reports the fibrillar force F_i^* vs. fibrillar displacement δL_i curves, derived from the experimentally-measured response of the untwisted fibers according to the procedure detailed in Section 6.2.1. These results are interpolated with a third-degree polynomial fitting as defined in Eq. (6.2.6), for which the coefficients are collected in Table 6.2. For this interpolation, an ultimate elongation of $\delta\bar{L} = \bar{\varepsilon} H_0 = 2.596\,\mathrm{mm}$ is estimated. A post-critical constitutive continuation beyond $\delta\bar{L}$ is considered for the helically wound fibrils, evaluated using four distinct constitutive behaviors, as detailed below.

i. **Failure model.** The fibrils undergo immediate failure when the elongation limit is exceeded:

$$F_i = \begin{cases} 0\,, & \text{if} \quad \delta L_i \le 0\,, \\ F_i^*(\delta L_i)\,, & \text{if} \quad 0 < \delta L_i \le \delta\bar{L}\,, \\ 0\,, & \text{if} \quad \delta L_i > \delta\bar{L}\,. \end{cases} \tag{6.3.14}$$

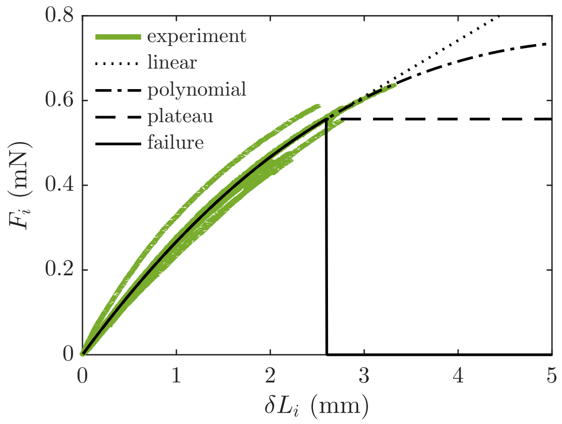

Figure 6.8. Tensile response of the CNT fibril in the i-th layer: experimentally-derived fibrillar tensile force F_i vs. fibrillar elongation δL_i curves (obtained from different tests on untwisted fibers), and least-square-fitted third-degree polynomial, with four different continuations beyond the limit $\delta\bar{L} = 2.596\,\text{mm}$.

ii. **Plateau model.** The fibrils carry a constant load after the elongation limit:

$$F_i = \begin{cases} 0\,, & \text{if} \quad \delta L_i \le 0\,, \\ F_i^*(\delta L_i)\,, & \text{if} \quad 0 < \delta L_i \le \delta\bar{L}\,, \\ F_{lim}\,, & \text{if} \quad \delta L_i > \delta\bar{L}\,, \end{cases} \tag{6.3.15}$$

where $F_{lim} = c_3\delta\bar{L}^3 + c_2\delta\bar{L}^2 + c_1\delta\bar{L} + c_0$ is the force at the strain limit.

iii. **Linear continuation model.** The fibrils show a linear response after the critical elongation, whose slope is determined by the tangent line at the elongation limit:

$$F_i = \begin{cases} 0\,, & \text{if} \quad \delta L_i \le 0\,, \\ F_i^*(\delta L_i)\,, & \text{if} \quad 0 < \delta L_i \le \delta\bar{L}\,, \\ F_{lim} + k(\delta L_i - \delta\bar{L})\,, & \text{if} \quad \delta L_i > \delta\bar{L}\,, \end{cases} \tag{6.3.16}$$

where $k = 3c_3\delta\bar{L}^2 + 2c_2\delta\bar{L} + c_1$ is the slope of the tangent line at $\delta L_i = \delta\bar{L}$.

iv. **Polynomial continuation model.** The fibrils follow the original polynomial fitting beyond the elongation limit:

$$F_i = \begin{cases} 0\,, & \text{if} \quad \delta L_i \le 0\,, \\ F_i^*(\delta L_i)\,, & \text{if} \quad \delta L_i > 0\,. \end{cases} \tag{6.3.17}$$

Figure 6.9 compares the theoretical predictions with the experimentally-measured tensile response of CNT Fibers for different pre-twist values ($\tau = 8.4, 16.8, 25.1\,\text{rad/mm}$). In all cases, the model accurately captures the twist-induced reduction in axial stiffness up to the point where the critical elongation $\delta\bar{L}$ is reached in the outer-layer fibrils. Beyond this point, the *failure* continuation model predicts a strain-softening

coefficient	value $\times 10^{-4}$
c_0	$0.0000\,\mathrm{N}$
c_1	$3.0412\,\mathrm{N/mm}$
c_2	$-0.3804\,\mathrm{N/mm^2}$
c_3	$0.0132\,\mathrm{N/mm^3}$

Table 6.2. Coefficients of the polynomial fitting for the force-elongation curves.

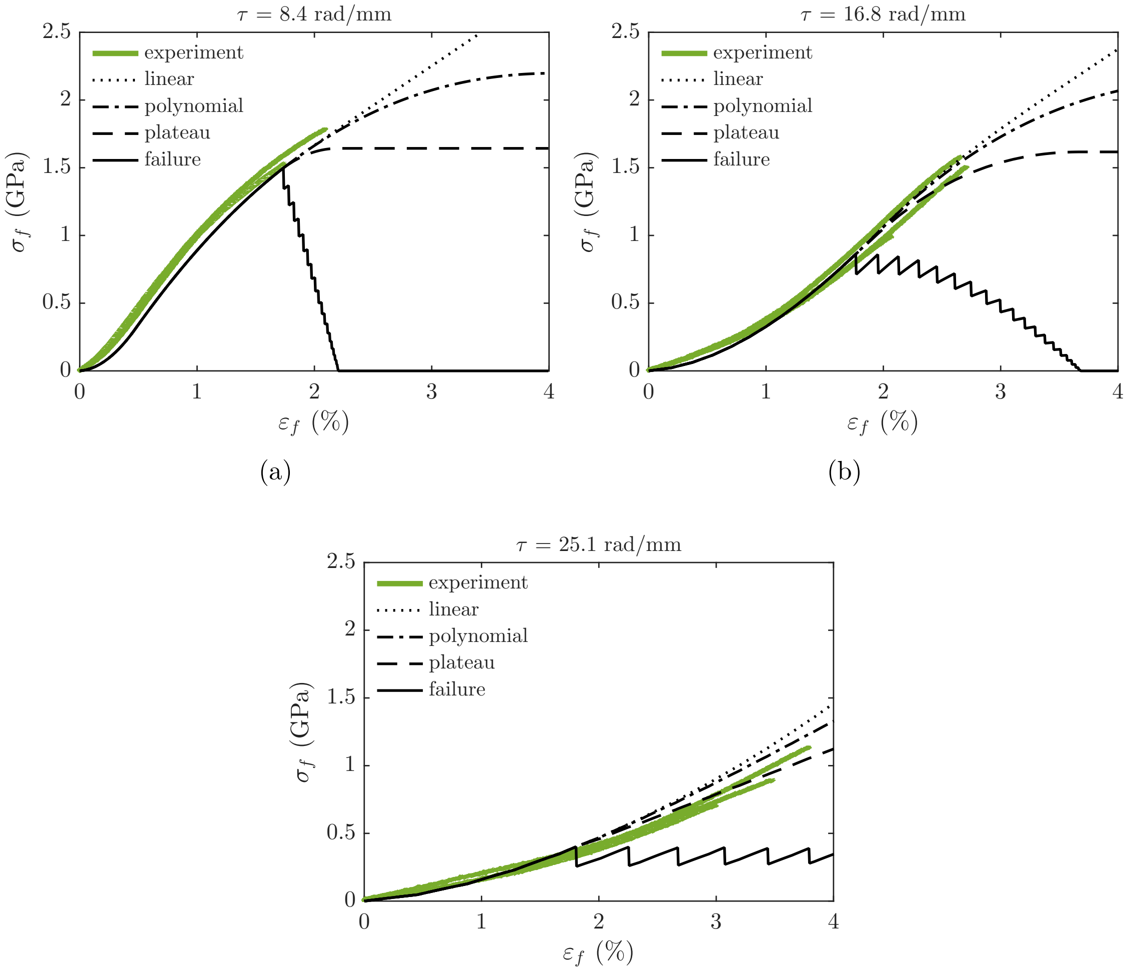

(a)

(b)

(c)

Figure 6.9. Experimentally-measured tensile response of twisted CNT Fibers compared with the results from the theoretical model for different values of pre-twist: (a) $\tau = 8.4\,\mathrm{rad/mm}$, (b) $\tau = 16.8\,\mathrm{rad/mm}$, (c) $\tau = 25.1\,\mathrm{rad/mm}$.

response accompanied by oscillations resulting from the progressive failure of fibrils from the outer to inner layers. Although this trend is not experimentally observed, the peak stress aligns with experimental results for $\tau = 8.4\,\mathrm{rad/mm}$ (Figure 6.9(a)).

The *linear* continuation model generally overestimates the fiber stiffness, particularly at higher values of τ. The best agreement is achieved with the *plateau* and *polynomial* continuation models. For the highest twist angle, the plateau model provides the most accurate fit. In general terms, the curves for $\tau = 16.8\,\text{rad/mm}$ (Figure 6.9(b)) and $\tau = 25.1\,\text{rad/mm}$ (Figure 6.9(c)) confirm that the fibrils do not fail abruptly at the critical elongation $\delta\bar{L}$ but continue to carry load. This indicates that twisting enhances ductility, even though it reduces both global axial stiffness and failure load due to the mechanism of progressive engagement of the fibrils.

The agreement between experimental data and model predictions further supports the hypothesis that the mechanical behavior of CNT Fibers is governed by their hierarchical twist-induced helical structure. The proposed model represents a useful basic framework for understanding and designing twisted-CNT-Fiber-based materials.

6.4 Discussion

Tensile experiments on pre-twisted CNT Fibers show a decay in axial strength and stiffness with increasing applied twist, accompanied by a substantial increase in ductility. This trade-off is explained by considering, as confirmed by microscopy observations, that the fiber is composed of weakly bonded CNT clusters (fibrils). These are parallel to each other in the untwisted state, and arrange into concentric helices upon twisting. A model has been proposed, based on the axial strain mismatch in the fibrils resulting from pre-twist. This causes them to become progressively engaged, from the outer to the inner layers, as the fiber is elongated. This concept is demonstrated using a macroscopic physical analogue made of nylon filaments. However, to accurately reproduce the experimental results, it is necessary to account for the fact that single fibrils exhibit an apparent increase in ductility when in a helical configuration. Without this, the model would predict an ultimate elongation far below experimental findings, with the discrepancy increasing at higher twist angles. To address this, a parametric analysis using constitutive continuation models with various shapes has been presented, concluding that plastic-like responses can provide excellent agreement between the experimental data and theoretical predictions.

The enhanced elongation capacity of fibrils beyond the limit observed in untwisted material is attributed to centripetal pressures induced by their helical geometry under increasing tension. This confinement likely enhances the effective shear transfer between the Carbon NanoTubes that form each fibril. Although this explanation remains conjectural at present, it holds significant importance for the design of high-performance structural cables made from CNT Fibers and merits further investigation in future work.

Despite its limitations, this study provides a foundation for better understanding load-sharing mechanisms in twisted CNT Fibers, offering a basis for engineering CNT-Fiber-based structures under combined loading conditions and for optimizing their design. The findings establish a foundational framework for rationally designing advanced hierarchical structures since, by strategically controlling pre-twist, the properties of CNT Fibers can be tailored, guiding the bottom-up engineering of superior macroscale cables for structural applications. The results indicate that while the fundamental mechanics of twisted CNT Fibers has been elucidated, the material exhibits complex ductility behavior that warrants further investigation.

The work discussed in this chapter has been summarized in a manuscript submitted to Soft Matter (Royal Society of Chemistry). The manuscript has undergone peer review, and comments from the referees and the editor have been received.

Chapter 7

Integration of CNTFs into Carbon Fiber composites for enhanced anti-intrusion performance

Carbon NanoTube Fibers represent an emerging class of reinforcement for advanced composite materials, offering a unique combination of high strength, toughness, and multifunctionality. Their integration into Carbon Fiber (CF) laminates is particularly attractive for applications where both structural performance and additional functionalities, such as electrical conductivity or energy absorption, are required. This chapter presents a comprehensive experimental and analytical study on the development and characterization of hybrid CNTF/CF composites, with a focus on anti-intrusion performance for high-value applications in the automotive and aerospace sectors. The research methodology followed a structured approach, beginning with a proof-of-concept literature review and comparative analysis, progressing through parametric optimization of baseline CF laminates, and culminating in the design, fabrication, and testing of hybrid CNTF/CF specimens. The experimental campaign was specifically designed to evaluate the penetration resistance of these novel hybrid composites simulating anti-intrusion scenarios.

7.1 CNTFs vs. commercial fibers for structural reinforcement

The mechanical data reported for various reinforcement fibers are predominantly expressed in terms of tensile strength and stiffness. In these parameters, CNTFs exhibit a remarkably wide range of values, primarily dictated by the specific production method. For instance, wet-spun CNTFs are typically characterized by functional properties rather than the superior tensile performance observed in dry-spun CNTFs [54, 136]. It is important to note, however, that the wet-spinning technique is continuously achieving rapid technological progress [127].

7.1.1 Material properties and performance potential

What makes CNTFs attractive for structural applications is their possession of distinctive bending, twisting, and shear characteristics that fundamentally differ from those of conventional fibers: knot tests on 10-filament CNTF bundle (Figure 7.1) have demonstrated exceptionally high shear and flexural strength, often retaining up to 70% of their original tensile strength when knotted, as shown in Figure 7.2. Furthermore, their pronounced ductility indicates a high degree of resilience, suggesting a strong potential for applications requiring enhanced damage tolerance and impact resistance.

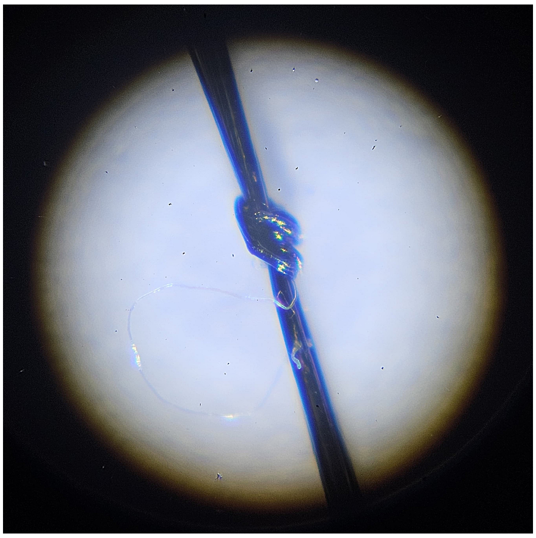

Figure 7.1. Magnification of a knotted untwisted 10 filaments CNTF bundles.

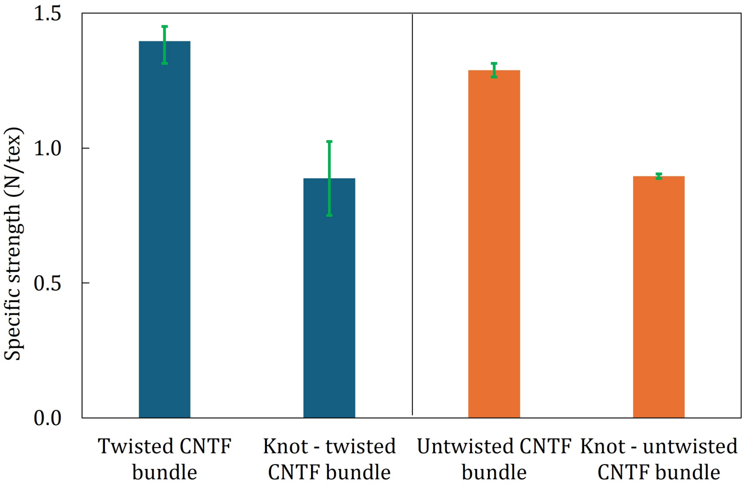

Figure 7.2. Comparison of maximum specific strength values obtained from knotted, twisted, and untwisted 10-filament CNTF bundles..

Resilience, flexibility, and high shear resistance, render CNTFs compelling candidates for advanced anti-intrusion applications. These characteristics are of paramount importance in sectors where performance and safety justifies a higher material cost, such as in motorsports and aerospace engineering.

A promising implementation involves the strategic integration of CNTFs as interleaves between plies of conventional Carbon Fiber composites. This architectural approach aims to develop next-generation anti-intrusion panels and energy-absorbing structures with enhanced damage tolerance. A proposed strategy to enhance the crashworthiness of components like winglets involves the embedding of CNTF grids within the composite laminate. This approach could mitigate the inherent brittleness of Carbon Fiber composites by promoting a transition in the failure mode. The CNTF grid could potentially act as a bridging phase, inhibiting crack propagation and preventing catastrophic shattering, thereby leading to improved structural integrity and energy absorption upon impact. This is critically relevant for high-performance scenarios, including Formula and IndyCar racing, where component failure poses significant safety risks.

Furthermore, the multi-functional nature of CNTFs enables their use in systems that concurrently bear structural loads and transmit data or electrical current. CNTF-based cables can be embedded within a composite matrix to create integrated structural health monitoring networks or power distribution pathways, thereby reducing system weight and complexity while adding smart functionality. This convergence of structural and functional capabilities is particularly advantageous for aerospace applications, such as in satellite shielding against micrometeoroid and orbital debris (MMOD) impacts, where every component must be mass-optimized and multipurpose.

A comprehensive benchmarking of CNTFs against conventional high-performance fibers, including Carbon Fibers (CF), aramid (Kevlar), and ultra-high molecular weight polyethylene (Dyneema), was conducted, leveraging an extensive review of literature and commercial datasheets [6, 124, 136, 147–160].

The analysis of high-performance fibers reveals a consistent trade-off between mechanical properties and practical limitations such as cost, environmental resistance, or manufacturability. Carbon Fiber stands out for its versatile balance of specific strength and stiffness, alongside good thermal and chemical resistance, though its brittleness under impact and high production cost remain constraints. Similarly, Kevlar and Dyneema offer exceptional tensile strength and durability, with the latter providing superior strength-to-weight ratio and UV resistance, yet both exhibit vulnerabilities: Kevlar to UV degradation and Dyneema to elevated temperatures. [147–153, 155, 298, 299]. More specialized materials like Zylon and Vectran demonstrate superior strength and stability, but their high cost and susceptibility to UV radiation limit widespread adoption. Quartz offers excellent thermal and chemical stability but suffers from high density, while Glass Fiber provides a cost-effective alternative with good corrosion resistance, albeit with penalties in weight and impact tolerance. Conversely, bio-based

Fibers like Flax offer sustainability and biodegradability but are limited by lower mechanical strength and moisture sensitivity. Innegra, valued for impact resistance and vibration dampening, fills a niche in hybrid composites but lacks the recognition and absolute strength of established synthetic fibers. CNTF present unparalleled strength, flexibility, electrical conductivity, and very high temperature resistance. [6, 136, 154, 156–160, 298, 299].

In summary, the selection of a high-performance fiber is inherently application-dependent, requiring careful consideration of the specific mechanical, environmental, and economic requirements. A comparison of specific strength (y-axis) versus modulus (x-axis) across various high-performance fiber classes is presented in Figure 7.3 according to the paradigm advocated by Ashby [300]. Unlike conventional high-performance fibers, such as CF, Kevlar, and Dyneema, which occupy well-defined and clustered performance ranges (indicated by the shaded areas), CNTFs exhibit highly scattered values (the red shaded area). This significant variability across the CNTF data points is directly related to the producer or research group, the specific fabrication method (e.g., wet-spun vs. dry-spun), and the processing history. This wide scatter indicates that the CNTF technology is still in a rapid development phase, unlike the mature conventional fiber industry. Critically, the upper range of reported CNTF performance, particularly those reaching above 4 N/tex in laboratory reports [136], suggests an high potential. The experimental results from Seoul National University and KAIST [136], published in *Nature*, are particularly notable, reporting a maximum tensile strength of 4.44 N/tex and average values of 4.08 N/tex (indicated by the top red line in the graph), effectively surpassing any other known fiber plotted in terms of specific strength, including the highest-grade Carbon Fibers and Dyneema (e.g., T1100G and SK99). However, it is imperative to note that these outstanding results are derived from laboratory-scale experiments, and the high performance values, while demonstrating ultimate potential, remain difficult to reproduce consistently on an industrial scale, posing a key challenge for commercial market penetration.

7.2 Parametric optimization of Carbon Fiber laminates

A systematic parametric study was conducted to establish the optimal baseline configuration for CF laminates before introducing CNTF reinforcement. The investigation encompassed multiple variables to identify the most effective configurations for anti-intrusion applications, including:

- fiber type and modulus (standard, intermediate, high modulus);
- resin type (epoxy, thermoplastic, toughened resins);
- areal weight (gram/square meter - gsm) of the Carbon fabric;
- fiber-to-resin volume fraction;

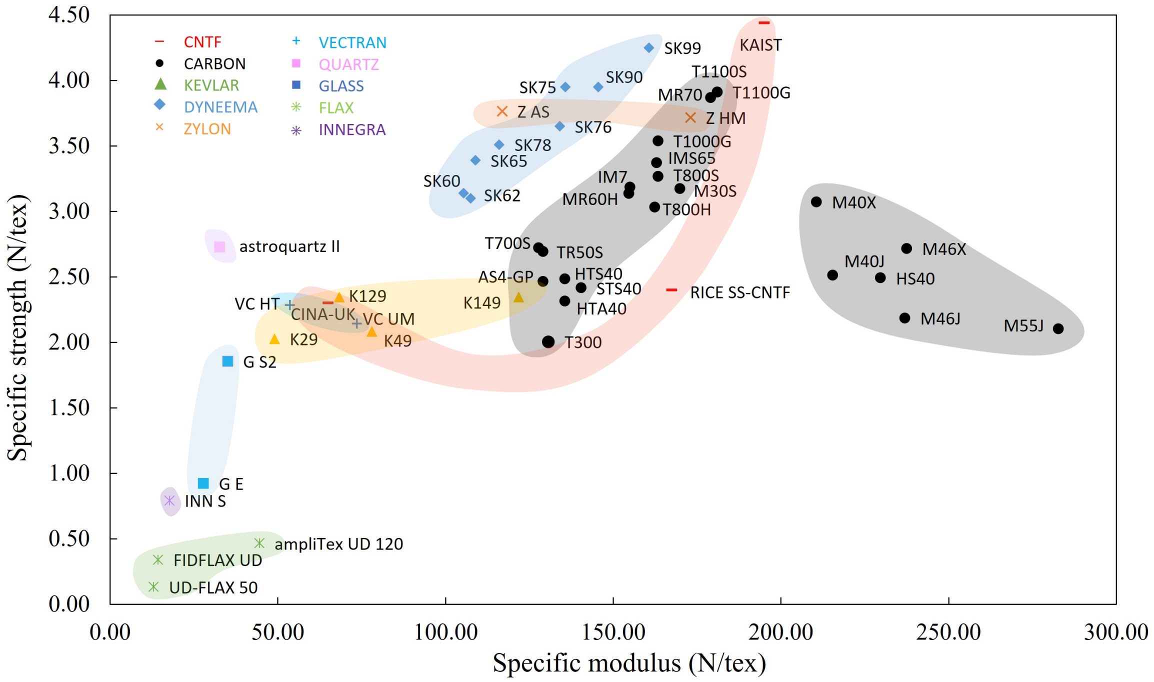

Figure 7.3. Comparison of specific strength versus specific modulus for CNTFs and conventional high-performance fibers: Carbon, Kevlar, Dyneema, Zylon, Quartz, Vectran, Glass, Flax, and Innegra [6, 124, 136, 147–160].

- weave type (plain, twill, unidirectional);
- fiber orientation and stacking sequence;
- number of plies and total thickness;
- curing cycle (temperature, pressure, dwell time).

The objective was to identify combinations of parameters that improve penetration resistance while maintaining acceptable weight.

7.2.1 Testing protocol and evaluation methodology

To assess the anti-intrusion performance of the materials, penetration tests were carried out and compared with reference data from conventional CF laminates. The measured load was normalized by the indented lateral surface of the specimen, calculated as the product of the laminate thickness and the indenter perimeter. This quantity, which has the dimension of stress, represents an indicator of the out-of-plane shear stress components $\sigma_{13} = \sigma_{23}$, illustrated in Figure 7.4 for a representative unit cell of CF 2D laminated composite. This parameter will be denoted as $\sigma_{\text{dir.3}}$ to emphasize that it refers to the out-of-plane direction. To enable a fair comparison between materials

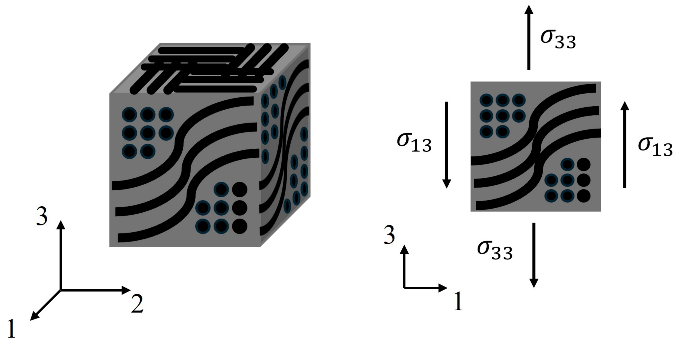

Figure 7.4. Unit cell of a composite material and corresponding out-of-plane stress components along the 1–3 plane.

Figure 7.5. MTS Insight 150 kN testing machine with dedicated fixture for penetration tests.

with different densities, $\sigma_{\mathrm{dir.3}}$ was further divided by the specimen density ρ, providing a specific stress metric that allows performance evaluation on an equal weight basis.

Mechanical testing was performed using an MTS Insight 150 kN electromechanical testing machine equipped with 250 kN hydraulic grips, a linear variable differential transformer (LVDT) position transducer with a range of ±300 mm and resolution of 0.001 mm, and a load cell with a capacity of ±150 kN and resolution of 0.002 kN (Figure 7.5). Tests were conducted at a constant displacement rate of 1 mm/min.

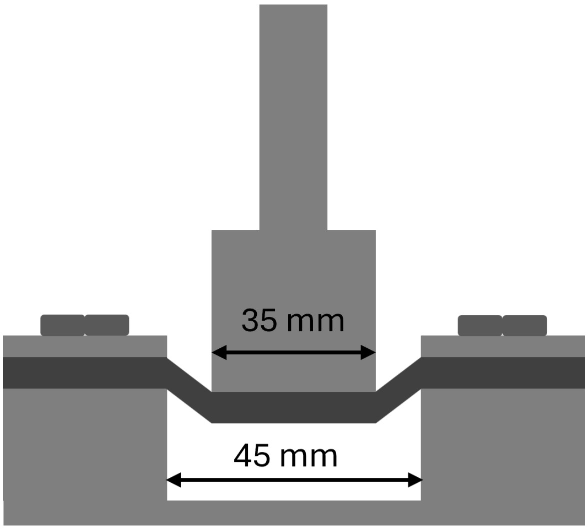

Figure 7.6. Experimental setup for penetration and out-of-plane shear tests.

The experimental setup for penetration resistance evaluation utilized a 35 × 35 mm^2 indenter pressing on specimens supported by a 45 × 45 mm^2 perforated plate (Figure 7.6).

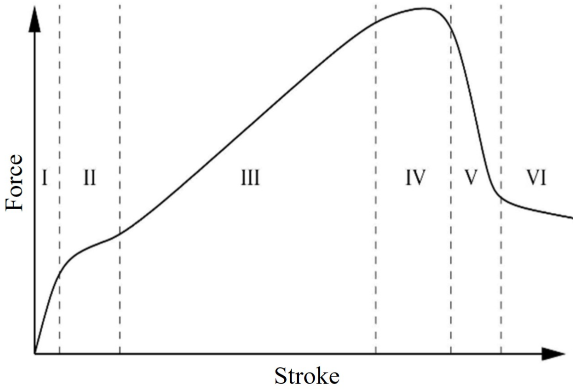

Figure 7.7. Force-stroke curve of the small punch test with different zones [301].

This test can be traced back to the small punch test [302] commonly used for test metallic plates. The typical force-stroke curve of the small punch test with different zones is illustrated in Figure 7.7: Zone I describes the elastic properties of the material. Zone II represents the transition between the elastic and plastic behavior of the material. Zone III corresponds to the hardening properties of the material. Zone IV describes the achieved maximum force as well as the initiation of softening in the material. Zones V and VI reflect the development of the crack and the failure of the specimen [301].

7.2.2 Characteristics of composite materials

Composite laminates are obtained by stacking and curing multiple layers of *prepregs*, i.e., fiber reinforcements pre-impregnated with a polymer matrix. The use of prepregs ensures a controlled fiber-to-resin ratio, uniform wetting, and reproducible mechanical performance. The following subsections describe the defining features of prepregs and their relation to the properties of the final laminate.

Prepreg characteristics

The term *prepreg* refers to a reinforcement fabric made of continuous fibers pre-impregnated with a partially cured thermosetting resin, typically an epoxy. This semi-cured state allows the material to be handled, cut, and laid up before the final curing process, where polymerization is completed under heat and pressure.

The nomenclature of a prepreg encodes its main constituents and structural characteristics. For example, a designation such as C540 T800S 24K 2x2T ER451 36% provides detailed information about its composition, as illustrated in Figure 7.8.

C	**540**	**T800S**	**24K**	**2x2T**	**ER451**	**36%**
Fiber material	Areal weight	Fiber commercial name	Number of fibers in each tow	Weaving pattern	Resin commercial name	Resin percentage

Figure 7.8. Example of composite laminate nomenclature.

Fiber type The prefix identifies the reinforcement family:

- C: carbon fiber
- K: aramid fiber (Kevlar)
- Z: polymeric fiber (Zylon)
- D: ultra-high-molecular-weight polyethylene fiber (Dyneema)
- G: glass fiber

Areal weight The numerical value (e.g., 540) indicates the areal weight of the dry fabric in g/m^2 (mass per unit area of reinforcement).

Fiber designation The code (e.g., T800S) specifies the commercial grade and performance level of the fiber. Manufacturers typically classify fibers as:

- HS (high strength) — e.g., Toray T300, T700;
- HM (high modulus) — e.g., Toray M40, M46.

Tow size The indication 24K denotes the number of filaments in each fiber tow, i.e., approximately 24,000 filaments per tow. Tow size affects the architecture, porosity, and final mechanical behavior of the woven fabric.

Weave pattern The notation (e.g., 2x2T) defines the interlacing geometry of fiber bundles:

- unidirectional (UD): all fibers aligned in a single, parallel direction (0-degree axis), not interwoven, typically held by a light stitching or binder.
- plain weave (PW): simple orthogonal interlacing,
- 2x2 twill (2x2T): diagonal pattern with two-over/two-under crossing,
- satin (5H): longer floats for smoother surfaces and higher drapability.

Resin system The resin code (e.g., ER451, 2573) identifies the commercial name of the polymer matrix.

Resin content The nominal resin content, expressed as a weight percentage (e.g., 36%), defines the proportion of polymer to fiber in the prepreg, influencing stiffness, toughness, and interlaminar strength.

Laminate properties

A composite laminate results from stacking multiple prepreg plies, aligning them according to a desired lay-up sequence, and curing under heat and pressure (typically in an autoclave). The curing cycle, temperature, pressure, and duration, governs polymer cross-linking and the resulting mechanical performance.

The number of plies directly influences laminate thickness, bending stiffness, and out-of-plane behavior. Fibers in woven fabrics are generally oriented at 0° and 90°, producing anisotropic in-plane properties. Different ply orientations (e.g., 0°/45°/90°) can be adopted to homogenize the overall response.

It must be accounted that during curing, part of the resin is expelled due to compaction, slightly reducing the final resin content and laminate thickness.

Materials used in this study The composites investigated include:

- carbon-fiber laminates (T700, T800, T1100),
- hybrid carbon/Dyneema (C/D) laminates,
- Zylon-based composites,
- carbon/CNTF hybrid laminates incorporating CNT fibers as reinforcing elements.

All layers of the tested composites are aligned in the same direction to isolate the effects of layer orientation. These configurations were selected to compare the effects of different parameters on anti-intrusion and out-of-plane performance.

7.2.3 Mechanical characterization

The fiber architecture was varied across standard, intermediate, and high-modulus Carbon Fibers with different weave patterns (plain, twill, unidirectional) and areal weights (from 200 to 400 gsm). Resin systems including standard epoxy, thermoplastic, and toughened formulations were evaluated at different fiber-to-resin volume fractions (35-45%). Curing parameters were optimized through systematic variation of temperature (80-180°C), pressure (3-6 bar), and dwell time (60-180 minutes). Stacking sequence and ply orientation were methodically altered to maximize out-of-plane properties.

Mechanical characterization confirmed that penetration resistance depends strongly on matrix toughness and interlaminar shear properties, in addition to fiber strength. The optimized baseline laminate was then selected as a reference system into which CNTFs would be introduced.

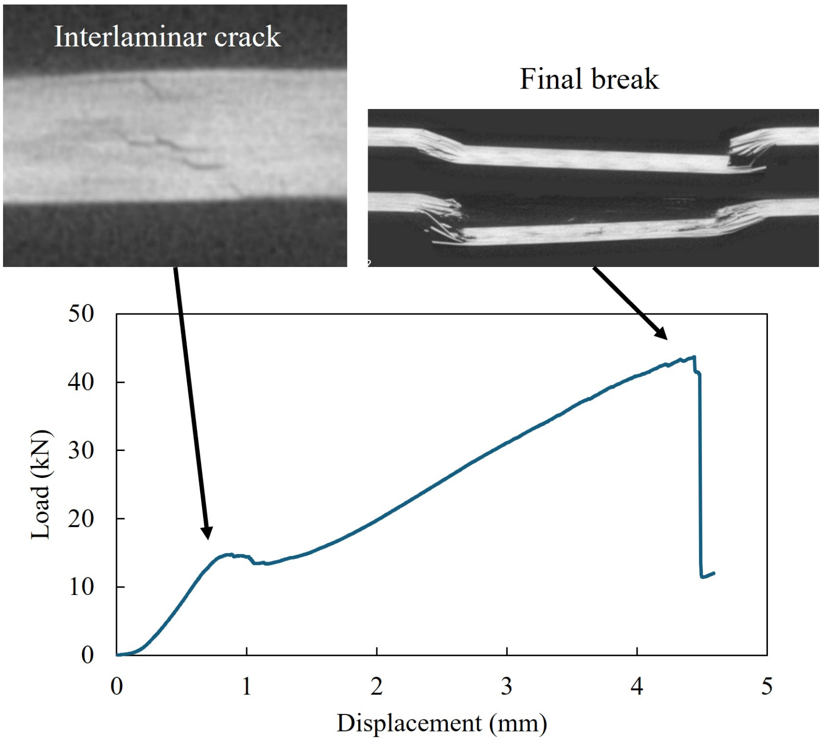

Figure 7.9. Penetration test curve for C370 T800 2573 38% showing the identification of the first peak and the maximum peak. Tomographic analysis of a test on a specimen interrupted at the first peak, highlighting resin cracking and delamination fronts, while tomography of the broken sample show the details of the completed delamination and fiber break.

From the penetration test graphs (Figure 7.9), two distinct force peaks can typically be identified in the response of the laminates. Accordingly, it is possible to define a first-peak stress, $\sigma_{\text{dir.3, first}}$, and a maximum stress, $\sigma_{\text{dir.3, max}}$.

The origin of the first peak was further investigated through tomographic analysis of specimens interrupted at intermediate loading stages shown in Figure 7.9. In addition, a dedicated rectangular specimen and a custom test fixture were developed to directly observe the internal evolution of damage within the laminate as shown in Figure 7.10.

The results clearly indicate that at the first peak the resin matrix undergoes cracking, initiating delamination between adjacent plies. From that point onward, the resin continues to fracture progressively, while the fibers sustain the load until the final collapse. Thus, it can be concluded that the first-peak behavior is mainly governed by the resin properties, whereas the final failure is predominantly influenced by the strength of the fibers.

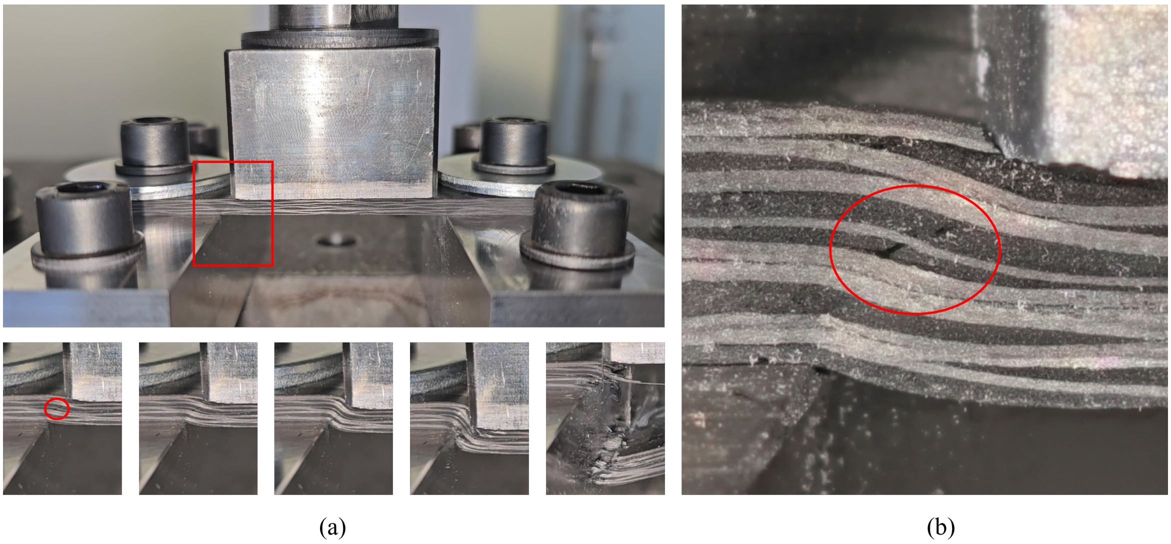
(a)

(b)

Figure 7.10. (a) Representative snapshots of the laminate behavior during intrusion, showing crack initiation and delamination development, which are particularly evident in (b) the magnified view of the crack initiation.

The curing cycle plays a crucial role in this specific application. A shorter curing time leads to partial under-polymerization of the resin, resulting in a matrix that is less brittle and more deformable. This increased ductility allows the composite to accommodate deformation more effectively and to absorb higher amounts of energy under loading. Table 7.1 illustrates a representative example comparing two specimens cured at 6 bar and at a temperature of 135 °C, for 90 and 180 minutes, respectively. The specimen subjected to the shorter curing cycle exhibited noticeably higher performance, confirming the importance of controlling curing conditions to optimize anti-intrusion behavior.

The resin content is also a relevant parameter. Based on experimental results,

Material	**Cycle time (min)**	$\boldsymbol{\sigma_{\mathrm{dir.3,\,max}}/\rho}$ **(MPa/(g/cm^3))**
C 370 T800 2573 38%	90	106.03
C 370 T800 2573 38%	180	91.13

Table 7.1. Effect of cycle time on composite material strength

lower resin fractions generally provided better overall performance, since the resin contributes significantly to the weight while adding comparatively less to the mechanical strength of the laminate. Conversely, specimens with a higher resin content exhibited higher values at the first peak, reflecting the predominant role of the matrix in governing this stage of the response as shown in Table 7.2 and Table 7.3 for T800 ER451.

Material	**Effective resin (%)**	$\boldsymbol{\sigma_{\mathrm{dir.3,\,max}}/\rho}$ **(MPa/(g/cm^3))**
C 370 T800 ER451 36%	40	57.64
C 370 T800 ER451 36%	33	89.39

Table 7.2. Effect of effective resin content on composite material strength

Material	**Effective resin (%)**	$\boldsymbol{\sigma_{\mathrm{dir.3,\,first}}/\rho}$ **(MPa/(g/cm^3))**
C 370 T800 ER451 36%	40	29.3
C 370 T800 ER451 36%	33	18.2

Table 7.3. Effect of effective resin content on composite material strength at first peack

In Table 7.4, it can be observed that, when all other parameters are kept constant, variations in the fiber areal weight do not produce a significant effect on the overall mechanical performance. This can be explained by the fact that the areal weight scales proportionally with the specimen mass; consequently, the specific out-of-plane stress $\sigma_{\mathrm{dir.3,,max}}/\rho$ remains essentially unchanged.

Material	**Fiber areal weight (g/m^2)**	$\boldsymbol{\sigma_{\mathrm{dir.3,\,max}}/\rho}$ **(MPa/(g/cm^3))**
C 370 T800 ER451 36%	370	89.39
C 540 T800 ER451 36%	540	88.09

Table 7.4. Effect of fiber areal weight on composite material strength

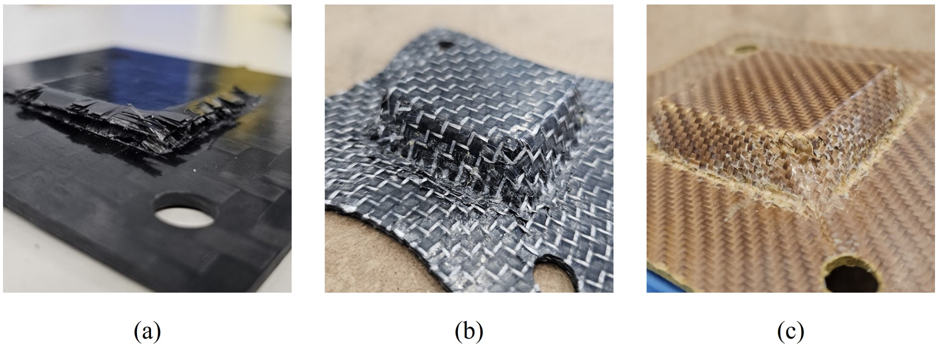

(a) (b) (c)

Figure 7.11. Tested samples of (a) C 370 T800 2573 38%, (b) C/D 295 T700/SK99 ER432 43% and (c) Z 300 Zylon HM 2573 38% show different deformability.

Material	**Effective resin content (%)**	$\boldsymbol{\sigma_{\mathrm{dir.3,\,max}}/\rho}$ **(MPa/(g/cm^3))**
C 384 T700 ER450	34	61.4
C 630 T700 DT120	34	88.9
C 370 T800 ER451	33	89.4
C 280 T1100 2573	36	93.8
C 370 T800 2573	37	106.0
Z 300 Zylon HM 2573	35	121.1
C/D 295 T700/SK99 ER432	37	149.8

Table 7.5. Comparative analysis of composite materials for quasi-static punching resistance

In Figure 7.11, the deformation behavior of CF laminates is compared with that of Zylon and hybrid Carbon–Dyneema laminates, which exhibits a much larger deformation capacity and reach significantly higher strength/density values. As a consequence, the total energy absorbed is considerably greater. This trend is also confirmed in Table 7.5, where the most representative laminates tested are reported.

Based on this detailed comparative analysis, it can be concluded that the most suitable baseline for designing a CF–CNTF hybrid composite is the C370 T800 2573 38% system as the optimal balance of performance, manufacturability, and cost-effectiveness for anti-intrusion applications.

7.3 Experimental methodology and results of CF-CNTF hybrid composites

The experimental design required a careful definition of CNTF format (unidirectional or woven fabric bundle or yarn based), the choice of appropriate CF reference materials, and the optimization of stacking patterns.

7.3.1 Specimen design and manufacturing

Due to the high cost and limited availability of CNTFs also the dimensions of the specimen were optimized. A preliminary evaluation was performed to estimate the necessary mass fraction for CNTF to produce measurable improvements, considering the test setup. Square specimens of CNTF fabrics of at least $60 \times 60\,\mathrm{mm}^2$ of different grammages (from 65 to 165 g/m^2) were evaluated in order to balance cost efficiency and performance.

Two distinct hybrid configurations were designed and fabricated for experimental evaluation:

- **Configuration A:** 3 layers of C 370 T800 2573 38% + 1 layer 60×60 mm of CNTF 140 gsm
- **Configuration B:** 3 layers of C 370 T800 2573 38% + 1 layer 70×70 mm of CNTF 80 gsm

The composite specimens were fabricated using a square mold measuring 250 × 250 mm, divided into four quadrants. The lamination sequence consisted of one layer of Carbon Fiber prepreg, specifically C 370 T800 24K 2x2T 2573 38%, followed by a layer of compatible epoxy adhesive film (150 Unsupported AF163-2U 3M Red) to ensure uniform resin impregnation of the CNTF fabric, which was positioned in the first quadrant, with two additional layers of CF prepreg on top, as illustrated in Figure 7.12.

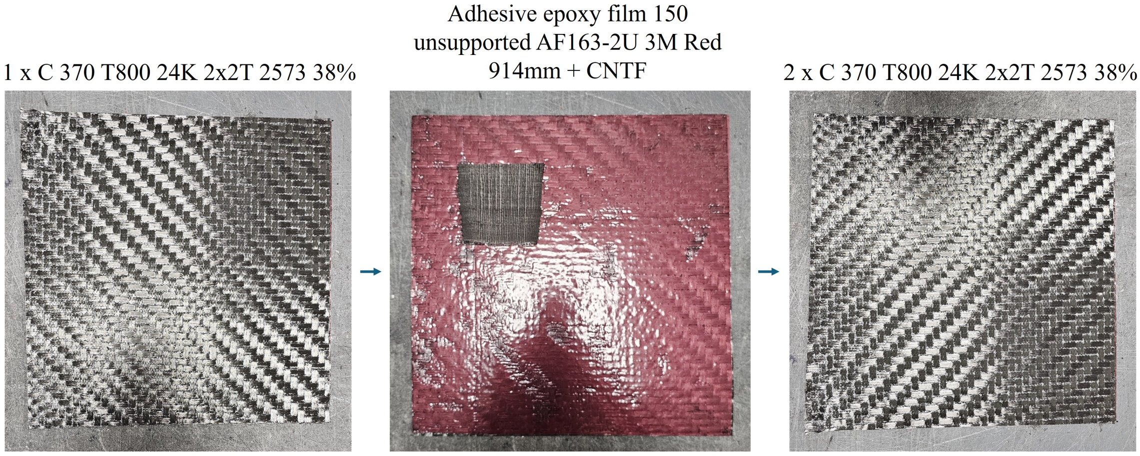

Figure 7.12. Lamination sequence for hybrid CF-CNTF composites showing layer orientation and CNTF placement strategy.

The laminated structure was subsequently cured in an autoclave at a pressure of 6 bar, following a thermal cycle of 30 minutes at 80°C and 120 minutes at 135°C, as depicted in Figure 7.13.

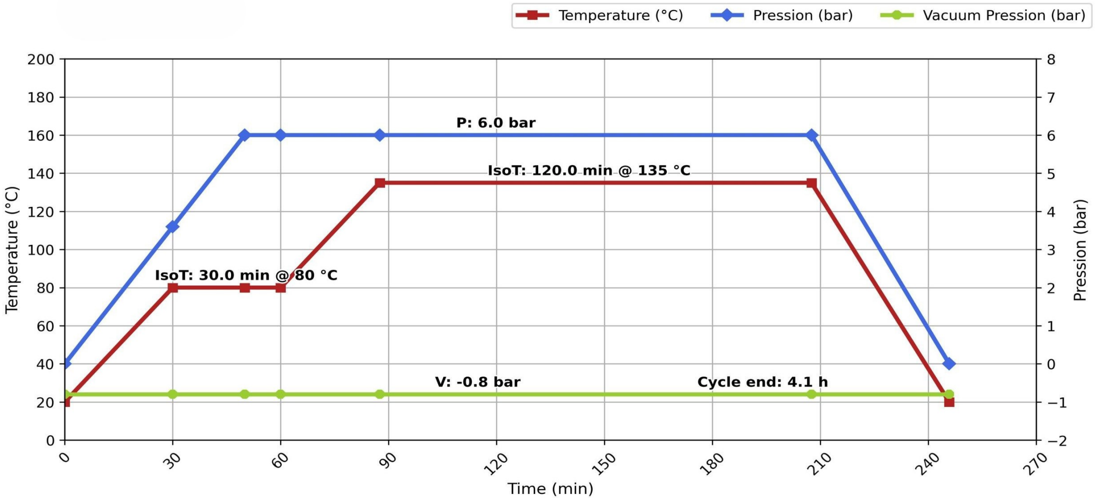

Figure 7.13. Cure cycle parameters used for hybrid CF-CNTF composites.

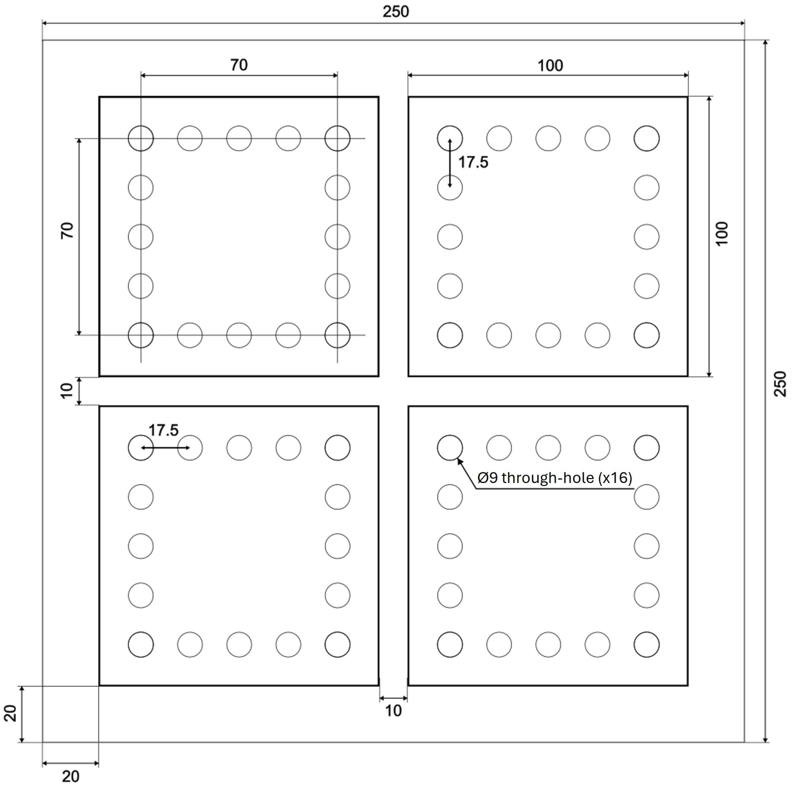

Figure 7.14. Specimen design and dimensions for penetration tests on hybrid CF-CNTF composites.

Upon completion of the curing process, the laminate was removed from the mold, and four test specimens were extracted via waterjet cutting with drilled holes according to technical specifications (Figure 7.14). This process results in one specimen containing a plain weave CNTF fabric (Figure 7.15(a)) and three specimens without CNTF, which serve as a reference for comparative analysis, that were mounted in the test apparatus as shown in Figure 7.15(b).

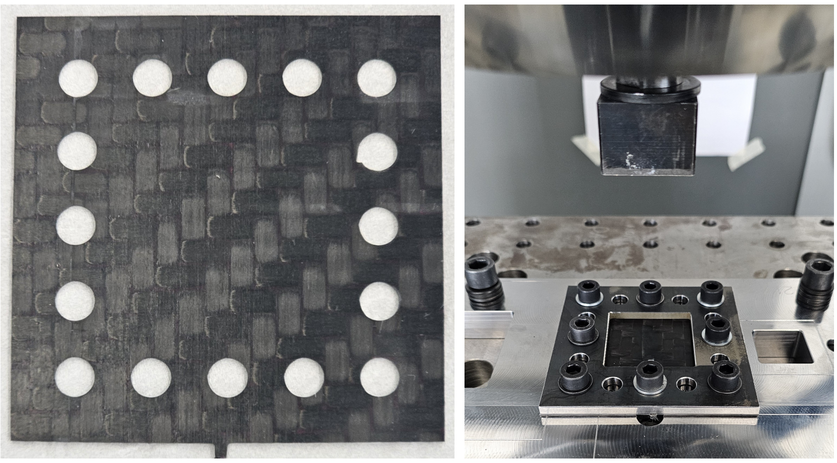

(a) (b)

Figure 7.15. (a) Final specimen for penetration tests on hybrid CF-CNTF composites and (b) specimen mounting

In designing the test, the influence of the intruder's shape on the mechanical response of the material was considered, as investigated by [303]. Specifically, for the case of a square-shaped punch, the geometry introduces unique stress concentration effects at the corners, which can significantly affect the contact mechanics compared to circular or other punch shapes. According to [303], the square punch's sharp edges lead to higher localized stresses, necessitating precise control of the punch's dimensions and alignment during testing to ensure accurate results. Despite these known stress concentration effects, the square shape was chosen to comply with the testing procedures outlined in the FIA (Fédération Internationale de l'Automobile) Regulations for F1 anti-intrusion panels [304].

7.3.2 Mechanical performance enhancement

Comparative tests revealed that even with a CNTF mass fraction of approximately 5%, the hybrid composites exhibited significant improvement in strength. Configuration A (140 gsm CNTF) demonstrated a 20% increase in penetration resistance compared to baseline CF specimens with only 6% increase in total mass, while Configuration B (80 gsm CNTF) showed a 18% improvement, with only 4% increase in total mass as illustrated in Table 7.6 and 7.7.

Analysis of the load-displacement curves presented in Figure 7.16(a) and 7.16(b) reveals that hybrid specimens exhibit a higher ultimate peak load compared to non-hybrid counterparts. The initial peak, instead, is significantly less pronounced. This

Conf. A	**$\sigma_{\mathrm{dir.3,\,max}}/\rho$** (MPa/(g/cm^3))	**Force max** (kN)	**Modulus** (MPa)	**Mass** (g)	**Thickness** (mm)
CF only	92.6	22.1	46.2	17.0	1.3
CF + CNTF	110.7	28.1	59.4	18.1	1.4
DIFF	18.08	5.97	13.26	1.07	0.07
Δ	20%	27%	29%	6%	6%

Table 7.6. Comparison between CF-only and CF+CNTF hybrid samples for configuration A.

Conf. B	**$\sigma_{\mathrm{dir.3,\,max}}/\rho$** (MPa/(g/cm^3))	**Force max** (kN)	**Modulus** (MPa)	**Mass** (g)	**Thickness** (mm)
CF only	83.2	20.8	47.3	17.9	1.2
CF + CNTF	97.4	25.5	55.6	18.7	1.3
DIFF	14.27	4.69	8.28	0.80	0.05
Δ	17%	23%	18%	4%	4%

Table 7.7. Comparison between CF-only and CF+CNTF hybrid samples for configuration B.

behavior suggests that the hybrid specimens possess enhanced resistance to deformation under increasing load, likely due to the synergistic interaction of their constituent materials, which contributes to greater structural integrity at higher loads. These observations underscore the importance of material composition in optimizing mechanical performance for specific applications.

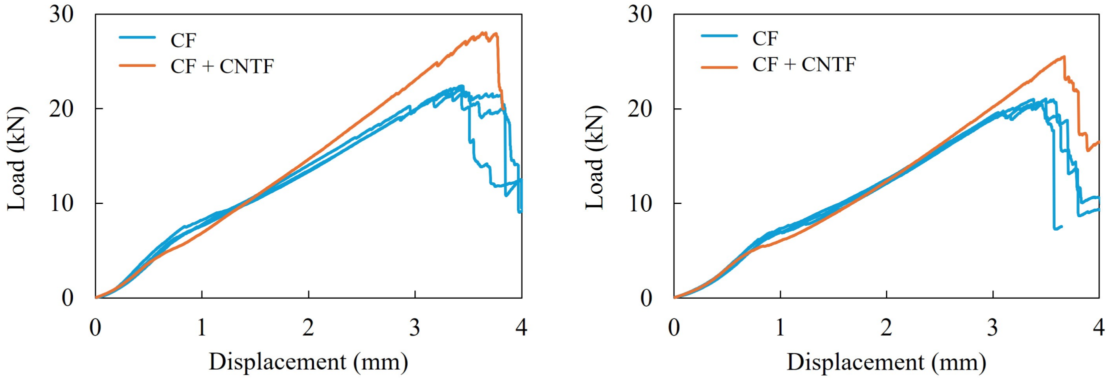

(a) (b)

Figure 7.16. Comparative load-displacement curves for baseline CF and CF+CNTF, (a) specimens A (b) specimens B.

Direct observation on the broken samples shown in Figure 7.17 revealed distinct

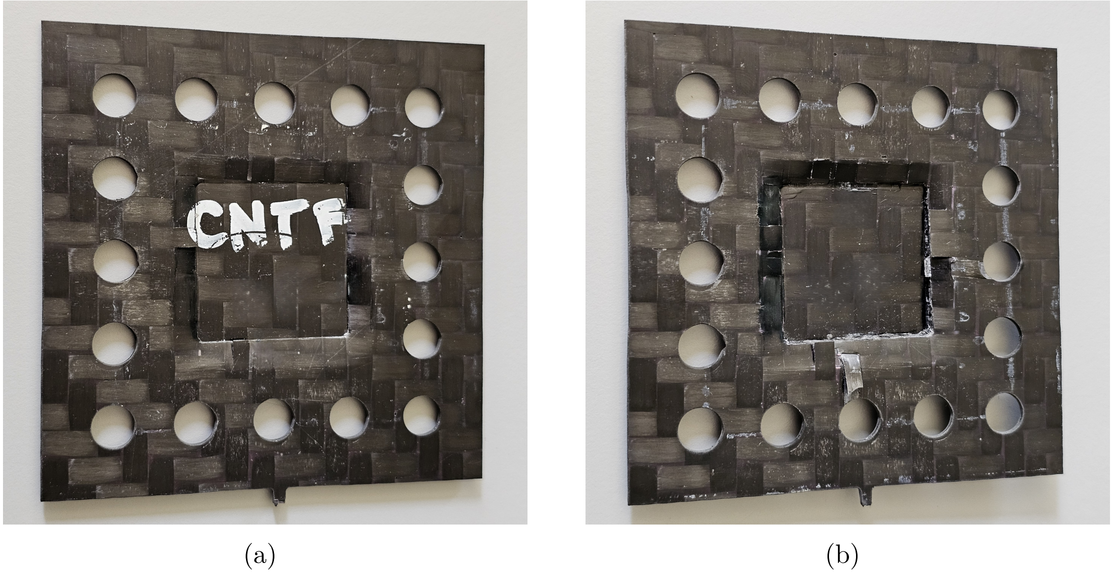

(a) (b)

Figure 7.17. Comparison of penetration test results of specimen A (a) with and (b) without CNTF integration.

failure mechanisms between conventional CF and hybrid specimens. While pure CF laminates exhibited brittle fracture with extensive fiber breakage, the CNTF-reinforced specimens showed more progressive failure with enhanced delamination resistance and fiber bridging effects.

7.4 Discussion and perspectives

Beyond mechanical reinforcement, CNTFs exhibit significant electrical conductivity, with volume resistivity approaching that of copper. This enables their use as embedded sensors for structural health monitoring and as distributed heating elements for deicing in different applications. Table 7.8 compares the electrical resistivity of CNTF, CF, and copper for a 1 cm wire segment of 1 g mass.

Measuring the electrical resistance of CNTF networks, integrated in composite components, under applied load, allows in-situ strain monitoring and creating structural–electronic hybrid components. CNTFs can be directly integrated within composite structures without dedicated wiring channels, preserving structural integrity, replacing embedded copper cabling, providing weight savings and design simplification while serving as conductive pathways for integrated sensors. Additionally, CNTF layers can provide electromagnetic interference shielding, combining structural reinforcement with EMI protection. These properties enable multifunctional composites that integrate mechanical performance with sensing, communication, and energy management capabilities.

Such integration opens the way to novel structural-electronic hybrid components, particularly appealing for aerospace and automotive applications where load-bearing capacity must coexist with sensing, communication, or energy management functionalities. For instance, CNTFs embedded within a wing element could simultaneously provide structural reinforcement, power transmission, and strain sensing capabilities.

Parameter	**CNTF**	**CF**	**Copper**
Mass [g]	1	1	1
Density [g/cm^3]	1	1.8	8.96
Volume [cm^3]	1	0.556	0.112
Length [cm]	100	100	100
Cross-section [cm^2]	0.01	0.00556	0.00112
Resistivity [Ω·cm]	3.13×10^{-5}	1.60×10^{-3}	1.68×10^{-6}
Resistance [Ω]	0.3125	28.8000	0.1505

Table 7.8. Comparison of electrical resistance for 1 m of wire with a mass of 1 g. Data for CNTF and CF were experimentally measured from the available materials, while the value for copper was obtained from publicly available sources [305].

The experimental investigation demonstrated that strategic integration of CNTF layers into CF composites significantly enhances anti-intrusion performance, with measured improvements of 18-20% in penetration resistance for only 4-6% mass increase. This performance enhancement derives from the shear and bending properties of CNTFs, which complement the tensile-dominated performance of Carbon Fibers.

The demonstrated performance benefits justify further research for high-value applications where weight savings and safety are critical.

These features, plus the multifunctional capabilities, make CNTFs a candidate for future generations of lightweight structural composites, particularly in high-end sectors. Ongoing developments in CNTF manufacturing are expected to substantially optimize their large-scale production, reduce costs, while improving property consistency.

Chapter 8

Conclusions

This doctoral dissertation has presented a comprehensive multiscale investigation into the mechanical behavior of Carbon NanoTube Fibers (CNTFs), pursuing a bottom-up, micro-to-macro approach. The research has successfully integrated theoretical modeling, extensive experimental validation, and manufacturing innovation to bridge the gap between the properties of individual Carbon NanoTubes (CNTs) and the macroscale performance of structural elements like yarns, ropes, and advanced composite materials. The ultimate goal was to establish a systematic understanding and provide reliable predictive tools for the design of next-generation, lightweight, high-performance materials for demanding applications in sectors such as structural, electronic, automotive, aerospace, and defense.

The research journey began at the nanoscale, with the development of a refined micromechanical model to predict the effective tensile stiffness of CNTFs. This model, unlike previous approaches that assumed CNTs to be axially rigid, accounts for their compliance, as well as for critical nanoscale phenomena such as misalignment, van der Waals interactions, and cross-linking effects. The governing mechanics were described by a delayed-advanced differential equation, solved numerically, which demonstrated that neglecting CNT compliance leads to an overestimation of the fiber's macroscopic stiffness. The micromechanical framework developed in Chapter 3 relies on the shear stiffness κ of van der Waals interactions, a parameter that is highly dependent on various chemical and geometric factors. While the adoption of $\kappa = 0.1$ MPa provides a reasonable starting point based on available literature, it introduces some uncertainty that warrants further investigation in future work. Additionally, the model assumes a perfectly square lattice arrangement of CNTs, whereas SEM images reveal a more disordered morphology with defects. This idealization, while necessary for computational tractability, represents a simplification that could be refined through statistical mechanics approaches incorporating disorder and defect distributions. The linear approximation used for nanoscale interactions, though validated within the elastic regime, would benefit from extension to capture nonlinear behavior and improve failure predictions. Despite these opportunities for refinement, the model's predictions show excellent agreement with experimental data, confirming its accuracy and practical value, especially as manufacturing technologies advance towards producing longer

CNTs.

The investigation then scaled up to the meso- and macro-scale, addressing the complex mechanics of twisted structures. A theoretical framework based on differential geometry was established to model twisted rods and multi-ply yarns. To validate these analytical formulations, an experimental campaign was conducted on a surrogate system of twisted rubber filaments. This investigation yielded a crucial insight: twisted yarns harbor a significant eigenstress state in their reference, balanced configuration, characterized by a high residual twist dictated by the ratio of bending to torsional stiffness. This intrinsic twist was found to produce a noteworthy stiffening effect on the constituent rods, a phenomenon that proved essential for accurately predicting the tensile response of the final yarn assembly.

Building on these foundational insights, the focus shifted to the modeling and manufacturing of yarns made from actual CNTFs. A yarn-making kinematic model was developed, enabling the production of CNTF yarns with tailored properties for mechanical testing. Experimental results identified an optimal twist level for maximizing CNTF bundle strength, although it was coupled with a decrease in stiffness. The model was consequently designed to replicate this optimal twist in the yarn's constituent bundles to improve its overall mechanical properties. These findings were synthesized into a comprehensive geometric-kinematic model and implemented in a software tool capable of simulating the yarn-making process and predicting the optimal machine parameters to achieve peak performance consistently. Long-term performance characterization revealed important considerations for structural applications. Creep tests demonstrated that CNTFs exhibit time-dependent behavior under sustained loading; at 67% of ultimate tensile strength, continuous strain accumulation was observed. This behavior highlights the need for further investigation to establish appropriate safety margins and develop predictive models for long-term reliability. Understanding creep mechanisms in CNTFs represents an essential step toward their use in load-bearing applications where sustained stresses are anticipated. Additionally, the ratio of bending to torsional stiffness (B/A) in CNTF bundles was found experimentally to vary with twist level, deviating from the classical Kirchhoff rod assumption of constant material properties. This suggests that twisted CNTF bundles exhibit more complex mechanical behavior than conventional homogeneous elastic rods, presenting an interesting direction for advanced modeling approaches. The optimization model currently relies on empirically fitted relationships, which capture the observed behavior effectively but could be further strengthened through integration with fundamental micromechanical principles. Developing such connections would enhance the model's generalizability and extend its applicability to a broader range of CNTF configurations and processing conditions. Despite these opportunities for further development, the application of the kinematic model resulted in a tangible 14% improvement in the mechanical properties of the produced yarns, confirming the initial hypothesis. Furthermore, post-twist hardening treatments were successfully employed to recover the initial stiffness lost during the twisting process, enhancing the overall balance of properties in the final yarn.

A deeper microscopic analysis revealed that CNTFs are themselves hierarchical structures, composed of smaller, tightly-bound CNT clusters or fibrils. Pre-twisting a single CNTF reorganizes these fibrils into a helical architecture, creating a strain mismatch between the concentric layers. A model was proposed based on the mechanism of progressive cluster engagement, where outer fibrils bear load earlier than inner ones. This mechanism successfully explains the experimentally observed mechanical trade-off in twisted fibers: a reduction in stiffness and strength, coupled with a remarkable enhancement in ductility and failure strain. This principle was validated through a macroscopic physical analogue constructed from nylon filaments. Several experimental observations suggest opportunities for model refinement. The marked ductility enhancement in twisted CNTFs (Chapter 6) was captured using different constitutive continuation models, indicating that the underlying mechanism would benefit from more detailed micromechanical characterization. While microscopy suggests enhanced lateral confinement as a contributing factor, a comprehensive mechanistic description at the fibril scale remains an open avenue for future research.

Finally, the thesis explored the integration of CNTFs into practical structural applications by creating hybrid composite laminates. CNTF interlayers were strategically incorporated into optimized Carbon Fiber (CF) laminates to enhance their anti-intrusion performance. Experimental testing demonstrated that the inclusion of a small mass fraction of CNTFs (4-6%) led to a significant 18-20% increase in penetration resistance. Beyond structural reinforcement, the intrinsic electrical conductivity of CNTFs opens avenues for multifunctional applications, such as embedded sensors for structural health monitoring or integrated wiring, adding significant value to the composite structure. To fully characterize the potential of CNTF-reinforced laminates in protective applications, future work should extend the testing regime to high-rate dynamic conditions. While the quasi-static penetration tests (1 mm/min) provided valuable insights into the underlying reinforcement mechanisms, realistic anti-intrusion scenarios involve impact velocities orders of magnitude higher. Characterizing the strain-rate dependence of these hybrid composites would provide important validation of their performance under actual impact loading conditions and enable more confident predictions for applications.

In conclusion, this research establishes a foundational framework for CNTF mechanics and demonstrates promising performance enhancements across multiple scales, from individual fibers to structural composites. While the work has successfully achieved its primary objectives, it also opens several important avenues for future investigation that will further strengthen the path from laboratory demonstration to industrial application. Building on the insights gained, several research directions emerge as natural next steps. To advance predictive capability, the development of a comprehensive multi-scale model would be valuable, one that accurately bridges single-fiber mechanics to bundle-level and ultimately yarn-level behavior. A refined constitutive framework incorporating key micromechanical phenomena—such as torsional and bending stiffness of individual fibers and bundles, inter-filament frictional effects, and material viscosity—would extend the current models beyond linear elasticity. The micromechanical origins of the enhanced ductility observed in twisted fibrils merit deeper investigation, as understanding this mechanism could enable the design of yarns with tailored toughness properties. Further characterization efforts would strengthen the framework's applicability to industrial contexts. Direct nano-mechanical characterization of van der Waals interactions, advanced multi-physics modeling, and extended creep and fatigue testing would refine model parameters and enhance long-term performance predictions. Dynamic validation at realistic strain rates would confirm the composite reinforcement benefits observed under quasi-static conditions, while comprehensive safety and toxicity assessments would address regulatory requirements for widespread adoption. At the composite level, continued optimization of CNTF layer architecture could maximize synergistic effects with traditional reinforcements, while advancements in manufacturing processes, guided by the established modeling principles, will continue to reduce costs and improve property consistency. By pursuing these research directions through rigorous experimental and theoretical work, the scientific community can build upon this foundation to develop increasingly reliable and competitive CNTF technologies for the next-generation applications they promise to enable.

Appendix A

Computational algorithm for helical wire configuration

Consider a helical winding configuration consisting of m wires of radius R_e (outer radius) wound around a central wire or cylindrical void of radius R_i (inner radius). The winding follows a helical path characterized by a helix angle α. The objective is to determine the ratio R_i/R_e that satisfies the geometric constraints of tangency between adjacent wires.

For computational convenience, the outer radius is normalized to unity: $R_e = 1$. Consequently, the ratio R_i/R_e reduces to R_i itself.

The algorithm begins with an approximate analytical estimate of the inner radius based on the following geometric relationships:

$$b_1 = \tan(\alpha) \tag{A.1}$$

$$b_2 = \tan\left(\alpha - \frac{5\pi}{2}\right) \tag{A.2}$$

$$\theta_{c1} = \frac{2\pi}{1 - b_1/b_2} \tag{A.3}$$

$$\theta_{c2} = \frac{b_1}{b_2}\theta_{c1} \tag{A.4}$$

$$\theta_0 = \left|\frac{\theta_{c2}}{\cos(\alpha - \pi/2)}\right| \tag{A.5}$$

$$R_i^{(0)} = \frac{R_e}{\sin(\theta_0/(2m))/(1 - \sin(\theta_0/(2m)))} \tag{A.6}$$

where b_1 and b_2 represent helix pitch parameters, θ_{c1} and θ_{c2} are intersection angles between the axial helix and its complementary helix, and θ_0 is the associated circumferential angle.

The initial estimate is refined through an iterative process. At each iteration $k = 2, 3, \ldots, p$ (where p is the precision parameter), the algorithm solves the following nonlinear constraint equation:

$$\frac{\frac{b^2 t}{r}\cos(t) + \left(r - R_e\sqrt{1-\frac{b^2t^2(b^2+r^2)}{R_e^2 r^2}}\right)\sin(t)}{\left(r - R_e\sqrt{1-\frac{b^2t^2(b^2+r^2)}{R_e^2 r^2}}\right)\cos(t) - \frac{b^2 t}{r}\sin(t)} = \tan\left(\frac{\pi}{m}\right) \tag{A.7}$$

where:

$$r = R_i + R_e \quad \text{(mean helix radius)} \tag{A.8}$$

$$b = r\tan(\alpha) \quad \text{(helix pitch)} \tag{A.9}$$

This constraint equation enforces the geometric tangency condition between adjacent wires in the helical configuration.

Algorithm Description

Algorithm 1. Helical Radius Ratio Calculation

```
Require: Helix angle $\alpha$, number of wires $m$, precision parameter $p \geq 3$
Ensure: Radius ratio $R_i/R_e$
Set $R_e \leftarrow 1$ (normalization)
Compute initial estimate $R_i^{(0)}$ using equations (A.1)–(A.6)
for $k = 2$ to $p$ do
    solution ← NaN
    while solution is NaN do
        Compute $r = R_i + R_e$ and $b = r\tan(\alpha)$
        Solve equation (A.7) for $t$ using numerical root-finding
        Store solution in solution
        $R_i \leftarrow R_i - 10^{-k}$
    end while
    $R_i \leftarrow R_i + 10^{-k}$
end for
return $R_i/R_e = R_i$
```

Implementation Notes

- The algorithm employs a bracketing approach where R_i is decremented by 10^{-k} at iteration k until the constraint equation (A.7) admits no solution, then adjusted by $+10^{-k}$.

- The numerical solution of equation (A.7) is obtained using the `fzero` function in MATLAB, with an initial guess of $t = 0.001$.

- The precision parameter p controls the accuracy of the solution. Higher values of p yield more accurate results at the cost of increased computational time. A minimum value of $p = 3$ is recommended.
- The normalization $R_e = 1$ simplifies the computation without loss of generality, as the problem is scale-invariant.

List of publications

The research work presented in this dissertation has resulted in the following published and submitted scientific articles:

- L. Galuppi, V. A. Muratore. *A refined model for the effective tensile stiffness of Carbon NanoTube fibers. International Journal of Mechanical Sciences*, vol. 251, 2023, p. 108303.
- C. Boni, V. A. Muratore, G. Royer-Carfagni. *Experimental assessment of the eigenstress state in two-ply yarns and its effect on tensile properties. Journal of the Mechanics and Physics of Solids*, vol. 187, 2024, p. 105613.
- V. A. Muratore, C. Boni, G. Royer-Carfagni. *The Effect of Controlled Pre-Twisting on the Tensile Properties of Individual Carbon Nanotube Fibers.* Submitted to *Soft Matter* (Royal Society of Chemistry), 2025.

References

[1] M. Monthioux, V. L. Kuznetsov. “Who should be given the credit for the discovery of carbon nanotubes?” In: *Carbon* 44.9 (2006), pp. 1621–1623.

[2] H. Dai, E. W. Wong, C. M. Lieber. “Probing electrical transport in nanomaterials: conductivity of individual carbon nanotubes”. In: *Science* 272.5261 (1996), pp. 523–526.

[3] D. S. Su. *20 years of carbon nanotubes*. 2011.

[4] R. Guoqiang. *Carbon nanotube*. `https://www.britannica.com/science/carbon-nanotube`. Encyclopedia Britannica. 2018.

[5] L. M. Ericson et al. “Macroscopic, neat, single-walled carbon nanotube fibers”. In: *Science* 305.5689 (2004), pp. 1447–1450.

[6] L. W. Taylor et al. “Improved properties, increased production, and the path to broad adoption of carbon nanotube fibers”. In: *Carbon* 171 (2021), pp. 689–694.

[7] L. Galuppi, M. Pasquali, G. Royer-Carfagni. “The effective tensile and bending stiffness of nanotube fibers”. In: *International Journal of Mechanical Sciences* 163 (2019), p. 105089.

[8] I. Ostanin et al. “A distinct element method for large scale simulations of carbon nanotube assemblies”. In: *Journal of the Mechanics and Physics of Solids* 61.3 (2013), pp. 762–782.

[9] V. N. Popov. “Carbon nanotubes: properties and application”. In: *Materials Science and Engineering: R: Reports* 43.3 (2004), pp. 61–102.

[10] S. Arepalli et al. “Protocol for the characterization of single-wall carbon nanotube material quality”. In: *Carbon* 42.8-9 (2004), pp. 1783–1791.

[11] K. S. Ibrahim. “Carbon nanotubes-properties and applications: a review”. In: *Carbon letters* 14.3 (2013), pp. 131–144.

[12] Y. Nakayama, S. Akita. “Nanoengineering of carbon nanotubes for nanotools”. In: *New Journal of Physics* 5.1 (2003), p. 128.

[13] V. A. Davis et al. “True solutions of single-walled carbon nanotubes for assembly into macroscopic materials”. In: *Nature nanotechnology* 4.12 (2009), pp. 830–834.

[14] P. L. McEuen, M. S. Fuhrer, H. Park. “Single-walled carbon nanotube electronics”. In: *IEEE transactions on nanotechnology* 1.1 (2002), pp. 78–85.

[15] C. Wang et al. “Carbon nanotube electronics–moving forward”. In: *Chemical Society Reviews* 42.7 (2013), pp. 2592–2609.

[16] A. Eatemadi et al. “Carbon nanotubes: properties, synthesis, purification, and medical applications”. In: *Nanoscale research letters* 9.1 (2014), pp. 1–13.

[17] V. Raphey et al. “Advanced biomedical applications of carbon nanotube”. In: *Materials Science and Engineering: C* 100 (2019), pp. 616–630.

[18] M. J. Treacy, T. W. Ebbesen, J. M. Gibson. “Exceptionally high Young’s modulus observed for individual carbon nanotubes”. In: *nature* 381.6584 (1996), pp. 678–680.

[19] A. Krishnan et al. “Young’s modulus of single-walled nanotubes”. In: *Physical review B* 58.20 (1998), p. 14013.

[20] M. Moniruzzaman, K. I. Winey. “Polymer nanocomposites containing carbon nanotubes”. In: *Macromolecules* 39.16 (2006), pp. 5194–5205.

[21] V. Mittal. *Polymer nanotubes nanocomposites: synthesis, properties and applications.* John Wiley & Sons, 2014.

[22] J. Chen et al. “A review of the interfacial characteristics of polymer nanocomposites containing carbon nanotubes”. In: *RSC advances* 8.49 (2018), pp. 28048–28085.

[23] P. Goh, A. Ismail, B. Ng. “Directional alignment of carbon nanotubes in polymer matrices: Contemporary approaches and future advances”. In: *Composites Part A: Applied Science and Manufacturing* 56 (2014), pp. 103–126.

[24] M. Liu et al. “Polymer nanocomposites with improved mechanical and thermal properties by magnetically aligned carbon nanotubes”. In: *Polymer* 166 (2019), pp. 81–87.

[25] R. B. Pipes et al. “Flexural deflection as a measure of van der Waals interaction forces in the CNT array”. In: *Composites science and technology* 66.9 (2006), pp. 1125–1131.

[26] S. Acquah, D. Ventura, H. Kroto. “Strategies to successfully cross-link carbon nanotubes”. In: *Electronic Properties of Carbon Nanotubes.* IntechOpen, 2011.

[27] O.-K. Park et al. “High-modulus and strength carbon nanotube fibers using molecular cross-linking”. In: *Carbon* 118 (2017), pp. 413–421.

[28] S. Iijima. “Helical microtubules of graphitic carbon”. In: *nature* 354.6348 (1991), pp. 56–58.

[29] L. V. Radushkevich, V. M. Lukyanovich. “On the structure of carbon formed during the thermal decomposition of carbon monoxide on an iron contact”. In: *Zhurnal Fizicheskoi Khimii* 26 (1952). In Russian, pp. 88–95.

[30] M. Monthioux, J. Spreadborough. “Action of graphite as a lubricant”. In: *Nature* 186.4718 (1960), p. 29.

[31] M. Endo, T. Koyama, Y. Hishiyama. “High resolution electron microscopy of graphitizable carbon fiber prepared by benzene decomposition”. In: *Japanese Journal of Applied Physics* 15.11 (1976), p. 2073.

[32] A. Oberlin, M. Endo, T. Koyama. “Filamentous growth of carbon through benzene decomposition”. In: *Journal of Crystal Growth* 32 (1976), pp. 335–349.

[33] J. Abrahamson. “The surface energies of graphite”. In: *Carbon* 17 (1979), pp. 539–554.

[34] H. W. Kroto et al. “C60: Buckminsterfullerene”. In: *Nature* 318.6042 (1985), pp. 162–163.

[35] D. Bochvar, E. Galpern. “On hypothetical systems: carbodioide. Polymeric carbon modifications”. In: *Reports of the USSR Academy of Sciences* 257.6 (1981). [On hypothetical systems: carbodioide. Polymeric carbon modifications], pp. 1356–1360.

[36] T. W. Ebbesen, P. M. Ajayan. “Large-scale synthesis of carbon nanotubes”. In: *Nature* 358 (1992), pp. 220–222.

[37] J. W. Mintmire, B. I. Dunlap, C. T. White. “Are fullerene tubules metallic?” In: *Physical Review Letters* 68 (1992), p. 631.

[38] S. Iijima, T. Ichihashi. “Single-shell carbon nanotubes of 1-nm diameter”. In: *nature* 363.6430 (1993), pp. 603–605.

[39] D. S. Bethune et al. “Cobalt-catalysed growth of carbon nanotubes with single-atomic-layer walls”. In: *Nature* 363 (1993), pp. 605–607.

[40] P. Nikolaev et al. “Gas-phase catalytic growth of single-walled carbon nanotubes from carbon monoxide”. In: *Chemical Physics Letters* 313.1-2 (1999), pp. 91–97.

[41] T. Vodenitcharova, L. Zhang. “Effective wall thickness of a single-walled carbon nanotube”. In: *Physical Review B* 68.16 (2003), p. 165401.

[42] C. A. Poland et al. “Carbon nanotubes introduced into the abdominal cavity of mice show asbestos-like pathogenicity in a pilot study”. In: *Nature nanotechnology* 3.7 (2008), pp. 423–428.

[43] E. T. Thostenson, C. Li, T.-W. Chou. “Nanocomposites in context”. In: *Composites science and technology* 65.3-4 (2005), pp. 491–516.

[44] C. Li, T.-W. Chou. “A structural mechanics approach for the analysis of carbon nanotubes”. In: *International journal of solids and structures* 40.10 (2003), pp. 2487–2499.

[45] D.-M. Tang et al. “Chirality engineering for carbon nanotube electronics”. In: *Nature Reviews Electrical Engineering* 1.3 (2024), pp. 149–162.

[46] E. J. Radauscher. “Design, fabrication, and characterization of carbon nanotube field emission devices for advanced applications”. PhD thesis. Duke University, 2016.

[47] J. P. Lu. “Elastic properties of carbon nanotubes and nanoropes”. In: *Physical review letters* 79.7 (1997), p. 1297.

[48] B. Peng et al. “Measurements of near-ultimate strength for multiwalled carbon nanotubes and irradiation-induced crosslinking improvements”. In: *Nature nanotechnology* 3.10 (2008), pp. 626–631.

[49] M.-F. Yu et al. “Strength and breaking mechanism of multiwalled carbon nanotubes under tensile load”. In: *Science* 287.5453 (2000), pp. 637–640.

[50] J. Sun et al. “Experimental determination of the Young’s modulus of individual single-walled carbon nanotubes with single chirality”. In: *Nano Research* 17.8 (2024), pp. 7522–7532.

[51] A. Takakura et al. “Strength of carbon nanotubes depends on their chemical structures”. In: *Nature communications* 10.1 (2019), p. 3040.

[52] Y. Chen et al. “A theoretical evaluation of load transfer in multi-walled carbon nanotubes”. In: *Carbon* 49.1 (2011), pp. 193–197.

[53] Z. Zhang et al. “Ultra-strong collagen-mimic carbon nanotube bundles”. In: *Carbon* 77 (2014), pp. 1040–1053.

[54] N. Behabtu et al. “Strong, light, multifunctional fibers of carbon nanotubes with ultrahigh conductivity”. In: *science* 339.6116 (2013), pp. 182–186.

[55] J. Hone. “Phonons and thermal properties of carbon nanotubes”. In: *Carbon Nanotubes*. Springer, 2001, pp. 273–286.

[56] P. Kim et al. “Thermal transport measurements of individual multiwalled nanotubes”. In: *Physical review letters* 87.21 (2001), p. 215502.

[57] J. Hone et al. “Thermal conductivity of single-walled carbon nanotubes”. In: *Physical review B* 59.4 (1999), R2514.

[58] P.-X. Hou, C. Liu, H.-M. Cheng. “Purification of carbon nanotubes”. In: *Carbon* 46.15 (2008), pp. 2003–2025.

[59] P. Li et al. “High-Quality, Highly Concentrated Semiconducting Single-Wall Carbon Nanotubes for Use in Field Effect Transistors and Biosensors”. In: *ACS Nano* 7.10 (2013), pp. 8453–8460. DOI: `10.1021/nn401998r`.

[60] C. Wang et al. “Metallic Single-Walled Carbon Nanotubes for Conductive Nanocomposites”. In: *Journal of the American Chemical Society* 130.49 (2008), pp. 16373–16377. DOI: `10.1021/ja0768035`.

[61] *Optical properties of carbon nanotubes*. `https://en.wikipedia.org/wiki/Optical_properties_of_carbon_nanotubes`. Accessed: 2025-10-08.

[62] *Carbon Nanotube Based Actuators*. `https://sist.sathyabama.ac.in/sist_coursematerial/uploads/SBTA5301.pdf`. Accessed: 2025-10-08.

[63] D-Day. *Batterie 10 volte più potenti e molto più leggere nel 2023: la promessa di un'azienda francese*. `https://www.dday.it/redazione/37409/batterie-10-volte-piu-potenti-e-molto-piu-leggere-nel-2023-la-promessa-di-una-azienda-francese`. 2022.

[64] Focus. *Materiale più nero: Vantablack e il nuovo dei nanotubi di carbonio*. `https://www.focus.it/scienza/scienze/materiale-piu-nero-vantablack-nuovo-nanotubi-carbonio`. 2022.

[65] U. of Padova. *HELIOS Group - People*. `https://wwwdisc.chimica.unipd.it/helios/people.html`. 2022.

[66] I. Rago et al. "Carbon nanotubes, directly grown on supporting surfaces, improve neuronal activity in hippocampal neuronal networks". In: *Advanced Biosystems* 3.5 (2019), p. 1800286.

[67] V. Martinelli et al. "Carbon nanotubes instruct physiological growth and functionally mature syncytia: nongenetic engineering of cardiac myocytes". In: *ACS nano* 7.7 (2013), pp. 5746–5756.

[68] H. Sun et al. "Carbon nanotubes enhance intercalated disc assembly in cardiac myocytes via the β1-integrin-mediated signaling pathway". In: *Biomaterials* 55 (2015), pp. 84–95.

[69] B. Gorain et al. "Carbon nanotube scaffolds as emerging nanoplatform for myocardial tissue regeneration: A review of recent developments and therapeutic implications". In: *Biomedicine & Pharmacotherapy* 104 (2018), pp. 496–508.

[70] K. Turcheniuk, V. N. Mochalin, Y. Gogotsi. "Functionalized Multiwalled Carbon Nanotubes as Ultrasound Contrast Agents". In: *Nano Letters* 12.11 (2012), pp. 5711–5717. DOI: `10.1021/nl303206k`.

[71] R. Studio. *Vantablack: il nuovo materiale più nero del mondo*. `https://www.rivistastudio.com/vantablack-nuovo-materiale-piu-nero-del-mondo/`. 2022.

[72] D. W. Porter et al. "Multiwalled carbon nanotube-induced pulmonary inflammatory and fibrotic responses and genomic changes following aspiration exposure in mice: A 1-year post-exposure study". In: *Toxicology and Applied Pharmacology* 288 (2015), pp. 9–20. DOI: `10.1016/j.taap.2015.06.009`.

[73] J. Dong, Q. Ma. "Integration of inflammation, fibrosis, and cancer induced by carbon nanotubes". In: *Nanotoxicology* 13.9 (2019), pp. 1244–1274. DOI: `10.1080/17435390.2019.1651920`.

[74] C. A. Poland et al. "Inhaled carbon nanotubes reach the subpleural tissue in mice". In: *Nature Nanotechnology* 4 (2009), pp. 747–751. DOI: `10.1038/nnano.2009.305`.

[75] A. A. Shvedova et al. “Unusual inflammatory and fibrogenic pulmonary responses to single-walled carbon nanotubes in mice”. In: *American Journal of Physiology - Lung Cellular and Molecular Physiology* 289.5 (2005), pp. L698–L708. DOI: `10.1152/ajplung.00084.2005`.

[76] J. P. Ryman-Rasmussen et al. “Profibrotic Activity of Multiwalled Carbon Nanotubes Upon Prolonged Exposures in Different Human Lung Cell Types”. In: *Applied In Vitro Toxicology* 3.2 (2017), pp. 114–124. DOI: `10.1089/aivt.2017.0033`.

[77] Y. Sato et al. “Distribution and Fibrotic Response Following Inhalation Exposure to Multi-Walled Carbon Nanotubes”. In: *Particle and Fibre Toxicology* 10.33 (2019), pp. 1–17. DOI: `10.1186/s12989-016-0172-2`.

[78] Z. T. Gwanzura, W. J. Perold, A.-M. Engelbrecht. “In Vitro Cytotoxicity of Single Walled Carbon Nanotube Bioconjugates on Cancer Cells”. In: *Engineering Proceedings* 109.1 (2025), p. 6.

[79] K. Donaldson, C. A. Poland, et al. “Asbestos, carbon nanotubes and the pleural mesothelium: a review of the hypothesis regarding the role of long fibre retention in the parietal pleura, inflammation and mesothelioma”. In: *Particle and Fibre Toxicology* 7.5 (2010), pp. 1–29. DOI: `10.1186/1743-8977-7-5`.

[80] I. A. for Research on Cancer (IARC). *Assessment of the Carcinogenicity of Carbon Nanotubes in the Respiratory System.* IARC Monographs, Working Group Report. 2022.

[81] H. Haniu et al. “Carbon Nanotube and Asbestos Exposures Induce Overlapping but Distinct Profiles of Lung Pathology in Non-Swiss Albino CF-1 Mice”. In: *Toxicologic Pathology* 44.7 (2016), pp. 1020–1032. DOI: `10.1177/0192623315620587`.

[82] M. Ali, B.-G. Kim, P. J. Kim. “Applications and environmental risks of carbon nanotubes in agriculture”. In: *Applied Biological Chemistry* 59.6 (2016), pp. 845–856.

[83] A. G. Nasibulin et al. “Carbon nanotubes in wind turbine blades and composite hulls”. In: *Wikipedia: Applications of Carbon Nanotubes* (2024). Accessed May 2025.

[84] M. J. Biercuk et al. “Carbon nanotube composites for thermal management”. In: *arXiv preprint cond-mat/0205418* (2002).

[85] Y. Bai et al. “Carbon nanotube bundles with tensile strength over 80 GPa”. In: *Nature nanotechnology* 13.7 (2018), pp. 589–595.

[86] B. Vigolo et al. “Macroscopic fibers and ribbons of oriented carbon nanotubes”. In: *Science* 290.5495 (2000), pp. 1331–1334.

[87] K. Jiang, Q. Li, S. Fan. “Spinning continuous carbon nanotube yarns”. In: *Nature* 419.6909 (2002), pp. 801–801.

[88] H. Zhu et al. “Direct synthesis of long single-walled carbon nanotube strands”. In: *Science* 296.5569 (2002), pp. 884–886.

[89] N. Behabtu, M. J. Green, M. Pasquali. “Carbon nanotube-based neat fibers”. In: *Nano today* 3.5-6 (2008), pp. 24–34.

[90] R. J. Headrick et al. “Structure–property relations in carbon nanotube fibers by downscaling solution processing”. In: *Advanced Materials* 30.9 (2018), p. 1704482.

[91] S. Duan et al. “Enhanced osteogenic differentiation of mesenchymal stem cells on poly (l-lactide) nanofibrous scaffolds containing carbon nanomaterials”. In: *Journal of Biomedical Materials Research Part A* 103.4 (2015), pp. 1424–1435.

[92] K. Li et al. “Self-assembly of graphene on carbon nanotube surfaces”. In: *Scientific reports* 3.1 (2013), pp. 1–4.

[93] P. Saini, M. Arora. “Microwave absorption and EMI shielding behavior of nanocomposites based on intrinsically conducting polymers, graphene and carbon nanotubes”. In: *New polymers for special applications* 3 (2012), pp. 73–112.

[94] W. Khan, R. Sharma, P. Saini. “Carbon nanotube-based polymer composites: synthesis, properties and applications”. In: *Carbon Nanotubes-Current Progress of their Polymer Composites*. InTech, 2016.

[95] G. Berrod et al. “Reinforcement of siloxane elastomers by silica. Interactions between an oligomer of poly (dimethylsiloxane) and a fumed silica”. In: *Journal of Applied Polymer Science* 23.9 (1979), pp. 2579–2590.

[96] P. Saini. *Fundamentals of conjugated polymer blends, copolymers and composites: synthesis, properties, and applications*. John Wiley & Sons, 2015.

[97] V. Mittal. *Thermoset nanocomposites*. John Wiley & Sons, 2013.

[98] I. Ostanin, R. Ballarini, T. Dumitrică. “Distinct element method modeling of carbon nanotube bundles with intertube sliding and dissipation”. In: *Journal of applied mechanics* 81.6 (2014).

[99] J.-F. Colomer et al. “Electron diffraction and microscopy of single-wall carbon nanotube bundles produced by different methods”. In: *The European Physical Journal B-Condensed Matter and Complex Systems* 27.1 (2002), pp. 111–118.

[100] A. Thess et al. “Crystalline ropes of metallic carbon nanotubes”. In: *science* 273.5274 (1996), pp. 483–487.

[101] E. Gao, W. Lu, Z. Xu. “Strength loss of carbon nanotube fibers explained in a three-level hierarchical model”. In: *Carbon* 138 (2018), pp. 134–142.

[102] A. N. Kolmogorov, V. H. Crespi. “Smoothest bearings: interlayer sliding in multiwalled carbon nanotubes”. In: *Physical Review Letters* 85.22 (2000), p. 4727.

[103] D. Qian, W. K. Liu, R. S. Ruoff. “Load transfer mechanism in carbon nanotube ropes”. In: *Composites science and technology* 63.11 (2003), pp. 1561–1569.

[104] J. Cumings, A. Zettl. "Low-friction nanoscale linear bearing realized from multiwall carbon nanotubes". In: *science* 289.5479 (2000), pp. 602–604.

[105] M. Duchamp et al. "Reinforcing multiwall carbon nanotubes by electron beam irradiation". In: *Journal of Applied Physics* 108.8 (2010), p. 084314.

[106] T. Filleter, H. Espinosa. "Multi-scale mechanical improvement produced in carbon nanotube fibers by irradiation cross-linking". In: *Carbon* 56 (2013), pp. 1–11.

[107] I. Kumar, S. Rana, J. W. Cho. "Cycloaddition reactions: a controlled approach for carbon nanotube functionalization". In: *Chemistry–A European Journal* 17.40 (2011), pp. 11092–11101.

[108] A. Kis et al. "Reinforcement of single-walled carbon nanotube bundles by intertube bridging". In: *Nature materials* 3.3 (2004), pp. 153–157.

[109] J.-P. Salvetat et al. "Elastic and shear moduli of single-walled carbon nanotube ropes". In: *Physical review letters* 82.5 (1999), p. 944.

[110] L. Zalamea, R. B. Pipes. "Interfacial Properties of Carbon Nanotube Arrays". In: *NSTI-Nanotech*. Vol. 1. 2006, pp. 194–197.

[111] L. Galuppi, G. Royer-Carfagni. "Enhanced effective thickness of multi-layered laminated glass". In: *Composites Part B: Engineering* 64 (2014), pp. 202–213.

[112] R. Massabo, F. Campi. "Assessment and correction of theories for multilayered plates with imperfect interfaces". In: *Meccanica* 50 (2015), pp. 1045–1071.

[113] Y.-L. Li, I. A. Kinloch, A. H. Windle. "Direct spinning of carbon nanotube fibers from chemical vapor deposition synthesis". In: *Science* 304.5668 (2004), pp. 276–278.

[114] M. Zhang, K. R. Atkinson, R. H. Baughman. "Multifunctional carbon nanotube yarns by downsizing an ancient technology". In: *Science* 306.5700 (2004), pp. 1358–1361.

[115] OCSiAl. *OCSiAl: Single-Wall Carbon Nanotubes*. `https://ocsial.com/en/`. Accessed: January 18, 2026. 2016.

[116] OCSiAl. *TUBALL Price List*. `https://ocsial.com/assets/documents/TUBALL_Price_List_USA`. Accessed: January 18, 2026. 2022.

[117] S. Badaire et al. "In situ measurements of nanotube dimensions in suspensions by depolarized dynamic light scattering". In: *Langmuir* 20.24 (2004), pp. 10367–10370.

[118] J. Wu et al. "Nanohinge-Induced Plasticity of Helical Carbon Nanotubes". In: *Small* 9.21 (2013), pp. 3561–3566.

[119] J. Wu et al. "Nanotube-chirality-controlled tensile characteristics in coiled carbon metastructures". In: *Carbon* 133 (2018), pp. 335–349.

[120] G. Migliaccio, R. Des Roches, G. Royer-Carfagni. “Theoretical mechanical properties of strands and cables made of wound carbon nanotube fibers”. In: *International Journal of Mechanical Sciences* 236 (2022), pp. 107706/1–19.

[121] J. Park et al. “Accurate measurement of specific tensile strength of carbon nanotube fibers with hierarchical structures by vibroscopic method”. In: *Rsc Advances* 7.14 (2017), pp. 8575–8580.

[122] W. Xie et al. “Dynamic strengthening of carbon nanotube fibers under extreme mechanical impulses”. In: *Nano letters* 19.6 (2019), pp. 3519–3526.

[123] S. Ursache, C. Cerbu, A. Hadăr. “Characteristics of carbon and kevlar fibres, their composites and structural applications in civil engineering–a review”. In: *Polymers* 16.1 (2023), p. 127.

[124] X. Zhang et al. “Simultaneously enhanced tenacity, rupture work, and thermal conductivity of carbon nanotube fibers by raising effective tube portion”. In: *Science advances* 8.50 (2022), eabq3515.

[125] M. Adnan et al. “Bending behavior of CNT fibers and their scaling laws”. In: *Soft Matter* 14.41 (2018), pp. 8284–8292.

[126] X. Wang et al. “High-ampacity power cables of tightly-packed and aligned carbon nanotubes”. In: *advanced functional materials* 24.21 (2014), pp. 3241–3249.

[127] G. Migliaccio, R. Des Roches, G. Royer-Carfagni. “Structures that can be made with carbon nanotube fibers but not with other materials”. In: *Journal of Engineering Mechanics* 148.12 (2022), p. 04022077.

[128] L. Galuppi, V. A. Muratore. “A refined model for the effective tensile stiffness of Carbon NanoTube fibers”. In: *International Journal of Mechanical Sciences* 251 (2023), p. 108303.

[129] B. Natarajan. “Processing-structure-mechanical property relationships in direct formed carbon nanotube articles and their composites: A review”. In: *Composites Science and Technology* 225 (2022), p. 109501.

[130] H. Kim et al. “Bio-inspired stretchable and contractible tough fiber by the hybridization of GO/MWNT/polyurethane”. In: *ACS applied materials & interfaces* 11.34 (2019), pp. 31162–31168.

[131] J. A. Lee, R. H. Baughman, S. J. Kim. “High performance electrochemical and electrothermal artificial muscles from twist-spun carbon nanotube yarn”. In: *Nano Convergence* 2.1 (2015), p. 8.

[132] J. Foroughi, G. Spinks. “Carbon nanotube and graphene fiber artificial muscles”. In: *Nanoscale Advances* 1.12 (2019), pp. 4592–4614.

[133] Y. Jang et al. “Carbon nanotube yarn for fiber-shaped electrical sensors, actuators, and energy storage for smart systems”. In: *Advanced Materials* 32.5 (2020), p. 1902670.

[134] U. o. T. a. D. Mei Zhang. *Scientific Image — Multiwalled Carbon Nanotube Yarn.* https://www.nisenet.org/catalog/scientific-image-multiwalled-carbon-nanotube-yarn-0. Accessed: 2025-10-09; Provided to NISE Network partners with attribution for non-profit educational use. 2014.

[135] A. Bogdanovich et al. "Fabrication and mechanical characterization of carbon nanotube yarns, 3-D braids, and their composites". In: *SAMPE journal* 43.1 (2007), pp. 6–19.

[136] J. Lee et al. "Direct spinning and densification method for high-performance carbon nanotube fibers". In: *Nature communications* 10.1 (2019), p. 2962.

[137] S. Ramesh et al. "Dissolution of pristine single walled carbon nanotubes in superacids by direct protonation". In: *The Journal of Physical Chemistry B* 108.26 (2004), pp. 8794–8798.

[138] A. N. G. Parra-Vasquez et al. "Spontaneous dissolution of ultralong single-and multiwalled carbon nanotubes". In: *Acs Nano* 4.7 (2010), pp. 3969–3978.

[139] C. Jiang et al. "Macroscopic nanotube fibers spun from single-walled carbon nanotube polyelectrolytes". In: *ACS nano* 8.9 (2014), pp. 9107–9112.

[140] D. E. Tsentalovich et al. "Influence of carbon nanotube characteristics on macroscopic fiber properties". In: *ACS applied materials & interfaces* 9.41 (2017), pp. 36189–36198.

[141] H. H. Yang. "Aromatic high-strength fibers". In: *(No Title)* (1989).

[142] V. Sabelkin et al. "Tensile loading behavior of carbon nanotube wires". In: *Carbon* 50.7 (2012), pp. 2530–2538.

[143] H.-i. Kim et al. "Tensile properties of millimeter-long multi-walled carbon nanotubes". In: *Scientific reports* 7.1 (2017), p. 9512.

[144] I. R. Siqueira et al. "Fully recyclable carbon nanotube fibers". In: *Carbon* 233 (2025), p. 119899.

[145] K. Koziol et al. "High-performance carbon nanotube fiber". In: *Science* 318.5858 (2007), pp. 1892–1895.

[146] X. Zhang et al. "Carbon nanotube fibers with dynamic strength up to 14 GPa". In: *Science* 384.6702 (2024), pp. 1318–1323.

[147] I. Toray Industries. *Torayca Carbon Fiber Products Overview.* Accessed: 2025-10-25. URL: https://www.cf-composites.toray/products/carbon_fiber/.

[148] I. Toray Industries. *Typical Properties of TORAYCA® Carbon Fibers.* Accessed: 2025-10-25. URL: https://toray-cfe.com/wp-content/uploads/2020/12/toray-torayca-fibers-typical-properties.pdf.

[149] T. C. E. GmbH. *Product Data Sheet: TSG01 Carbon Fiber Filament Yarn.* Accessed: 2025-10-25. URL: https://www.teijincarbon.com/fileadmin/user_upload/Datenblaetter/Filament_Yarn/Product_Data_Sheet_TSG01en__EU_Filament_.pdf.

[150] M. C. Corporation. *Carbon Fiber Tow (Continuous Fiber) Product Data Sheet.* Accessed: 2025-10-25. URL: `https://www.m-chemical.co.jp/carbon-fiber/pdf/tow/Carbon%20Fiber%20Tow%20(Continuous%20Fiber)%2020210730.pdf`.

[151] Dragonplate. *AS4 HexTow Carbon Fiber Datasheet.* Accessed: 2025-10-25. URL: `https://dragonplate.com/images/uploaded/pdfs/fiberspecs/as4_hextow_datasheet.pdf`.

[152] H. Corporation. *HexTow IM7 Carbon Fiber Datasheet.* Accessed: 2025-10-25. URL: `https://www.hexcel.com/user_area/content_media/raw/IM7_HexTow_DataSheet.pdf`.

[153] D. Safety, Construction. *Kevlar Technical Guide.* Accessed: 2025-10-25. URL: `https://www.dupont.com/content/dam/dupont/amer/us/en/safety/public/documents/en/Kevlar_Technical_Guide_0319.pdf`.

[154] L. Toyobo Co. *Zylon (PBO) High-Performance Fiber Overview.* Accessed: 2025-10-25. URL: `https://www.aramid.com/zylon-pbo/`.

[155] FibrXL. *Dyneema Performance Data Sheet.* Accessed: 2025-10-25. URL: `https://fibrxl.com/wp-content/uploads/2020/07/FibrXL-PDS-performance-0720-DEF-Dyneema.pdf`.

[156] A. H. Corp. *High-Performance Glass Fiber Products.* Accessed: 2025-10-25. URL: `https://www.agy.com/`.

[157] I. Technologies. *Innegra S Fiber Datasheet.* Accessed: 2025-10-25. URL: `https://media.easycomposites.eu/datasheets/InnegraSfibre.pdf`.

[158] B. Ltd. *ampliTex 5039 Flax Fiber Reinforcement Datasheet.* Accessed: 2025-10-25. URL: `https://pdf.nauticexpo.it/pdf-en/bcomp-ltd/amplitex-5039/51016-100888.html`.

[159] I. RheTech. *RheVision Flax Fiber Reinforced Composites.* Accessed: 2025-10-25. URL: `https://www.rhetech.com/what-we-offer/rhevision/flax-fiber-reinforced/`.

[160] C. T. Ltd. *CompPair Healable Composite System Technical Datasheet.* Accessed: 2025-10-25. URL: `https://www.comppair.ch/_files/ugd/7c6329_1657ea7c85584e8f826a6a4bc00ae397.pdf`.

[161] DexMat. *cnt-products.* `https://dexmat.com/cnt-products/`. 2022.

[162] P. Porwal, I. Beyerlein, S. Phoenix. “Statistical strength of twisted fiber bundles with load sharing controlled by frictional length scales”. In: *Journal of Mechanics of materials and Structures* 2.4 (2007), pp. 773–791.

[163] F. Vitale et al. “Neural stimulation and recording with bidirectional, soft carbon nanotube fiber microelectrodes”. In: *ACS nano* 9.4 (2015), pp. 4465–4474.

[164] M. D. McCauley et al. “In vivo restoration of myocardial conduction with carbon nanotube fibers”. In: *Circulation* 134.1 (2016), pp. 1–13.

[165] J. S. Yan et al. “Biocompatibility studies of macroscopic fibers made from carbon nanotubes: Implications for carbon nanotube macrostructures in biomedical applications”. In: *Carbon* 173 (2021), pp. 462–476.

[166] L. W. Taylor et al. “Washable, sewable, all-carbon electrodes and signal wires for electronic clothing”. In: *Nano Letters* 21.17 (2021), pp. 7093–7099.

[167] National Nanotechnology Coordination Office (NNCO). *Cable Harnesses from Carbon Nanotube Materials*. Tech. rep. National Nanotechnology Initiative, 2018. URL: `https://www.nano.gov/sites/default/files/cableharnesses%20fromcntmaterials-nro.pdf`.

[168] W. Gao et al. “Macroscopically aligned carbon nanotubes for flexible and high-temperature electronics, optoelectronics, and thermoelectrics”. In: *Journal of Physics D: Applied Physics* 53.6 (2019), p. 063001.

[169] C. A. Materials. *Transparent Conductive Films with Carbon Nanotubes*. `https://chasmtek.com/technology/transparent-conductive-films/`. Accessed: 2025-06-04. 2019.

[170] K. M. Joseph, colleagues. “Lightweight Copper–Carbon Nanotube Core–Shell Composites with Enhanced Strength and Electrical Conductivity”. In: *C* 9.2 (2023), p. 43.

[171] M. Park et al. “Performance enhancement of graphene assisted CNT/Cu composites for lightweight electrical cables”. In: *Carbon* 179 (2021), pp. 53–59.

[172] K.-H. Ryu et al. “Core-sheath composite electric cables with highly conductive self-assembled carbon nanotube wires and flexible macroscale insulating polymers for lightweight, metal-free motors”. In: *Advanced Composites and Hybrid Materials* 8.2 (2025), pp. 1–10.

[173] F. Mirri et al. “Lightweight, flexible, high-performance carbon nanotube cables made by scalable flow coating”. In: *ACS applied materials & interfaces* 8.7 (2016), pp. 4903–4910.

[174] Y. Zhang et al. “Carbon nanotube fiber supercapacitors for wearable electronics”. In: *Advanced Functional Materials* 32.8 (2022), p. 2109226.

[175] A. B. Dalton et al. “Super-tough carbon-natube fibres”. In: *Nature* 423 (2003), p. 703.

[176] F. Stüssi. *Über die Entwicklung der Wissenschaft im Brückenbau*. Naturforschenden Gesellschaft, 1964.

[177] M. De Miranda. “Long-span bridges”. In: *Innovative bridge design handbook*. Elsevier, 2022, pp. 463–508.

[178] G. Galilei. *Discorsi e Dimostrazioni Matematiche intorno a due Nuove Scienze Attinenti alla Meccanica*. Elsevier, 1638.

[179] J.-W. Kim et al. “Modifying carbon nanotube fibers: A study relating apparent interfacial shear strength and failure mode”. In: *Carbon* 173 (2021), pp. 857–869.

[180] S. Damolini. “Carbon nanotubes and their application to very long span bridges”. PhD thesis. Massachusetts Institute of Technology, 2009.

[181] A. Carpinteri, N. M. Pugno. “Super-bridges suspended over carbon nanotube cables”. In: *Journal of Physics: Condensed Matter* 20.47 (2008), p. 474213.

[182] WeBuildValue. *Messina Strait Bridge — Stories Behind Projects*. `https://www.webuildvalue.com/en/stories-behind-projects/messina-strait-bridge.html`. Accessed: 2025-10-10. n.d.

[183] F. Mazzolani, B. Faggiano, G. Martire. “Design aspects of the AB prototype in the Qiandao Lake”. In: *Procedia Engineering* 4 (2010), pp. 21–33.

[184] A. Minoretti et al. “The Future of the Tunnel Crossing: The Submerged Floating Tube Bridge”. In: *Structural Engineering International* 30.4 (2020), pp. 493–497. DOI: `10.1080/10168664.2020.1775165`.

[185] H. Ren et al. “Design and Evaluation of Novel Submerged Floating Tunnel Models Based on Dynamic Similarity”. In: *Applied Sciences* 14.9 (2024), p. 3724. DOI: `10.3390/app14093724`.

[186] X. Luo et al. “Numerical Simulation of Dynamic Response of Submerged Floating Tunnel under Regular Wave Conditions”. In: *Shock and Vibration* 2022 (2022). DOI: `10.1155/2022/4940091`.

[187] Tungt. *Rorbruer nærmere realisering*. `https://www.tungt.no/article/view/768837/rorbruer_naermere_realisering`. 2022.

[188] D. Appell. “Stairway to the heavens”. In: *Physics World* 24.12 (2011), p. 30.

[189] G. Migliaccio. *Mechanical properties of cables made with helically wound carbon-nanotube fibers for advanced structural applications*. Presentazione XXV Convegno AIMETA, Palermo, 4-8 settembre. 2022.

[190] N. M. Pugno. “On the strength of the carbon nanotube-based space elevator cable: from nanomechanics to megamechanics”. In: *Journal of Physics: Condensed Matter* 18.33 (2006), S1971.

[191] RBTH. *L’ascensore spaziale: il sogno*. `https://it.rbth.com/scienza-e-tech/81553-lascensore-spaziale-il-sogno`. 2022.

[192] N. M. Pugno. “The role of defects in the design of space elevator cable: From nanotube to megatube”. In: *Acta Materialia* 55.15 (2007), pp. 5269–5279.

[193] Technovelgy. *Diamond Crystal - A continuous pseudo-one dimensional diamond crystal maybe a nanotube?* `http://www.technovelgy.com/ct/Science-Fiction-News.asp?NewsNum=720`. 2006.

[194] B. C. Edwards, E. A. Westling. *The space elevator*. Bc Edwards, 2003.

[195] C. Boni, G. Royer-Carfagni. “Flextegrity arched structures for Lunar bases built from indigenous materials”. In: *Acta Astronautica* 215 (2024), pp. 107–116.

[196] J. A. Happel. “Indigenous materials for lunar construction”. In: (1993).

[197] K. Liew, C. Wong, M. Tan. “Tensile and compressive properties of carbon nanotube bundles”. In: *Acta materialia* 54.1 (2006), pp. 225–231.

[198] T. S. Gspann et al. “Mechanical properties of carbon nanotube fibres: St Venant’s principle at the limit and the role of imperfections”. In: *Carbon* 93 (2015), pp. 1021–1033.

[199] X. Liu et al. “Microstructural evolution of carbon nanotube fibers: deformation and strength mechanism”. In: *Nanoscale* 5.5 (2013), pp. 2002–2008.

[200] X. Wei, M. Naraghi, H. D. Espinosa. “Optimal length scales emerging from shear load transfer in natural materials: application to carbon-based nanocomposite design”. In: *ACS nano* 6.3 (2012), pp. 2333–2344.

[201] X. Sun et al. “An elastic model for bioinspired design of carbon nanotube bundles”. In: *Acta Mechanica Sinica* 31.2 (2015), pp. 205–215.

[202] D. Mählich, O. Eberhardt, T. Wallmersperger. “Numerical simulation of the mechanical behavior of a carbon nanotube bundle”. In: *Acta Mechanica* 232.2 (2021), pp. 483–494.

[203] X. Wei et al. “A new Monte Carlo model for predicting the mechanical properties of fiber yarns”. In: *Journal of the Mechanics and Physics of Solids* 84 (2015), pp. 325–335.

[204] M. Bathe et al. “Cytoskeletal bundle mechanics”. In: *Biophysical journal* 94.8 (2008), pp. 2955–2964.

[205] Y. W. Lin et al. “A Non-Linear Spring Model for Predicting Modal Behavior of Oscillators Built from Double Walled Carbon Nanotubes”. In: *Journal of Nano Research*. Vol. 60. Trans Tech Publ. 2019, pp. 21–32.

[206] C. Li, T.-W. Chou. “Elastic moduli of multi-walled carbon nanotubes and the effect of van der Waals forces”. In: *Composites Science and Technology* 63.11 (2003), pp. 1517–1524.

[207] Y. Huang, J. Wu, K.-C. Hwang. “Thickness of graphene and single-wall carbon nanotubes”. In: *Physical review B* 74.24 (2006), p. 245413.

[208] V. Iakovleva, C. J. Vanegas. “On the solution of differential equations with delayed and advanced arguments”. In: *Electronic Journal of Differential Equations (EJDE)[electronic only]* 2005 (2005), pp. 57–63.

[209] Y. Kyrychko, S. Hogan. “On the use of delay equations in engineering applications”. In: *Journal of vibration and control* 16.7-8 (2010), pp. 943–960.

[210] A. C. Eringen, D. G. B. Edelen. “On nonlocal elasticity”. In: *International journal of engineering science* 10.3 (1972), pp. 233–248.

[211] A. C. Eringen. “On differential equations of nonlocal elasticity and solutions of screw dislocation and surface waves”. In: *Journal of applied physics* 54.9 (1983), pp. 4703–4710.

[212] S. A. Silling, M. Zimmermann, R. Abeyaratne. “Deformation of a peridynamic bar”. In: *Journal of Elasticity* 73.1 (2003), pp. 173–190.

[213] A. R. Aguiar et al. “Boundary layer effects in a finite linearly elastic peridynamic bar”. In: *Latin American Journal of Solids and Structures* 15 (2018).

[214] A. R. Aguiar, G. Royer-Carfagni, A. B. Seitenfuss. “Wiggly strain localizations in peridynamic bars with non-convex potential”. In: *International Journal of Solids and Structures* 138 (2018), pp. 1–12.

[215] A. Kosov, E. Semenov. “On analytic periodic solutions to Nonlinear Differential Equations with Delay (Advance)”. In: *Russian Mathematics* 62.10 (2018), pp. 30–36.

[216] K. C. Patidar, K. K. Sharma. “Uniformly convergent non-standard finite difference methods for singularly perturbed differential-difference equations with delay and advance”. In: *International Journal for Numerical Methods in Engineering* 66.2 (2006), pp. 272–296.

[217] K.-S. Chiu, M. Pinto. “Oscillatory and periodic solutions in alternately advanced and delayed differential equations”. In: *Carpathian Journal of Mathematics* (2013), pp. 149–158.

[218] A. Coco et al. “A second order finite-difference ghost-point method for elasticity problems on unbounded domains with applications to volcanology”. In: *Communications in Computational Physics* 16.4 (2014), pp. 983–1009.

[219] J. Renaudeau et al. “Implicit modelling of geological structures: A Cartesian grid method handling discontinuities with ghost points”. In: *WIT Transactions on Engineering Sciences* 122 (2019), pp. 189–199.

[220] C. Li et al. “Interfacial shear strengths between carbon nanotubes”. In: *Nanotechnology* 21.11 (2010), p. 115704.

[221] S. H. Kordkheili, H. Moshrefzadeh-Sani. “Mechanical properties of double-layered graphene sheets”. In: *Computational Materials Science* 69 (2013), pp. 335–343.

[222] M. Lin et al. “Load-transfer and failure behaviors of crosslinked interfaces in collagen-mimic carbon nanotube bundles”. In: *International Journal of Mechanical Sciences* 135 (2018), pp. 376–382.

[223] A. Matatyaho Ya’akobi et al. “Electron microscopy study of BNNTs synthesized by high temperature–pressure method and purified by high-temperature steam”. In: *Journal of Materials Research* (2022), pp. 1–14.

[224] A. Cardou, C. Jolicoeur. “Mechanical models of helical strands”. In: *Applied mechanics reviews* 50.1 (1997), pp. 1–14.

[225] C. M. Leech. “The modelling and analysis of the mechanics of ropes”. In: *Solid Mechanics and its Applications.* Vol. 209. Springer, 2014, pp. 1–132.

[226] Z.-L. Zhao et al. “Mechanical properties of carbon nanotube ropes with hierarchical helical structures”. In: *Journal of the Mechanics and Physics of Solids* 71 (2014), pp. 64–83.

[227] J. D. Watson, F. H. C. Crick. “The structure of DNA”. In: *Cold Spring Harbor symposia on quantitative biology.* Vol. 18. Cold Spring Harbor Laboratory Press. 1953, pp. 123–131.

[228] B. D. Coleman, D. Swigon, I. Tobias. “Elastic stability of DNA configurations. II. Supercoiled plasmids with self-contact”. In: *Physical Review E* 61.1 (2000), p. 759.

[229] I. Tobias, D. Swigon, B. D. Coleman. “Elastic stability of DNA configurations. I. General theory”. In: *Physical Review E* 61.1 (2000), p. 747.

[230] J. M. T. Thompson, G. H. M. van der Heijden, S. Neukirch. “Supercoiling of DNA plasmids: mechanics of the generalized ply”. In: *Proceedings of the Royal Society of London. Series A: Mathematical, Physical and Engineering Sciences* 458.2020 (2002), pp. 959–985.

[231] B. D. Coleman, D. Swigon. “Theory of self–contact in Kirchhoff rods with applications to supercoiling of knotted and unknotted DNA plasmids”. In: *Philosophical Transactions of the Royal Society of London. Series A: Mathematical, Physical and Engineering Sciences* 362.1820 (2004), pp. 1281–1299.

[232] S. Neukirch, A. Goriely, A. C. Hausrath. “Chirality of coiled coils: elasticity matters”. In: *Physical review letters* 100.3 (2008), p. 038105.

[233] N. Clauvelin, B. Audoly, S. Neukirch. “Mechanical response of plectonemic DNA: An analytical solution”. In: *Macromolecules* 41.12 (2008), pp. 4479–4483.

[234] B. DJuričković, A. Goriely, J. H. Maddocks. “Twist and stretch of helices explained via the Kirchhoff-Love rod model of elastic filaments”. In: *Physical review letters* 111.10 (2013), p. 108103.

[235] E. L. Starostin, G. H. M. Van der Heijden. “Theory of equilibria of elastic 2-braids with interstrand interaction”. In: *Journal of the Mechanics and Physics of Solids* 64 (2014), pp. 83–132.

[236] J. Kalliauer et al. “A new approach to the mechanics of DNA: Atoms-to-beam homogenization”. In: *Journal of the Mechanics and Physics of Solids* 143 (2020), p. 104040.

[237] S. Neukirch, G. H. M. van der Heijden. “Geometry and mechanics of uniform n-plies: from engineering ropes to biological filaments”. In: *Journal of elasticity* 69 (2002), pp. 41–72.

[238] G. Bellussi et al. *Ullmann’s encyclopedia of industrial chemistry.* 7th ed. Wiley-VCH, 2011.

[239] L. R. G. Treloar. “The Geometry of Multi-Ply Yarns”. In: *Journal of the Textile Institute Transactions* 47.6 (1956), T348–T368.

[240] W. B. Fraser, D. M. Stump. “The equilibrium of the convergence point in two-strand yarn plying”. In: *International journal of solids and structures* 35.3-4 (1998), pp. 285–298.

[241] G. H. M. van der Heijden et al. “Instability and self-contact phenomena in the writhing of clamped rods”. In: *International Journal of Mechanical Sciences* 45.1 (2003), pp. 161–196.

[242] H. M. James, E. Guth. “Theory of the elastic properties of rubber”. In: *The Journal of Chemical Physics* 11.10 (1943), pp. 455–481.

[243] P. J. Flory. “Molecular theory of rubber elasticity”. In: *Polymer journal* 17.1 (1985), pp. 1–12.

[244] R. S. Rivlin. “Large Elastic Deformations of Isotropic Materials: VI. Further Results in the Theory of Torsion, Shear and Flexure”. In: *Philosophical Transactions of the Royal Society of London* 242.845 (1949), pp. 173–195.

[245] S. S. Antman. “The theory of rods”. In: *Linear Theories of Elasticity and Thermoelasticity: Linear and Nonlinear Theories of Rods, Plates, and Shells.* Springer, 1972, pp. 641–703.

[246] A. E. H. Love. *A treatise on the mathematical theory of elasticity.* Vol. 2. Cambridge University Press, 1893.

[247] A. E. H. Love. *A treatise on the mathematical theory of elasticity.* 4th edition. Dover Publications, 1944.

[248] R. R. Archer et al. *An introduction to the mechanics of solids.* McGraw-Hill Book Company, Inc., 1959.

[249] T. G. Sano, M. Pezzulla, P. M. Reis. “A Kirchhoff-like theory for hard magnetic rods under geometrically nonlinear deformation in three dimensions”. In: *Journal of the Mechanics and Physics of Solids* 160 (2022), p. 104739.

[250] W. Thomson, P. G. Tait. *Treatise on natural philosophy.* Vol. 1. Cambridge University Press, 1912.

[251] P. Grandgeorge, T. G. Sano, P. M. Reis. “An elastic rod in frictional contact with a rigid cylinder”. In: *Journal of the Mechanics and Physics of Solids* 164 (2022), p. 104885.

[252] L. Liu et al. “Mechanics and topology of twisted hyperelastic filaments under prescribed elongations: Experiment, theory, and simulation”. In: *Journal of the Mechanics and Physics of Solids* 182 (2024), p. 105478.

[253] L. da Vinci. *Codex Atlanticus.* Original handwritten manuscript at the Veneranda Biblioteca Ambrosiana in Milan, digitalized version available online. 1478–1518.

[254] C. K. L. Davies, D. K. De, A. G. Thomas. “Characterization of the behavior of rubber for engineering design purposes. 1. Stress-strain relations”. In: *Rubber chemistry and technology* 67.4 (1994), pp. 716–728.

[255] M. Yamamoto. “Phenomenological theory of visco-elasticity of three dimensional bodies”. In: *Journal of the Physical Society of Japan* 14.3 (1959), pp. 313–330.

[256] G. A. Costello. *Theory of wire rope*. Springer Science & Business Media, 2012.

[257] C. Boni, V. A. Muratore, G. Royer-Carfagni. “Experimental assessment of the eigenstress state in two-ply yarns and its effect on tensile properties”. In: *Journal of the Mechanics and Physics of Solids* 187 (2024), p. 105613.

[258] B. L. Hardy et al. “Direct evidence of Neanderthal fibre technology and its cognitive and behavioral implications”. In: *Scientific Reports* 10.1 (2020), p. 4889.

[259] Wikimedia Commons. *File: Egyptian display - San Diego Museum of Man - DSC06931 02.JPG — Wikimedia Commons, the free media repository*. `https://commons.wikimedia.org/w/index.php?title=File:Egyptian_display_-_San_Diego_Museum_of_Man_-_DSC06931_02.JPG&oldid=1043348037`. [Online; accessed 7 July 2025]. 2025.

[260] Wikipedia contributors. *Sumer — Wikipedia, The Free Encyclopedia*. `https://en.wikipedia.org/w/index.php?title=Sumer&oldid=1297726803`. [Online; accessed 7 July 2025]. 2025.

[261] S. Rana, R. Fangueiro. *Braided structures and composites: production, properties, mechanics, and technical applications*. CRC Press, 2015.

[262] R. W. Hertzberg. *Deformation and Fracture Mechanics of Engineering Materials*. 4th. John Wiley & Sons, 1996.

[263] M. Zhang, K. Atkinson, R. Baughman. “Strong, transparent, multifunctional, carbon nanotube sheets”. In: *Science* 306.5700 (2004), pp. 1358–1361.

[264] P. K. Porwal, I. J. Beyerlein, S. L. Phoenix. “Statistical strength of a twisted fiber bundle: an extension of Daniels equal-load-sharing parallel bundle theory”. In: *Journal of Mechanics of Materials and Structures* 1.8 (2006), pp. 1425–1447.

[265] M. Piggott. *Load Bearing Fibre Composites*. Pergamon Press, 1980.

[266] J. Hearle, P. Grosberg, S. Backer. *Structural Mechanics of Fibers, Yarns, and Fabrics*. Wiley-Interscience, 2001.

[267] H. Li et al. “Abrasion performance and failure mechanism of fiber yarns based on molecular segmental differences”. In: *Journal of Engineered Fibers and Fabrics* 19 (2024), p. 15589250241228263.

[268] R. Frisch-Fay. *Flexible Bars*. Butterworths, 1962.

[269] R. LeBlanc, B. Windecker. *Joining of Ropes and Cables: Principles and Practice*. Technical Memorandum NASA-TM-104427. NASA, 1991.

[270] C. D. A/S. *Technical Description of Steel Wire Rope*. https://www.certex.dk/en/knowhow/articles-about-steel-wire-rope/technical-description-steel-wire-rope. Accessed: 2025-09-30. n.d.

[271] S. Liu, Z. Du. “Study on the Tensile Behavior of Helical Auxetic Yarns with Finite Element Method”. In: *Materials* 16.1 (2022), p. 122.

[272] L. Pires da Costa et al. “Geometrical and mechanical modeling of polymeric multi-ply yarns”. In: *Applied Sciences* 14.11 (2024), p. 4597.

[273] H. K. Dalfi, M. Tausif, Z. Yousaf. “Effect of twist level on the mechanical performance of S-glass yarns and non-crimp cross-ply composites”. In: *Journal of Industrial Textiles* 51.2_suppl (2022), 2921S–2943S.

[274] J. Hearle, P. Grosberg, S. Backer. “Structural mechanics of fibers, yarns, and fabrics, vol. 1Wiley”. In: *New York* (1969).

[275] D. Phillips et al. “Torsional properties of staple fibre plied yarns”. In: *The Journal of The Textile Institute* 101.7 (2010), pp. 595–612.

[276] *Shimadzu Scientific Instruments*. URL: https://www.shimadzu.it/products/materials-testing/uni-ttm/ez-test/index.html.

[277] W. Weibull. “A statistical theory of strength of materials”. In: *IVB-Handl.* (1939).

[278] Y. Rao, R. J. Farris. “A modeling and experimental study of the influence of twist on the mechanical properties of high-performance fiber yarns”. In: *Journal of applied polymer science* 77.9 (2000), pp. 1938–1949.

[279] A. Lobovsky et al. *Spinning, processing, and applications of carbon nanotube filaments, ribbons, and yarns*. US Patent 6,682,677. Jan. 2004.

[280] V. Gupta. “Solution-spinning processes”. In: *Manufactured fibre technology*. Springer, 1997, pp. 124–138.

[281] A. Mikhalchan et al. “Simultaneous improvements in conversion and properties of molecularly controlled CNT fibres”. In: *Carbon* 179 (2021), pp. 417–424.

[282] W. Lu et al. “State of the art of carbon nanotube fibers: opportunities and challenges”. In: *Advanced materials* 24.14 (2012), pp. 1805–1833.

[283] X. Zhang et al. “Spinning and processing continuous yarns from 4-inch wafer scale super-aligned carbon nanotube arrays”. In: *Advanced materials* 18.12 (2006), pp. 1505–1510.

[284] S.-H. Lee, J. H. Park, S. M. Kim. “Synthesis, property, and application of carbon nanotube fiber”. In: *Journal of the Korean Ceramic Society* 58.2 (2021), pp. 148–159.

[285] S.-Y. Jeon et al. “A predictive model of the tensile strength of twisted carbon nanotube yarns”. In: *Nanotechnology* 28.1 (2016), p. 015703.

[286] D. Asadollahi, M. Shariati. “Investigation of shear forces in twisted carbon nanotube bundles using a structural mechanics approach”. In: *Acta Mechanica* 232.6 (2021), pp. 2425–2441.

[287] S. Vassiliadis, A. Kallivretaki, C. Provatidis. “Mechanical modelling of multi-filament twisted yarns”. In: *Fibers and Polymers* 11.1 (2010), pp. 89–96.

[288] N. Pan, D. Brookstein. “Physical properties of twisted structures. II. Industrial yarns, cords, and ropes”. In: *Journal of applied polymer science* 83.3 (2002), pp. 610–630.

[289] D. Liu, S. Zheng, Y. He. “Effect of friction on the mechanical behavior of wire rope with hierarchical helical structures”. In: *Mathematics and Mechanics of Solids* 24.7 (2019), pp. 2154–2180.

[290] R. Mirzaeifar, Z. Qin, M. J. Buehler. “Mesoscale mechanics of twisting carbon nanotube yarns”. In: *Nanoscale* 7.12 (2015), pp. 5435–5445.

[291] D. U. Shah, P. J. Schubel, M. J. Clifford. “Modelling the effect of yarn twist on the tensile strength of unidirectional plant fibre yarn composites”. In: *Journal of Composite Materials* 47.4 (2013), pp. 425–436.

[292] A. M. Beese et al. “Key factors limiting carbon nanotube yarn strength: exploring processing-structure-property relationships”. In: *ACS nano* 8.11 (2014), pp. 11454–11466.

[293] Y. Shang et al. “Highly twisted double-helix carbon nanotube yarns”. In: *ACS nano* 7.2 (2013), pp. 1446–1453.

[294] J. N. Israelachvili. *Intermolecular and surface forces*. Academic press, 2011.

[295] Y. Zhang et al. “Failure mechanisms of carbon nanotube fibers under different strain rates”. In: *Carbon* 50.8 (2012), pp. 2887–2893.

[296] J. J. Vilatela, J. A. Elliott, A. H. Windle. “A model for the strength of yarn-like carbon nanotube fibers”. In: *ACS nano* 5.3 (2011), pp. 1921–1927.

[297] C. Boni, G. Royer-Carfagni. “Micro-mechanical interpretation of the non-linear tensile response of structured rods. Experiments on prototyped Gedankenmodelle with wavy sub-rods and application to Carbon NanoTube fibers”. In: *International Journal of Non-Linear Mechanics* 160 (2024), p. 104650.

[298] H. Avci et al. “High Performance Fibers: A Review on Current State of Art and Future Challenges”. In: *Journal of Engineering and Architecture Faculty of Eskisehir Osmangazi University* 27.2 (2019), pp. 130–155.

[299] B. Mahltig, T. Grethe. “High-performance and functional fiber materials—a review of properties, scanning electron microscopy SEM and electron dispersive spectroscopy EDS”. In: *Textiles* 2.2 (2022), pp. 209–251.

[300] M. F. Ashby, D. Cebon. “Materials selection in mechanical design”. In: *Le Journal de Physique IV* 3.C7 (1993), pp. C7–1.

[301] M. Abendroth, M. Kuna. “Identification of ductile damage and fracture parameters from the small punch test using neural networks”. In: *Engineering fracture mechanics* 73.6 (2006), pp. 710–725.

[302] ASTM International. *Standard Test Method for Small Punch Testing of Metallic Materials*. ASTM E3205-20. West Conshohocken, PA, USA: ASTM International, 2020.

[303] M. Ciavarella, D. Hills, G. Monno. “The influence of rounded edges on indentation by a flat punch”. In: *Proceedings of the Institution of Mechanical Engineers, Part C: Journal of Mechanical Engineering Science* 212.4 (1998), pp. 319–327.

[304] Fédération Internationale de l’Automobile (FIA). *2026 Formula 1 Technical Regulations*. Issue 8. Approved by the WMSC on multiple dates, most recently 21/06/24 (Chassis) and 11/06/24 (General). Fédération Internationale de l’Automobile (FIA). June 2024. URL: `https://www.fia.com/regulations/fia-formula-1-technical-regulations`.

[305] Wikipedia contributors. *Copper — Wikipedia, The Free Encyclopedia*. `https://en.wikipedia.org/wiki/Copper`. Accessed: 2025-10-28. 2025.

Acknowledgments

I would like to express my deepest gratitude to my supervisor, Prof. Gianni Royer-Carfagni, for his invaluable guidance, wisdom, and great humanity throughout these three years. Like a father in academia, he has shown me the path, allowing me to grow both as a researcher and as a person. His generosity and profound insight into complex problems, together with his constant stream of brilliant ideas and insightful advice, have been fundamental throughout my doctoral journey and for the successful completion of this work.

A special thanks goes to Dr. Claudio Boni, co-supervisor of this thesis and collaborator in many works. Sharing the office with him has been a source of invaluable learning. His clarity, attention to detail, and remarkable intuition have guided me throughout the development of this thesis. A precise, honest and straightforward person, he has been not only a colleague but also a true friend.

I am also sincerely grateful to Prof. Laura Galuppi, who has guided me since my Bachelor's studies through to my Master's degree and encouraged me to pursue this PhD path. Her constant support, insightful guidance, and genuine friendship have been an invaluable source of motivation throughout my academic journey.

I wish to thank Prof. Alessandro Tasora and my colleagues Dr. Salman Zandekarimi, Dr. Peng Chao, Dr. Dario Mangoni, Dr. Dario Fusai, Dr. Lorenzo Santi and Dr. Ali Haydar for their support, collaboration, and stimulating discussions during these years.

I would like to acknowledge DexMat, Inc. for co-founding my PhD scholarship, as well as their kind hospitality in their laboratories in Houston and for the materials supply. I would also like to acknowledge the entire DexMat team, Dmitri Tsentalovich, Prof. Matteo Pasquali, Oliver Dewey, Sofia Izaguirre, Barivure Norbana, Cody Jones, Maayan Hotam, Bryan Guido Hassin, Jill Dupré, Asena Hert, and in particular Dr. Colin Young, for the fruitful scientific discussions and the guidance during my stay in Houston. My gratitude also goes to Dallara for welcoming me in their laboratories and giving me the opportunity to broaden my research experience in the automotive field.

I am grateful to Prof. Luca Collini, Asst. Prof. Corrado Sciancalepore, Asst. Prof. Emanuele Ghio, and Mr. Luca Barchi from the University of Parma for kindly providing access to their laboratories and for their support during several experimental activities, including SEM and optical microscopy observations.

I would like to express my deepest gratitude to my family. To my father Diego and my mother Maria, my grandparents, Vincenzo and Graziella, Angela and Totò, my sister Vanessa, my uncles Massimiliano and Gianluca, my aunts Sabrina and Grazia, my companion Gabrielle and to all my relatives, for their closeness, care, and encouragement.

Finally, I extend my heartfelt thanks to all those who have supported me, directly or indirectly, throughout this journey.

The scholarship for this PhD was jointly funded by DexMat, Inc. and the Italian Government through the National Recovery and Resilience Plan (NRRP), Mission 4, Component 2, Investment 3.3 - Call for tender No. 352 of 09/04/2022 of Italian Ministry of University and Research funded by the European Union – NextGenerationEU.

Part of this research was also supported by Carbon Hub (carbonhub.rice.edu), a research center established within Rice University, Houston, TX, USA.